Modeling and Model-Based Control of Multi-Mode Combustion Engines for Closed-Loop SI/HCCI Mode Transitions with Cam Switching Strategies

by

Patrick H. Gorzelic

A dissertation submitted in partial fulfillment
of the requirements for the degree of
Doctor of Philosophy
(Mechanical Engineering)
in The University of Michigan
2015

Doctoral Committee:

Professor Anna G. Stefanopoulou, Chair
Professor Andre L. Boehman
Erik Hellström, Ford Motor Co.
Professor Ilya Kolmanovsky

This page is dedicated to the 'umthesis' Latex template, which cannot meet Rackham formatting guidelines without a dedication page.

Acknowledgments

Prof. Stefanopoulou and Members of the Dissertation Committee
Jake Larimore, Shyam Jade, and Sandro Nüesch
Jason Martz
Prasad Shingne, Adam Vaughan, and Vas Triantopoulous
Jeff Sterniak (thank God for that guy)
Tom Marino
Li Jiang, Jason Schwanke, Kivanc Temel, Ben Wilcox
Jordan Easter, Niket Prakash, and Shima Nazari
All the people at the Automotive Research Lab who helped out on various occasions
...and everyone else who helped along the way...

Contents

Dedication ii

Acknowledgments iii

List of Tables vii

List of Figures viii

List of Appendices xiii

Abstract xiv

Nomenclature xv

Chapter 1 Introduction 1
1.1 Problem Background and Motivation 1
1.1.1 Overview of Gasoline Multi-mode Combustion 1
1.1.2 The Necessity of Mode Transitions 3
1.1.3 The Challenges of Mode Transitions 4
1.2 Previous Research in SI/HCCI Mode Transitions 7
1.2.1 Open-loop Experimental Studies 7
1.2.2 Modeling and Model-Based Control Approaches 11
1.3 Contribution of the Research 13
1.4 Outline of the Dissertation 14

Chapter 2 Mean Value Engine Model for Multi-Mode SI/HCCI Combustion . . 16
2.1 Engine Modeling Overview 16
2.2 Air Path Model 18
2.2.1 Manifold Dynamics and Flow Restrictions 19
2.2.2 Turbocharger 20
2.2.3 Actuator Dynamics 24
2.2.4 Integrating Continuous Cam Phaser Dynamics with Instantaneous Cam Switching 26
2.3 SI Combustion Model 27
2.3.1 Overview 27

2.3.2 Model Calculations . . . 29
2.3.3 Steady-State Parameterization Results . . . 34
2.4 HCCI Combustion Model . . . 35
2.4.1 Model Calculations . . . 38
2.4.2 Steady-State Fitting Results . . . 45

Chapter 3 Capturing Transient Data in SI-HCCI Mode Transitions . . . 48
3.1 Augmented Parameter for SI-HCCI Mode Transitions . . . 48
3.1.1 Overview of Open-Loop Mode Transtion Experiments . . . 48
3.1.2 Mode Transition Predictions Using Crank Angle-Based Model . . . 51
3.1.3 Residual Gas Temperature Correction for Initial HCCI Cycle . . . 53
3.2 Adaptive Tuning of Augmented Parameter . . . 54
3.2.1 Motivation and Description of Adaptive Tuning Method . . . 54
3.2.2 Adaptive Tuning Simulations . . . 56
3.3 Model Evaluation in Multiple SI-HCCI Transition Conditions . . . 58

Chapter 4 SI-HCCI Mode Transition Control . . . 63
4.1 High-Level Mode Transition Strategy . . . 63
4.1.1 Cam Phasing Versus Cam Switching Strategies . . . 64
4.1.2 Considerations for the Cam Switching Strategy . . . 66
4.1.3 Walkthrough of SI-HCCI Transitions with Chosen Strategy . . . 70
4.2 SI Phase Controller . . . 73
4.2.1 Control Problem Overview . . . 73
4.2.2 Air path control . . . 76
4.2.3 Combustion Control . . . 78
4.2.4 Cam Switching Logic and the Final SI Cycle . . . 81
4.2.5 Controller Tuning Variables . . . 81
4.3 HCCI Phase Controller . . . 82
4.3.1 Control Problem Overview . . . 82
4.3.2 Combustion Control . . . 84
4.3.3 Combustion State Estimator . . . 89
4.3.4 Controller Tuning Variables . . . 91
4.4 Experimental Results . . . 92
4.4.1 Calibration Effort . . . 97

Chapter 5 Online Parameter Adaptation for Improved Model-Based Combustion Control in SI/HCCI Transitions . . . 102
5.1 Parameter Adaptation Method . . . 103
5.1.1 Overview . . . 103
5.1.2 SI Model Adaptation . . . 104
5.1.3 HCCI Model Adaptation . . . 105
5.2 Experimental Results . . . 107
5.2.1 Successive Adaptations at One Operating Condition . . . 108
5.2.2 Differing Operating Conditions . . . 119

Chapter 6 HCCI-SI Mode Transition Control . . . 123

6.1 High-Level Mode Transition Strategy . . . 123
6.1.1 Considerations for the Cam Switching Strategy . . . 124
6.1.2 Walkthrough of HCCI-SI Transitions with Chosen Strategy . . . 129
6.2 HCCI Phase Controller . . . 131
6.2.1 Control Problem Overview . . . 131
6.2.2 Air Path Control . . . 134
6.2.3 Cam Switch Logic and the Final HCCI Cycle . . . 140
6.2.4 Controller Tuning Variables . . . 140
6.3 SI Phase Controller . . . 141
6.3.1 Control Problem Overview . . . 141
6.3.2 Air Path Control . . . 142
6.3.3 Combustion Control . . . 153
6.3.4 Controller Tuning Variables . . . 155
6.4 Experimental Results . . . 155
6.4.1 Calibration Effort . . . 162
6.4.2 The SI/HCCI Transition Control Architecture as a Full HCCI Controller . . . 164

Chapter 7 Conclusions and Future Work . . . 166
7.1 Research Summary and Conclusions . . . 166
7.1.1 Control-Oriented Modeling . . . 167
7.1.2 Control Development . . . 168
7.2 Future Work . . . 174

Appendices . . . 176

Bibliography . . . 189

List of Tables

Table

1.1 Summary of operating condition differences among SI, and HCCI combustion modes for the recompression HCCI method. . . . 6

2.1 Geometry of experimental engine used for model development and controller implementation. . . . 17
2.2 Swept range of inputs and outputs in SI model parameterization data. Mean and max absolute error between model and measurement listed for outputs. θ_{50} error reported in CAD to avoid division by small numbers at θ_{50} near TDC. . . . 36
2.3 Summary input/output listing for SI and HCCI models. . . . 38
2.4 Swept range of inputs and outputs in HCCI model parameterization data. Mean and max absolute error between model and measurement listed for outputs. θ_{50} error reported in CAD to avoid division by small numbers at θ_{50} near TDC. . . . 47

4.1 Control problem formulation for SI phase of SI-HCCI transition. . . . 75
4.2 Tuning variables of SI phase controller. . . . 82
4.3 Control problem formulation for HCCI phase of SI-HCCI transition. . . . 83
4.4 Tuning variables of HCCI phase controller. . . . 91
4.5 Properties of 93 AKI pump gasoline used as fuel in SI-HCCI transition experiments. 92
4.6 Tuning variable values for SI-HCCI transition controller. . . . 99

5.1 Properties of Corrigan UTG 96 gasoline used as fuel in adaptive SI-HCCI transition experiments. . . . 108

6.1 Control problem formulation for HCCI phase of HCCI-SI transition. . . . 132
6.2 Tuning variables of HCCI phase controller. . . . 140
6.3 Control problem formulation for SI phase of HCCI-SI transition. . . . 142
6.4 Tuning variables of SI phase controller. . . . 155
6.5 Tuning variable values for HCCI-SI transition controller. . . . 162

C.1 Summary estimates for SI-HCCI transition duration and fuel economy penalty. All data are taken at 2000 RPM. . . . 185
C.2 Summary estimates for HCCI-SI transition duration and fuel economy penalty. All data are taken at 2000 RPM. . . . 185

List of Figures

Figure

1.1 Experimental data of HCCI combustion phasing limits at different loads. 4
1.2 Experimental speed-load map of the multi-mode combustion engine considered in this study with the operating ranges for SI, HCCI, and SACI combustion modes shown. 5

2.1 Schematic of a turbocharged 4 cylinder engine with variable valve timing. 17
2.2 Two-stage cam profiles to enable dual SI/HCCI operation. 18
2.3 Compressor mass flow and efficiency regressions to manufacturer maps. 21
2.4 Turbine mass flow and efficiency regressions to manufacturer map. Note that a version of the turbine mass flow scaled by $p_{in}/\sqrt{T_{in}}$ is shown as this was the only quantity available from the map, however this scaling does not affect the accuracy of the fit. Additionally, the Gaussian efficiency regression profile of (2.18) is shown along with a standard quadratic efficiency regression profile so that the desirable extrapolation characteristics of the Gaussian can be seen. 23
2.5 Linear second order actuator dynamics model predictions for the throttle (left) and cam phasing (right). 25
2.6 Method to model continuous cam phaser dynamics with discrete jumps in valve timings due to cam profile switching. IVO timing used for example. 27
2.7 Cycle definition of the SI combustion model. 28
2.8 Input grid and modeled vs. measured outputs for steady-state SI model parameterization data. Mass of air m_a shown in place of λ as because a stoichiometric AFR was maintained throughout the sweeps. 35
2.9 Diagram of combustion model cycle division showing how exhaust gas states link SI and HCCI combustion models during an SI-HCCI switch. 37
2.10 Top: IMEP measurements in steady-state actuator sweeps with high AFR variation. Bottom: Profile of model combined thermal and combustion efficiency as a function of λ_c. 43
2.11 Profile of late phasing combustion efficiency η_{50} across different loads. 44
2.12 Input grid and modeled vs. measured outputs for steady-state HCCI model parameterization data. Bottom subplot shown with close-ups so that the θ_{50} standard deviation $\sigma(\theta_{50})$ can be compared to the model's mass of unburnt fuel calculation m_{uf} more clearly. 46

3.1 Cycle by cycle input and outputs and crank angle resolved in-cylinder pressure during open-loop SI-HCCI mode transition. *SI -1* indicates the final SI cycle and *HCCI 0* indicates the first HCCI cycle. Model reproduction of outputs with and without the introduced residual temperature correction are shown. 50
3.2 Comparison of experimental versus GT-Power simulation in-cylinder pressure during an SI-HCCI mode transition. 51
3.3 In-cylinder temperature traces generated by GT-Power SI-HCCI mode transition simulation. The final SI cycle whose recompression event yields an extremely high temperature leading into the first HCCI cycle is highlighted. 52
3.4 Block diagram summary of k_r parameter update method. All quantities evaluated on cycle *HCCI 0* during an SI-HCCI transition. 56
3.5 Demonstration of k_r adaptation for the SI-HCCI mode transition sequence of Fig. 3.1 with perfect repeatability (left) and additive noise (right) in the θ_{50} measurement that is assimilated on cycle *HCCI 0*. Top: Adaptive parameter dynamics as a function of mode transition iteration. Middle: θ_{50} value on cycle *HCCI 0* that is fed to the adaptation after being corrupted by ensemble noise. Bottom: Refinement in model θ_{50} response as $\hat{k}_r$ adapts for fixed $G = 0.1$. 57
3.6 Demonstration of k_r adaptation for the SI-HCCI mode transition sequence of Fig. 3.1 in the presence of perturbations to the modeled m_r and $T_{bd}(HCCI\ 0)$. Top: Adaptive parameter dynamics with consecutive mode transition iterations. Middle/Bottom: Model reproduction of measured θ_{50} response from the mode transition with varying amounts of adaptive iteration for +/- 5% model perturbation. 59
3.7 Experimental SI-HCCI mode transitions at low load HCCI with varying initial conditions for the HCCI phase of the transition. Left: Delayed throttle opening when switching to HCCI. Middle: Higher fuel quantity on final SI cycle. Right: Earlier EVC timing when switching to HCCI. 60
3.8 Experimental SI-HCCI mode transitions across the HCCI load range at 2000 RPM. Left: Low load. Middle: Mid load. Right: High load. 61

4.1 Schematic illustrating main differences between actuator trajectories of cam switching (left) and cam phasing (right) SI-HCCI mode transition strategies. 65
4.2 Steady-state actuator sweep data of throttle (left) and EVC (right) under constraints of stoichiometric AFR and MBT combustion phasing. In the EVC sweep, the throttle is opened as necessary with advancing EVC to maintain constant torque. 67
4.3 Steady-state intake valve timing sweeps with both high lift and low lift intake cam to examine which intake lift to use in SI phase of SI-HCCI transition. 69
4.4 Representative depiction of high-level actuator trajectories for cam switching SI-HCCI transition strategy. θ_{soi} shown with reference to bTDC; all other timings shown with reference to aTDC. 71
4.5 In-cylinder pressure data from a cam switching SI-HCCI mode transition illustrating the changes in combustion features over the course of the transition. 73
4.6 Block diagram of controller for SI phase of the transition. Variable names are as defined in Table 4.1. P blocks indicate calculations using the plant model, and C blocks indicate output feedback controllers. 75

4.7 Block diagram of controller for HCCI phase of the transition. Variable names are as defined in Table 4.3 with x_c representing combustion states. P blocks indicate calculations using the plant model, and C blocks indicate output feedback controllers. 84
4.8 Diagram of IMC structure. $Q(z)$ represents a linear low pass filter, and P and $\tilde{P}$ represent the true and controller model of the plant. 85
4.9 Linearized versus full nonlinear HCCI model input and state responses for steps of θ_{soi} (left) and m_f (right). 88
4.10 Frequency response of linearized IMC open-loop transfer function at low (left), mid (center), and high (right) load linearization points. Frequency response for $\theta_{soi} \rightarrow \theta_{50}$ open-loop transfer function shown in upper two subplots; Frequency response for $\theta_{soi} \rightarrow \theta_{50}$ open-loop transfer function shown in lower two subplots. 89
4.11 Diagram of HCCI combustion state estimator. 90
4.12 Controlled SI-HCCI transition at mid load HCCI at 2000 RPM. Inputs shown in left column and outputs shown in right column. The first and second cylinders to enter HCCI are referred to as $H1$ and $H2$, respectively. 93
4.13 Controlled SI-HCCI transition experimental results across the HCCI load regime at 2000 RPM. Left: Low load of 1.8 bar NMEP Right: High load of 3.1 bar NMEP. The first and second cylinders to enter HCCI are referred to as $H1$ and $H2$, respectively. 95
4.14 Repeated SI-HCCI mode transition experiments at 2000 RPM. Left: Low load of 1.8 bar NMEP. Center: Mid load of 2.4 bar NMEP. Right: High load of 3.1 bar NMEP. 97
4.15 Data from open-loop SI-HCCI transition wherein all input commands are specified through a linear ramp from the nominal SI condition to the SI-HCCI switch point in the SI phase of the transition, for examination of efficacy of simple open-loop actuator profiles. 100

5.1 SI-HCCI mode transitions before (left) and after (right) successive adaptations at an intermediate HCCI load operating condition. The first and second cylinders to enter HCCI are referred to as $H1$ and $H2$, respectively. 109
5.2 Successive SI-HCCI mode transition trials at an intermediate HCCI load operating condition with adaptation active. The first and second cylinders to enter HCCI are referred to as $H1$ and $H2$, respectively. 110
5.3 SI combustion phasing (left) and torque (right) model parameter variation with succesive SI-HCCI adaptations. The first and second cylinders to enter HCCI are referred to as $H1$ and $H2$, respectively. 112
5.4 HCCI combustion phasing (left) and torque (right) model parameter variation with succesive SI-HCCI adaptations. The first and second cylinders to enter HCCI are referred to as $H1$ and $H2$, respectively. 114
5.5 Parameter trajectories for each adaptive model correlation in simulation of successive closed-loop SI-HCCI adaptive trials for the baseline recursive least squares algorithm. HCCI model correlations shown in upper two subplots; SI model correlations shown in bottom two subplots. Forgetting factor kept at value of 0.94 from successive adaptation experiments. 116

5.6 Input (left) and output (right) simulation responses at severeal instances throughout successive closed-loop SI-HCCI adaptive trials with baseline recursive least squares algorithm. Forgetting factor kept at value of 0.94 from successive adaptation experiments. . . . 117
5.7 P matrix condition number (CN) of baseline recursive least squares algorithm in simulation of successive closed-loop SI-HCCI adaptive trials. Forgetting factor kept at value of 0.94 from successive adaptation experiments. . . . 118
5.8 SI-HCCI mode transitions near the low load HCCI limit before (left) and after (right) successive adaptations at the operating condition of Sec. 5.2.1. . . . 120
5.9 SI-HCCI mode transitions near the high load HCCI limit before (left) and after (right) successive adaptations at the operating condition of Sec. 5.2.1. . . . 120
5.10 SI-HCCI mode transitions with negative 250 RPM speed perturbation before (left) and after (right) successive adaptations at the operating condition of Sec. 5.2.1. . . . 122
5.11 SI-HCCI mode transitions with positive 250 RPM speed perturbation before (left) and after (right) successive adaptations at the operating condition of Sec. 5.2.1. . . . 122

6.1 Data from an experimental HCCI-SI transition at 2000 RPM illustrating the time required for the intake manifold pressure to reduce to SI levels even with very aggressive throttle control. Continuous air path variables interpolated to be plotted versus engine cycle. . . . 125
6.2 Steady-state throttle sweeps in HCCI mode for two different injection timings depicting the loss in combustion stability as HCCI becomes throttled. . . . 127
6.3 Representative depiction of high-level actuator trajectories for cam switching HCCI-SI transition strategy. θ_{soi} shown with reference to bTDC; all other timings shown with reference to aTDC. . . . 129
6.4 In-cylinder pressure data from a cam switching HCCI-SI mode transition illustrating the changes in combustion features over the course of the transition. . . . 130
6.5 Block diagram of controller for HCCI phase of the transition. Variable names are as defined in Table 6.1. P blocks indicate calculations using the plant model, and C blocks indicate output feedback controllers. . . . 133
6.6 Linear approximation of λ_c versus λ HCCI actuator sweep data of Appendix A. Note that only $\lambda \in [1, 1.2]$ is considered. . . . 136
6.7 Block diagram of controller for SI phase of the transition. Variable names are as defined in Table 6.3. P blocks indicate calculations using the plant model, and C blocks indicate output feedback controllers. . . . 143
6.8 Illustrative profiles of cylinder flow rate and the cylinder flow rate state cost term versus throttle (left) and EVC (right) inputs for inspection of minimization conditions. 150
6.9 Controlled HCCI-SI transition at mid load SI condition at 2000 RPM. Inputs shown in left column and outputs shown in right column. The first and second cylinders to enter HCCI are referred to as $H1$ and $H2$, respectively. . . . 157
6.10 Second controlled HCCI-SI transition at mid load condition HCCI at 2000 RPM. Inputs shown in left column and outputs shown in right column. The first and second cylinders to enter SI are referred to as $H1$ and $H2$, respectively. . . . 160
6.11 Controlled HCCI-SI transition at high load HCCI condition at 2000 RPM. Inputs shown in left column and outputs shown in right column. . . . 161

6.12 Full SI-HCCI-SI experimental scenario using proposed SI/HCCI control architecture to control mode transitions as well as nominal HCCI operation. Inputs shown in left column and outputs shown in right column. 165

A.1 Input grid and modeled vs. measured outputs for steady-state SI model reparameterization data to replica experimental engine. The λ output is shown as opposed to mass of air to convey the AFR changes that were made in the sweep data. 179
A.2 Input grid and modeled vs. measured outputs for steady-state HCCI model reparameterization data to replica experimental engine. 180

B.1 Flow chart depicting iterative regression method for both steady-state and transient k_r model parameters. 182

D.1 Parameter trajectories for each adaptive model correlation in simulation of successive closed-loop SI-HCCI adaptive trials for the modified recurisve least squares algorithm with directional forgetting. Forgetting factor kept at value of 0.94 from successive adaptation experiments. 187
D.2 P matrix condition number of directional forgetting recursive least squares algorithm in simulation of successive closed-loop SI-HCCI adaptive trials. Forgetting factor kept at value of 0.94 from successive adaptation experiments. 188
D.3 Input (left) and output (right) simulation responses at severeal instances throughout successive closed-loop SI-HCCI adaptive trials with directional forgetting recursive least squares algorithm. Forgetting factor kept at value of 0.94 from successive adaptation experiments. 188

List of Appendices

Appendix

A Model Reparameterization for Replica Experimental Engine 177
A.1 SI Combustion Model Reparameterization 177
A.2 HCCI Combustion Model Reparameterization 178

B HCCI Combustion Model Parameterization Routine 181

C Estimation of SI/HCCI Mode Transition Fuel Economy Penalty 184

D Modified Recursive Least Squares Parameter Update Law to Avoid Estimator Wind-Up . 186

Abstract

Homogeneous charge compression ignition (HCCI) combustion has been investigated by many researchers as a way to improve gasoline engine fuel economy through highly dilute unthrottled operation while maintaining acceptable tailpipe emissions. A major concern for successful implementation of HCCI is that it's feasible operating region is limited to a subset of the full engine regime, which necessitates mode transitions between HCCI and traditional spark ignition (SI) combustion when the HCCI region is entered/exited. The goal of this dissertation is to develop a methodology for control-oriented modeling and model-based feedback control during such SI/HCCI mode transitions. The model-based feedback control approach is sought as an alternative to those in the SI/HCCI transition literature, which predominantly employ open-loop experimentally derived actuator sequences for generation of control input trajectories. A model-based feedback approach has advantages both for calibration simplicity and controller generality, in that open-loop sequences do not have to be tuned, and that use of nonlinear model-based calculations and online measurements allows the controller to inherently generalize across multiple operating points and compensate for case-by-case disturbances.

In the dissertation, a low-order mean value modeling approach for multi-mode SI/HCCI combustion that is tractable for control design is described, and controllers for both the SI to HCCI (SI-HCCI) and HCCI to SI (HCCI-SI) transition are developed based on the modeling approach. The model is shown to fit a wide range of steady-state actuator sweep data containing conditions pertinent to SI/HCCI mode transitions, and is extended to capture transient SI-HCCI transition data through using an augmented residual gas temperature parameter. The mode transition controllers are experimentally shown to carry out SI-HCCI and HCCI-SI transitions in several operating conditions with minimal tuning, though the validation in the SI-HCCI direction is more extensive. The model-based control architecture is also equipped with an online parameter updating routine, to attenuate error in model-based calculations and improve robustness to engine aging and cylinder to cylinder variability. Experimental examples at multiple operating conditions illustrate the ability of the parameter update routine to improve controller performance by using transient data to tune the model parameters for enhanced accuracy during SI-HCCI mode transitions.

Nomenclature

Mathematical Symbols

Symbol	Description
b_{bd}	Burned gas fraction after blowdown
c_p/c_v	Constant pressure/constant volume specific heat
θ_{soc}	Crank angle at start of ignition
θ_{50}	Crank angle for 50% fuel mass fraction burned
θ_{evc}	Exhaust valve closing timing
u_{evc}	Exhaust valve closing timing command
θ_{evo}	Exhaust valve opening timing
η_λ	Combined thermal & combustion efficiency (HCCI only)
η_{50}	Late phasing combustion efficiency (HCCI only)
f_{bd}	Unburnt fuel mass fraction after blowdown
H1/H2	First/second cylinder to switch modes during a combustion mode transition
HCCI 0,1,...	Index for 1st, 2nd, 3rd, etc. HCCI cycles after switching to HCCI in an SI-HCCI transition
HCCI -1,-2,...	Index for last, 2nd to last, 3rd to last etc. HCCI cycles prior to switching to SI in an HCCI-SI transition
θ_{ivc}	Intake valve closing timing
θ_{ivo}	Intake valve opening timing
u_{ivo}	Intake valve opening timing command
k_r	Residual gas temperature correction factor for first HCCI cycle in SI-HCCI transitions
K_{th}	Arrhenius reaction threshold
λ	Relative air-fuel ratio in the exhaust
λ_c	Relative air-fuel ratio in the cylinder before combustion
λ_r	Relative air-fuel ratio during recompression (HCCI only)
m_a^{in}	Mass of inducted air
m_a	Total mass of air

m_{ra}	Mass of residual air (HCCI only)
m_c	Total cylinder mass
m_f	Mass of fuel injected
m_f^{tot}	Total mass of fuel
m_{uf}	Mass of unburnt fuel
m_{rf}	Mass of residual fuel (HCCI only)
m_r	Total residual gas mass
N_{eng}	Engine speed
p_θ	In-cylinder pressure at crank angle event θ
p_{im}	Intake manifold pressure
p_{em}	Exhaust manifold pressure
Q_{lhv}	Lower heating value
R	Mass-specific gas constant
θ_{sp}	Spark timing
θ_{soi}	Start of injection timing
SI -1,-2,...	Index for last, 2nd to last, 3rd to last etc. SI cycles prior to switching to HCCI in an SI-HCCI transition
SI 0,1,...	Index for 1st, 2nd, 3rd, etc. SI cycles after switching to SI in an HCCI-SI transition
T_θ	In-cylinder temperature at crank angle event θ
T_{bd}	Temperature after blowdown
T_{im}	Intake manifold temperature
T_{em}	Exhaust manifold temperature
W_{cyl}	Air mass flow rate into cylinders
W_t	Air mass flow rate through throttle
V_θ	Volume at crank angle event θ
V_{im}	Intake manifold volume

Acronyms

Acronym	**Meaning**
AFR	Air-fuel ratio
AKI	Anti-knock index
BDC	Bottom dead center
COV	Coefficient of variation
EGR	Exhaust gas recirculation
EVC	Exhaust valve closing

EVO	Exhaust valve opening
HCCI	Homogeneous charge compression ignition
IMC	Internal model control
IMEP	Gross mean effective pressure
IVC	Intake valve closing
IVO	Intake valve opening
LQR	Linear quadratic regulator
NMEP	Net mean effective pressure
NOx	Nitrogen oxides
PI	Proportional + integral
PMEP	Pumping mean effective pressure
PVO	Positive Valve overlap
NVO	Negative valve overlap
RGF	Residual gas fraction
TDC	Top dead center
VVT	Variable valve timing
SACI	Spark assisted compression ignition
SI	Spark ignition
VO	Valve overlap

Chapter 1
Introduction

1.1 Problem Background and Motivation

1.1.1 Overview of Gasoline Multi-mode Combustion

In recent years, research in highly dilute, low temperature combustion modes for gasoline engines has gained increasing attention [1], [2]. The key benefit of these combustion modes is that the unreactive diluents that accompany the combustible fuel and air in the cylinder charge absorb additional heat release from combustion, lowering the burn temperature. The lower burn temperature increases the ratio of specific heats $\gamma = c_p/c_v$ of the mixture and also reduces heat losses to the cylinder walls, both of which effects increase thermal efficiency [3], [4]. As automotive manufacturers continue to push gasoline engines to their limits for fuel economy, introducing low temperature combustion modes into conventional spark ignition (SI) engine operation is one option that has been extensively pursued.

Perhaps the most well-known gasoline low temperature combustion mode is homogeneous charge compression ignition (HCCI). First reported on by Onishi *et al.* [5], HCCI is often viewed as the "best of both worlds" between diesel and SI engines, in that it runs unthrottled with a dilute charge and ignites the mixture from high compression as in a diesel engine, but pre-mixes the fuel and air as in an SI engine. The dilution and high compression increase fuel efficiency, allowing HCCI to reap the same fuel economy benefits as diesel engines, but without the associated emissions problems from mixing controlled combustion since these are avoided by pre-mixing the charge. In many cases, HCCI is run so dilute that burn temperatures are prevented from reaching the formation threshold for nitrogen oxides (NOx) of ≈1600 to 1800 K, offering the potential for ultra-low NOx emissions. These outstanding benefits of HCCI have made it a subject of much research in the engines community [6], [7].

An inherent drawback of HCCI is that it lacks a direct trigger to ignite the cylinder charge. The reason is that the charge is pre-mixed, so when it is compressed to ignition, it auto-ignites due to high temperatures and pressures in the cylinder without any external trigger. The implication is that the ignition timing is controlled by the intensive thermodynamic state of the charge, instead of

a direct control actuator such as the spark in SI combustion or the fuel injection event in diesel combustion. As a consequence, careful control of the in-cylinder conditions must be exerted to achieve successful HCCI combustion [6].

HCCI can be realized through several methods, each of which require some type of hardware addition beyond what is commonly available on standard SI engines. Each method is centered around manipulating the thermodynamic state of the cylinder charge so as to plan for appropriate combustion timing relative to TDC, or combustion phasing. Adequate dilution must also be supplied, with the two most common diluents being air that is in excess of the stoichiometric amount and exhaust gas recirculation (EGR). EGR is typically recirculated internally in HCCI by retaining burned residual gasses in the cylinder because these gasses possess a high internal energy and so have a great authority to influence the auto-ignition properties of the charge [8], [9], [10], [11], though external EGR that is rerouted from the exhaust manifold back to the intake manifold can be used as well [12]. Both excess air and EGR are almost always present to some degree, since HCCI runs unthrottled and lean, and there is always some fraction of exhaust gas that does not leave the cylinder that is recycled. The methods then differ in the amount of each diluent they employ. The most commonly used method is to equip the engine with a variable valve timing (VVT) device, which allows the valve timings to be phased relative to the motion of the crank in order to promote internal exhaust gas recirculation, where the recirculated exhaust gas amount is chosen such that it transfers an appropriate amount of heat to the intake charge on the following cycle to ensure proper auto-ignition timing. The internal exhaust gas recirculation can be achieved by either closing the exhaust valve early in the exhaust stroke to trap residual gas in the cylinder [8], [9], [10], or by holding the exhaust valve open during the intake stroke to rebreathe exhaust gas into the cylinder [11], [12]. Another method to enable HCCI is to heat the intake air with a heat exchanger or electric heater to give the appropriate in-cylinder charge temperature for proper combustion phasing [13], [14]. A last method is to design the cylinder so that compression ratio can be varied during engine operation, so that the compression ratio can be continuously adjusted by the control system to give the correct amount of compression for auto-ignition of the mixture [15].

Another gasoline low temperature combustion mode that has experienced a growing research focus is spark assisted compression ignition (SACI). SACI operates with a pre-mixed charge as in SI and HCCI, but combines characteristics of both these combustion modes. The mixture is ignited with the spark to induce pre-mixed flame propagation as in SI, however the thermodynamic state of the charge is controlled such that as the pre-mixed flame expands into the unburnt charge, the unburnt charge crosses the auto-ignition threshold and detonates through auto-ignition as in HCCI. In this regard SACI occurs through the same mechanism as knock in SI engines, however SACI operates with much more dilution than standard SI so that when auto-ignition occurs, the pressure rise rates are tolerable [16], [17]. Other gasoline combustion methods that seek to take advantage of the efficiency gains associated with high charge dilution also exist, such as stratified lean direct

injection [18].

The scope of this research is limited to the HCCI combustion mode, which is assumed to be achieved through the recompression method with early exhaust valve closure to trap hot exhaust gases to enable auto-ignition. The ideas presented herein may be helpful as a baseline for future applications to the SACI combustion mode, as SACI is "between" SI and HCCI and so many of the concerns which are addressed for SI/HCCI multi-mode combustion also play a role for SI/SACI multi-mode combustion. As will be seen in the upcoming sections, integration of HCCI into conventional engines presents several significant control challenges.

1.1.2 The Necessity of Mode Transitions

A major limitation of the HCCI combustion mode is that it can only function in a subsection of the full operation space of conventional engines. The reason is that the range for reliable auto-ignition combustion is bounded in terms of auto-ignition phasing. When the charge auto-ignites too early, the mixture burns very quickly, releasing the heat of combustion over a short period of time and causing high pressure rise rates. Pressure rise rates that are too high can cause audible noise and damage the engine hardware. When pressure rise rates become very high, oscillations emerge in the cylinder pressure trace in a phenomenon known as ringing. When the charge auto-ignites too late, the mixture is pushed closer to the point where the auto-ignition threshold is barely crossed and misfires can occur. The late phasing region is usually characterized by high cyclic variability (CV), because as auto-ignition gets closer to the misfire limit, stochastic fluctuations in the cylinder charge can result in very poor auto-ignition burns, which can then lead to oscillatory patterns by recycling of unburnt fuel and air to subsequent cycles [19].

A diagram illustrating the combustion phasing limits for HCCI on a single cylinder research engine is shown in Fig. 1.1, which is modified after [19], [16]. The diagram plots the limits in terms of load vs. phasing, where load is represented by the indicated mean effective pressure (IMEP) and combustion phasing is represented by the crank angle at which 50% of the charge mass has burned (θ_{50}). As can be seen, as the load increases, the early phasing limit for ringing index (RI) shifts later because the fuel quantity is greater and so it cannot be burned as quickly without causing pressure rise rates that are too high. At the top of the diagram, the early and late phasing limits become very close together, marking the point where HCCI is no longer practically feasible without violating either of these limits. A similar meeting of the early and late phasing limits happens at low loads, where the internal energy of the mixture must be higher in order to sustain auto-ignition with the now smaller amount of fuel in the diluted charge. As a result, the late phasing limit advances and becomes very close to the early phasing limit. Note that engine speed also has an effect in limiting the feasibility region of auto-ignition combustion, with low engine speeds causing the charge to lose too much energy to heat transfer and enter the late phasing region, and high engine speeds

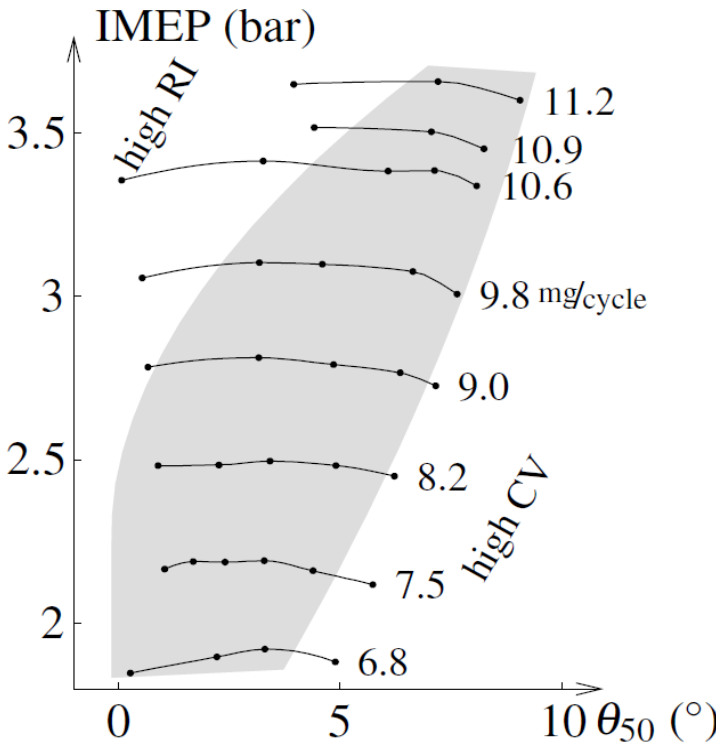

Figure 1.1: Experimental data of HCCI combustion phasing limits at different loads.

causing aggressive combustion by reducing the time for heat transfer from the combustion products between consecutive cycles [6]. A speed-load operating map which defines approximate ranges of feasibility for SI and HCCI for the experimental multi-mode combustion engine that will be used in this study is shown in Fig. 1.2. The diagram makes clear that HCCI combustion can only cover a fraction of the range of SI combustion.

The boundaries on the feasible operating conditions for HCCI combustion imply that to realize this combustion mode, it must be integrated into a multi-mode combustion framework wherein conventional SI combustion is engaged at operating conditions outside the regions where HCCI is possible. A further implication is that transitions must be carried out between SI and HCCI combustion modes during online operation, in a manner that does not violate standard gasoline engine performance objectives. In the next section, the challenges involved with conducting online mode transitions while maintaining engine performance will be discussed.

1.1.3 The Challenges of Mode Transitions

The difficulty in transitioning between SI and HCCI lies in the drastically different conditions in which these modes operate. The differences between the operating conditions of the modes depends

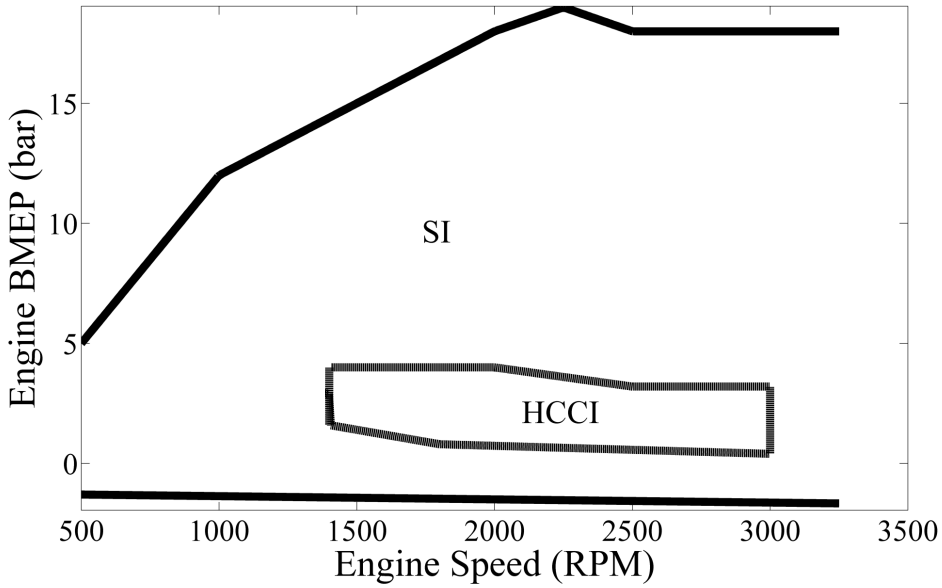

Figure 1.2: Experimental speed-load map of the multi-mode combustion engine considered in this study with the operating ranges for SI, HCCI, and SACI combustion modes shown.

on the method that is used to enable HCCI (EGR, intake air heating, or variable compression ratio, see Sec. 1.1.1 for an explanation of these methods), but all cases present underlying challenges that overlap. Here the recompression method is taken for example in order to highlight the differences between the combustion modes, since it is the focus of this research. While in standard SI mode, the engine will be throttled with a stoichiometric air-fuel ratio (AFR), a low amount of EGR dilution, and positive valve overlap (PVO), where valve overlap (VO) is defined as the difference in exhaust valve closing (EVC) and intake valve opening (IVO) timings

$$VO = \theta_{evc} - \theta_{ivo} \tag{1.1}$$

where θ has been used to designate a crank angle at some point in the engine cycle. On the other hand, while in HCCI, the engine will be unthrottled with an AFR $\geq$ stoichiometric, a large amount of EGR dilution, and negative valve overlap (NVO). NVO is the result of closing the exhaust valve early in the exhaust stroke, which makes $\theta_{evc} < \theta_{ivo}$ in (1.1). In addition, to attain NVO and trap a high residual gas amount, the lift and duration of the cams that open/close the cylinder valves must be smaller for HCCI than for nominal SI operation; thus, not only the valve timings have to change between the modes, but the cam profiles as well. A last major difference is that SI combustion produces a much higher exhaust gas temperature than HCCI because SI does not possess as high a diluent concentration to absorb the heat of combustion. This is of concern because recompression

HCCI depends on a large amount of internally recycled exhaust gas to manipulate the temperature of the cylinder charge for proper auto-ignition timing, and so if the exhaust temperature changes drastically during a mode transfer, it can result in undesirable transients in combustion phasing. A summary of the differences between SI and HCCI is given in Table 1.1.3.

Attribute	**SI**	**HCCI**
Air control	Throttled	Unthrottled
Air-Fuel Ratio	Stoichiometric	Lean
EGR	Low	High
Valve Overlap	PVO	NVO
Cam Profile	High-lift	Low-lift
Exhaust temperature	High	Low

Table 1.1: Summary of operating condition differences among SI, and HCCI combustion modes for the recompression HCCI method.

The myriad of differences between SI and HCCI implies that at least one combustion mode must pass through conditions outside it's normal operating regime during a transition between the two, because several of the differing attributes (e.g. throttling, valve timings) cannot be changed instantaneously to give an immediate shift of operating condition from one mode to the other. Which mode(s) goes outside nominal conditions and to what degree is to be determined by the control strategy.

Despite having to transfer through atypical, potentially adverse operating conditions during a mode transition, the combustion must be regulated such that driver comfort is not disturbed, emissions are kept to an acceptable level, and no hazardous combustion abnormalities occur that can threaten the cylinder hardware or the safe operation of the engine. Moreover, the transition should be completed in the shortest time possible, to reach the desired mode quickly and minimize the window where the control system is occupied in carrying out the mode transition, and also to mitigate potential fuel economy losses that can occur as the combustion passes through conditions outside its nominal optimized operation. These performance criteria are restated in the list below as they will play a central role in formulating the control strategy and tracking design for SI-HCCI transitions:

Performance Objectives for SI-HCCI Mode Transitions

1. Deviations of the engine torque from the driver pedal demand must be kept small enough to prevent disturbances to driver comfort
2. Emissions must be kept to an acceptable level throughout the duration of the mode transition, where the acceptable level depends on the emissions tier that is targeted for the engine.
3. Combustion abnormalities such as ringing and misfire must be avoided during a mode transition for engine durability and safe operation.
4. Mode transitions should be carried out in the minimum time possible while satisfying the

above criteria.

1.2 Previous Research in SI/HCCI Mode Transitions

1.2.1 Open-loop Experimental Studies

Many mode transition studies have focused on developing SI/HCCI transition strategies through purely open-loop experimentation [20–29]. Actuator sequences for the mode transition are proposed and experimentally optimized on a test engine until the final control sequences are ascertained. The experimental mode transition studies to date have overwhelmingly employed the recompression method for enabling HCCI combustion, with all the studies [20–30] utilizing recompression HCCI. This is important to keep in mind when interpreting the strategies and results of these studies as their approaches are shaped around the recompression method.

Koopmans et al. [20] first demonstrated an SI-HCCI-SI mode switch in 2003 on both a single cylinder and multi-cylinder engine equipped with electromechanical cylinder valves. The core idea of their strategy was to dethrottle the engine in SI mode while regulating the cylinder air charge through use of the flexible cylinder valves. It was noted that careful optimization of actuator sequences was necessary during the first few cycles following a mode switch in order to avoid undesirable transients. The SI-HCCI direction of the mode transition was concluded to be more difficult than its HCCI-SI counterpart due to the precise actuator manipulation necessary to attain successful auto-ignition when the mode changes from SI to HCCI. In 2005, Santoso et al. [21] used a similar strategy to Koopmans et al., running the SI combustion mode fully dethrottled and controlling the air charge with a fully flexible electromagnetic valve train. To compensate for delays in air charge regulation due to dynamics of their valve train, a policy of using a reduced fuel quantity on the first cycle of HCCI during an SI-HCCI transition was applied in order to avoid rich and advanced combustion on the first HCCI cycle. Conversely, the fuel quantity was increased on the first cycle of SI during an HCCI-SI transition to avoid lean misfire from the higher intake manifold pressure. This yielded a stable transition, but a noticeable fluctuation was apparent in the engine torque response. The strategy of switching into HCCI from a dethrottled SI state and controlling air charge with a fully flexible valve train was also employed by Widd et al. [30], with the distinguishing feature that the SI combustion was dethrottled using early IVC timing. Milovanovic et al. [23] conducted SI-HCCI-SI mode transitions on a single cylinder engine with a fully flexible valve train as well, though their strategy differed from the previous studies in that the SI combustion mode was not kept perpetually dethrottled. Instead, the throttle opening/closing during a mode change was coordinated with the cam profile switching, with the throttle command being issued one cycle prior to cam profile switching in both SI-HCCI and HCCI-SI directions. Noticeable torque fluctuations were apparent

in both directions, though the fluctuation was larger in the HCCI-SI direction as a result of lean misfire during the first few SI cycles due to the intake manifold requiring several cycles to reduce after throttling and switching the cams. This corresponds to the same effect that Santoso et al. avoided by injecting a higher fuel quantity in the first SI cycle of the HCCI-SI transition, though the effect was less pronounced in their work because they relied on the faster fully flexible valve train to control the air charge instead of the throttle. Milovanovic et al. also noted that, when performing mode transitions at different operating conditions, actuator sequences had to be optimized specific to the operating condition.

In 2007, Zhang et al. [22] performed a SI/HCCI mode switching study on a single cylinder engine with fully flexible valve actuation wherein they explored what they termed "hybrid SI-HCCI" combustion, which corresponds to SACI. Using SACI as an intermediate mode between SI and HCCI was found to be beneficial for transition smoothness. The existence of a "residual gas fraction (RGF) gap" was also highlighted, which is a region between SI and SACI where the internal recycled exhaust gas amount is too high for stable SI combustion but too low to give auto-ignition for SACI combustion, resulting in poor combustion work output. Kakuya et. al [29] acknowledged the same "RGF gap" in a 2008 mode transition study on a multi-cylinder fully flexible valve train engine, which they referred to as the "unstable area". Their mode transition strategy involved passing through the "unstable area" with the assistance of advanced spark timing and a stratified split injection to give locally rich areas in the cylinder charge that are more likely to burn and prevent misfires. This strategy of passing through the unstable area by directly phasing the exhaust cam earlier to gradually increase internal residual while simultaneously opening the throttle differs from many other studies in the literature where HCCI is engaged suddenly with a switch of the cams and fast opening of the throttle. The differences between these two strategy types will be considered later when the high-level strategy for the mode transition is explained. Matsuda et. al [31] studied the afore mentioned "RGF gap" or "unstable area" region and found that for a certain range of loads at 1200 RPM, combustion could be achieved in this region which maintained cylinder pressure rise rates within 6 bar/CAD and COV IMEP less than 10%. This suggests that transitioning through this region may be possible in the load range determined in [31]. However, a very high compression ratio of 14.3:1 was used in these experiments, which offers greater authority in stabilizing highly dilute combustion. Additionally, the load range where acceptable combustion could be achieved was limited to greater than 3.5 bar NMEP, which is near the high end of the HCCI spectrum.

The above studies all utilized fully flexible cylinder valve actuation devices, which give benefits for speed and range of actuator manipulation, but are not practical from an implementation standpoint due to their high cost. Other studies [8]-[12] have used a more practical two-stage cam system with a set of long duration, high-lift cams for SI operation, and a set of short duration, low-lift cams for HCCI operation. A hydraulic actuator switches which cam profile is active when a mode transition is commanded. In 2007, Tian et al. [24] carried out a "stepped switch" strategy on a two cylinder

engine, wherein the cam profile was switched prior to opening the throttle valve in the SI-HCCI direction, giving a rich and advanced combustion on the first HCCI cycle. To reduce the richness and ringing of the first HCCI cycle, a policy of injecting a lower fuel quantity on the first HCCI cycle was adopted, similar to the approach in [21]. This gave the stepped switch strategy good stability at the cost of increased torque fluctuations when the combustion mode was changed. Cairns and Blaxill [25] studied SI-HCCI-SI mode transitions on a four cylinder engine, where it was noted that SACI (which was referred to as hybrid SI/CAI) is helpful in smoothing the transition as Zhang et al. [22] did. Cairns and Blaxill also showed that incorporating external EGR in the SI-HCCI direction could help reduce ringing on the first HCCI cycle where the exhaust temperature was much higher. In 2008, Kalian et. al [26] carried out an investigation on a six cylinder engine mainly focused on how to on schedule the throttle opening/closing command and EVC timing to attain stable combustion in SI-HCCI-SI mode transitions. The investigation concluded that the throttle should only be partially opened during SI-HCCI transitions, and that the throttle closure during HCCI-SI transitions should be accompanied by a late EVC timing. Wu et al. [27] also explored multiple strategies for coordinating the timing of the throttle opening/closing with the cam profile switching, in addition to varying the fuel injection amount. Their results show a smooth transition from SI to HCCI, but lean misfire was experienced in the SI phase of the HCCI-SI direction from the same phenomena seen in [23] of the intake manifold pressure requiring several to reduce to acceptable SI levels even when the throttle is closed and the cams are switched. In 2012, Nier et al. [28] investigated SI-HCCI-SI mode transitions during boosted HCCI operation on a single cylinder HCCI engine. A major concern of this study was maintaining acceptable pressure rise rates during mode transitions at the higher load HCCI operating conditions that can be accessed via boosting. Towards this end, a policy of leaning the SI combustion to reduce exhaust temperatures before switching into HCCI combustion as well as using a compression stroke fuel injection during the first few HCCI cycles was adopted.

The perceptive reader will note from the above discussion that the body of open-loop experimental work on SI/HCCI mode transitions is vast and complex, with numerous studies that each put forth multi-faceted strategies and experimental results, which sometimes overlap with other studies, and sometimes conflict with other studies. Despite that this myriad of strategt options and experimental conclusions can be difficult to collect into a summary suited for making engineering design decisions, several common themes throughout the experimental literature can be discerned and are listed below:

Recurring Observations in Experimental Mode Transition Literature

- For successful mode transitions to be executed via open-loop actuator sequences, extensive tuning and calibration is necessary, and the calibration must be specific to the operating point.
- Incorporation of SACI as an intermediate mode between SI and HCCI may help to smooth

SI/HCCI transitions.

- The use of a practical two-stage cam switching system to enable SI-HCCI operation makes the mode transition task more difficult than when a fully flexible valve train is used.
- The throttle must be coordinated with the cam timing and cam profile switching to give adequate cylinder charge regulation and avoid combustion abnormalities.
- There is a region between SI and HCCI modes where the in-cylinder residual amount is too high for robust flame propagation in SI combustion but not high enough for autoignition in HCCI, and so it is not desirable to operate in this region.
- Injection timing strategies, such as stratifed injection to stabilize combustion in highly dilute SI conditions or late injection in HCCI to retard combustion and avoid ringing, are often used and appear to be helpful.
- During an SI-HCCI transition, the first cycle of HCCI tends to have an early combustion with high pressure rise rates due to the higher exhaust temperature of SI raising the charge temperature and advancing combustion.
- During an HCCI-SI transition, there is a danger of lean misfire during the first few SI cycles because the intake manifold requires a few cycles to discharge its stored air mass and reduce from the near-atmospheric pressures of HCCI to the sub-atmospheric pressures of SI.

Open-loop Experimental Studies on Computational Fluid Dynamics Models

To gain additional insight into the dynamics of the unmeasurable quantities during SI/HCCI mode transitions and afford greater flexibility in actuator sequence tuning, a few studies have implemented open-loop mode transition sequences on computational fluid dynamics models instead of directly in experiment. In [32], the authors of [27] used a stochastic reactor HCCI combustion model embedded within GT-Power to simulate the mode transitions carried out in [27]. The model reproduces most trends in the in-cylinder pressure, air-fuel ratio, and residual gas fraction, all of which were measured in the experiments of [27], and is able to shed some light on the thermodynamic processes that occur during the SI-HCCI mode transition. However, the model is only validated at one operating condition and simulated for a single SI-HCCI mode transition sequence from [27], and so it provides little insight into how varying the input sequence for the SI-HCCI mode transition affects the evolution of the thermodynamic state . In 2012, Kuboyama et al. [33] also employed a GT-Power model to simulate SI/HCCI mode transitions on an engine equipped with their blowdown super charging system, though a simple Arrhenius model for HCCI combustion was employed instead a detailed chemical kinetic model. In simulation, the authors are able to transition from HCCI to SI without the problem of lean misfire observed in [23], [27], though this seems to necessitate use of their proposed blowdown super charging system. The authors also simulate the SI-HCCI direction, and are able to complete the transition but not without excessively advanced combustion on the first several HCCI cycles.

1.2.2 Modeling and Model-Based Control Approaches

While experimental open-loop studies are useful for physical insight into the mode transition problem, the studies in literature concur that extensive calibration is necessary to develop open-loop actuator sequences that can successfully transition among combustion modes. Moreover, the calibration must be carried out for each operating point in a grid defined over the entire speed-load region where transitions are feasible. Model-based feedback control methods have the advantage that a feedback controller determines the transient actuator commands, and so the calibrator must only specify set points and/or controller gains and tuning parameters. If designed appropriately, this can result in a much simpler calibration task as opposed to specifying open-loop actuator sequences over the entire transition speed-load region. In a real situation where open-loop control sequences must interpolate between calibrated operating points, model-based feedback control may have advantages for generality and robustness it can respond to case-by-case disturbances and variations by operating condition using online measurements. These advantages suggest that model-based feedback control may be a useful alternative to open-loop methods, and so it has been pursued by some researchers in the literature.

The work in modeling and model-based control methods for SI/HCCI transitions has been sparser than the work experimental open-loop methods. Widd et al. [30] employed a simple linear system identification around one HCCI operating condition to determine a black box model in addition to their open-loop experimental work. The model was used to design a linear proportional + integral (PI) and linear quadratic regulator (LQR) state feedback controllers to control torque and combustion phasing using valve overlap and fuel quantity. The controllers, however, was not activated until 3-4 cycles after entering HCCI during the SI-HCCI transition, and so did not address the first few critical cycles of HCCI where the in-cylinder thermodynamic state rapidly shifts from SI conditions to HCCI conditions. Moreover, it is unclear whether an approach based on simple black box linear system identification around an operating condition could manage such a transient, as large regions of the state and input space are traversed in a short number of cycles. A more sophisticated model was developed by Roelle et al. in 2004 [34]. The crank angle-based HCCI combustion model contained states for the in-cylinder concentrations of dominant chemical species, the cylinder temperature, as well as for the thermodynamic state of the exhaust manifold because the model was developed for rebreathing HCCI operation. The model was shown to reproduce qualitative trends in in-cylinder pressure during an SI-HCCI mode switch, though a comparison of performance outputs was not given. The model was modified in a later paper [35] to include a Wiebe function [36] for SI combustion and a few additional states. While useful for physical insight and simulation purposes, the crank angle-based high dimensional (7-9 states) model possesses a high amount of complexity for control design purposes. Additionally, mode transitions are modeled assuming that intake pressure is maintained at atmospheric throughout the transition, which overlooks the complexity associated with dethrottling the SI combustion when a fully flexible valve

train is not available that was observed in [26], [27].

Another higher order crank-angle based model for use in SI-HCCI mode transitions was put forth by Yang et al. [37, 38] . The model was first introduced as one-zone in 2010 [37] and was expanded to two-zones in 2011 [38], where one-zone indicates a lumped model for both the burned and unburned gas and two-zone indicates a model with separate burned and unburned gas zones. The modeling approach has the advantage of being able to simulate SI, SACI, and HCCI with a single model, so that the combustion mode can be changed solely by changing the model inputs without having to switch among separate models for each combustion mode. However, the modeling approach is complex, especially in the two-zone case where the solution of a system of five nonlinear equations must be carried out at each crank angle during the burning process. Moreover, it is not clear from the papers how to parameterize the multiple Wiebe functions and Arrhenius rate integral employed by the model in order to match measured engine performance outputs, and in the paper the model is only sparsely validated by comparison with a GT-Power model.

The later controls work of Yang and Zhu [39] employed iterative learning control to generate sequences for the fuel command in offline SI-HCCI transition simulations on the previously developed model, which were proposed to be stored in a look-up table and implemented as open-loop maps in conjunction with a PI controller. An LQR throttle feedback controller was also included to track an intake manifold pressure reference. The remainder of the control architecture was given by open-loop calibrated sequences, similar to the experimental approaches in Sec. 1.2.1. Considering that the iterative learning control fuel commands and throttle intake manifold pressure reference trajectory were also tuned as open-loop sequences, it is clear that the control structure still relies strongly on the principle of open-loop sequence scheduling put forth in the experimental works in Sec. 1.2.1, with model-based and/or feedback elements playing a lesser role. Perhaps influenced by this fact, it was found that the control approach of [39] was not robust to case-by-case variations [40], and so in a later work a sensitivity-based feedforward controller for the fuel command was designed. The controller was shown to attenuate disturbances to the torque in simulation at one operating condition, however modeling error in the sensitivity calculation was not considered, and the remainder of the control structure was still given by open-loop scheduled sequences. Another work by Ravi et al. [41] addressed the problem of combustion phasing control in the HCCI portion of the SI-HCCI transition with closed-loop linear quadratic Gaussian (LQG) control of fuel injection timing. The controller was shown in experiments on a single cylinder engine to aid in combustion phasing regulation relative to a purely open-loop scheduled controller at two different operating points. However, all control inputs other than injection timing were still given by open-loop scheduled sequences, which had to vary significantly between the two operating points. It can thus been seen that the works of [39–41] focus on integrating model-based and/or feedback control elements into SI-HCCI transition control architectures whose baseline design consists of open-loop scheduled input sequences as in the works of Sec. 1.2.1. While undoubtedly advantageous for improving the robustness of such control

architectures to operating condition and helping them compensate for disturbances, the underlying principle of open-loop sequence scheduling for SI/HCCI mode transitions still persists. Additionally, the HCCI to SI direction of the mode transition was not addressed in these works.

1.3 Contribution of the Research

As explained in Sec. 1.2, the SI/HCCI transition control problem has been approached predominantly with open-loop calibration of control input sequences in the literature to date. Few studies have explored the use of model-based and/or feedback control elements in SI/HCCI transitions [30,39–41], and have done so from the standpoint of introducing a small number of model-based/feedback elements into a baseline architecture which remains comprised of open-loop input sequences. While these studies represent important steps for improved robustness and reduced calibration complexity in SI/HCCI transitions, they are still largely dependent on the original notion of experimental calibration for determination of input sequences. Moreover, the studies in [30,39–41] are fragmented in that each only addresses a subset of the SI-HCCI transition control objectives, with [30] addressing torque and combustion phasing after the first 3-4 HCCI cycles only, [39, 40] addressing torque and air-fuel ratio (AFR), and [41] addressing combustion phasing in the HCCI mode only. Additionally, the high-level SI-HCCI transition strategies employed by [39–41] are all similar to that of [29] in that HCCI is gradually transitioned to with direct phasing of the valve timings, where as many studies in literature [20–28] employ a different strategy where HCCI is engaged abruptly by a cam profile switch. The work of [30] counts itself amongst one of these whose strategy relied on a fully flexible valve actuation system, which is impractical for production implementation. Lastly, none of the works which employed feedback and/or model-based elements [30,39–41] addressed the HCCI-SI direction of the transition, and were tested either only in simulation [39, 40] or on single cylinder engines [30, 41].

The focus of this research is on the development of a methodology for control-oriented modeling and model-based feedback control of cam switching SI/HCCI transitions which easily generalizes to multiple operating conditions and requires calibration of only set points and gains, as opposed to entire actuator sequences. The term "cam switching" refers to a high-level strategy like those in [20–28] where the combustion mode is abruptly changed with a cam profile switch. The target engine platform is taken to be a multi-cylinder engine with a practical two-stage cam switching mechanism for enabling dual SI/HCCI operation similar to [24–28], so that the control approach addresses additional difficulties that arise with this practical hardware compared to when a more costly fully flexible valve actuation device is used [20–22, 34, 35].

The modeling approach focuses on low-order mean value combustion models which are tractable for control design and real-time implementation, while many previous models for SI/HCCI transitions [34, 35, 37, 38] are crank angle-based in nature, imposing long computation time and complex and

implicit input/output dependencies. The combustion models are shown to fit a wide range of steady-state data that encompasses conditions which are pertinent to mode transitions, such as AFRs which vary from sweep from rich to very lean in and throttled conditions in HCCI. Models with the ability to capture this range of conditions were instrumental for enabling model-based SI/HCCI transition control, and appeared in [42]. Transient validation of the model in the SI-HCCI direction of the mode transition is also considered, and additional measures are taken which allow the model to reproduce SI-HCCI transition data in multiple conditions.

Control architectures for the SI-HCCI and HCCI-SI transitions are proposed which integrate the model predictions into online nonlinear calculations which inherently generalize across operating points and are reactive to the measured outputs of the engine. Tracking of torque, combustion phasing, and AFR based on the performance objectives listed in Sec. 1.1.3 are all considered in the control design. The controllers are shown in experimental implementation to carry out successful SI/HCCI transitions at multiple operating conditions while requiring calibration of only controller gains and several physically intuitive set points. The validation in the SI-HCCI direction is more extensive than the HCCI-SI direction, however.

A parameter adaptation method is given which uses online SI/HCCI transition data to continuously update the controller model's parameters, in order to make the controller more robust to engine drifts, cylinder to cylinder variability, and parameterization error in general. The parameter adaptation is shown to achieve notable benefits over the baseline controller performance in multiple operating conditions in SI-HCCI transitions, and is also used in HCCI-SI transitions to compensate for the fact that the conditions during the first few cycles after switching to SI are outside the baseline parameterization.

1.4 Outline of the Dissertation

The thesis proceeds by first presenting the mean-value modeling methodology for SI/HCCI multi-mode combustion in Chapter 2, which forms the foundation of the model-based control approach. Models for the engine air path and SI and HCCI combustion are described, as well as the details involved with transitioning between the SI and HCCI models and capturing instantaneous cam switching. Parameterization results over a wide range of steady-state actuator sweep data which are pertinent to SI/HCCI mode transitions are presented for the SI and HCCI combustion models, and the models are shown to reproduce the data with good accuracy.

Chapter 3 considers the model's ability to capture transient phenomena in SI-HCCI mode transitions. It is found that, despite fitting a wide range of steady-state parameterization data with good accuracy, the model encounters difficulty reproducing data from SI-HCCI mode transitions. The cause of the model error is explored and a corrective parameter is introduced based on the residual gas temperature, after which the model is shown to reproduce transient data in multiple

SI-HCCI mode transition conditions with good accuracy. Following its introduction, an adaptive algorithm to tune the corrective residual temperature parameter using online SI-HCCI transition data is described, which allows feedback to be used to compensate for model errors on the initial HCCI cycle of the transition. The adaptive algorithm is shown in simulation examples to compensate for imposed model prediction errors and improve the model's reproduction of SI-HCCI transient data.

After the modeling methodology is described, Chapter 4 presents the first major control component of the dissertation, the control architecture for the SI-HCCI direction of the mode transition. An overview of the progression of SI-HCCI transitions as well as the high-level strategy to carry out the transition is described, noting several possible choices for actuator trajectories and discussing their advantages and disadvantages. The control acrchitecture which implements the chosen high-level strategy through nonlinear model-based calculations with several physically intuitive set points is then presented. The control architecture is implemented on an experimental engine and shown to be capable of carrying out successful SI-HCCI transitions over the HCCI load range at 2000 RPM with only very simple set point adjustments from one operating condition to the next.

Chapter 5 seeks to improve the model-based calculations in the control architecture of Chapter 4 by augmenting an adaptive parameter update scheme to the baseline controller. The purpose of the parameter update scheme is to adjust the controller model's parameters through learning over time, in order to enable the proposed control approach to better handle the effects of engine aging, cylinder to cylinder variability, and model error in general. These attributes are especially pertinent in SI/HCCI transitions where the engine goes through a large state and input transient in a short time period, which gives direct output feedback control a small window over which to act. Application of the parameter adaptation method in experimental SI-HCCI transition examples shows significant performance benefits over the baseline controller in compensating for model errors and cylinder to cylinder variability.

The final major control component of the dissertation covers the HCCI-SI direction of the mode transition and is presented in Chapter 6. The Chapter is structured similar to the presentation of the SI-HCCI control architecture in Chapter 3, first presenting the high-level strategy and progression of the HCCI-SI transition, then moving onto the control design, and finally presenting experimental results. Similar to the SI-HCCI direction, the controller calibration includes only set points and gains with one minor actuator sequencing variable for a cam phasing ramp constant. The torque regulation performance of the controller cannot attain the levels of the SI-HCCI direction, mainly due to physical constraints imposed by air path dynamics when torque and emissions control objectives are simultaneously considered. However, relative to other studies with similar hardware [23–28] which only considered torque and not emissions performance objectives, the controller performance is encouraging and generalizes to multiple operating conditions more easily.

Chapter 2

Mean Value Engine Model for Multi-Mode SI/HCCI Combustion

2.1 Engine Modeling Overview

The engine platform for which the model of this work is developed is a direct injected downsized 2.0 liter 4 cylinder engine with variable valve timing (VVT), which is exhaust gas turbocharged to maintain a high peak power capacity. A schematic of a turbocharged 4 cylinder engine with variable valve timing is shown in Fig. 2.1, which is adapted from [43]. The major variables used to characterize the engine in the control-oriented modeling approach are pressures p and temperatures T at key points throughout the air path, one dimensional flows W, and engine and turbocharger speeds N_{eng} and N_{tc}. Also of concern for controller performance are combustion features such as cycle work and combustion phasing. The control inputs which are pertinent to SI/HCCI mode transitions are the intake throttle valve θ_t, the intake and exhaust cam phasing characterized by intake valve opening (IVO) timing θ_{ivo} and exhaust valve closing (EVC) timing θ_{evc}, the fuel injection quantity and timing m_f and θ_{soi}, and the spark timing θ_{sp}.

The geometry of the experimental engine is summarized in Table 2.1. The engine air path contains standard measurements for induction volume and intake manifold pressure and temperature, as well as cylinder averaged flow rate and exhaust AFR which are only used in steady-state due to transport delays and sensor dynamics. Engine speed is measured by way of a crankshaft encoder. Feedback of combustion features on a cylinder-individual basis is made available through in-cylinder pressure sensors.

Operation in both SI and HCCI combustion is enabled with a two-stage cam system with a set of high lift cams for SI operation and low lift cams for HCCI operation, similar to the configurations in [24–28]. Each low-lift cam is offset from its corresponding high lift cam by a fixed crank angle amount, such that when the cam profiles are switched, all of the valve events instantaneously shift by some constant crank angle difference, where the shift occurs during the closed-valve portion of the cycle. A sketch of the two-stage cam profiles is displayed in Fig. 2.2 to clarify this concept. The offset between the cams is characterized by the difference in EVC timings ΔEVC_{H-L} for the

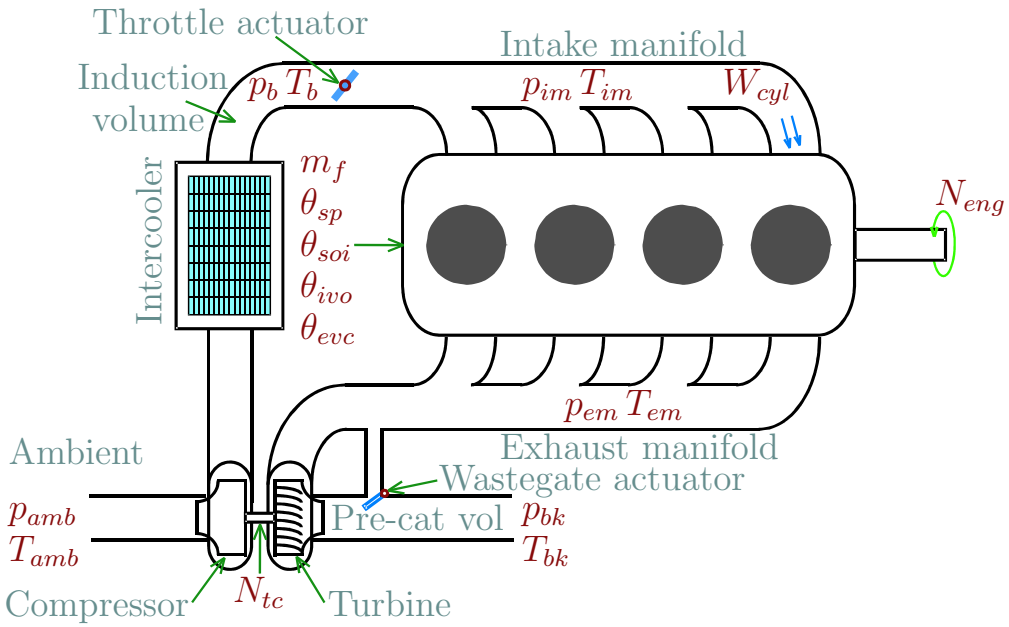

Figure 2.1: Schematic of a turbocharged 4 cylinder engine with variable valve timing.

Compression Ratio (Geometric)	11.7:1
Bore	86 mm
Stroke	86 mm
Connnecting Rod Length	145.5 mm
Wrist Pin Offset	0.8 mm
High/low cam lifts	10 mm/4 mm
High/low cam durations	225°/114°
Intake Valve Opening High-Low Lift Cam Offset	47°
Exhaust Valve Closing High-Low Lift Cam Offset	34°

Table 2.1: Geometry of experimental engine used for model development and controller implementation.

exhaust cams and the difference in IVO timings ΔIVO_{H-L} for the intake cams,

$$\Delta EVC_{H-L} = \theta_{evc}^{high} - \theta_{evc}^{low} \equiv constant, \qquad \Delta IVO_{H-L} = \theta_{ivo}^{high} - \theta_{ivo}^{low} \equiv constant. \tag{2.1}$$

The EVC and IVO timings have been chosen to represent the high-lift to low-lift offset because these timings serve as the valve timing control inputs, which makes them most pertinent to the control system.

An overview of the approach taken to model multi-mode combustion operation is:

- The air path is modeled as a series of steady-flow devices connected by plenums with continuous manifold filling dynamics that are governed by conservation of mass, conservation of energy,

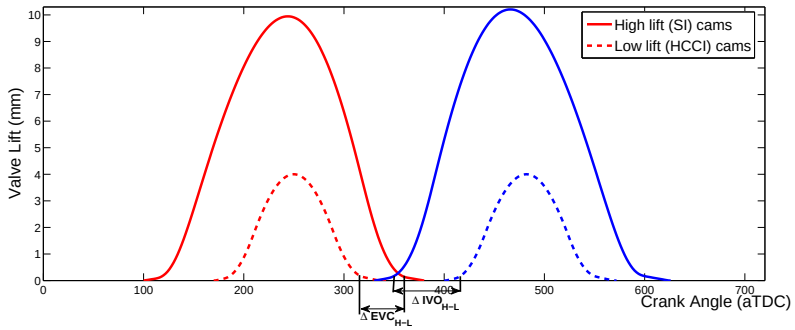

Figure 2.2: Two-stage cam profiles to enable dual SI/HCCI operation.

and the ideal gas law.

- The combustion is modeled as a modified Otto cycle with empirical relations for quantities that are difficult to calculate physically, such as residual gas fraction and combustion phasing. The combustion operates in discrete time, executing once per engine cycle following the mean value modeling approach. A separate model is used for each combustion mode.
- Switching between combustion modes is carried out by disengaging the present combustion mode's model and engaging the destination combustion mode's model. The combustion models are coupled through reisudla gas temperature and composition states which carry over from the final cycle of the terminating combustion mode to the initial cycle of the destination combustion mode.

The above summary will be expanded in detail in what follows.

2.2 Air Path Model

The air path modeling approach is similar to that employed in [44], [45], [46] wherein each of the major engine components are described by a combination of thermodynamic relations and empirical regressions. These major components are:

- The compressor of the turbocharger
- The intake air throttle
- The cylinder array
- The turbine of the turbocharger
- The catalyst

To capture transient mass and energy storage effects along the air path, 0-D manifold filling dynamics are introduced between each of the major engine components at the following locations:

- The induction volume (intercooler outlet)
- The intake manifold
- The exhaust manifold
- The pre-catalyst or "back" volume

2.2.1 Manifold Dynamics and Flow Restrictions

The states of pressure and temperature are chosen to characterize the manifold filling dynamics, giving the state equations [44]

$$\dot{T} = \frac{RT}{pVc_v}(\dot{H}_{in} + \dot{H}_{out} - c_v p(W_{in} + W_{out})) \tag{2.2}$$

$$\dot{p} = \frac{R}{c_v V}(\dot{H}_{in} + \dot{H}_{out}) \tag{2.3}$$

where T represents temperature of the control volume (K), p represents pressure of the control volume (bar), V is the volume of the control volume (m^3), R is the ideal gas constant taken = 287 J/kgK everywhere, c_v is the constant volume specific heat, $\dot{H}$ represents an enthalpy flow rate (J/s), and W represents a mass flow rate (g/s). To obtain a simpler model, temperature dynamics may be taken to be algebraic, which reduces the state description of the manifold dynamics to a single equation [44]

$$\dot{p} = \frac{RT}{V}(W_{in} + W_{out}) \tag{2.4}$$

The intake air throttle valve as well as the wastegate valve of the turbine are modeled using a modified form of the compressible flow orifice equation, which enforces a linear slope at high pressure ratios to avoid the very large derivatives exhibited by the standard orifice flow equation in this region, since such high derivatives can be problematic for numerical simulation:

$$W = A_{eff}\frac{p_{in}}{\sqrt{RT_{in}}}\phi \tag{2.5}$$

$$\phi = \begin{cases} \sqrt{\gamma\left(\frac{2}{\gamma+1}\right)^{\frac{\gamma+1}{\gamma-1}}}, & \frac{p_{out}}{p_{in}} < \left(\frac{2}{\gamma+1}\right)^{\frac{\gamma}{\gamma-1}} \\ \left(\frac{p_{out}}{p_{in}}\right)^{1/\gamma}\sqrt{\frac{2\gamma}{\gamma-1}\left(1-\left(\frac{p_{out}}{p_{in}}\right)^{\frac{\gamma-1}{\gamma}}\right)}, & \left(\frac{2}{\gamma+1}\right)^{\frac{\gamma}{\gamma-1}} \le \frac{p_{out}}{p_{in}} < pr_{lin} \\ \Phi(pr_{lin})\frac{\frac{p_{out}}{p_{in}}-1}{pr_{lin}-1}, & pr_{lin} \le \frac{p_{out}}{p_{in}} \le 1 \end{cases}$$

where W is the mass flow rate (g/s), γ is the ratio of specific heats, T_{in} is the inlet temperature (K), p_{in} is the inlet pressure (bar), p_{out} is the outlet pressure (bar), and A_{eff} is the effective area (cm^2), which is regressed to the valve position. A simplified incompressible form of the orifice equation is used to model the flow out of the back volume (into the catalyst)

$$W_{cat} = \sqrt{\frac{p_{in}(p_{in} - p_{out})}{CT_{in}}} \tag{2.6}$$

where the flow resistance C is modeled as a function of pressure drop across the catalyst

$$\frac{1}{C} = f(p_{bk} - p_{atm}) \tag{2.7}$$

where the function f can be linear, quadratic, or logarithmic, with the linear dependence being sufficient but the logarithmic dependence fitting the best.

2.2.2 Turbocharger

The compressor and turbine of the turbocharger are considered as steady-flow, constant specific heat devices, which allows each of their thermodynamic outputs to be calculated when their flow rate and isentropic efficiency are known. Thus, the main task of the compressor and turbine models is to regress the mass flow rate and isentropic efficiency to manufacturer map data; the rest of the quantities can then be calculated through well-known thermodynamic equations.

The compressor mass flow is regressed using a functional form put forth in [47] which is elaborated on in [48],

$$W = \frac{\pi}{4}\Phi\rho d^2 U, \qquad U = \frac{\pi}{60}N_{tc,cor}d \tag{2.8}$$

$$\Phi = \frac{k_3\Psi - k_1}{k_2 + \Psi}, \qquad each \quad k_i = k_{i1}M + k_{i2} \tag{2.9}$$

$$\Psi = \frac{c_p T_{in}((\frac{p_{out}}{p_{in}}^{\frac{\gamma-1}{\gamma}} - 1)}{\frac{U^2}{2}} \tag{2.10}$$

Here, ρ is the air density (kg/m^3), d is compressor diameter (mm), U is the blade tip speed, $M = \frac{U}{\sqrt{\gamma R T_{in}}}$ is the Mach number, and Φ and Ψ are dimensionless quantities for the mass flow and pressure ratio, respectively. The compressor efficiency regression is unmodified from that in [46]. The regression first correlates the dependence peak efficiency and the corresponding volumetric flow rate at peak efficiency to turbocharger speed, and then uses the functional form of Eq. (2.13) to regress the actual efficiency to the peak efficiency. The regression to peak efficiency (2.13) depends on whether the current flow rate is above or below the flow rate for the peak efficiency at the current turbocharger speed.

$$\dot{V} = \frac{WRT_{in}}{p_{in}}, \qquad \dot{V}_{\eta*} = a_1 N_{tc} + a_0 \tag{2.11}$$

$$\eta^* = b_2 N_{tc}^2 + b_1 N_{tc} + b_0 \tag{2.12}$$

$$\eta = \begin{cases} \eta^*[c_1(\dot{V} - \dot{V}_{\eta*})^{c_2} + 1], & \dot{V} > \dot{V}_{\eta*} \\ \eta^*[c_3(\dot{V}_{\eta*} - \dot{V})^{c_4} + 1], & \dot{V} \leq \dot{V}_{\eta*} \end{cases} \tag{2.13}$$

Here, $\dot{V}$ is the volumetric flow rate, η is the compressor efficiency, and η^* is the peak efficiency at a given turbocharger speed in the manufacturer data. Once the compressor mass flow and efficiency have been obtained, the output temperature and enthalpy flow can be calculated from the thermodynamic relations [48]

$$\Delta h = \frac{h_{in}}{\eta + 10^{-4}} \frac{p_{out}}{p_{in}}^{\frac{\gamma-1}{\gamma}} \tag{2.14}$$

(10^{-4} added in denominator to avoid division by 0.)

$$h_{out} = h_{in} + \Delta h \qquad \dot{H}_{out} = h_{out} W \qquad T_{out} = \frac{h_{out}}{c_p} \tag{2.15}$$

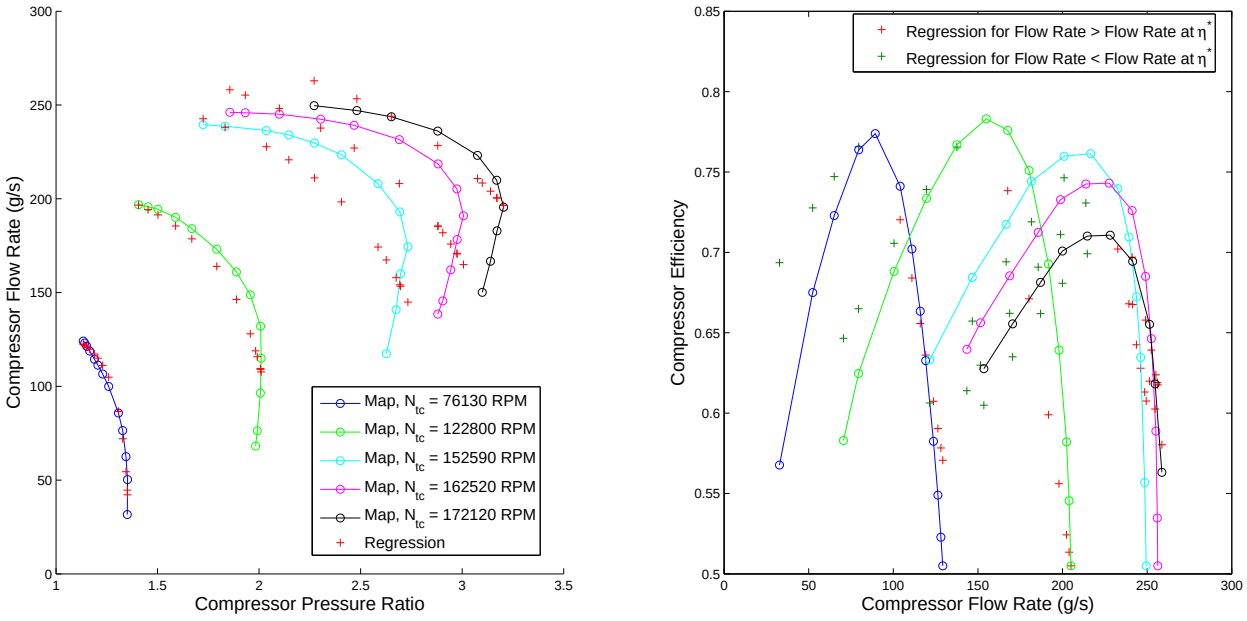

Figure 2.3: Compressor mass flow and efficiency regressions to manufacturer maps.

Since the turbine acts as a restriction to the exhaust gas flow, the turbine mass flow is modeled with the same compressible orifice flow equation (2.5) used to model the throttle and wastegate valves, following the approach in [48]. The major regression involved with this approximation is the effective area for the equivalent orifice, which has been modeled here as a piece-wise linear function

of turbocharger speed and pressure ratio:

$$A_{eff,t} = a_1 \frac{p_{out}}{p_{in}} + a_0, \qquad each \quad a_i = \alpha_1(N_{tc})N_{tc} + \alpha_0(N_{tc}) \tag{2.16}$$

where the values for the coefficients α_1 and α_0 are split into 3 turbocharger speed regions. The turbine efficiency typically takes the form of an inverted parabola in the blade-speed ratio U/C

$$\frac{U}{C} = \frac{\pi d N_{tc}}{60\sqrt{2c_p T_{in}(1 - \frac{p_{out}}{p_{in}}^{\frac{\gamma-1}{\gamma}})}} \tag{2.17}$$

and hence is often fit using a quadratic polynomial in U/C as in [48]. However, manufacturer maps typically contain only of narrow range of U/C values (from about 0.5 to 0.7 while U/C can vary from 0 to 1), and so when required to extrapolate outside the available range of U/C, a quadratic polynomial quickly falls < 0 giving unrealistic behavior. To obtain a regression that more reasonably extrapolates to U/C values outside the manufacturer maps, a Gaussian curve in U/C is used to model the turbine efficiency

$$\eta_{nom} = a_1 e^{\left(-\left(\frac{\frac{U}{C} - a_2}{a_3}\right)^2\right)} + 0.2, \qquad each \quad a_i = \alpha_1 N_{tc} + \alpha_0 \tag{2.18}$$

where the $+0.2$ term limits the efficiency at a minimum value of 0.2, based on the physical reasoning that the turbine will always be spinning and producing work to some extent while the engine is in operation. In addition to the nominal regression to manufacturer maps, a correction factor is added in order to increase the peak boosting capacity of turbocharger between engine speeds of 1500 and 2500 RPM

$$\eta_{cor} = [u_s(N_{eng} - 1500) - u_s(N_{eng} - 2500)][0.1 - .00017|2000 - N_{eng}|] \tag{2.19}$$

$$\eta = \eta_{nom} + \eta_{cor} \tag{2.20}$$

where u_s is the Heaviside step function. This correction factor was added because it was found that the turbocharger model was unable to achieve boost pressures near the peak boosting capacity of 1.8-2.2 bar observed in experiment between engine speeds of 1500-2500 RPM, despite fitting the manufacturer maps fairly well. A similar underboosting effect between 1500 and 2500 RPM was observed in a higher fidelity GT-Power model which used the same turbocharger maps. The problem may be that the manufacturer turbine map data are all recorded a constant intake temperature which is fairly low (873 K), and so as the exhaust temperature gets higher there may be some strong nonlinear effect that increases the work extracted by the turbine which is not captured by the map.

Once the turbine mass flow and efficiency have been obtained, the output temperature and enthalpy flow can be calculated from the thermodynamic relations [48]

$$\Delta h = \eta h_{in} \left((\frac{p_{out}}{p_{in}})^{\frac{\gamma-1}{\gamma}} - 1 \right) \tag{2.21}$$

$$h_{out} = h_{in} + \Delta h \qquad \dot{H}_{out} = h_{out} W \qquad T_{out} = \frac{h_{out}}{c_p} \tag{2.22}$$

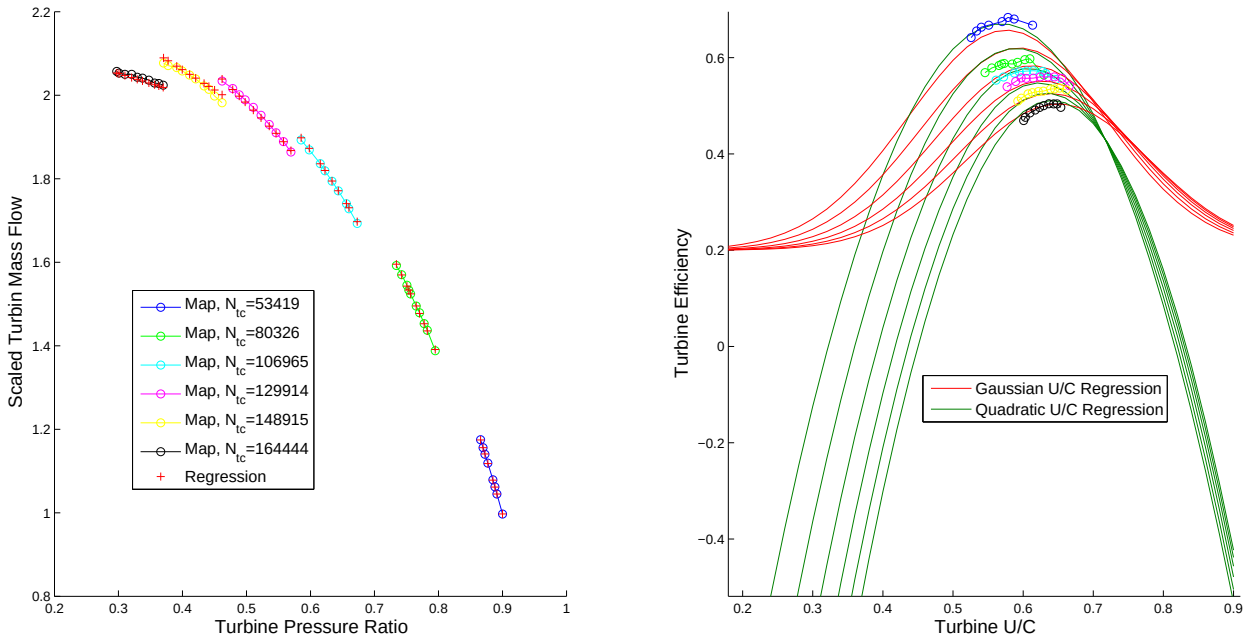

Figure 2.4: Turbine mass flow and efficiency regressions to manufacturer map. Note that a version of the turbine mass flow scaled by $p_{in}/\sqrt{T_{in}}$ is shown as this was the only quantity available from the map, however this scaling does not affect the accuracy of the fit. Additionally, the Gaussian efficiency regression profile of (2.18) is shown along with a standard quadratic efficiency regression profile so that the desirable extrapolation characteristics of the Gaussian can be seen.

To estimate the turbocharger shaft speed, a state is introduced whose dynamics are governed by a power balance between the compressor and turbine as in [48], [46]

$$\dot{N}_{tc} = \frac{1}{J_{tc} N_{tc}} (W_{turb} \Delta h_{turb} - W_{comp} \Delta h_{comp}) \tag{2.23}$$

where J_{tc} is the turbocharger moment of inertia and $P = W\Delta h$ has been used to calculate the power of the turbine and compressor. The intercooler at the outlet of the compressor is modeled as

a steady-flow, zero pressure drop heat exchanger as in [45], [46]

$$T_{out} = T_{in} - \eta_{ic}(T_{in} - T_{ic}^*) \tag{2.24}$$

$$\eta_{ic} = a_1 W_c + a_0 \tag{2.25}$$

where the efficiency of temperature exchange η_{ic} is linearly dependent on air flow and T_{ic}^* is the set point temperature of the cooler.

2.2.3 Actuator Dynamics

Because the manifold dynamics and cycle to cycle combustion dynamics can vary on a time scale of tens of milliseconds, it is important to consider the dynamics of the valves in the air path because the electronic actuators that move these valves have time constants on the scale of tens to even hundreds of milliseconds. The actuator dynamics are modeled considering the effect of the lower level proportional + integral + derivative (PID) controllers which govern the tracking of the actuators to the commanded set points in the loop. This loses some generality in that the parameterization of the actuator dynamics depends on the tuning of the lower level PID controllers, however it simplifies the modeling task in that the dynamics of the full closed-loop system consisting of both the actuator and PID controller does not have to be considered.

The throttle and VVT dynamics are modeled as prototype second order linear systems

$$\ddot{\theta} + 2\zeta\omega_n\dot{\theta} + \omega_n^2\theta = \omega_n^2 u \tag{2.26}$$

where θ is the valve position, u is the input command, ζ is the damping ratio, and ω_n is the natural frequency. The values of ζ and ω_n are identified from measured step and ramp response data, and take the values

$$\zeta_t \equiv .7265, \qquad \omega_{n,t} \equiv 30.665 \text{ rad/s} \tag{2.27}$$

$$\zeta_{vvt} \equiv .4842, \qquad \omega_{n,vvt} \equiv 15.2 \text{ rad/s} \tag{2.28}$$

Plots of the linear second order approximations of the measured throttle (left) and exhaust valve timing (right) actuator dynamics are shown in Fig. 2.2.3. The overshoot predicted by the throttle modeled response when in fact there is none is perhaps the most unfavorable aspect of the simple second order approximations, however the accuracy of the predictions are sufficient for controls purposes. Note that the exhaust valve timing is shown in units of crank angle degrees relative to the max retard position, because throughout this trial the exhaust cam was switched from high lift to low lift in order to subject the model to both cam lifts. The cam switch shifts the EVC timing as explained in Sec. 2.1, but does not affect the relative phasing. More details on this matter are

given in Sec. 2.2.4. Also note that the dynamics of the intake and exhaust cam phaser were very similar (both use the same actuator), and so the same ζ and ω_n values are used for both intake and exhaust valve timings.

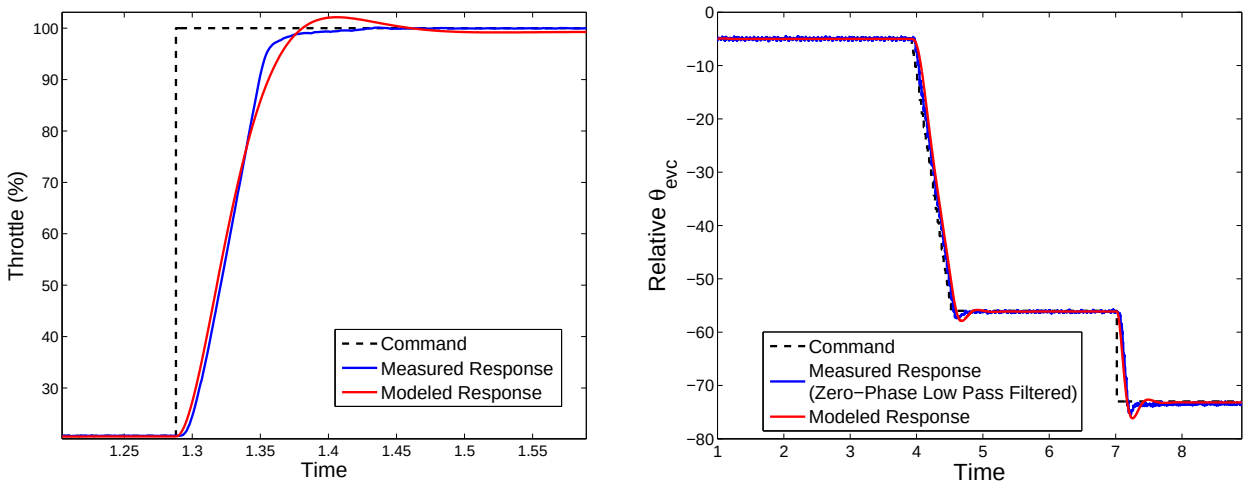

Figure 2.5: Linear second order actuator dynamics model predictions for the throttle (left) and cam phasing (right).

The remaining air path actuator is the wastegate of the turbocharger. No time response data for wastegate position was available for identification of the wastegate dynamics, so a simple first order linear approximation is imposed as a rough estimate.

$$\dot{\theta}_{wg} + \frac{1}{\tau_{wg}}\theta_{wg} = \frac{1}{\tau_{wg}}u_{wg} \tag{2.29}$$

$$\tau_{wg} \equiv 125 \text{ msec} \tag{2.30}$$

The time constant τ_{wg} is chosen to give a significantly slower response than that of the throttle, as the wastegate is typically slower than the throttle. Additionally, this model is selected assuming an electronic wastegate which can be freely actuated; for a pneumatically actuated wastegate, the dynamics could be even more significant and contain several saturation type nonlinearities. While the choice of wastegate actuator dynamics is a crude approximation, the wastegate is not an important actuator for SI/HCCI transitions with naturally aspirated HCCI operation, as these transitions occur in the lower load regime of SI operation where turbocharging effects are negligible.

2.2.4 Integrating Continuous Cam Phaser Dynamics with Instantaneous Cam Switching

Though the VVT device has significant actuator dynamics as portrayed in Fig. 2.5, instantaneous shifting of the valve timings can occur during a cam switch due to the offset between the high lift and low lift cam profiles of the two-stage cam mechanism (see Fig. 2.2). This implies that to model the dynamics of the valve timings with the two-stage cam mechanism, it is necessary to include continuous actuator dynamics as well as discrete jumps that occur when the cams are switched. In order to capture both of these effects, observe from Fig. 2.2 that because the crank angle offset between the high-lift and low-lift cams is fixed, if the high-lift cams are phased by a given amount so that the high-lift profile shifts to the left or right along the crank angle axis, then the low-lift cams must also necessarily be phased by the same amount. A single variable must thus be sufficient to characterize the phasing of both the high-lift and low-lift cams, which is here chosen to be the angle of the cam phaser relative to its max retard position, which we define as θ^{rel}. θ^{rel} can be calculated by taking the difference between the crank angle of any valve event and the crank angle of the same valve event when the cam phaser is at its max retard position θ^{max}. For example, the intake θ^{rel} can be calculated by taking the difference between the current IVO timing and IVO timing at max retard, and similarly the exhaust θ_{rel} can be calculated by taking the difference between the current EVC timing and EVC timing at max retard,

$$\theta_i^{rel} = \theta_{ivo} - \theta_{ivo}^{max}, \qquad \theta_e^{rel} = \theta_{evc} - \theta_{evc}^{max} \tag{2.31}$$

where θ_i^{rel} and θ_e^{rel} denote the intake and exhaust cam shaft relative phasing, respectively. While IVO and EVC are obvious choices of valve events to use to calculate θ^{rel}, any valve event such as IVC or EVO can be used as long as the corresponding θ^{max} value is correct.

With the definition of θ_i^{rel} and θ_e^{rel} in Eq. (2.31), both the high-lift and low-lift IVO and EVC timings can be calculated by knowing the θ_{rel} value for the intake and exhaust cam phasers:

$$\theta_{ivo}^{H} = \theta_i^{rel} + \theta_{ivo}^{H,max}, \qquad \theta_{evc}^{H} = \theta_e^{rel} + \theta_{evc}^{H,max} \tag{2.32}$$

$$\theta_{ivo}^{L} = \theta_i^{rel} + \theta_{ivo}^{L,max}, \qquad \theta_{evc}^{L} = \theta_e^{rel} + \theta_{evc}^{L,max} \tag{2.33}$$

where superscript H indicates a value for high-lift cams and superscript L indicates a value for low-lift cams. Note $\theta_{ivo}^{H,max} - \theta_{ivo}^{L,max} = \Delta IVO_{H-L}$ and $\theta_{evc}^{H,max} - \theta_{evc}^{L,max} = \Delta EVC_{H-L}$ as defined in Eq. (2.1). Thus, the continuous cam phaser dynamics can be captured solely through θ_i^{rel} and θ_e^{rel}, and when the cams switch, the instantaneous shift of the valve timings is captured simply by changing the θ^{max} values to those of the cams that are now in place. A block diagram of the method to capture continuous cam phaser dynamics with instantaneous cam profile switching is depicted in Fig. 2.6 taking the IVO position for example, where Λ^{cam} represents the cam profile

(high or low lift) that is in place.

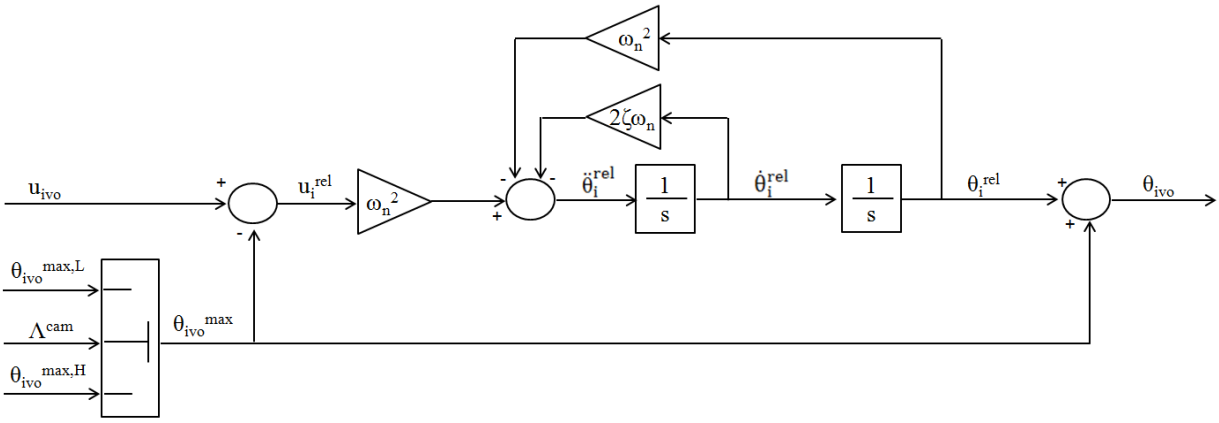

Figure 2.6: Method to model continuous cam phaser dynamics with discrete jumps in valve timings due to cam profile switching. IVO timing used for example.

It is briefly noted here that for simulation implementation of continuous VVT dynamics with instaneous cam switching, characterizing the exhaust valve timing dynamics with respect to EVO instead of EVC becomes advantageous because the cams switch during the closed-valve portion of the cycle, and the cycle division is drawn at EVO. This means that on a cycle where the cams switch, the EVO at the end of the engine model's cycle will have a different lift than that at the start (i.e. the EVO which is delayed from the end of the previous cycle), and so the shift needs to be taken into consideration directly on the switching cycle. For the EVC timing, the effect of the cam switch is not felt until the first cycle after the cams are switched. This convention does not change the actuator dynamics model Eq. (2.26) and need not be considered in controller design.

2.3 SI Combustion Model

2.3.1 Overview

The SI combustion model follows a structure similar to that of [46], with extensive modifications for additional functionalities and better agreement with data. The basic premise of the model is to carry out a modified Otto cycle, with polytropic compression and expansion processes and an instantaneous combustion. The model's most challenging tasks are to obtain the necessary quantities for the thermodynamic cycle calculation to be carried out, and to introduce realistic effects into the idealized Otto cycle so that the model can accurately predict outputs seen in experiment.

The combustion model operates in discrete time, executing its calculations once per engine cycle

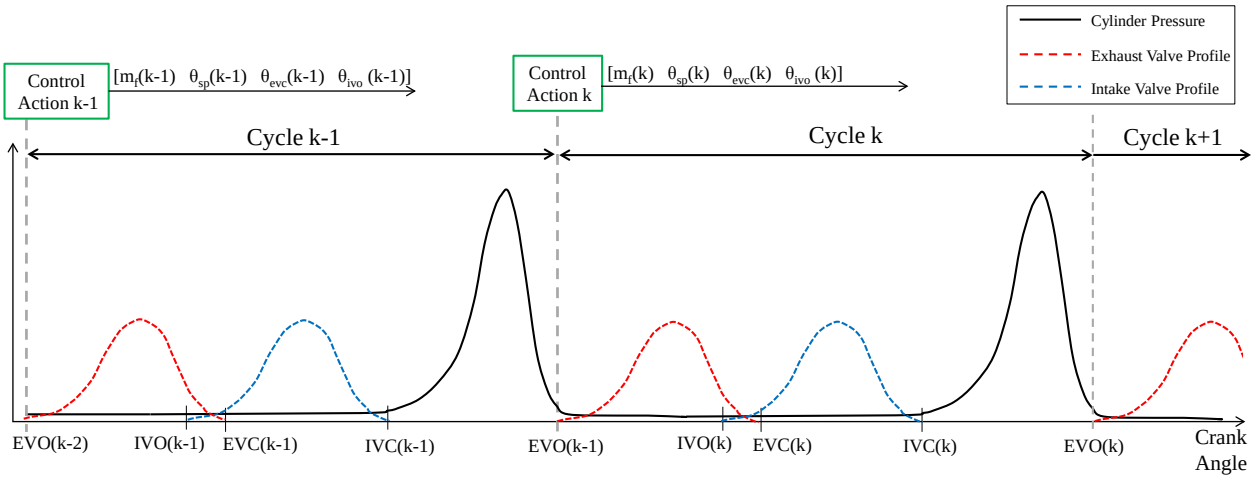

Figure 2.7: Cycle definition of the SI combustion model.

following the mean value modeling approach. Note that this approach assumes that the engine speed is known and changes slowly relative the cycle duration. The combustion model cycle is divided at the exhaust valve opening (EVO) event as depicted in Fig. 2.7. It is clear from the diagram 2.7 that with this cycle definition, the EVC timing for the current cycle is dictated by the EVO timing for the past cycle,

$$\theta_{evc}(k) = \theta_{evo}(k-1) + \Delta EV \tag{2.34}$$

where ΔEV is the exhaust cam duration and k is the cycle index. This EVC convention is not a consequence of the valve event's underlying physical process, but rather a necessity for implementation of the mean value model in simulation. Also indicated in Fig. 2.7 are the instants where control inputs can be calculated and applied to the combustion model, so the interface between a controller and the model can be seen. Each control action is assumed to occur at the end of the combustion model cycle, so that the cycle completes and any combustion outputs can be fed back to the controller to calculate the control inputs to be applied to the next cycle. Note that the valve timings θ_{evc} and θ_{ivo} are technically states and not input commands due to the actuator dynamics (see Sec. 2.2.3), but are taken to be externally specified by the air path model and so are input once per cycle as with the other input variables. The injection timing θ_{soi} is not counted amongst the inputs to the SI model as it is not used in control of the SI combustion mode, as it has been found to have minimal effect on combustion for a wide range of timings in the intake stroke. Lastly, note that both the intake and exhaust valves in Fig. 2.7 follow the high lift profile with PVO; in a later Section, SI/HCCI mode transitions will be considered where the SI combustion operates with a low lift intake cam profile and high lift exhaust cam profile, which is chosen based on the

mode transition strategy. For SI/HCCI transitions with that strategy, the SI combustion model will be parameterized assuming a low lift intake cam profile, and any adjustments to the model with the high lift intake profile presented here will be described.

Before going onto describe the combustion model equations, we first note the following assumptions employed by the combustion model.

Model Assumptions

1. The mixture can be treated as an ideal gas with constant specific heats. The specific heat during the intake and compression strokes is equivalent to the specific heat of atmospheric air; the specific heat of the gases during combustion is indeterminate, and can be chosen to give a reasonable temperature rise due to combustion.
2. The compression and expansion strokes can be treated as polytropic processes with a constant polytropic coefficient, and the combustion can be treated as constant volume, adiabatic heat addition.
3. The point of instantaneous combustion is taken at $|\theta_{50} - \theta_{50,MBT}|$ as in [49], where θ_{50} is the crank angle where 50% of the fuel mass has burned and $\theta_{50,MBT}$ is the θ_{50} timing for maximum brake torque, taken = 7° aTDC. This selection logic causes the cylinder volume during combustion to be larger as θ_{50} moves further from its max brake torque position, which causes the extracted work and hence torque output to reduce in a trend similar to that seen in experiments as spark is advanced/retarded from its optimal position.
4. Cylinder to cylinder variations can be neglected - the combustion model is parameterized to a single cylinder only.
5. Cycle to cycle couplings are negligible in the SI combustion mode due to a low quantity of recycled exhaust gas. The combustion can be modeled as a static nonlinear mapping that is independent of previous cycles, and so contains no states. To justify this assumption, it is noted that the maximum residual gas fraction as processed from steady-state actuator sweep data in SI/HCCI transtion relevant conditions is $\approx 25\%$, and will in general tend to be lower than this value because of the EVC placement necessary to attain the residual gas fraction this large. Also note that this is only about half of the minimum residual gas fraction observed in HCCI steady-state sweep data of $\approx 47\%$.

2.3.2 Model Calculations

Cylinder Charge and IVC Conditions

The SI combustion model calculations begin by determining the charge mass and composition. The flow rate into the cylinders is obtained through a speed-density like regression modified after [50]

$$W_{cyl} = \alpha_1(\theta_{evc}, \theta_{ivo})p_{im} + \alpha_0(\theta_{evc}, \theta_{ivo}) \tag{2.35}$$

$$\alpha_i = a_{i1}\theta_{evc}^2 + a_{i2}\theta_{evc} + a_{i3}\theta_{ivo}^2 + a_{i4}\theta_{ivo} + a_{i5} \tag{2.36}$$

where p_{im} is the intake manifold pressure and all a_i represent regression coefficients. In general, the coefficients α_1 and α_0 will be functions of engine speed, valve timings, and intake temperature, however the parameterization data contained only one engine speed and a small variation in intake temperature and so the α_1 and α_0 are simple quadratic functions of valve timings. The mass of fresh air can then be calculated assuming a uniform cylinder flow rate over the duration of the intake stroke

$$m_a^{in} = \frac{W_{cyl}}{N_{eng}/120 N_{cyl}} \tag{2.37}$$

where N_{cyl} is the number of cylinders.

To calculate the total in-cylinder mas, it is also necessary to know the residual gas amount, which is obtained from a regressed through the residual gas fraction $x_r := m_r/m_c$, where m_r is the residual mass and m_c is the total mass. The regression is developed manually to fit post-processed data and takes the form

$$x_r = a_1\theta_{evc}^2 + a_2\theta_{evc} + a_3\theta_{ivo} + a_4 p_{im} + a_5 m_f^0 + a_6\theta_{sp}^0 + a_7 \tag{2.38}$$

which has a quadratic dependency on θ_{evc} to capture the inflection in residual quantity between rebreathing (θ_{evc} aTDC) and trapping (θ_{evc} bTDC). θ_{ivo} and p_{im} are included to represent effects on intake air charge affecting the fraction of residal gas, and cycled delayed values for fuel mass and spark timing m_f^0 and θ_{sp}^0 are included to capture the affect of these inputs on exhaust temperature, which can affect the storage of residual gas. Note that the cycle delays on inputs m_f^0 and θ_{sp}^0 are trivial to implement as these quantities are specified by the control system and so are always known explicitly.

With m_a^f and x_r determined, the complete charge mass can then be obtained from the equation

$$m_c = \frac{m_a^{in} + m_f}{1 - x_r} \tag{2.39}$$

where the relation $m_r = x_r m_c$ has been used. The AFR can also be calculated, which we quantify in terms of the relative to the stoichiometric air-fuel ratio λ

$$\lambda = \frac{\frac{m_a^{in}}{m_f}}{AFR_s} \tag{2.40}$$

where $AFR_s \approx 14.6$ for gasoline. Here it is assumed that $m_a \equiv m_{air}^{in}$, i.e. that there is no recycled air, so that λ represents the AFR in the exhaust. In typical SI operation with near-stoichiometric mixtures and small residual amounts, this should also be very close to the AFR in the cylinder, which includes recycled air.

After the cylinder charge mass and composition have been determined, the pressure and temperature at IVC are found, starting with the pressure p_{ivc} which is obtained as a linear function

intake manifold pressure as in [46]

$$p_{ivc} = \beta_1 p_{im} + \beta_0. \tag{2.41}$$

The temperature T_{ivc} can be calculated using the ideal gas law with the known cylinder charge mass

$$T_{ivc} = \frac{p_{ivc} V_{ivc}}{R m_c}. \tag{2.42}$$

Here $R \approx 287 J/kgK$ is the ideal gas constant for air, and the volume at IVC is calculated from the crank-slider equation

$$V(\theta) = V_{cl} + \frac{\pi B_{cyl}^2}{4}\left(L_{cr} + a_c - a_c\cos(\theta) - \sqrt{L_{cr}^2 - (a_c \sin(\theta))^2}\right) \tag{2.43}$$

where θ is the crank angle of a given event (here IVC), V_{cl} is the chamber clearance volume, L_{cr} is connecting rod length, B_{cyl} is the cylinder bore, and a_c is one half the stroke length.

Polytropic Compression/Expansion and Constant Volume Combustion

The next step of the engine cycle is to proceed with polytropic compression and constant volume combustion. Before doing this, the crank angle of instantaneous combustion θ_{cmb} must be found. As discussed in Assumption 3 in Sec. 2.3.1, the point of instantaneous combustion is defined through the 50% burn angle θ_{50} following [49],

$$\theta_{cmb} = |\theta_{50} - \theta_{50}^{MBT}| \tag{2.44}$$

where the θ_{50} for max brake torque θ_{50}^{MBT} is taken $\equiv 7°$. This implies that θ_{50} must be found prior to polytropic compression, which is determined through the regression

$$\theta_{50} = a_1\theta_{sp}^2 + a_2\theta_{sp} + a_3 m_f + a_4\theta_{evc}^2 + a_5\theta_{evc} + a_6\theta_{ivo}^2 + a_7\theta_{ivo} + a_8 \tag{2.45}$$

Now polytropic compression can be carried out

$$p_{bc} = p_{ivc}\left(\frac{V_{ivc}}{V_{cmb}}\right)^{n_c} \tag{2.46}$$

$$T_{bc} = T_{ivc}\left(\frac{V_{ivc}}{V_{cmb}}\right)^{n_c - 1} \tag{2.47}$$

where $V_{cmb} = V(\theta_{cmb})$ is the volume where combustion occurs, n_c is the (constant) polytropic exponent during compression, and the subscript "bc" indicates before combustion. At θ_{cmb}, combustion is taken to occur as constant volume adiabatic head addition, giving the expression for the

temperature rise

$$T_{ac} = T_{bc} + \frac{m_f Q_{lhv}}{c_v m_c} \tag{2.48}$$

where Q_{lhv} is the lower heating value for the fuel, c_v is the constant volume specific heat during combustion (taken constant), and the subscript"ac" indicates after combustion. The assumption of constant volume combustion causes the ideal gas law for the pressure after combustion to reduce to

$$p_{ac} = p_{bc}\left(\frac{T_{ac}}{T_{bc}}\right). \tag{2.49}$$

The cylinder gasses are then expanded polytropically to EVO from the point of instantaneous combustion

$$p_{evo} = p_{ac}\left(\frac{V_{cmb}}{V_{evo}}\right)^{n_e} \tag{2.50}$$

$$T_{evo} = T_{ac}\left(\frac{V_{cmb}}{V_{evo}}\right)^{n_{exp}-1} \tag{2.51}$$

where n_e is the (constant) polytropic exponent during expansion.

End of Cycle Outputs

After the EVO event, the outputs from the cylinders to the air path including the exhaust temperature and flow rate are calculated, along with the cycle work. Exhaust gas blowdown is assumed to occur immediately following the EVO event at constant volume, giving a polytropic expansion down to exhaust manifold pressure

$$T_{bd} = T_{evo}\left(\frac{p_{em}}{p_{evo}}\right)^{1-\frac{1}{n_{bd}}} \tag{2.52}$$

where T_bd represents the temperature after blowdown and n_{bd} is the (constant) polytropic exponent during blowdown. From the blowdown temperature, the temperature of the gas flowing into the exhaust manifold is calculated using an expression based on steady-state heat convection for pipe flow put forth in Model 1 of [51]

$$T_{em} = T_w + (T_{cyl,out} - T_w)\exp\left(\frac{h(W_{cyl})A}{c_p W_{cyl}}\right) \tag{2.53}$$

where the temperature at the cylinder exhaust port $T_{cyl,out}$ is calculated assuming a temperature drop during the exhaust stroke that linearly increases with mass flow, and the convection coefficient

h is a cubic regression to mass flow rate

$$T_{cyl,out} = T_{bd} - kW_{cyl} \tag{2.54}$$

$$\frac{h(W_{cyl})A}{c_p} = a_3 W_{cyl}^3 + a_2 W_{cyl}^2 + a_1 W_{cyl} + a_0 \tag{2.55}$$

This calculation is different from the model in [51] in that it introduces a temperature drop to the cylinder exhaust port using (2.54) and the wall temperature T_w is let vary as a coefficient in the regression instead of being taken at atmospheric temperature.

The mass and enthalpy flow output to the exhaust manifold are computed from

$$W_{ex} = (m_a^{in} + m_f)\frac{N_{eng}}{120}N_{cyl} \tag{2.56}$$

$$\dot{H}_{ex} = W_{ex} c_{p,ex} T_{ex} \tag{2.57}$$

$$c_{p,ex} = a_1 T_{ex} + a_0 + R \tag{2.58}$$

where the constant volume specific heat of the exhaust gas has been approximated as a linear function of exhaust manifold temperature for the SI combustion operation regime. Note that expression (2.56) assumes that the exact amount of mass that entered the cylinder on the current cycle also leaves the cylinder during the exhaust stroke, i.e. the system is in steady-state. Another way to state this is that the residual mass is assumed to be the same on the upcoming cycle as on the current cycle.

The gross work output of the cycle is calculated noting that the compression and expansion strokes were assumed to be polytropic processes, so that the expression for work of a polytropic process can be used

$$W_{cig} = \frac{p_{bc}V_{cmb} - p_{ivc}V_{ivc}}{1 - n_c} + \frac{p_{evo}V_{evo} - p_{ac}V_{cmb}}{1 - n_e} \tag{2.59}$$

where W_{cig} refers to the gross indicated cycle work. The gross indicated mean effective pressure (IMEP) can be obtained by dividing out by the cylinder displacement volume V_d

$$IMEP = \frac{W_{cig}}{V_d} \tag{2.60}$$

and finally the net indicated mean effective pressure (NMEP) is calculated assuming a rectangular pumping loop

$$NMEP = IMEP - (p_{em} - p_{im}) \tag{2.61}$$

A last detail of the SI model calculations concerns syncing the SI model with HCCI model during mode transitions. Because the HCCI model contains states for cycle-cycle couplings as will be noted

in Sec 2.4, during an SI-HCCI transition these states must be initialized by the SI combustion to be passed to the HCCI model for the first HCCI cycle. Thus, these state values are calculated during the SI/HCCI coupling cycle of an SI-HCCI transition, and are otherwise discarded. One of these states is the blowdown temperature T_{bd}, which is already necessary for the SI model in Eq. 2.52. The other states correspond to the compositional variables of burned gas fraction and fuel mass fraction. The burned gas fraction b_{bd} can be shown to reduce to an algebraic function of AFR in steady-state, so that the cycle to cycle coupling in the following equation is not necessary

$$b_{bd} = \frac{m_f(AFR_s + 1)}{m_c} + x_r b_{bd}(k-1) = \frac{AFR_s + 1}{\lambda AFR_s + 1} \quad \text{in steady-state} \tag{2.62}$$

The fuel mass fraction f_{bd} is set to 0 unless the mixture is rich past a specified threshold λ_{min} until which it is declared that all fuel burns for simplicity in the model's compositional relations

$$m_{uf} = \max\{0, (\lambda_{min} - \lambda)m_f\}, \quad \lambda_{min} \leq 1 \tag{2.63}$$

$$f_{bd} = \frac{m_{uf}}{m_c} \tag{2.64}$$

where m_{uf} is the mass of unburnt fuel and λ_{min} is chosen = 0.97.

2.3.3 Steady-State Parameterization Results

The parameters of the SI combustion model are determined in regression against a grid of steady-state actuator sweep data at 2000 RPM with a constant stoichiometric AFR. Because the SI model contains no cycle to cycle couplings, fitting of the model coefficients can be done easily by determining each regesssion's coefficients from a least squares fit from the measured inputs to the measured outputs of the regression. In the HCCI case where cycle to cycle couplings play a role, the regression method is not as straightforward because it depends on states from the previous cycle whose values inherently change as the regression fit changes, creating an internal feedback. The regressions of the SI model are fit sequentially, starting with W_{cyl} and x_r, and then moving onto θ_{50} and finally W_{cig}, using the modeled values from previous regressions as inputs to those which follow, in order to account for the effects of compounding model error.

In the parameterization data, fuel and air were varied simultaneously to change the load through adjusting the throttle with constant AFR. The innermost variable of the input grid was spark timing, followed by fuel (and hence air) mass, then the intake valve timing and finally exhaust valve timing. The exhaust valve timing was swept to very advanced positions, as the mode transition strategy involves advanced EVC timings in SI mode as will be explained in future Chapters. The 451 point input grid and modeled versus measured outputs of θ_{50}, $NMEP$, and air mass m_a are shown in Fig. 2.8. Air mass is shown as opposed to λ because AFR is held fixed. A summary of

the ranges swept and fit statistics are given in Table 2.2. Inspection of the results in Fig. 2.8 and Table 2.2 shows that the model fits the data with good accuracy considering the simplicity of the model and the wide range of actuator settings.

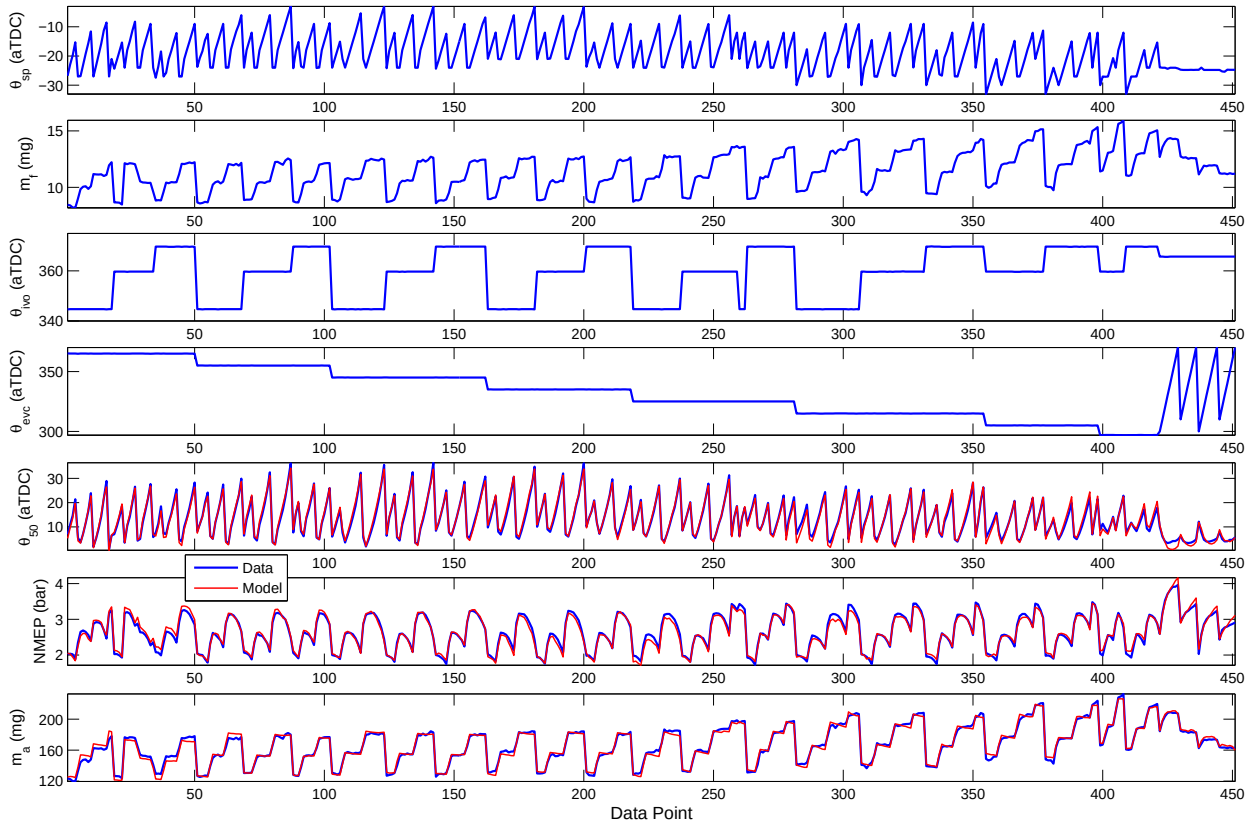

Figure 2.8: Input grid and modeled vs. measured outputs for steady-state SI model parameterization data. Mass of air m_a shown in place of λ as because a stoichiometric AFR was maintained throughout the sweeps.

2.4 HCCI Combustion Model

The basic structure of the HCCI combustion model is similar to that of the SI combustion model, in that it carries out polytropic compression and expansion processes with an instantaneous combustion and uses regressions for quantities which are difficult to estimate physically. The HCCI model's cycle division is also drawn at EVO for easy integration of the two models for multi-mode combustion, which means that Eq. (2.34) applies to the HCCI model as well. The model draws several ideas from the model of [52], the main ones being the cycle division at EVO, recycled exhaust gas thermal and compositional states, an energy balance at IVC to determine the charge properties before

	Min	Max	Mean Abs. Error	Max Abs. Error
θ_{sp} (aTDC)	-33	-6	-	-
m_f (mg)	8.19	15.95	-	-
θ_{ivo} (aTDC)	344	370	-	-
θ_{evc} (aTDC)	297	370	-	-
θ_{50} (aTDC)	0.4	34.2	0.89°	4.38°
$NMEP$ (bar)	1.7	3.95	2.43%	9.13%
m_a (mg)	120	226	1.57%	6.44%

Table 2.2: Swept range of inputs and outputs in SI model parameterization data. Mean and max absolute error between model and measurement listed for outputs. θ_{50} error reported in CAD to avoid division by small numbers at θ_{50} near TDC.

combustion, and an integrated Arrhenius rate to determine combustion phasing. However, the cylinder charge determination and combustion phasing correlation are extensively modified to fit a wider range of steady-state conditions and better extrapolate to SI-HCCI mode transitions than the model of [52], so that the governing equations for these components which encompass all major correlations of the model are significantly different than in [52]. The portion of the model that remains similar to that [52] is the Otto cycle-like component relating to polytropic The model also uses relationships from previous work [19, 53] to introduce recompression heat release (RCHR) effects.

Unlike the SI combustion mode, recompression HCCI typically operates with a high amount of internal residual gas, which creates a strong coupling from one cycle to the next. This means that Assumption 5 of the SI combustion model (see Sec. 2.3.1) does not hold for HCCI. All other assumptions of the SI combustion model are applied to the HCCI model as well, however. The HCCI model captures the cycle to cycle couplings with three cycle delayed thermal and compositional states, which are the temperature, burned gas fraction, and fuel mass fraction at blowdown,

$$T_{bd} := T_{cyl}|_{EVO^+} \tag{2.65}$$

$$b_{bd} := \left.\frac{m_b}{m_c}\right|_{EVO^+} \tag{2.66}$$

$$f_{bd} := \left.\frac{m_{uf}}{m_c}\right|_{EVO^+} \tag{2.67}$$

where m_b denotes the mass of complete combustion products, m_{uf} denotes the mass of unburnt fuel from main combustion, and EVO^+ indicates immediately after EVO. The states T_{bd} and b_{bd} are the same as in the model of [52], while the f_{bd} state is modified after the unburnt fuel state m_{uf} from [53] to eliminate steady-state assumptions. Note that the model's basic composition calculations lump the cylinder mass into three categories, being fuel, air, and combustion products.

A schematic diagram depicting how the combustion model states preserve cycle to cycle couplings is shown in Fig. 2.9 for the important case of capturing couplings across combustion modes in an SI-HCCI transition. The SI combustion model executes on the final SI cycle $k-1$ and generates T_{bd}, b_{bd}, and f_{bd} values for the exhaust gas, which are stored with a discrete unit (cycle) delay. The delayed state values are passed to the HCCI combustion model on the next cycle, k, so that the effect of the thermal and compositional properties of the SI exhaust gas on the HCCI combustion can be felt. The cycle to cycle state passing of the HCCI model follows the same procedure in nominal HCCI to preserve cyclic couplings within the HCCI mode. In the description of the HCCI model calculations which follows, the manner in which the cycle delayed states affect the HCCI model will be shown explictly through the model's equations.

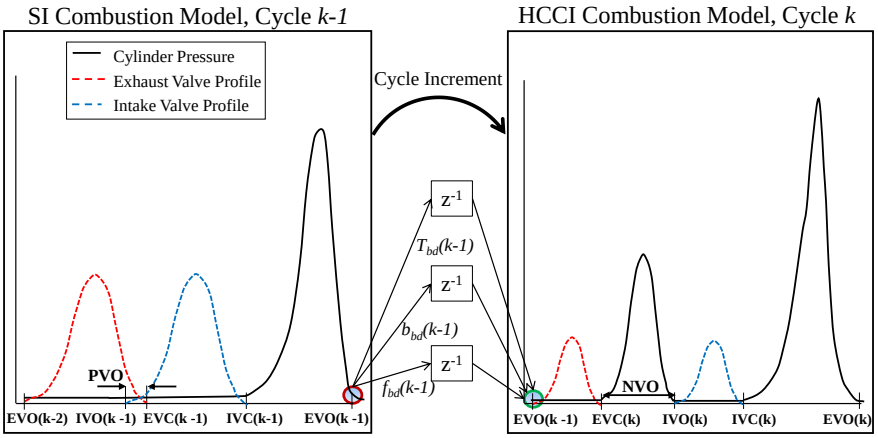

Figure 2.9: Diagram of combustion model cycle division showing how exhaust gas states link SI and HCCI combustion models during an SI-HCCI switch.

A summary of the input/output and state differences between the SI and HCCI combustion models is given in Table 2.4. Notice that the control inputs of the HCCI combustion model are different from the SI combustion model, namely in that there is no spark timing, and the start of injection (SOI) timing θ_{soi} has been added as an input. The injection timing is included as an input because it has been observed to have a significant effect on the auto-ignition timing through thermal effects from fuel evaporation and heat release during recompression as well as chemical effects on the fuel ignition delay through pyrolisis (advancing) and reformation (retarding) chemical reactions [54, 55]. In general, earlier SOI tends to give earlier ignition by increasing the time and temperature for reactions during recompression, though the investigation of which reaction types dominate and the importance of chemical versus thermal effects is still an open topic.

Model	Inputs	Outputs	States
SI	m_f	θ_{50}	-
	θ_{sp}	NMEP	
	θ_{evc}	λ	
	θ_{ivo}	T_{em}	
HCCI	m_f	θ_{50}	T_{bd}
	θ_{soi}	NMEP	b_{bd}
	θ_{evc}	λ	f_{bd}
	θ_{ivo}	T_{em}	

Table 2.3: Summary input/output listing for SI and HCCI models.

2.4.1 Model Calculations

In the following equations, a_i represent fitting coefficients and superscript ^{0} indicates a delayed state from the previous cycle,

$$x^0 = x^{k-1} \tag{2.68}$$

where x^k is the value of some state quantity on cycle k. All volumes V are calculated using the crank-slider equation (2.43).

Recompression Period

The HCCI model's calculations start with the delayed states T_{bd}^0, b_{bd}^0, and f_{bd}^0 during the recompression period, as the recompression event plays an important role in the outcome of the cycle due to a high amount of NVO. The first calculation is for the trapped residual mass, which is obtained from a regression of the form

$$m_r = \frac{(a_1\theta_{evc} + a_2)V_{evc}}{R(a_3T_{bd}^0 + a_4)} \tag{2.69}$$

where V_{evc} is the volume at EVC and $R \equiv 287$ is the gas constant. This regression was developed based on the form of the expression for the ideal gas law at EVC. Some HCCI models [56], [57] directly employ the ideal gas law at EVC with pressure approximated as atmospheric and temperature approximate as T_{bd}. This calculation was found to give a poor fit to data, which motivated introducing the additional regressor dependencies of Eq. (2.69). A regression for residual mass was selected in place of residual gas fraction as in [52] because the residual gas fraction relation includes a monotonically decreasing dependence on T_{bd}, which does not capture the effect that higher exhaust temperature tends to reduce the inducted air mass, hence giving an increase in residual gas fraction. This caused problems when extrapolating to the high exhaust temperatures involved in SI-HCCI

transitions, where the residual gas fraction relation of [52] lead to strong underpredicitons of the in-cylinder temperature at IVC and necessitated an unreasonably large correction parameter for residual gas temperature. The residual temperature correction parameter mentioned here will be explained when transient SI-HCCI transtion data is considered in Ch. 3.

Using the estimated m_r value from Eq. (2.69), the portion of the residual mass that corresponds to unburnt fuel and air from the previous cycle can be found from

$$m_{rf} = \frac{m_r}{m_c^0} m_{uf}^0 = m_r f_{bd}^0 \tag{2.70}$$

$$m_{ra} = \frac{m_r}{m_c^0} m_{ua}^0 = m_r (1 - b_{bd}^0 - f_{bd}^0) \tag{2.71}$$

where m_{rf} is the mass of residual fuel, m_{ra} is the mass of residual air, and m_{ua} indicates the unburnt air from main combustion which is not calculated explicitly. The temperature of the trapped mass at EVC is modeled as a linear function of the blowdown temperature

$$T_{evc} = a_1 T_{bd}^0 + a_0 \tag{2.72}$$

Recompression heat release of the unburnt residual fuel mass m_{rf} is incorporated in a simple manner by injecting an instantaneous heat addition to the temperature at EVC. The heat release is assumed to occur with unity combustion efficiency, a decision which is motivated mainly by observations from post-processed experimental data which shows very little trends in recompression combustion efficiency. The RCHR is thus more intended to capture the trend of cyclic couplings through unreacted chemical energy, as opposed to absolute numerical values:

$$T_{rc} = T_{evc} + \Delta T_{rc} \tag{2.73}$$

$$\Delta T_{rc} = \mu \frac{m_{rf}^b Q_{lhv}}{c_v m_r} \tag{2.74}$$

where T_{rc} is the temperature after recompression heat release and μ is a tuning factor to account for idealities of constant volume, adiabatic heat release. The term m_{rf}^b accounts for slightly lean/ rich scenarios where there is not enough oxygen present in the residual gas to combust all the residual fuel,

$$m_{rf}^b = \min[m_{rf}, \quad m_{ra}/AFR_s]. \tag{2.75}$$

After the mass of fuel that burns during recompression is known, it can be used in conjunction with the injected fuel mass to determine the total fuel mass

$$m_f^{tot} = m_f + (m_{rf} - m_{rf}^b). \tag{2.76}$$

The relative AFR during recompression λ_r is calculated to characterize the oxygen concentration

during recompression, which was noted in [**?**, 55] to have a significant impact on the outcome of recompression chemical reactions.

$$\lambda_r = \frac{m_{ra}}{AFR_s m_f^{tot}} \tag{2.77}$$

where $m_f^{tot} = m_f + m_{rf}$ is the total fuel mass. Note that λ_r is allowed to take negative values in order to detect that the mixture was rich during the previous combustion and the resulting effect on the recompression period. This is simply a construct based on the model's basic composition dynamics which assume that the stoichiometric amount of air burns during main combustion, which imposes that rich mixtures produce negative values for residual air m_{ra}. These negative values are used as an indicator of rich combustion. m_{ra} is saturated at 0 when used in the model's cylinder breathing calculations, however, to retain physicality.

Air Induction and IVC Conditions

The cylinder charge properties after the intake process are determined from a combination of conservation of mass and energy along with several empirical regressions at the intake valve closing (IVC) event. The pressure at IVC p_{ivc} is obtained from a linear regression to intake manifold pressure as with the SI model

$$p_{ivc} = a_1 p_{im} + a_0 \tag{2.78}$$

The mass of inducted air m_a^{in} is determined from an equation whose functional form is derived by substituting the ideal gas law for m_c into an energy balance at IVC, upon which the mean gas temperature term cancels and m_a^{in} can be isolated

$$m_a^{in} = \frac{1}{T_{im}} \left[a_1 p_{ivc} V_{ivc} - (m_r + m_f^{in}) T_r + a_2 \right] \tag{2.79}$$

where V_{ivc} is volume at IVC, and T_{im} is the intake manifold temperature which is assumed to be the temperature of the inducted air. The coefficients a_1 and a_2 are introduced to improve the fit to data. The temperature which serves to characterize the effect of the residual gas internal energy on Eq. (2.79) is modeled as a linear function of T_{rc} representing energy losses during recompression

$$T_r = a_1 T_{rc} + a_2 \lambda_r \theta_{soi} + a_3 \tag{2.80}$$

where $0 \leq a_1 \leq 1$. The term $\lambda_r \theta_{soi}$ is meant to capture increases to the residual gas temperature from reforming and exothermic reactions during recompression, the extent of which are proportional to the amount of available oxygen during recompression and the time allowed for reactions to take place as noted in [55]. Hence $a_2 > 0$ in Eq. (2.80), assuming that θ_{soi} is defined bTDC main

combustion. The coefficients a_1 - a_3 in Eq. (2.80) are ultimately regressed in conjunction with the coefficients in Eq. (2.79) to match the inducted air mass, and so the model's T_r calculation represents an intermediate variable as opposed to the actual residual temperature in data.

With p_{ivc} and m_a obtained, the total mass and mean gas temperature at IVC T_{ivc} can be found from conservation of mass and the ideal gas law, respectively

$$m_c = m_r + m_a + m_f \tag{2.81}$$

$$T_{ivc} = \frac{p_{ivc} V_{ivc}}{R m_c} \tag{2.82}$$

The total air mass (including residual air) is then calculated and used to determine the burned gas fraction before combustion b_c

$$m_a = m_a^{in} + m_{ra} \tag{2.83}$$

$$b_c = \left.\frac{m_b}{m_c}\right|_{IVC} = \frac{m_c - m_a - m_f}{m_c} \tag{2.84}$$

Finally, the relative AFR is calculated both in the exhaust (excluding residuals) and in the cylinder

$$\lambda_{ex} = \frac{m_a^{in}}{m_f AFR_s} \tag{2.85}$$

$$\lambda_c = \frac{m_a}{m_f^{tot} AFR_s} \tag{2.86}$$

Integrated Arrhenius Rate for Combustion Phasing

As in many other HCCI models [52, 57–59], the combustion phasing is determined through an integrated Arrhenius rate which dictates the start of combustion θ_{soc} and the resulting θ_{50}. The Arrhenius rate expression takes the same form as in [52], however the Arrhenius threshold K_{th} is expanded from a linear function of θ_{soi} to a linear function of θ_{soi} whose coefficients depend quadratically on λ_r. This functional form is based on observations from [55], which found that an optimum point for advancing combustion phasing via recompression reaction was achieved at intermediate AFRs where a balance was struck between ignitability enhancing pyrolysis reactions and ignitability inhibiting fuel reformation reactions. The quadratic λ_r dependence captures such an optimum, which is cross-coupled to θ_{soi} since injection timing affects the recompression reaction duration. [55] also found that the temperature during recompression affected the rate of reactions, and so a term for T_{rc} is included with a cross coupling to λ_r and θ_{soi} . These recompression reaction

dependencies are incorporated into K_{th} following the logic in [60].

$$K_{th}(\theta_{soi}, \lambda_r, T_{evc}) = \int_{\theta_{ivc}}^{\theta_{soc}} \frac{1}{\omega} p_c(\theta)^{n_p} e^{\left(\frac{-E_a}{RT_c(\theta)}\right)} d\theta \tag{2.87}$$

$$K_{th}(\theta_{soi}, \lambda_r, T_{rc}) = (a_{12}\lambda_r^2 + a_{11}\lambda_r + a_{10})\theta_{soi} + a_{02}\lambda_r^2 + a_{01}\lambda_r + a_{00} + (a_{T1}\lambda_r\theta_{soi} + a_{T0})\, T_{rc} \tag{2.88}$$

$$p_c(\theta) = p_{ivc}\left(\frac{V_{ivc}}{V(\theta)}\right)^{n_c},\ T_c(\theta) = T_{ivc}\left(\frac{V_{ivc}}{V(\theta)}\right)^{n_c-1} \tag{2.89}$$

where ω is the engine speed in rad/s, E_a is the activation energy, and the polytropic compression exponent $n_c \equiv 1.32$. Without these added recompression reaction dependencies, fits to combustion phasing data were poor, even when multiple correlations from the literature [57, 58, 61, 62] were tried. Note that as a precautionary measure to prevent extreme sensitivity to λ_r if the quadratic dependence Eq. (2.88) is extrapolated far outside the parameterized range, the λ_r value used in Eq. (2.88) is modified by a hypertangent function which has negligible effect within the parameterized range but forces λ_r to roll off if it significantly exceeds this range

$$\tilde{\lambda}_r = a_{sat}\lambda_r^{max} \tanh\left(\frac{\lambda_r}{a_{sat}\lambda_r^{max}}\right) \tag{2.90}$$

where λ_r^{max} represents the maximum λ_r to which the model parameterization extends, and a_{sat} is such that the value of $\tilde{\lambda}_r$ ultimately saturates at $a_{sat}\lambda_r^{max}$. λ_r^{max} is let vary as a linear function of θ_{soi} which upper bounds the maximum λ_r values in the data, as typically earlier θ_{soi} timings allow higher λ_r values to be reached while maintaining stable combustion phasing. After θ_{soc} is found, it is used to calculate θ_{50} in a linear regression

$$\theta_{50} = a_1\theta_{soc} + a_0 \tag{2.91}$$

Polytropic Compression/Expansion and Constant Volume Combustion

The polytropic compression and expansion strokes and constant volume combustion are carried out with the same procedure as in the SI model, following Eqs. (2.44), (2.46) - (2.51). The temperature rise due to combustion is modified with two efficiency terms

$$T_{ac} = T_{bc} + \eta_\lambda \eta_{50} \frac{m_f Q_{lhv}}{c_v m_c} \tag{2.92}$$

The first efficiency term η_λ represents a combined thermal and combustion efficiency as a function of AFR,

$$\eta_\lambda = \frac{a_1 \lambda_c + a_2}{\lambda_c + a_3} \tag{2.93}$$

The η_λ term was necessary to capture the combustion work output over a wide range of AFRs, where significant changes were observed as AFR was varied as exemplified in the constant fuel actuator sweeps in Fig. 2.10. Note that $IMEP$ is plotted as opposed $NMEP$ in order to rule out the effects of pumping. As can be seen, the slope of η_λ becomes sharper at AFRs near stoichiometric, representing the effects of combustion efficiency and unburnt fuel, while the slope is milder at significantly lean AFRs, representing modest changes to the thermal efficiency from the effect of varying air dilution on the mixture's ratio of specific heats.

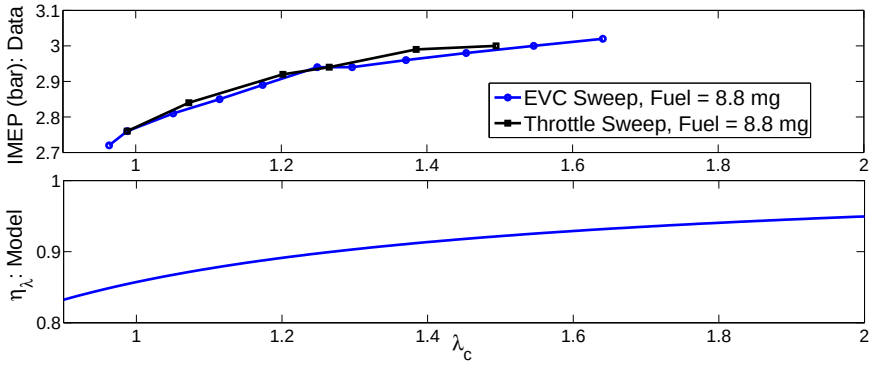

Figure 2.10: Top: IMEP measurements in steady-state actuator sweeps with high AFR variation. Bottom: Profile of model combined thermal and combustion efficiency as a function of λ_c.

The second efficiency term η_{50} is adopted after [53], which found that late phasing HCCI cycles could produce partial burns which create a coupling to the following cycle through the unburnt fuel quantity. The η_{50} term is parameterized as a sigmoidal function which rolls off at late combustion phasing where the combustion approaches the misfire limit. The dependent variable is taken to be θ_{50} , and the roll-off of the combustion efficiency curve is taken to vary with fuel quantity to account for changes in the late phasing limit with load:

$$\eta_{50} = \frac{a_1}{1 + \exp\left(\frac{\theta_{50} - \theta^*_{50}(m_f)}{a_2}\right)} \tag{2.94}$$

$$\theta^*_{50}(m_f) = a_3 m_f + a_4 \tag{2.95}$$

Note that it is ideal to tune the coefficients a_1 - a_4 with post-processed combustion efficiency estimates from late combustion phasing data as in [53], however such data was not available for the current study. Instead, the coefficients were manually tuned to position the roll-off of the sigmoid near the late phasing limit observed from steady-state data across different loads. Example profiles

of η_{50} are shown in Fig. 2.11, where it should be noted that the curve is upper saturated at 1 at any θ_{50} values where it slightly exceeds 1.

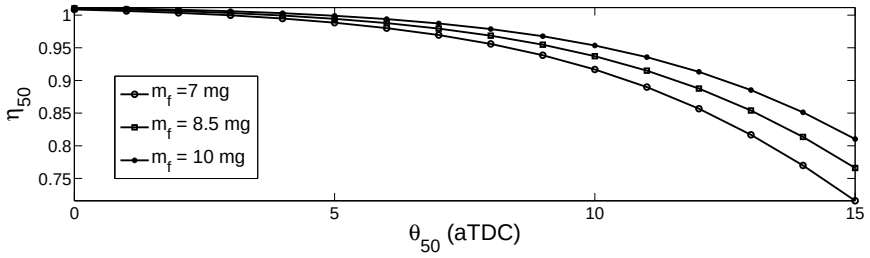

Figure 2.11: Profile of late phasing combustion efficiency η_{50} across different loads.

End of Cycle Outputs

After the expansion process completes, the HCCI model calculates the outputs at the end of the cycle at EVO, including the thermal and compositional states, the exhaust flow rate and temperature to be passed to the air path model, and the cycle work. The blowdown temperature T_{bd} is calculated with the same expression (2.52) as in the SI model, and the exhaust manifold temperature also follows from the same equations (2.53) - (2.55), though now the convection coefficient term in Eq. (2.55) is a simpler linear function of cylinder flow rate. The mass of unburnt fuel m_{uf} is necessary to determine the fuel mass fraction state, and is calculated from the total incomplete combustion due to both mixture richness and partial burns at late combustion phasing. The unburnt fuel due to mixture richness is calculated assuming a lower AFR threshold λ_{min} below which no additional fuel burns to allow for dissociation effects past stoichiometric as in the SI model,

$$m_{uf} = m_f(1 - \max[(\lambda_{min} - \lambda_c), 0]\eta_{50}) \tag{2.96}$$

where again λ_{min} is chosen equal to 0.97. To maintain consistency with the η_λ efficiency, the λ_c value in Eq. (2.93) is lower saturated at λ_{min}, and the burnt fuel mass is linearly interpolated from λ_{min} to 0 at $\lambda_c = 0$. The unburnt fuel mass fraction can then be found from

$$f_{bd} = \frac{m_{uf}}{m_c} \tag{2.97}$$

The burned gas fraction after combustion is calculated assuming that the stoichiometric amount of air burns during main combustion, considering the effect of unburnt fuel

$$b_{bd} = \frac{(AFR_s + 1)(m_f^{tot} - m_{uf})}{m_c} + b_c \tag{2.98}$$

The same expressions as in the SI model are used to calculate the exhaust mass and enthalpy flow rate (2.56) - (2.58), as well as the cycle work (2.59) (2.60). The NMEP is calculated assuming a constant $PMEP$, as attempts to match $PMEP$ values in data using polytropic processes to approximate the recompression period gave poor results.

$$NMEP = IMEP + PMEP, \quad PMEP = P\bar{M}EP \equiv constant \tag{2.99}$$

2.4.2 Steady-State Fitting Results

As discussed in Sec. 2.3.3, a simple approach can be used for parameterization of the SI model wherein each of the model's regressions is fit individually to match its respective measured/post-processed data values. However, for the HCCI model, the inherent cycle to cycle feedback induced by the recycled exhaust temperature and composition states of the model can result in large prediction errors from compounding of modeling error over many cycles, even if the individual regressions are satisfactory. To cope with this issue, the HCCI model parameters are regressed in an iterative routine wherein the exhaust gas states are recycled between subsequent iterations until the state values converge. A description of the iterative parameterization routine is given in Appendix B, which also takes measures to incoporate additional parameters which are later introduced to capture transient SI-HCCI transition data (see Ch.3).

The dataset used to parameterized the HCCI model consists of a 526 point grid of actuator sweeps at a single engine speed of 2000 RPM with the outermost swept variable being fuel mass, followed by intake manifold pressure (adjusted via throttle) and then EVC timing, and the innermost variable being injection timing. Several direct throttle and EVC sweeps were also carried out to clearly discern the trend in the outputs with respect to these variables. Intake valve timing was held fixed with intake valve closing (IVC) near BDC, as it was observed to have only a small effect on combustion when maintained in the vicinity of BDC. The grid of inputs and corresponding performance outputs of θ_{50},NMEP, and λ are shown in Fig. 2.12 with the model reproduction of the performance outputs plotted alongside the data values. Note that λ is plotted as it describes both AFR and trapped air mass, as opposed to the SI model parameterization data of Sec. 2.3.3 where AFR was held constant. As can be seen in Fig. 2.12, the model reproduces the performance outputs with good accuracy for a low-order model considering the wide range of actuator settings over which it is fit. A summary of the swept input and output range and mean and max absolute errors is given in Table 2.4.

The bottom subplot of Fig. 2.12 shows that for much of the parameterized range, the model's prediction of unburnt fuel mass m_{uf} follows the same trend as the combustion phasing standard deviation $\sigma(\theta_{50})$. This is consistent with the logic in [19], which explains that unburnt fuel from incomplete burns at late combustion phasing can create a cycle to cycle coupling which leads to

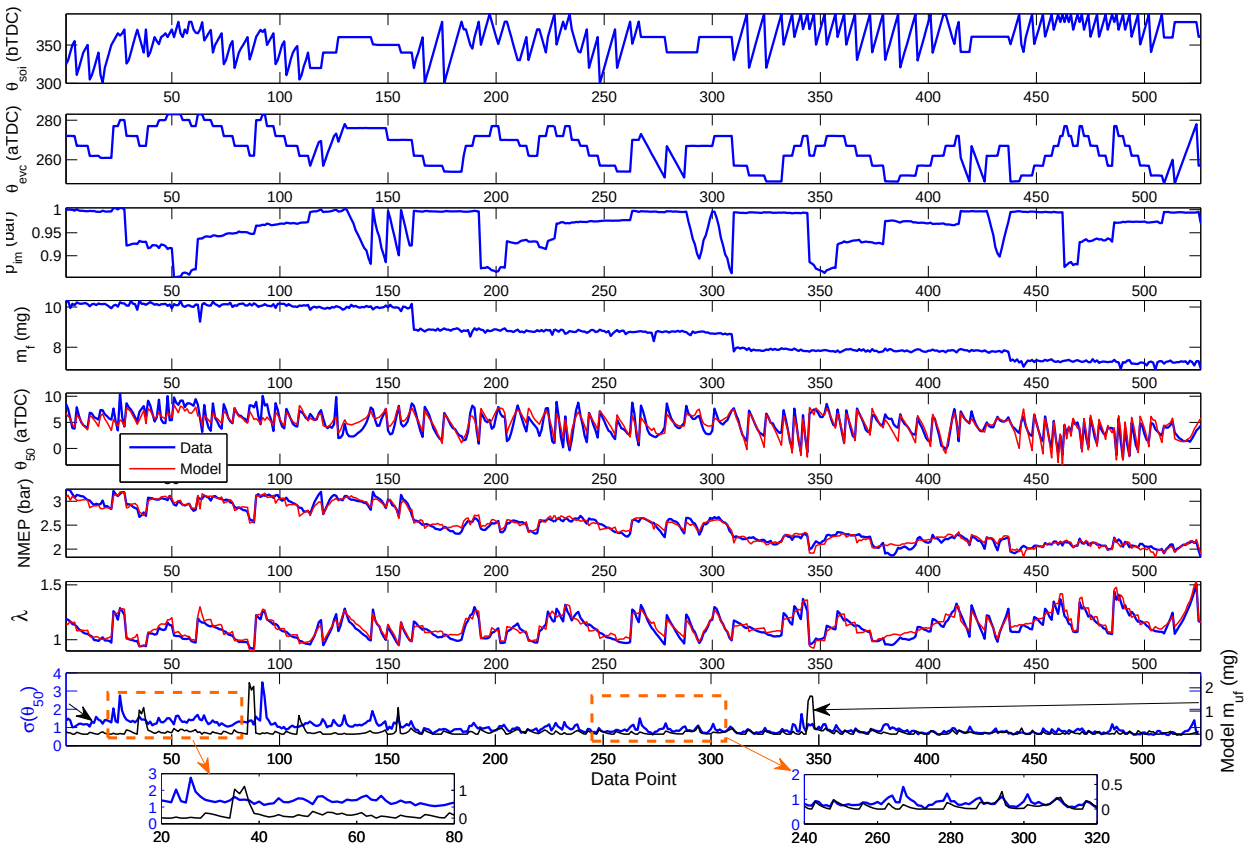

Figure 2.12: Input grid and modeled vs. measured outputs for steady-state HCCI model parameterization data. Bottom subplot shown with close-ups so that the θ_{50} standard deviation $\sigma(\theta_{50})$ can be compared to the model's mass of unburnt fuel calculation m_{uf} more clearly.

oscillatory behavior and hence higher standard deviation in the combustion phasing. There are some regions where the model's m_{uf} prediction does not follow $\sigma(\theta_{50})$ as exemplified in the left-hand close-up plot between points 20 and 80, at which points the model's θ_{50} fit can be observed to underpredict some of the late phasing conditions which give rise to unburnt fuel. This θ_{50} error may be influenced by the high sensitivity of the model's Arrhenius correlation for combustion phasing at very late, near-misfire conditions, which makes small modeling errors have a large effect. The model's trends in m_{uf} vs. $\sigma(\theta_{50})$ may also be enhanced if the model is conditioned on long duration cycle to cycle high cyclic variability data as in [53], which was not available for the current study.

	Min	Max	Mean Abs. Error	Max Abs. Error
θ_{soi} (bTDC)	300	390	-	-
θ_{evc} (aTDC)	248	283	-	-
p_{im} (bar)	0.85	1	-	-
m_f (mg)	7.2	10.5	-	-
θ_{50} (aTDC)	-2	11	0.86°	5.16°
$NMEP$ (bar)	1.7	3	2.06%	12.2%
λ	0.92	1.5	2.81%	11.2%

Table 2.4: Swept range of inputs and outputs in HCCI model parameterization data. Mean and max absolute error between model and measurement listed for outputs. θ_{50} error reported in CAD to avoid division by small numbers at θ_{50} near TDC.

Chapter 3

Capturing Transient Data in SI-HCCI Mode Transitions

As shown in Sec. 2.4.2, the baseline parameterization of the HCCI combustion model to steady-state data fits a wide range of actuator sweeps with good accuracy. For model-based control functionality during an SI-HCCI mode transition, it is desirable that the model also be able to capture transient data from SI-HCCI mode transitions. This Chapter considers the validation of the control-oriented multi-mode combustion model with SI-HCCI mode transition data, and is based on [42]. As will be seen, the baseline model of Ch. 2 experiences difficulties in reproducing performance output time histories in the HCCI phase of the SI-HCCI transition, despite its adequate steady-state fit. The source of the model's short comings are examined with a simplified GT-Power simulation, which motivates the introduction of a corrective parameter on the model's residual gas temperature calculation. Following its introduction, the corrective residual gas temperature parameter is used as a medium to assimilate transient SI-HCCI feedback to improve the model prediction accuracy for control applications in an online adaptation routine. With the baseline steady-state parameterization and augmented residual gas temperature parameter, the model is shown to reproduce transient performance output time histories from SI-HCCI transitions with considerable accuracy.

3.1 Augmented Parameter for SI-HCCI Mode Transitions

This Section motivates the introduction of a corrective model parameter for SI-HCCI mode transitions by examining data from an open-loop experimental SI-HCCI transition at a single operating condition.

3.1.1 Overview of Open-Loop Mode Transtion Experiments

The format for the mode transition experiments was to drive the engine to a steady-state condition in SI mode which was appropriate for switching to HCCI, then to switch the intake and exhaust cams to low lift simultaneously. While the mode transition sequence of this Section implements

a strategy of switching both intake and exhaust cam profiles simultaneously, later on a different strategy will be pursued where the intake cam is switched to low lift prior to the exhaust cam, though the dominant physical effects and modeling considerations remain the same for both approaches. The actuator trajectories of the mode transition were not optimized, as the goal was not to carry out a high performance mode transition, but rather implement a simple mode transition sequence for use in transient model validation. Details of actuator strategies to obtain good performance in SI-HCCI mode transitions will be covered in Sec. 4.1.3 and so are not discussed here. It is noted for interpretation of the data however that the SI switch point condition was set with an advanced exhaust cam phasing and late intake cam phasing, and so the resulting SI pressure traces include a slight recompression event. As stated in Section 2.1, the cams switch from high to low lift during the closed-valve portion of the final SI cycle, so that at the EVO event of this final SI cycle the low lift cams are in place. The throttle was commanded wide open roughly 20-30 milliseconds before the first low lift breathing event, and the spark timing is placed 20° aTDC when HCCI engages to prevent interaction with the combustion. To simulate the mode transition, the measured throttle position is input to the air path model on a time-sampled basis and the measured cam phaser positions and commanded fuel quantity, injection timing, and spark timing are input to the combustion model on a cycle by cycle basis.

The combustion response and corresponding input sequences for an SI-HCCI mode transition trial are shown in Fig. 3.1, where *SI -1* and *HCCI 0* designate the final SI cycle and first HCCI cycle, respectively, following the notation in [35]. The independent axis of the time-based measurements of intake manifold pressure and throttle command is transformed in order to plot these variables against the engine cycle. The cams switch during the closed-valve portion of cycle *SI -1* which causes a sudden increase in the recompression pressure and jump in the valve timings θ_{evc} and θ_{ivo}. In anticipation of the high exhaust temperature that is carried over from the final SI cycle, both the θ_{evc} and θ_{soi} timings are placed much later than their steady-state set points when HCCI is entered to retard combustion phasing. However, on cycle *HCCI 0*, the combustion phasing is still early, accompanied by a high pressure rise rate. The combustion phasing then shifts later on cycle *HCCI 1* where the exhaust temperature is now lower as a result of HCCI combustion. This initially early and then late combustion phasing caused by the cycle to cycle temperature coupling is the same phenomenon observed in the mode transition portrayed in [35]. Following the late combustion phasing and weak heat release on the cycle *HCCI 1*, the recompression event exhibits an enlarged peak pressure which occurs significantly after TDC, which indicates recompression heat release of unburnt fuel from the main combustion event. This recompression heat release in conjunction with the earlier injection timing cause the combustion phasing to advance on cycle *HCCI 2*, and from here the transient becomes milder and the combustion settles to steady-state.

As is apparent from the dash-square θ_{50} response in Fig. 3.1, the baseline model does not capture the extremely advanced combustion phasing on cycle *HCCI 0* in the data, despite that it

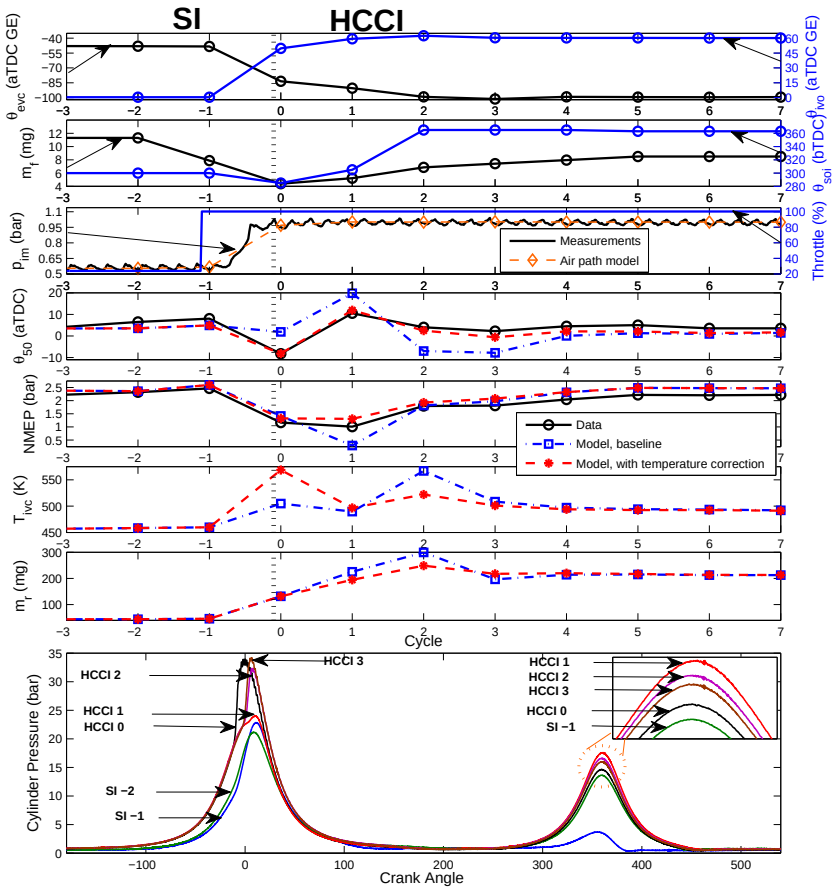

Figure 3.1: Cycle by cycle input and outputs and crank angle resolved in-cylinder pressure during open-loop SI-HCCI mode transition. *SI -1* indicates the final SI cycle and *HCCI 0* indicates the first HCCI cycle. Model reproduction of outputs with and without the introduced residual temperature correction are shown.

is equipped with exhaust temperature dynamics and fits a large steady-state dataset with good accuracy (see Sec. 2.4.2). Significant phasing and torque errors follow the next few transient cycles as well, which are influenced by the large initial error as will be seen. The plot of the predicted in-cylinder temperature at IVC, T_{ivc}, shows that the baseline model predicts a T_{ivc} value on cycle *HCCI 0* which is similar to the value at cycles *HCCI 6*, *HCCI 7* towards the end of the transition. Due to the higher exhaust temperature of SI combustion that is carried over into cycle *HCCI 0*, the T_{ivc} on this first HCCI cycle may be expected to be higher than the cycles towards the end of the transition where the residual temperature falls closer to nominal HCCI levels. If the model's T_{ivc} is under predicted on cycle *HCCI 0*, it could be responsible for the erroneous θ_{50} prediction. However, a competing effect is that the residual mass m_r is very low on cycle *HCCI 0* due to the very late θ_{evc} timing as well as low exhaust gas density from the higher exhaust temperature, which should act to reduce T_{ivc}. The uncertainty in the model's in-cylinder temperature prediction on

cycle *HCCI 0* warrants further investigation with higher fidelity modeling tools.

3.1.2 Mode Transition Predictions Using Crank Angle-Based Model

A simplified single-cylinder GT-Power simulation was carried out to aid in drawing conclusions about the baseline model's combustion phasing error on cycle *HCCI 0*. The GT-Power simulation is not intended to reproduce absolute values from the experiment, but rather to gain a better understanding of the unmeasured variables during the transient phase of the SI-HCCI mode transition, such as the in-cylinder temperature. Measured intake and exhaust manifold pressures and temperatures were specified as intake and exhaust runner boundary conditions on a crank angle basis, and the valve profiles/timings from the experiment were imposed to capture the effect of the cam switch from high to low lift and rapid cam phasing. The combustion portion of each cycle is specified by imposing measured burn angles and Weibe function parameters on a cycle by cycle basis, and the remainder of the cycle is generated through a crank angle-based engine model and 1-D gas dynamics calculations. To validate the GT-Power simulation, experimental pressure traces are compared versus those generated by the simulation in Fig. 3.2. The adequate agreement between GT-Power and experiment suggests reasonable GT-Power model prediction accuracy.

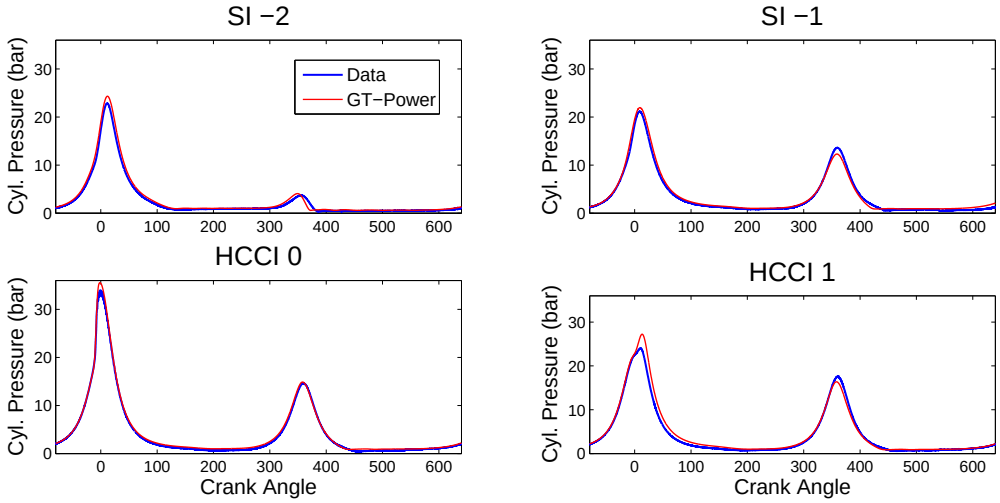

Figure 3.2: Comparison of experimental versus GT-Power simulation in-cylinder pressure during an SI-HCCI mode transition.

Fig. 3.3 plots consecutive in-cylinder temperature traces calculated by GT-Power during the mode switch from SI to HCCI. The switch of the cams from high to low lift is marked by a shift from an earlier blowdown process and milder recompression peak on cycle *SI -2* to a larger an approximately symmetric recompression peak on cycle *SI -1*. The sudden drop temperature drop near TDC of recompression on *SI -2* is due to an earlier IVO from the high lift intake cam, which is followed by a reversion process of the in-cylinder residual that is ejected into the intake manifold.

Comparing the recompression period on cycle *SI -1* leading into *HCCI 0* to the remainder of the HCCI cycles, there is a clear trend the temperature at the end of recompression is roughly 200 K higher than the others, which goes onto yield a significantly higher temperature after the intake event. This suggests that the baseline model does indeed under predict in-cylinder temperature on cycle *HCCI 0* in Fig. 3.1, as it's T_{ivc} shows only minor differences from the later HCCI cycles.

In tracing the source of model error on cycle *HCCI 0*, it can be noted that the exceedingly high recompression temperature leading into cycle *HCCI 0* only occurs during SI-HCCI switch transients when the high temperature SI exhaust undergoes recompression with the low-lift cams. It is thus uncertain how the low-order model will extrapolate to such a condition as it is outside the nominal steady-state HCCI parameterized range. The competing effect of low residual mass noted in Sec. 3.1.1 further complicates this extrapolation. Several other transient effects which occur only during SI-HCCI transitions may also be influencing the model error, such as amplified manifold dynamics due to the rapid dethrottling and increased intake temperature due to higher fluid velocities. However, for the simplified low-order modeling approach, the prediction error is lumped into the excursion of the residual temperature from nominal HCCI conditions, as this is an effect which clearly introduces model uncertainty.

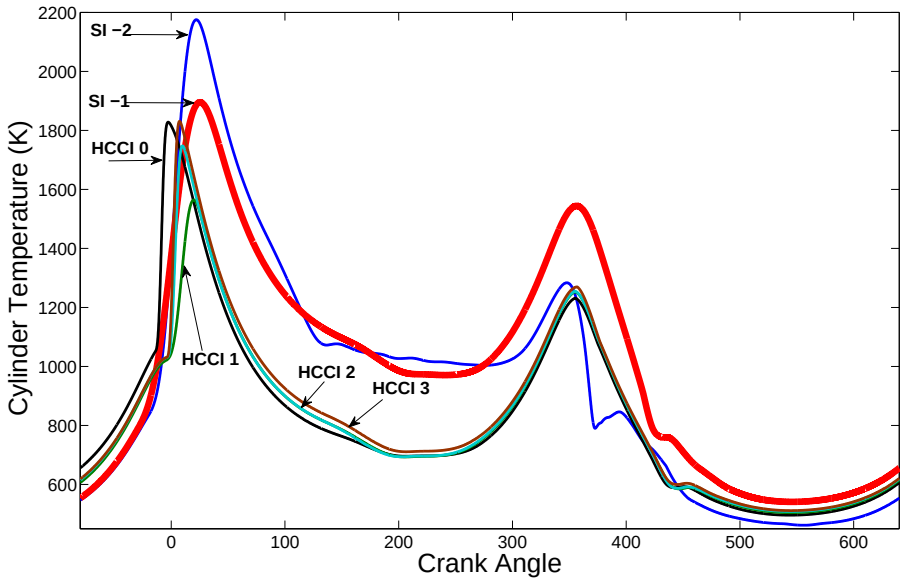

Figure 3.3: In-cylinder temperature traces generated by GT-Power SI-HCCI mode transition simulation. The final SI cycle whose recompression event yields an extremely high temperature leading into the first HCCI cycle is highlighted.

3.1.3 Residual Gas Temperature Correction for Initial HCCI Cycle

Based on the observations from Secs. 3.1.1, 3.1.2, the model's prediction error when entering HCCI is attributed solely the high residual temperature that is carried over from SI. To maintain low model order, the model error on cycle *HCCI 0* is accounted for with an empirical correction factor which parameterizes the model error into the residual temperature. The correction factor is placed on the model's residual gas temperature calculation T_r that appears in the energy balance type regression Eq. 2.79 for the mass of inducted air:

$$m_a^{in} = \begin{cases} \frac{1}{T_{im}} \left[a_1 p_{ivc} V_{ivc} - (m_r + m_f^{in})(k_r T_r) + a_2 \right], & HCCI\ 0 \\ \frac{1}{T_{im}} \left[a_1 p_{ivc} V_{ivc} - (m_r + m_f^{in}) T_r + a_2 \right], & else \end{cases} \tag{3.1}$$

where $k_r > 0$ is the residual gas correction factor, T_{im} is the intake manifold temperature, p_{ivc} and V_{ivc} are pressure and volume at IVC, and *HCCI 0* indicates the first cycle when switching to HCCI. In parameterization, k_r is regressed to match combustion phasing during the transient HCCI phase of the SI-HCCI transition. The reason for this choice is that k_r is coupled to the combustion phasing through the in-cylinder temperature, and that the combustion phasing is directly measurable during the transient SI-HCCI phase which makes it convenient for implementation. For the mode transition of Fig. 3.1, $k_r = 1.14$.

With the augmented residual temperature correction, the T_{ivc} predicted by the model on cycle *HCCI 0* in Fig. 3.1 is increased relative to its steady-state value, following the trend observed in the GT-Power simulation. Comparison of the model's T_r prediction with the temperature at IVO T_{ivo} produced by GT-Power suggested that the trend in residual temperature also matches the GT-Power simulation more closely when the residual temperature correction is applied, taking T_{ivo} as indicative of residual temperature in GT-Power. Comparing on a percentage basis to omit steady-state offsets between the model and GT-Power predictions, the model's T_r calculation on cycle *HCCI 0* was elevated by 37% relative to its steady-state value with the residual temperature correction active as opposed to only 14% without the correction, while the T_{ivo} in GT-Power was elevated by 33% relative its steady-state value on cycle *HCCI 0*. Fig. 3.1 also shows that the θ_{50} response predicted by the model in now matches the data well not only on cycle *HCCI 0* where the correction is active, but for the entire transient process. This indicates that the main effect driving the erroneous transient response predicted by the nominal model is the error induced by the extreme conditions on the cycle *HCCI 0*, which goes onto affect subsequent cycles though the cycle to cycle states. Once this error is corrected for, the nominal model can capture the remainder of the transient response, as the conditions become much closer to nominal HCCI.

3.2 Adaptive Tuning of Augmented Parameter

3.2.1 Motivation and Description of Adaptive Tuning Method

An important consideration from a control design standpoint for SI-HCCI transitions is that on the first HCCI cycle of the transition, no HCCI combustion feedback is yet available, and so a model-based controller must rely completely on the model predictions. The only way to incorporate feedback to improve the controller response on this first HCCI cycle is thus to assimilate transient data after the fact, to improve the model predictions for the next mode transition. It has also been discussed that the conditions on the first HCCI cycle tend to be outside the steady-state HCCI operating regime used to parameterize the model, and so using online data to improve the model predictions when such conditions are entered can help alleviate any shortcomings of the model in extrapolating to these conditions. The mode transition corrective parameter k_r serves as an ideal candidate for such an online model update, as it is specifically introduced to improve the model predictions on the first HCCI switching cycle, and is tuned exclusively to transient SI-HCCI mode transition data. Adjusting k_r may yield performance benefits for the transient cycles following the initial HCCI cycle as well, as the degree of model error on the first HCCI cycle has been shown to have a significant impact on the following cycles through the dynamic cycle to cycle coupling.

To develop an online parameter update method for k_r, a simplified approach is taken where k_r is adjusted to match combustion phasing on the first and only the first HCCI cycle of the SI-HCCI transition. This method neglects how the choice of k_r affects cycles after the first HCCI cycle through the thermal and compositional coupling, and so may yield suboptimal predictions for the overall transient response. However, limiting attention to the first HCCI cycle yields a far more tractable algorithm, and can still give significant improvements in model accuracy during the mode transition as will be shown.

The high-level method for the k_r parameter update is to back-track through the model to solve for the k_r value that yields a perfect match of θ_{50} on the first HCCI cycle of the transition, so that a linear update law can be used. The algorithm starts with the measured θ_{50} on the first HCCI cycle θ_{50}^{y}, which is used with Eqn. (2.91) to solve for the corresponding start of combustion θ_{soc}^{*}:

$$\theta_{soc}^{*} = \frac{1}{a_1}(\theta_{50}^{y} - a_0)\Big|_{HCCI\ 0} \tag{3.2}$$

where the coefficients a_1 and a_0 come from Eq. (2.91) and $|_{HCCI\ 0}$ indicates a quantity evaluated on the first HCCI cycle. Since k_r affects θ_{soc} through the in-cylinder temperature, it must ultimately be back-solved from the Arrhenius integral (2.87), which requires a numerical inversion. Towards this end, a simple Newton-Raphson inversion can be applied to solve for the T_{ivc} value which gives $\theta_{soc} = \theta_{soc}^{*}$ when inserted into the Arrhenius integral, which is denoted T_{ivc}^{*}. A method that is more

computationally tractable and better tailored for real-time implementation is to store the value of the Arrhenius integrand in Eq. (2.87) in a look-up table with T_{ivc} as an indepdent variable. A method to do this which is shown to be feasible in real-time will be given when the model and parameter adaptation are implemented in control of SI-HCCI mode transitions in Ch. 4. When T^*_{ivc} is found, it can be combined with Eqns. (3.1), (2.81), (2.42) to solve for the target correction k^*_r,

$$k^*_r = \left. \frac{p_{ivc}V_{ivc}\left(a_1 - \frac{T_{im}}{RT^*_{ivc}}\right) + (m_r + m_f)T_{im} + a_2}{(m_r + m_f)T_r} \right|_{HCCI\ 0} \tag{3.3}$$

where the coefficients a_1, a_2 come from Eq. (3.1).

In the general case where mode transitions must take place at varying operating conditions throughout a drive cycle [63], k^*_r will most likely vary with engine operating variables such as speed and load, as well as with time as the engine behavior drifts over the life-cycle of the engine. To capture this variation, it is advisable to parameterize k_r as a function of operating condition, and update the parameterization with each new mode transition measurement using a recursive parameter update method. This is in contrast to simply reseting the value of k_r equal to the solution of Eq. (3.3) after each new mode transition, which will not capture any operating condition dependency and will increase susceptibility to noise and disturbances by discarding older data. A simple linear parameterization for k_r based on EVC timing is employed in Sec. 3.3 and in implementation for controls purposes in Ch. 5 to capture an SI-HCCI transition dataset that extends to multiple operating conditions. For simplicity of illustration, the example adaptive tuning simulations in the current Section consider the case where k_r is adapted to account for drifts and parameter errors over time at a single operating condition. In this case, the operating condition dependence of k^*_r is unnecessary, and the so the estimate of k^*_r takes the form a single parameter $\hat{k}_r$ with only a time dependence,

$$k^*_r \approx \hat{k}_r(m) \tag{3.4}$$

where m is the iteration index which increments at each successive mode transition and so represents an event-based time dependence.

To facilitate real-time implementation of the proposed adaptation, it is desirable to use a linear parameter update law to tune the k_r value, which is applicable under the condition that the parameterization of k_r is linear in the fitting coefficients. Several linear parameter update laws exist, such as the recursive least squares and simplified the projection (gradient) algorithms, along with the stochastic counterpart to the projection algorithm, the stochastic approximation algorithm [64]. All of these algorithms follow a parameter update law of the form

$$\hat{k}_r(m) = \hat{k}_r(m-1) + G(m)\left(k^*_r(m) - \hat{k}_r(m-1)\right) \tag{3.5}$$

where the selection of the adaptive gain $G(m)$ is main differentiating factor among the algorithms. In general, the recursive least squares algorithm is preferable to use when possible, for its faster convergence and bounded parameter variance properties as compared to the simplified algorithms. However, the recursive least squares algorithm is more computationally demanding than the others, so that if the number of parameters becomes high, it may be prudent to use one of the simplified algorithms. For the basic example cases considered where only one parameter ($\hat{k}_r$) is being estimated as a function of time, it can be shown that each algorithm's expression for $G(m)$ reduces to a constant, so that all algorithms are equivalent and $G(m) \equiv G$ becomes a constant tuning factor. Parameter adaptation results are thus representative of all the mentioned algorithms. When more parameters are included in the k_r expression to capture dependency on operating condition, the value of $G(m)$ must be calculated for each new data point following the formula for the chosen algorithm, all of which can be found in, e.g., [64]. The parameter update method is summarized in the block diagram Fig. 3.4, where intermediate model variables necessary to carry out the update have been shown with a superscript "*mod*" and must be evaluated with Eqs. (2.69) - (2.80).

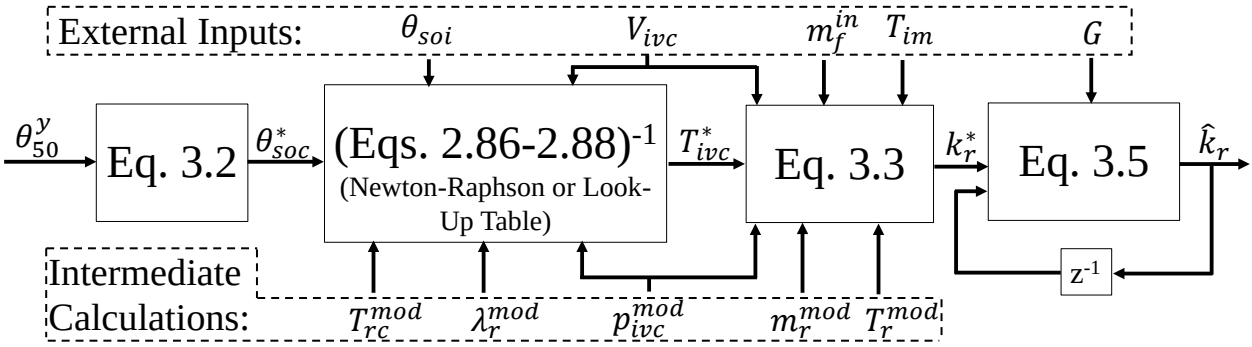

Figure 3.4: Block diagram summary of k_r parameter update method. All quantities evaluated on cycle *HCCI 0* during an SI-HCCI transition.

3.2.2 Adaptive Tuning Simulations

To demonstrate the effect of the k_r adaptation, a simple example is given wherein the estimate $\hat{k}_r$ is initialized with an error of 0.1 from the nominal value for the mode transition sequence in Fig. 3.1, and adapted to consecutive trials of the same mode transition sequence. For simplicity, only the HCCI phase of the mode transition is simulated on each mode transition trial, because on each iteration of the mode transition sequence the SI model predictions are exactly the same. The initial conditions generated by the SI model for cycle *HCCI 0* are stored and used to initialize each trial. Fig. 3.5 plots the $\hat{k}_r$ parameter dynamics as a function of mode transition iteration for several values of the adaptive gain G, along with the model's transient θ_{50} prediction as $\hat{k}_r$ adapts for a fixed $G = 0.1$ in the bottom subplot. The left column shows the perfect case where each iteration

of the mode transition yields exactly the same θ_{50} on cycle *HCCI 0*, which is the reason for the constant line in the middle subplot. In the right column, zero-mean Gaussian white noise with a standard deviation of 2 CAD is added to the base θ_{50} from the perfect case to emulate the effect of process and measurement noise altering the measured θ_{50} on each iteration of the mode transition sequence.

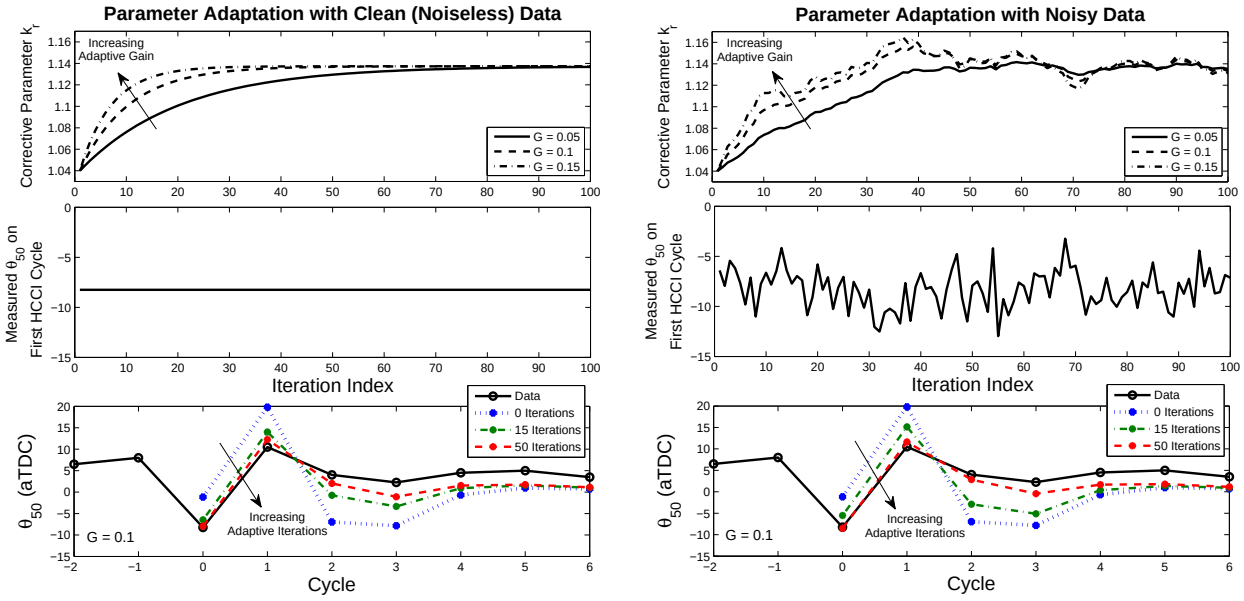

Figure 3.5: Demonstration of k_r adaptation for the SI-HCCI mode transition sequence of Fig. 3.1 with perfect repeatability (left) and additive noise (right) in the θ_{50} measurement that is assimilated on cycle *HCCI 0*. Top: Adaptive parameter dynamics as a function of mode transition iteration. Middle: θ_{50} value on cycle *HCCI 0* that is fed to the adaptation after being corrupted by ensemble noise. Bottom: Refinement in model θ_{50} response as $\hat{k}_r$ adapts for fixed $G = 0.1$.

Starting from the initialized value of $\hat{k}_r$ in Fig. 3.5, the model θ_{50} prediction has large errors both on the cycle *HCCI 0* as well as the following HCCI cycles. As consecutive iterations are carried out, the $\hat{k}_r$ estimate increases, resulting in a significant improvement in the model's θ_{50} prediction. The value to which $\hat{k}_r$ converges is the same for the both the clean and noisy θ_{50} measurement cases, though close comparison of the right and left columns of Fig. 3.5 shows that convergence speed can be slightly inhibited by the presence of noise. This indicates that the adaptation may be hindered to a minor extent in the presence of noise, but it is still able to converge robustly. The multiple G lines show how the adaptation can be sped up by increasing the gain, at the cost of increased noise amplification. Experimental tuning of the gain in further mode transition testing is necessary to definitively balance this trade off.

Another concern with the k_r adaptation is the effect of modeling error on the convergence of the

algorithm. To examine a scenario where the model parameters are perturbed from the nominal case, a 5% error is introduced into two uncertain quantities which affect the in-cylinder the temperature and hence the k_r adaptation: the model's prediction of residual mass m_r, and the initial condition for the exhaust temperature on cycle *HCCI 0* that is carried over from SI, denoted $T_{bd}(HCCI\ 0)$. The parameter adaptation is rerun starting from the same condition as in Fig. 3.5, using a constant $G = 0.1$ with no noise for simplicity. The results are plotted in Fig. 3.6, where the left column considers the m_r perturbation and the right column considers the $T_{bd}(HCCI\ 0)$ perturbation. As can be seen, for both positive and negative 5% error in these quantities, the adaptation adjusts the $\hat{k}_r$ so that the θ_{50} is matched cycle *HCCI 0*. The final value to which the parameter converges varies from the nominal case depending on the perturbation, as is necessary to match θ_{50} on cycle *HCCI 0* when the perturbation is applied. The model θ_{50} prediction as shown in the middle and bottom subplots improves with increasing adaptive iterations, however in the case of -5% error in m_r, the model θ_{50} predictions on the cycles following cycle *HCCI 0* still have large error after many iterations. This is because the combustion phasing on cycle *HCCI 1* is very late and near a misfire condition, where the Arrhenius integral for combustion phasing becomes very sensitive, and so the -5% error in m_r can result in large errors in combustion phasing for the model. In controller implementation, the controller will be tuned to avoid these near-misfire conditions so that the model predictions do not become so sensitive.

3.3 Model Evaluation in Multiple SI-HCCI Transition Conditions

To examine the ability of the proposed residual temperature correction method and to extend to various mode transition conditions with the mutli-mode combustion model of Ch. 2, several additional SI-HCCI transition experiments were carried out for comparison of the model predictions versus transient data. These experiments were run on a replica of the engine which was used to generate the data in Secs. 3.1, 3.2 and parameterize the combustion models in Secs. 2.3.3, 2.4.2. All the geometric specifications of this second instance of the engine remain the same as the original (see Table 2.1) except the geometric compression ratio, which takes a slightly lower value of 11.45:1. Before carrying out simulations of SI-HCCI transitions from the replica engine, the SI and HCCI combustion models were reparameterized to steady-state data from the replica engine, to eliminate the possibility of obscuring the results through differences in prediction accuracy between the two engine instances. The reparameterization data and the model fit of the data are given in Appendix A, as well as some minor modifcations to the model's regressions which were made in reparameterization.

The format of the SI-HCCI transitions in this Section differ from the previously presented mode transition in Sec. 3.1 and 3.2 in that the intake cam is switched to low lift prior to the exhaust cam, so that the SI phase of the transition operates with a low lift intake cam and the point of entry to

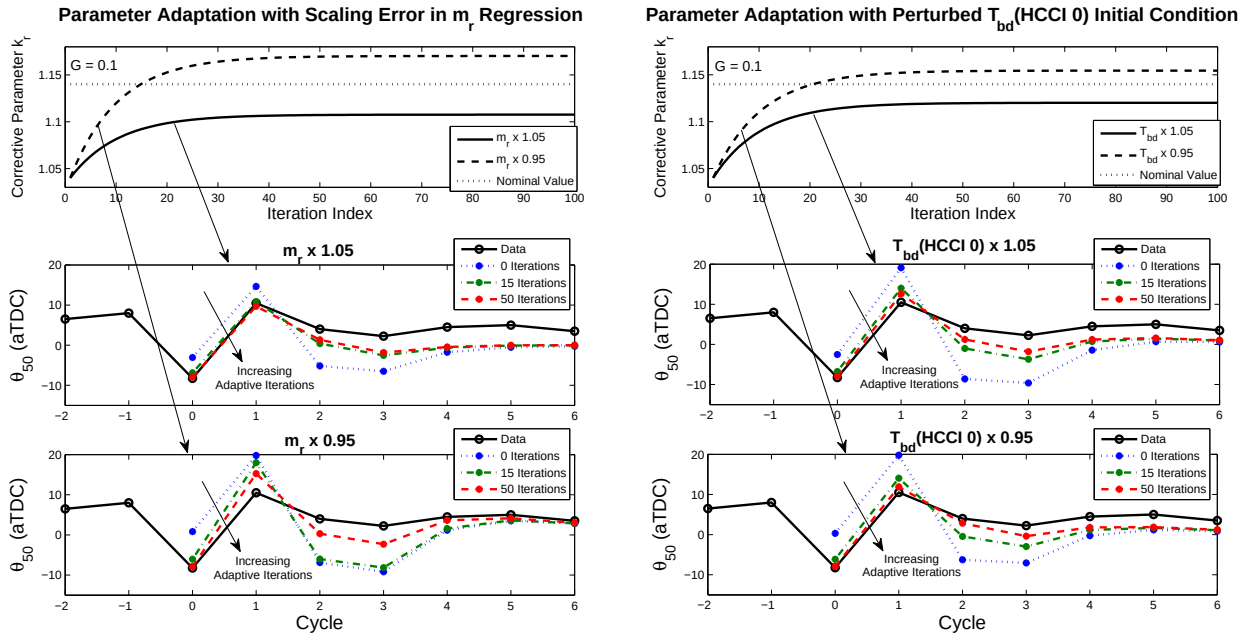

Figure 3.6: Demonstration of k_r adaptation for the SI-HCCI mode transition sequence of Fig. 3.1 in the presence of perturbations to the modeled m_r and $T_{bd}(HCCI\ 0)$. Top: Adaptive parameter dynamics with consecutive mode transition iterations. Middle/Bottom: Model reproduction of measured θ_{50} response from the mode transition with varying amounts of adaptive iteration for +/- 5% model perturbation.

HCCI is defined solely by the switch of the exhaust cam to low lift. This strategy is in line with the final closed-loop SI-HCCI mode transition approach that will be developed in Ch. 4. As will be discussed in Sec. 4.1.3, there is not much difference in mode transition effectiveness between the strategy of switching the intake cam to low lift prior to the exhaust cam and switching both the intake and exhaust cams simultaneously. The important thing to note is that experimentation indicates that for a wide range of intake cam phasings, the switch of the intake cam from high to low lift has minimal effect on the air path and combustion, so that the modeling considerations change little between either approach. In any case, the ability of the model to predict the combustion outputs in both Fig. 3.1 and the mode transitions of this Section corroborates that it can be used with either intake switching strategy.

As stated in Sec. 3.2.1, when multiple SI-HCCI transition conditions are considered, the value of the residual temperature correction k_r to match transient data will most likely vary with operating condition. Hence, the model accuracy can be improved by introducing a dependency of k_r on the engine operating variables, as opposed to the constant value in Secs. 3.1, 3.2 where a single mode transition case was considered. A simple linear parameterization of k_r to the EVC timing on cycle *HCCI 0* provided adequate model accuracy for a dataset of multiple mode transition trials at 2000

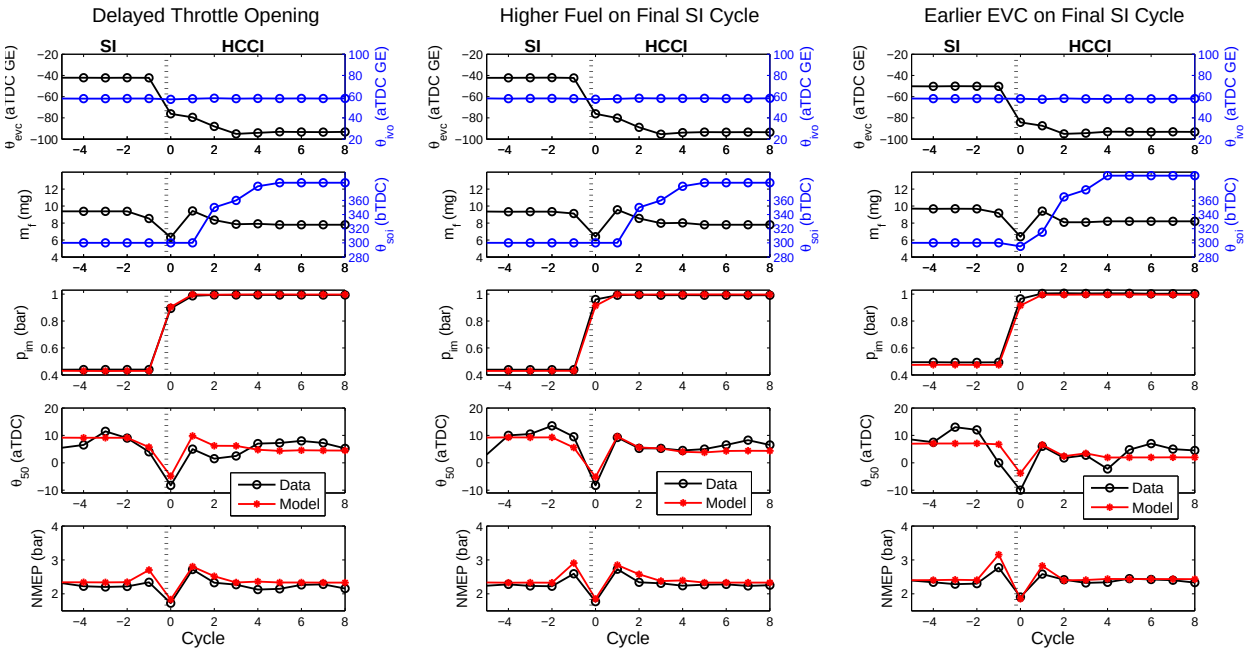

Figure 3.7: Experimental SI-HCCI mode transitions at low load HCCI with varying initial conditions for the HCCI phase of the transition. Left: Delayed throttle opening when switching to HCCI. Middle: Higher fuel quantity on final SI cycle. Right: Earlier EVC timing when switching to HCCI.

RPM engine speed which includes those presented in this Section,

$$k_r \approx a_1 \theta_{evc}^{HCCI0} + a_0 \tag{3.6}$$

The logic behind this choice of k_r parameterization is that the EVC timing when switching to HCCI presents significant uncertainty to the nominal model, because it tends to be later than any setting that can be reached in steady state HCCI for a given fuel injection quantity/timing due to the high exhaust temperature carried over from SI. The linear form of Eq. (3.6) maintains compatibility with the adaptive tuning method of Sec. 3.2, though now the adaptive gain G will vary based on measured quantities according to the chosen parameter update law.

Given that k_r in Eq. (3.6) depends on more than one parameter, a method to systematically regress the k_r parameters is warranted. In Appendix B, a parameterization routine is given which determines the parameters in both the base HCCI model and the k_r expression. The routine is iterative to account for cycle to cycle couplings and compounding of modeling error throughout the HCCI model's equations, and incorporates simulations of SI-HCCI transient data for use in determining the k_r parameters.

One aspect that was explored with additional mode transition experiments was the ability of

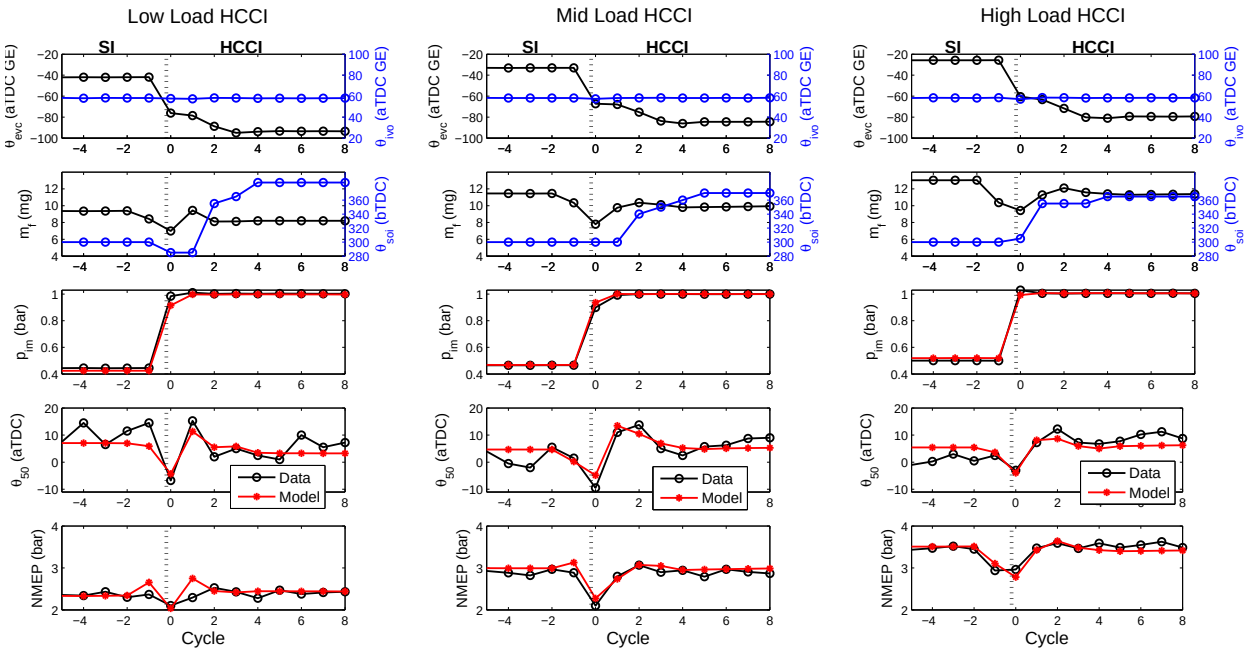

Figure 3.8: Experimental SI-HCCI mode transitions across the HCCI load range at 2000 RPM. Left: Low load. Middle: Mid load. Right: High load.

the model to capture the output responses when the initial conditions for switching to HCCI are changed, while keeping the operating condition similar to that in Fig. 3.1. The initial conditions are altered through adjusting several different input commands to the final SI cycle. Fig. 3.7 plots the most important inputs and modeled versus measured outputs for several different methods of perturbing the HCCI initial conditions. In the left column, the time at which the throttle is commanded open to switch to HCCI is delayed, so that the intake pressure is lower on cycle *HCCI 0*. In the center column, the fuel injected into cycle *SI -1* is increased relative to the nominal fuel sequence, increasing the exhaust temperature of the residual gas passed to cycle *HCCI 0*. In the right column, the SI switch point is set with an earlier exhaust valve timing, to increased the trapped residual mass leading into the cycle *HCCI 0*. Throughout these various perturbations to the HCCI initial condition, the model reproduces the general trend of the output time histories well, with quantitative accuracy that is acceptable for controls purposes. Note that the somewhat non-obvious reason for the increase of NMEP on cycle *SI -1* is the exhaust cam switch to low lift, which shifts the EVO timing later and elongates the expansion stroke, increasing the work output. The effect is more dramatic at the earlier exhaust valve timings present in the low load mode transitions of Fig. 3.7. It will be seen in the next set of experiments with higher load trials that the effect is mitigated at later exhaust valve timings.

Another set of SI-HCCI mode transition experiments were concerned with evaluating the model's

performance in varying operating conditions. The operating condition is adjusted by sweeping the load from near the lower HCCI limit to near the upper HCCI limit for the experimental engine at 2000 RPM. The engine speed is not changed because the model parameterization did not contain speed variation. The results for three of these experiments are presented in Fig. 3.8, starting near the lower load limit in the left column and increasing to the high load limit in the right column. As the load condition varies, the actuator sequences for the EVC timing and the fuel injection quantity/timing vary as well, which adds diversity to the dataset. Throughout the multiple actuator sequences, again the model is able to reproduce the output time histories well, with the only problem occurring with the NMEP prediction on cycle *HCCI 1* of the low load sequence. The model's overestimation of the NMEP on this cycle can be explained by the late combustion phasing present in the data, where the roll-off of combustion efficiency with combustion phasing becomes steep [19] and so even a few degrees of θ_{50} error can make a large difference in the NMEP prediction. The model predicted θ_{50} is several degrees earlier than the data value on this cycle, and so the model does not register the reduced torque from the late phasing. As with the late phasing observed on cycle *HCCI 1* in Sec. 3.2.2, in implementation the controller will be tuned to avoid these late phasing points so the model predictions do not become so sensitive. A last note is that the NMEP rise on cycle *SI -1* of the low load case is less pronounced than in the mode transition in the left column of Fig. 3.7 despite similar actuator settings, which may be due to deviation of the injected fuel quantity from the commanded value or other stochastic disturbances.

Chapter 4

SI-HCCI Mode Transition Control

This Chapter develops a model-based feedback control methodology for the SI-HCCI direction of SI/HCCI mode transitions based on the control-oriented SI/HCCI combustion model in Chapters 2 and 3. The chapter is modified after [65] with additional discussion on the investigation of actuator strategies for the SI-HCCI transition. The Chapter begins by first looking at SI-HCCI mode transitions from a high level, in order to elucidate the steps involved with switching from SI to HCCI and to establish the strategy which dictates the general trends in the control input trajectories throughout the transition. Once the strategy is decided, controllers for both the SI and HCCI phase of the SI-HCCI transition are developed which implement this strategy through model-based calculations and several physically intuitive set points. Following their development, the controllers are implemented in a multi-mode combustion control architecture on an experimental prototype engine, and are shown to carry out successful SI-HCCI transitions at multiple operating points.

4.1 High-Level Mode Transition Strategy

Before developing a control design, it is prudent to explore from a high-level the actuator manipulations involved with transitioning from SI to HCCI and determine an overall strategy. The strategy defines the general shape of the control input trajectories throughout the mode transition, and so will influence the selection of the controller structure, set points, and logical elements.

The core idea of the SI-HCCI transition is to shift the engine condition from one of stoichiometric AFR with low in-cylinder temperature and internal residual to one of a lean AFR with high in-cylinder temperature and internal residual. The initial condition is characteristic of flame-based SI combustion due to the lower temperatures needed to avoid end gas knock and lower dilution to facilitate flame propagation, while the final condition promotes auto-ignition combustion due to high pressures and temperatures. The major actuator alterations to accomplish this shift of condition are:

- Switching the cam profiles from higher lift SI settings to lower lift HCCI settings to enable entrapment of high amount of residual gas (see Fig. 2.2 for example high lift - low lift cam profiles)
- Advancing the (EVC) timing before TDC to trap a large quantity of residual exhaust gas

- Opening the throttle to compensate for the reduction in air flow caused by the advanced EVC and high residual quantity, and to lean the mixture

The timing and transient paths of these actuator changes are the main features defining the mode transition strategy. Numerous studies have investigated SI-HCCI mode transition strategies, but all these studies can be divided into two broad categories which will be discussed next.

4.1.1 Cam Phasing Versus Cam Switching Strategies

While the details of mode transition strategies in the literature vary from one study to the next, all studies tend to fall into one of two broad categories, which will be referred to as "cam phasing" and "cam switching". In cam phasing strategies [29, 39–41], the cam profiles are switched to low lift at the start of the mode transition, prior to entry to HCCI, and then the EVC timing is gradually advanced to its HCCI position while the throttle is gradually opened to compensate for the increase in trapped residual. In cam switching strategies [20–28, 30, 35], the cam switch is postponed until the valve timings are phased to a condition such that when the exhaust cam switches to low lift, enough residual is trapped to induce auto-ignition on the cycle immediately following. HCCI is thus abruptly engaged by a switch of the exhaust cam to low lift, which is accompanied by an opening of the throttle. A schematic illustrating the differences in the general trajectories of the throttle and EVC timing between cam phasing and cam switching strategies in shown in Fig. 4.1. A jump in the EVC timing is apparent when the exhaust cam switches to low lift due to the offset between the cam profiles (see Fig. 2.2). Note that the degree to which the EVC timing is phased in prior to switching to low lift in the cam switching strategy depends on how large the ΔEVC_{H-L} value from Eq. (2.1) is, with larger offsets requiring less phasing.

In weighing the costs and benefits fo the cam phasing and cam switching strategy, the type of valve train hardware first needs to be considered. In studies which employ fully flexible valve actuation systems [20–22, 30, 35], the cam switching strategy is relatively easy to implement, because the flow into the cylinders can be regulated through the flexibility in the valve train while running the engine with a wide-open throttle. This allows cylinder air charge to be kept to an appropriate level for stoichiometric SI combustion at the low loads pertinent for HCCI even with a wide-open throttle, so that the intake pressure can reach atmospheric levels before engaging HCCI. The valve lifts/timings can then be switched in one cycle to appropriate values to trap the correct amount of residual to engage HCCI on the cycle immediately following. When a more practical two-stage cam mechanism is used [23–28], however, it becomes infeasible to fully dethrottle the SI combustion prior to switching to HCCI while also maintaining the commanded load with a stoichiometric AFR. In this case, the abrupt entry to HCCI from the exhaust cam switch requires precise coordination of the throttle opening [23, 24, 26], and tends to result in high pressure rise rates on the first few cycles of HCCI due to high exhaust temperature advancing combustion phasing [25, 28]. The discrete

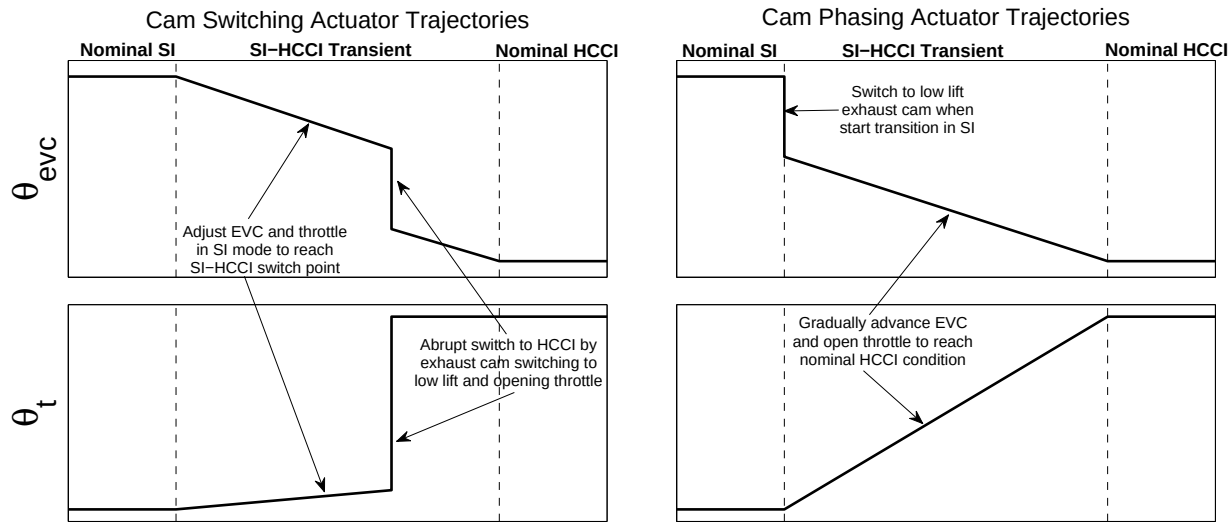

Figure 4.1: Schematic illustrating main differences between actuator trajectories of cam switching (left) and cam phasing (right) SI-HCCI mode transition strategies.

jump from SI to HCCI of cam switching strategies thus introduces additional difficulties and more sensitivity to imprecisions in practical scenarios.

Despite the disadvantages introduced by the abrupt nature of the cam switching SI-HCCI transition strategy, it offers one major benefit relative to the gradual nature of the cam phasing counterpart. The benefit has to do with what has been termed the "residual gas fraction gap" [22] or " unstable area" [29] which can arise between SI and HCCI combustion. This regions refers to operating conditions where the internal residual is significantly increased realtive to nominal SI, making flame propagation difficult due to high dilution, however it is not increased enough to give sufficient in-cylinder temperature for auto-ignition. Operation in this region is thus unfavorable because SI combustion is not robust, yet HCCI combustion cannot be achieved. With the cam switching SI-HCCI transition strategy, the abrupt switch of the exhaust cam to engage HCCI allows such conditions to be "jumped over" by the offset between the high lift and low lift cam sets (see Fig. 2.2) which discretely switches the residual quantity from SI levels to HCCI levels. With the cam phasing strategy, however, the residual quantity must be gradually increased, making passage through the "unstable area" inevitable. The studies [29, 41] have shown the ability to pass through the "unstable area" through use of advanced spark timing and fuel injection strategies, however the transition seems to be more robust at high loads due to the larger fuel quantity in the cylinder making flame propagation easier. Indeed, at the low load condition addressed in [41], a significant reduction in torque coupled with a late combustion phasing is apparent in the highly dilute SI portion of the experimental SI-HCCI transition. The data available in the literature may thus suggest that the cam phasing strategy is ideal at higher load HCCI conditions, while the cam

switching strategy becomes advantageous at lower load HCCI conditions.

Despite that experimental results in the literature seem to suggest that a combination of the cam phasing and cam switching strategies may give the best overall SI-HCCI topology, a policy of using a uniform cam switching SI-HCCI transition strategy is adopted here. It will be shown that proposed model-based controller built on the cam switching strategy is able to function robustly across the full HCCI load range, so that the complexity of integrating the cam phasing strategy into the overall SI-HCCI architecture is not necessary. The use of the cam phasing strategy may help reduce pressure rise rates near the high load end of the HCCI spectrum, however the pressure rise rates with the proposed control method still remain tolerable in this region. Thus, for the remainder of the Section, the cam switching strategy is the focus of the discussion.

4.1.2 Considerations for the Cam Switching Strategy

The Notion of Dethrottling the SI Combustion Mode

A major discrepancy between SI and HCCI operating conditions which must be overcome during a mode transition is the intake pressure at which each mode operates. At the low loads pertinent for HCCI combustion, SI tends to operate signifcantly throttled with intake manifold pressures of $p_{im} \in [0.3, 0.5]$ bar, while HCCI will be unthrottled with $p_{im} \approx 1$ bar. In the cam switching strategy, it is ideal to close this gap in intake pressure as much as possible before switching to HCCI, to promote a higher cylinder air charge during the first HCCI breathing event. Higher fresh air charge aids in moderating the in-cylinder temperature in the cam switching strategy, because the abrupt change of combustion mode implies that the residual gas will be the result of SI combustion and so will be much hotter than typical in HCCI operation. The higher residual temperature and hence in-cylinder temperature tends to give undesirable advanced auto-ignition timing and increased pressure rise rates.

The difficulty in increasing intake manifold pressure while in SI operation lies in the conflicting constraints of stoichiometric operation and drivability. Increasing the intake manifold pressure via opening the throttle necessitates greater fuel quantity maintain a stoichiometric AFR, which tends to increase the engine torque and make it deviate from the driver demand. This is illustrated in the stoichiometric throttle sweep data in the left column of Fig. 4.2, where it can be seen that even mild increase in p_{im} from opening the throttle induces a large change in NMEP when the mixture is held stoichiometric. It is possible to compensate for the higher NMEP by retarding the spark timing to reduce the torque output via non-optimal combustion phasing, however experiments showed that this method actually worsens the situation for the first HCCI cycle because the retarded spark and increased fuel quantity raise the exhaust temperature. Another option is to decouple the throttle and fuel control and open the throttle without increasing the fuel, leaning the mixture. This method

was employed in [28], and helps to both increase the intake pressure as well as reduce exhaust temperature. However, it is not considered as a viable approach here, because manipulation of the throttle to increase the intake pressure necessitates several lean cycles due to the finite response time of the manifold dynamics, and the degree of leaning must be high in order to achieve any worthwhile increase in intake pressure; for example, in one experiment at 2.4 bar NMEP at 2000 RPM, the mixture had to be leaned to $\lambda = 1.35$ to increase intake manifold pressure by 0.1 bar. Such large amounts of excess oxygen can quickly fill the catalyst oxygen capacity, which can be a major influencing factor for the allowable duration of the HCCI mode in regards to NOx emissions levels [63] . A high amount of leaning can also cause a high cyclic variability and engine roughness due to over-dilution of the SI combustion. In the finalized strategy in Sec. 4.1.3, an optional leaning of the mixture to reduce exhaust temperatures will be provided, but will be kept to one cycle through manipulation of the fuel command.

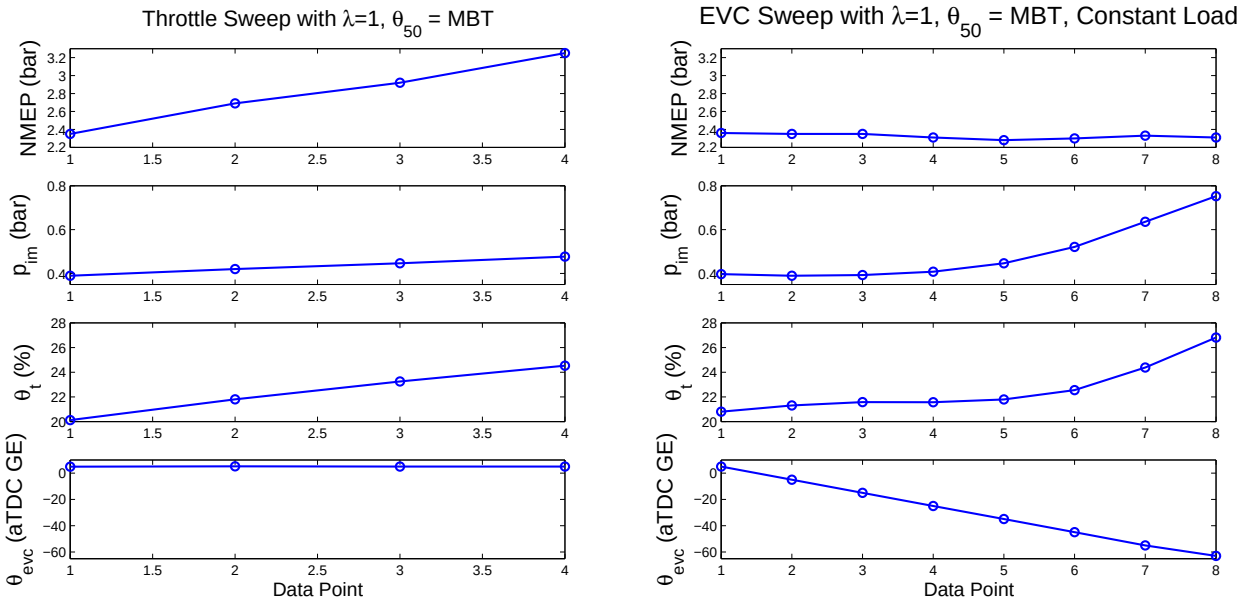

Figure 4.2: Steady-state actuator sweep data of throttle (left) and EVC (right) under constraints of stoichiometric AFR and MBT combustion phasing. In the EVC sweep, the throttle is opened as necessary with advancing EVC to maintain constant torque.

Another, more subtle way to increase the intake pressure is to advance the EVC timing prior to switching the exhaust cam to low lift, in order to increase trapped residual and restrict cylinder air flow and so increase the mass stored in the intake manifold. The sweep data in right column of Fig. 4.2 shows how this can be done while maintaining a constant load and a stoichiometric AFR. Note that the throttle must be opened throughout the sweep to maintain constant load, as the earlier EVC reduces the torque output from increased pumping losses and a shorter expansion stroke caused by earlier EVO, and so more fuel is necessary to offset these effects. The opening

of the throttle compounds with the advancing EVC to yield a very significant increase in p_{im} at the earlier end of the EVC spectrum, while maintaining constant load. Note that the intake valve timing can also be adjusted to increase intake pressure; this will be discussed in the next section.

The EVC sweep data in Fig. 4.2 suggests that the optimal way to carry out cam switching SI-HCCI mode transitions is to advance the exhaust valve timing very far before TDC prior to switching to low lift. While this tactic undoubedtly has advantages, it can be counterbalanced by one other aspect of the choice of EVC timing which has not been considered yet; that the EVC position on the final SI cycle dictates the EVC position on the first HCCI cycle through the constant high lift - low lift offset (see Fig. 2.2). This implies that if the EVC timing is excessively advanced in the SI mode, then the resulting EVC timing after the cam switch to low lift may be excessively advanced as well, trapping a high residual mass and leading to large in-cylinder temperature and high pressure rise rates. The optimal choice of the EVC placement in the SI mode thus depends on the offset between the high lift and low lift cams, ΔEVC_{H-L}. If ΔEVC_{H-L} is large, then if the EVC is advanced far before TDC in SI mode, the corresponding low lift EVC timing will be very early, and give a high amount of residual mass in HCCI and cause unwanted high pressure rise rates. However, if ΔEVC_{H-L} is small, then a very early EVC in SI mode may be acceptable, and can help bridge the gap in intake pressure between SI and HCCI. For the experimental hardware of this dissertation with $\Delta EVC_{H-L} = 34°$, it was found that the placement of the EVC timing when switching to HCCI had a far stronger impact on the first HCCI combustion event than the effect of advancing EVC to dethrottle the SI combustion, and so the EVC tended not to be advanced too far in SI mode, typically falling between 10 and 40 degrees bTDC GE.

Low Lift Versus High Lift Intake in SI Mode

As described in the previous Section, it is ideal to orient the engine actuators while in SI mode such that when the exhaust cam switches to low lift and HCCI engages, the air flow on the first HCCI cycle is maximized. One tactic which may have potential to assist in this regard is to switch the intake cam to low lift prior to the exhaust cam, so that the SI mode runs with a low lift intake cam. The logic behind this manuever is that the low lift intake cam should restrict cylinder air flow due to lower effective flow area, and hence increase the stored mass and pressure in the intake manifold. Additionally, switching the intake cam to low lift prior to HCCI may allow the low lift intake timing to be phased for the optimal cylinder breathing upon entering HCCI, while it may be difficult to reach such a phasing with the high lift intake cam in SI mode depending on the offset between the intake cams ΔIVO_{H-L}.

To explore the potential advantages of running the SI combustion with the low lift intake cam during SI-HCCI transitions, Fig. 4.3 plots steady-state intake valve timing sweeps over the majority of the cam phaser range for both high lift and low lift intake cams. The exhaust cam is kept in high

lift with EVC fixed at 4° aTDC throughout the sweeps. The most immediately apparent observation is that the low lift intake cam tends to result in *lower* intake manifold pressure in most cases than the high lift intake cam, despite that the cylinder air flow W_{cyl} changes little between the high lift and low lift intake cam phasing. This is contrary to the original hypothesis that the lower orifice area caused by the low lift intake cam would restrict air flow, and so drive p_{im} up for constant W_{cyl}. However, as can be seen in the bottom subplot, the low lift intake cam induces significantly large pumping losses. While somewhat counterintuitive, these results appear to indicate that the lower lift intake cam does not restrict air flow relative to the high lift intake cam, but simply make the piston work harder to pull the air into the cylinders. Additionally, the high lift intake cam is able to significantly increase p_{im} with late phased IVC timings, where the intake valve closure in the compression stroke causes a large quantity of the charge to be expelled back into the intake manifold. As can be seen, though, the degree to which late IVC timing can increase p_{im} is practically limited by high coefficient of variation (COV) in IMEP at very late IVC timings, mostly likely caused by strong cycle to cycle differences in the amount of air and fuel rejected into the intake manifold.

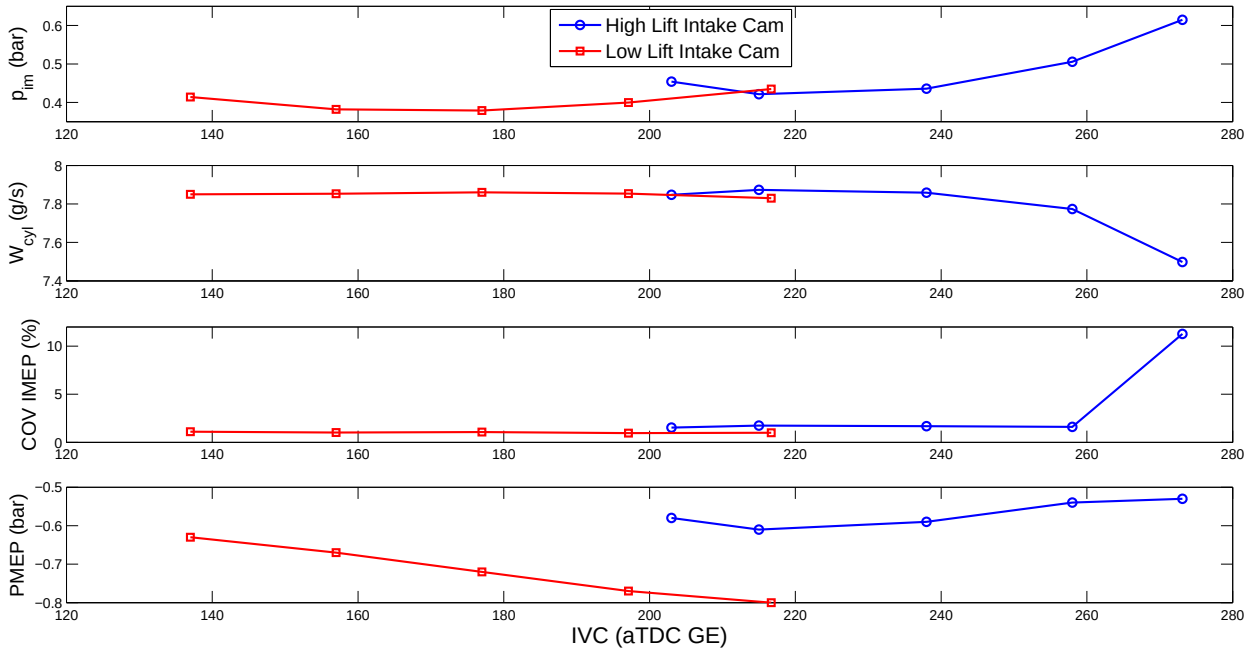

Figure 4.3: Steady-state intake valve timing sweeps with both high lift and low lift intake cam to examine which intake lift to use in SI phase of SI-HCCI transition.

The sweeps in Fig. 4.3 indicate that low lift intake SI operation offers no gains for increasing intake manifold pressure relative to standard high lift intake operation. However, it does allow the IVC timing to be freely adjusted with minimal effect on air flow to reach the optimal breathing position, which is the point at which the sweep in Fig. 4.3 bottoms out in p_{im} for relatively constant

air flow. Depending on the high lift-low lift intake cam offset, it may not be feasible to orient the high lift intake cam to result in an IVC timing near the optimal low lift setting upon switching the cams while also giving a strong increase in p_{im} prior to switching. For example, with the two-stage cam hardware of this dissertation, the high lift-low lift IVC timing is $\Delta IVC_{H-L} = -67^\circ$ (this can be calculated from ΔIVO_{H-L} and the cam duration), which necessitates a high lift IVC timing around 240° to induce a low lift IVC timing near the optimum around 175° in Fig. 4.3. Comparing the p_{im} value near IVC = 240° to that near the IVC=175° with the low lift timing, it can be seen that the difference in p_{im} between the two cam sets is not large. Additionally, the low lift intake cam gives larger PMEP, which necessitates additional dethrottling to compensate for the reduction in torque at fixed stoichiometric AFR.

The experimental results thus suggest that, for the given cam hardware, the choice of running the SI mode with either the high lift or low lift intake cam profile has little impact on the efficacy of the strategy. The choice is thus made to operate the SI mode with the low lift intake cam, for the simple reason that this reduces the calibration complexity in that the intake and exhaust cam do not have to be calibrated to both switch to low lift at the same time. If errors arise in the calibration of a simultaneous cam switching strategy due to improper estimation of the delays associated with the cam switching mechanism, the exhaust cam can switch to low lift prior to the intake cam. This can cause a large amount of residual to be ejected back into the intake manifold, which disrupts the cylinder air flow and can overheat the intake temperature sensors. Switching the cams separately avoids such scenarios and negates the need for precise calibration of the intake cam switching mechanism. It should be noted, however, that with different two-stage cam hardware with a different high lift-low lift intake cam offset, it may be possible to reap significant benefits for the SI-HCCI transition strategy with operation of the SI mode using the high lift intake cam, based on the analysis presented here. The control methodology that will be developed applies for both high lift and low lift intake SI operation, with the only consideration being that the SI model must be functional with whichever cam lift is used.

4.1.3 Walkthrough of SI-HCCI Transitions with Chosen Strategy

Based on the discussion in Secs. 4.1 and 4.1.2, the qualitative actuator paths for the SI-HCCI transition are defined through the cam switching strategy illustrated in Fig. 4.4. The figure shows the trajectories of the throttle θ_t and EVC timing θ_{evc} actuators discussed earlier, as well as those for the other relevant inputs θ_{sp}, θ_{soi}, m_f, and intake valve timing characterized by θ_{ivo}. Notice that at the start of the SI phase of the transition, the θ_{ivo} instantaneously jumps, signifying a cam switch to low lift based on the conclusions arrived at in Sec. 4.1.2. Note that the data in Sec. 4.1.2 indicated minimal influence on cylinder air flow from switching between high lift and low lift intake cams for a significant range of intake valve timings, meaning that the intake cam switch to low lift

can be accomplished with only minor compensation measures.

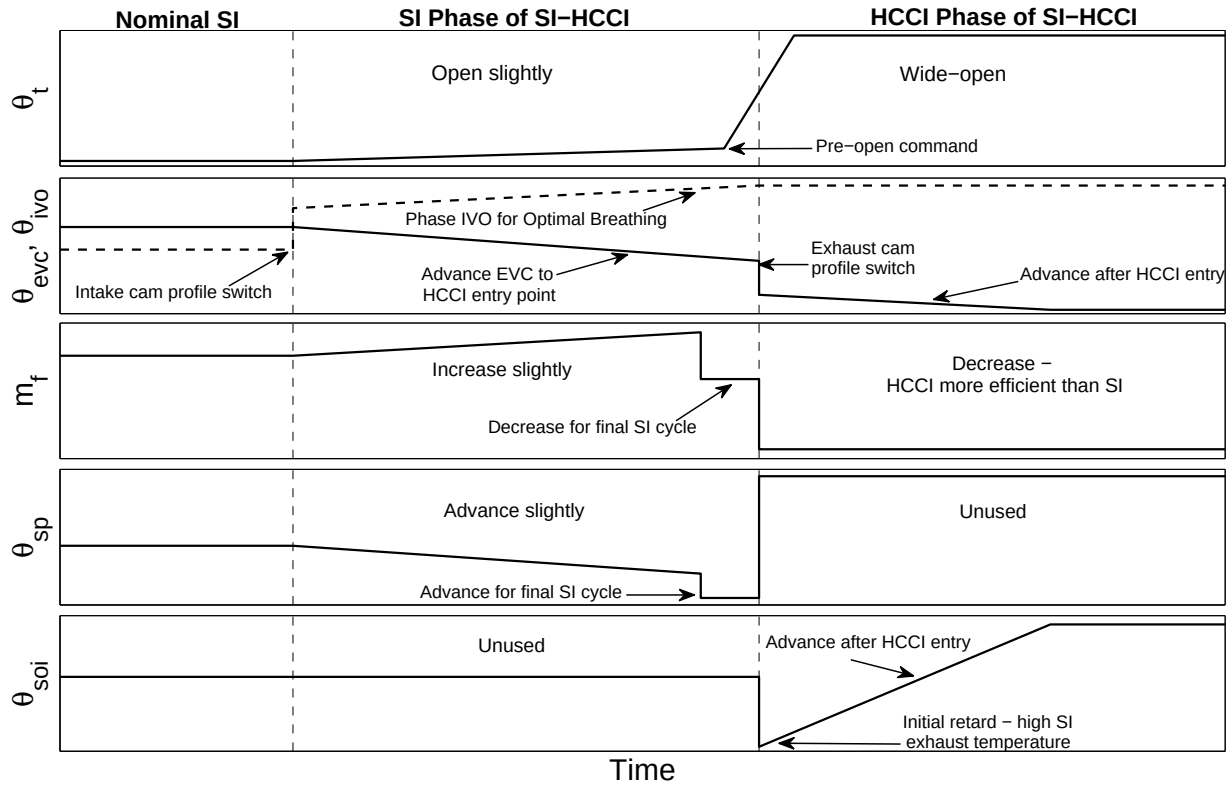

Figure 4.4: Representative depiction of high-level actuator trajectories for cam switching SI-HCCI transition strategy. θ_{soi} shown with reference to bTDC; all other timings shown with reference to aTDC.

After the intake cam switches to low lift, the SI phase of the mode transition proceeds. The EVC timing is advanced to its switch point for entry to HCCI, while the IVO timing is adjusted to its optimal breathing position for maximum air flow when HCCI is entered. While the valve timings adjust, the throttle compensates for the disturbance to the air flow and engine torque, which usually involves opening past its in nominal SI set point. The fuel quantity tends to increase for torque neutrality because the valve timings are phased to non-ideal conditions for SI combustion, and so more fuel is necessary to attain the same work output while maintaining a stoichiometric AFR. The spark timing adjusts as necessary to keep the combustion phasing in the desired range, which tends to require spark advance due to the advancing EVC increasing the in-cylinder dilution. The fuel injection timing is unused and left at its nominal SI set point, as it has been observed to have a minor effect on the SI combustion as long as the injection is in the intake stroke.

When the SI-HCCI switching boundary point is reached, a number of notable changes occur. Firstly, the throttle is commanded wide-open to increase the intake manifold pressure and allow for

sufficient air flow on the first HCCI cycle. This wide-open command comes slightly in advance of the first HCCI breathing event, to account for the transport delay and manifold/actuator dynamics which require time to overcome and build intake pressure. The fuel may be specified to reduce on cycle *SI -1*, in order to lean the mixture to reduce the exhaust temperature and combat early combustion phasing on the first HCCI cycle. This reduction in fuel was observed to have minimal impact on the torque for the two-stage cam system used in experiments, because it is compensated by an increase in the torque on the final SI cycle which results from the exhaust cam switch shifting the EVO timing shifting later (see Fig. 2.2) and elongating the expansion stroke. The spark timing is advanced to compensate for the increased dilution caused by the reduction in fuel.

When the exhaust cam switches to low lift, the EVC timing instantaneously jumps by the offset between the high and low lift cam sets, the spark is placed very late so as to not interact with combustion, and the injection timing actuator becomes active as HCCI engages. As stated in Sec. 2.4, the injection timing is hypothesized to affect the auto-ignition phasing through changing the degree of chemical reactions in recompression [54, 55], with earlier injection giving a longer time for reaction and tending to advance combustion phasing. Hence, SOI is typically late when HCCI is first entered in order to retard the combustion phasing in compensation of the high SI exhaust temperature. As the HCCI phase of the transition carries on, the exhaust temperature drops to HCCI levels, which tends to lower the in-cylinder temperature and retard combustion phasing. This is compensated for by advancing the EVC timing to trap greater residual mass, along with advancing the SOI timing as well. After several cycles, the exhaust temperature transient settles out and the EVC timing reaches its nominal HCCI condition, marking the start of nominal HCCI operation.

To gain a better grasp on the combustion dynamics throughout cam switching SI-HCCI mode transitions following the strategy of Fig. 4.4, in-cylinder pressure data from an SI-HCCI mode transition experiment is shown in Fig. 4.5. A key feature which distinguishes the characteristics of the the mode transition is the exhaust recompression/gas exchange event, and so this is pointed out in the Figure. The cycles are indexed with reference to the first HCCI cycle, defined as *HCCI 0*, as in Ch. 3. Starting several SI cycles before the switch to HCCI, the combustion can be observed to follow a typical SI profile with a mild and gradual pressure rise, and negligible recompression pressure is apparent during gas exchange. As the SI phase of the transition proceeds, the recompression pressure becomes slightly higher, which is caused by the advancing of the EVC timing while the high lift cam is still in place. The purpose of this advancing is to reach a point in SI such that when the exhaust cam profile is switched to low lift, the EVC timing that results with the low lift cam in place is early enough to trap sufficient residual gas to give auto-ignition. The recompression pressure remains mild because the high lift cam cannot trap a high amount of residual mass.

On the final SI cycle *SI -1* of Fig. 4.5 there is a drastic increase in recompression pressure between the start of the cycle and end of the cycle, which is the result of the exhaust cam switching to low

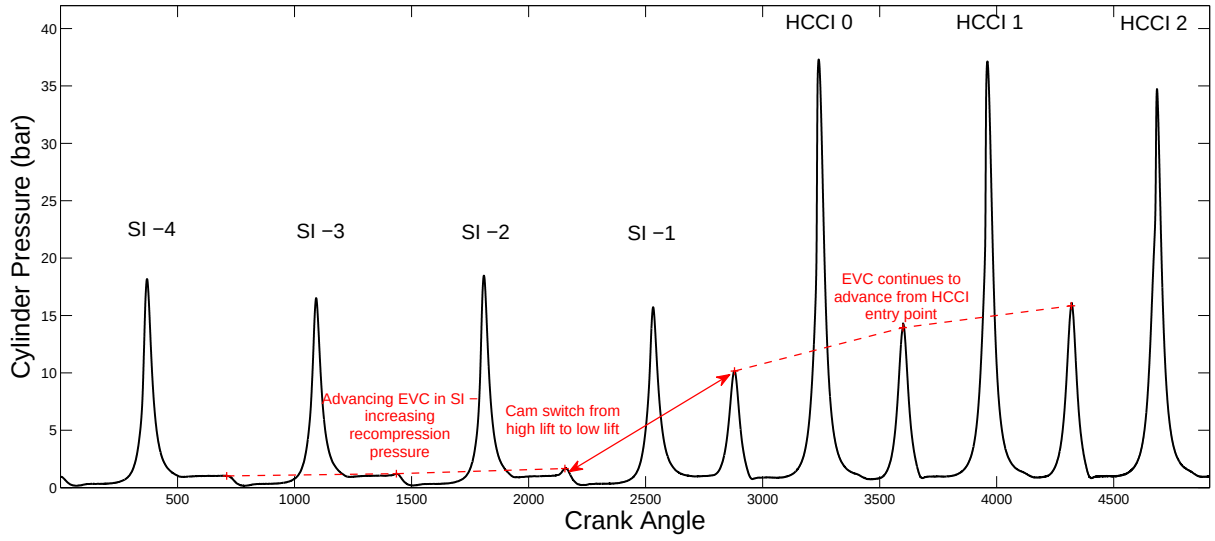

Figure 4.5: In-cylinder pressure data from a cam switching SI-HCCI mode transition illustrating the changes in combustion features over the course of the transition.

lift and suddenly increasing the trapped residual mass. The cam switch mechanism is designed to switch cam profiles during the closed valve portion of the cycle, so that after combustion on the EVO event of cycle *SI -1*, the low-lift cam is engaged. At this point, both the EVO and EVC timings have shifted by the high lift-low lift exhaust cam offset, which causes a significant advance of the EVC which significantly increases trapped residual and leads to a larger recompression pressure. Following the cam switch to low lift, the combustion exhibits a much faster and larger pressure rise, signifying auto-ignition and hence HCCI. After cycle *HCCI 0*, the recompression pressure continues to rise on subsequent cycles as the EVC timing advances to its nominal HCCI condition, which is earlier than the HCCI entry point due to the reduction in exhaust temperature from SI to HCCI.

4.2 SI Phase Controller

4.2.1 Control Problem Overview

The purpose of the SI phase of the SI-HCCI transition strategy outlined in Sec. 4.1.3 is to adjust the valve timings to a point suitable for the switch of the exhaust cam to low lift and entry to HCCI. Throughout this adjustment, there are four main control objectives to consider, based on the performance objectives in Sec. 1.1.3:

- Deviations of the engine torque from the driver demand should be minimized as per performance objective 1.

- Deviations of the combustion phasing from max brake torque (MBT) timing should be small enough to avoid deleterious effects on the engine torque and knock/misfire in the early/late extreme cases, as per performance objectives 1 and 3.
- AFR should be kept in the vicinity of stoichiometric for catalyst efficiency. Any leaning that occurs should be small relative to the catalyst oxygen storage capacity, as filling of the oxygen storage may affect the allowable stay duration in HCCI in regards to NOx emissions [63] and so can threaten performance objective 2.
- The SI-HCCI switch point should be reached as quickly as possible as per performance objective 4.

The controller development addresses these objectives assuming the intake cam has already been switched to low lift, which is the first action of the strategy given in Sec. 4.1.3. As stated in Sec. 4.1.3, the intake cam switch to low lift has been experimentally observed to have minimal impact on the engine breathing and combustion for a significant range of IVO timings, and so this component of the strategy is of little concern.

Given the stated control objectives and the model of Ch. 2, the control problem is formulated according to the logic in Table 4.1. The utilized control inputs are the throttle command, EVC command, IVO command, fuel quantity, and spark timing, which have units of %, aTDC GE, aTDC GE, mg/cycle, and aTDC comb, respectively. The performance variables of torque, combustion phasing, and AFR are characterized by the net mean effective pressure (NMEP), 50% burn angle θ_{50}, and relative AFR λ. Torque and combustion phasing are treated as reference inputs to be tracked to specified values, targeting the ideal case where the torque follows the driver command perfectly and the combustion phasing stays at the optimal point. The AFR is allowed to fluctuate within some constraints which are chosen in the vicinity of stoichiometric to retain acceptable after treatment performance. This policy affords some flexibility for the fuel control to compensate torque disturbances with minimal impact on emissions due to the short duration of the SI phase of the SI-HCCI transition. The feedback variables include the intake manifold pressure and temperature p_{im} and T_{im}, as well as the cam phasing and angles and engine speed N_{eng} which are assumed to be measured and treated as disturbances. Values for saturation limits for the actuators are listed, however all actuators tend to take values within the middle of their saturation range for the SI phase of the transition, and so input constraints are not a serious concern. The states of the air path model are reduced to contain only the intake manifold pressure actuator dynamics, where the intake temperature is eliminated with the isothermal assumption Eq. (2.4), and the exhaust manifold, post-turbine, and post-compressor pressures are assumed constant at atmospheric for low load operation in the relevant regime for switching to HCCI.

The structure of the SI phase controller to address the control problem laid out in Table 4.1 contains two separate subsystems for the air path and combustion control. This decentralized architecture circumvents the hyrbid nature of the control problem which arises from simultaneous consideration of the continuous air path dynamics in conjunction with discrete cycle to cycle

Control Inputs	$u = \begin{bmatrix} u_t & u_{ivo} & u_{evc} & m_f & \theta_{sp} \end{bmatrix}^T$
Feedback Variables	$y = \begin{bmatrix} p_{im} & T_{im} & \theta_{ivo} & \theta_{evc} & N_{eng} \end{bmatrix}^T$
Performance Variables	$w = \begin{bmatrix} NMEP & \theta_{50} & \lambda \end{bmatrix}^T$
Reference Commands	$r = \begin{bmatrix} NMEP^* & \theta^*_{50,S} \end{bmatrix}^T$
λ Output Bounds	$\lambda^{rich} \leq \lambda \leq \lambda^{lean}$
Input Lower Bounds	$u_{low} = \begin{bmatrix} 0 & 10 & -85 & 5 & -60 \end{bmatrix}^T$
Input Upper Bounds	$u_{high} = \begin{bmatrix} 100 & 110 & 15 & 50 & 50 \end{bmatrix}^T$
Model States	$x = [p_{im} \;\; \theta_t \;\; \dot{\theta}_t \;\; \theta_{evc} \;\; \dot{\theta}_{evc} \;\; \theta_{ivo} \;\; \dot{\theta}_{ivo}]^T$

Table 4.1: Control problem formulation for SI phase of SI-HCCI transition.

combustion inputs/outputs. It also allows the air path actuators to operate on a time-synchronous loop given their continuous nature and the combustion actuators to operate on a cycle-synchronous loop given their discrete cycle to cycle nature. Additionally, the decentralized architecture is also more convenient for multi-cylinder engines than a centralized approach that considers air path and combustion control simultaneously, because each cylinder has separate combustion outputs and so it becomes ambiguous which cylinder's outputs to select for feedback control of the air path actuators. A block diagram of the control architecture for the SI phase of the SI-HCCI transition is shown in Fig. 4.6. In what follows, each subsystem and the elements therein are explained.

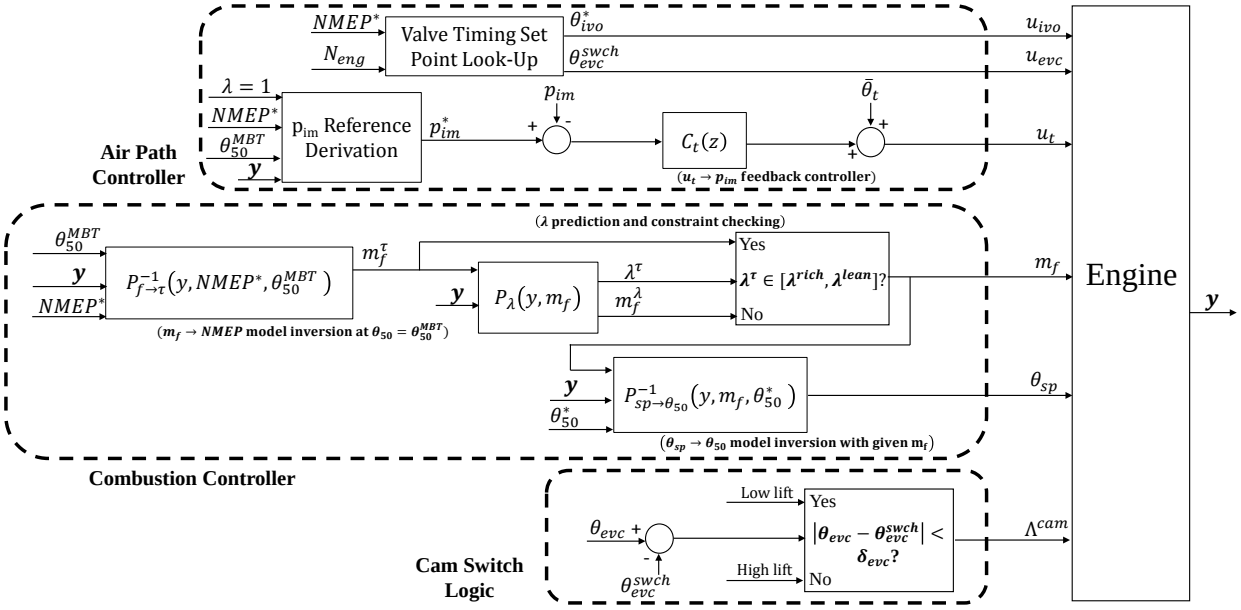

Figure 4.6: Block diagram of controller for SI phase of the transition. Variable names are as defined in Table 4.1. P blocks indicate calculations using the plant model, and C blocks indicate output feedback controllers.

4.2.2 Air path control

The overall architecture of the air path control is:

- u_{ivo} is stepped to the set point θ^*_{ivo}, which is calibrated for optimal low lift breathing and is stored in a look-up table versus engine speed.
- u_{evc} is stepped to the set point θ^{swch}_{evc}, which is calibrated to give a favorable starting point for the HCCI combustion when the exhaust cam is switched to low lift. It is stored in a look-up table versus engine speed and load.
- u_t is commanded through a linear feedback controller $C_t(z)$ to track a time-varying reference intake manifold pressure p^*_{im}.
- The reference p^*_{im} is derived from a model-based calculation to achieve $NMEP = NMEP^*$ under the constraints $\lambda = 1$ and $\theta_{50} = \theta^*_{50,S}$ with one step look-ahead valve timing disturbances.

The purpose of the IVO reference θ^*_{ivo} is to adjust the IVO timing for maximum air flow when HCCI is entered, in order to combat the high in-cylinder temperatures which can arise from the high SI exhaust temperatures and cause early combustion phasing as discussed in Sec. 4.1.2. The θ^{swch}_{evc} set point represents a key calibration factor, as it defines what the EVC timing will be on cycle *HCCI 0* through the high lift - low lift cam profile offset (see Fig. 2.2). This affects the EVC timing not only *HCCI 0*, but several cycles thereafter due to the cam phasing actuator dynamics. The EVC timing plays a large role in the first few HCCI cycles of the transition, because the exhaust temperature initially comes from SI combustion and so is much higher than that of HCCI, so that the trapped residual mass has a large effect on the in-cylinder temperature and combustion phasing. The motivation for the simple step commands for u_{ivo} and u_{evc} is to phase them to their desired HCCI entry points as quickly as possible, in order to minimize the time required to reach HCCI. This also results in a simple structure which requires specification of only set points as opposed to actuator sequences or possibly additional feedback control elements.

The intake manifold pressure reference p^*_{im} and throttle tracking controller $C_t(z)$ are meant to adjust u_t throughout the SI phase to compensate for the disturbance of the valve timing changes to the engine air flow. The reference p^*_{im} is estimated from the SI combustion model such that the resulting air flow is predicted to give $NMEP = NMEP^*$ when the stoichiometric amount of fuel is injected ($\lambda = 1$) and θ_{50} is at its reference. Thus, for perfect p^*_{im} tracking, the model predicts that torque can perfectly be maintained with a stoichiometric AFR. To assist the throttle in leading the valve timing disturbances, the θ_{evc} and θ_{ivo} values fed to the p^*_{im} calculation are first propagated one sample time ahead, using the identified second order actuator dynamics models of Sec. 2.2.3 discretized at the sampling frequency:

$$\theta^{k+1} = b_1 u^k - (a_1 \theta^k + a_0 \theta^{k-1}) \tag{4.1}$$

where $\theta^k,\ \theta^{k-1}$ are the current and previous valve timing measurements, u^k is the valve timing command, and the coefficients $a_1,\ a_0,\ b_1$ come from discretization of the continuous second order dynamics and are based on $\zeta,\ \omega_n$, and the sample period.

The throttle controller $C_t(z)$ is designed as a linear lead filter,

$$C_t(z) = k_t \frac{z + n_t}{z + p_t} \tag{4.2}$$

where k_t, n_t, and $p_t < n_t$ are the gain, zero, and pole, respectively. The linearity of the controller is justified given that the throttle orifice profile and manifold dynamics are strongly linear in the lower SI load range where it is possible to switch to HCCI, where the throttle position remains until it is commanded wide-open. The lead filter structure is chosen in order to follow the high frequency content in the p_{im}^* profile, which changes quickly as the valve timings change. The steady-state error of the controller suffers, however it is not as important because the SI phase of the transition does not dwell at steady-state; as soon as the desired HCCI entry point is reached, the cams are switched and SI phase terminates. The controller parameters $k_t,\ n_t,\ p_t$ are initially estimated from a linearized and discretized version of the air path model, however they are ultimately tuned in experiment. The set point $\bar{\theta}_t$ for the controller is taken equal to the throttle set point in nominal SI operation for simplicity.

The reference p_{im}^* is derived from an inversion of the SI combustion model using the current measurements y defined in Table 4.1 under the constraints that $NMEP = NMEP^*$, $\theta_{50} = \theta_{50}^*$, and $\lambda = 1$. The derivation starts with the model's gross cycle work calculation (2.59). This expression can be simplified using the expressions for polytropic compression and expansion

$$p_{bc} = p_{ivc} \left(\frac{V_{ivc}}{V_{cmb}} \right)^{n_c} := b_1 p_{ivc} \tag{4.3}$$

$$p_{evo} = p_{ac} \left(\frac{V_{cmb}}{V_{evo}} \right)^{n_e} := b_2 p_{ac} \tag{4.4}$$

where the V_{ivc} and V_{evo} are evaluated with the measured valve timings, and V_{cmb} is calculated from the definition of θ_{cmb} in Eq. (2.44). Substituing into (2.59),

$$W_{cig} = p_{ivc} \frac{b_1 V_{cmb} - V_{ivc}}{1 - n_c} + p_{ac} \frac{b_2 V_{evo} - V_{cmb}}{1 - n_e} \tag{4.5}$$

$$:= c_1 p_{ivc} + c_2 p_{ac} \tag{4.6}$$

From Eq. (2.49), (2.48),

$$p_{ac} = p_{bc} \left(\frac{T_{ac}}{T_{bc}} \right) = b_1 p_{ivc} \left(\frac{T_{bc} + \frac{m_f Q_{lhv}}{c_v m_c}}{T_{bc}} \right) \tag{4.7}$$

Substituting Eqs. (2.39), (2.47) into (4.7), the expression can be shown to reduce to

$$p_{ac} = b_1 p_{ivc} + \frac{m_f Q_{lhv} R}{c_v V_{cmb}} := b_1 p_{ivc} + c_3 \tag{4.8}$$

Substituting back into Eq. (4.6) gives,

$$W_{cig} = c_1 p_{ivc} + c_2(c_1 p_{ivc} + c_3) \tag{4.9}$$

Now write from Eqs. (2.60), (2.61),

$$W_{cig} = (NMEP - (p_{im} - p_{em}))V_d \tag{4.10}$$

and combine Eqns. (2.40), (2.37), (2.35) to write

$$m_f = \frac{m_a}{\lambda AFR_s} = \frac{W_{cyl}}{\lambda AFR_s}\frac{120}{N_{eng}N_{cyl}} := \frac{1}{c_4}\alpha_1 p_{im} + \alpha_0 \tag{4.11}$$

Finally, apply the constraints

$$NMEP = NMEP^* \tag{4.12}$$

$$\theta_{50} = \theta_{50}^* \tag{4.13}$$

$$\lambda = 1 \tag{4.14}$$

in Eqs. (4.10), (4.8), (4.11) and substitute into Eq. (4.9) with the relation (2.41) for p_{ivc}. This allows $p_i m$ to be isolated, giving the expression for p_{im}^*,

$$p_{im}^* = \frac{(NMEP^* + p_{em})V_d - (\beta_0 c_1 + \beta_0 c_2 b_1 + c_2 c_3 \alpha_0/c_4)}{c_1\beta_1 + c_2 b_1 \beta_1 + c_2 c_3 \alpha_1/c_4 + V_d} \tag{4.15}$$

where the β_i coefficients come from Eq. (2.41) and p_{em} is approximated at atmospheric pressure. In the reparameterized model for the replica engine which will provide the experimental apparatus for implementation of the SI-HCCI controller, p_{ivc} is approximated $\approx p_{im}$, in which case Eq. (4.15) reduces to

$$p_{im}^* = \frac{(NMEP^* + p_{em})V_d - c_2 c_3 \alpha_0/c_4}{c_1 + c_2 b_1 + c_2 c_3 \alpha_1/c_4 + V_d} \tag{4.16}$$

4.2.3 Combustion Control

The overall architecture of the combustion control is:

- m_f is calculated to give $NMEP = NMEP^*$ assuming $\theta_{50} = \theta_{50,S}^*$ while maintaining $\lambda \in [\lambda^{rich}, \lambda^{lean}]$ through a nonlinear model inversion. If the required m_f value for torque tracking violates the AFR constraints, m_f is chosen on the boundary of the AFR constraints.
- θ_{sp} is calculated to give $\theta_{50} = \theta_{50,S}^*$ through a nonlinear model inversion.

The idea behind the combustion control structure is to use model inverse-base calculations to cancel any disturbances to the performance outputs which result from valve timing changes and imperfect

air path control performance throughout the transition. The model inverse nature of the control laws is advantageous due to the relative degree 0 relationship between the combustion actuators and performance variables, which allows the outputs to be adjusted to their reference without any dynamics for immediate compensation for disturbances. Moreover, the controller need only invert static functions as opposed to system dynamics.

The m_f control input calculation is structured to take into account both torque tracking and the AFR constraints. The fuel quantity m_f^τ to attain $NMEP = NMEP^*$ with $\theta_{50} = \theta_{50,S}^*$ is first evaluated by inverting the $m_f \rightarrow NMEP$ relationship with the measured intake conditions and valve timings, signified by $P_{f-\tau}$ in Fig. 4.6. The AFR that will result with $m_f = m_f^\tau$ is then calculated using Eq. (2.40),

$$\lambda^\tau = \frac{m_a}{m_f^\tau AFR_s} \tag{4.17}$$

where m_a is the estimated air mass based on measured intake and valve conditions. Finally the m_f value is selected from the following logic, in order to enforce AFR constraints:

$$m_f = \begin{cases} \frac{m_a}{\lambda^{lean} AFR_s}, & \lambda^\tau > \lambda^{lean} \\ \frac{m_a}{\lambda^{rich} AFR_s}, & \lambda^\tau < \lambda^{rich} \\ m_f^\tau, & else \end{cases} \tag{4.18}$$

where the relation $\frac{m_a}{\lambda AFR_s}$ evaluates the fuel quantity necessary to enforce the λ constraints, denoted m_f^λ in Fig. 4.6.

The derivation of m_f^τ is similar to the derivation of p_{im}^* in that it involves an inversion of the SI combustion model subject to certain constraints, but now the constraints change to $NMEP = NMEP^*$ and $\theta_{50} = \theta_{50,S}^*$ without the $\lambda = 1$ constraint, and p_{im} is taken at its measured value p_{im}^y. Eq. (4.11) is also omitted. Substituting for c_3 from Eq. (4.8) into Eq. (4.9) allows m_f to be isolated

$$W_{cig} = c_1 p_{ivc} + c_2(c_1 p_{ivc} + \frac{m_f Q_{lhv} R}{c_v V_{cmb}}) \tag{4.19}$$

Substituting the definitions of $c_1,\ c_2$ from Eq. (4.6) along with Eq. (4.10) into Eq. (4.19), and finally setting $p_{ivc} = \beta_1 p_{im}^y + \beta_0$, the result for m_f^τ is

$$m_f^\tau = \frac{c_v V_{cmb}(\theta_{50,S}^*)}{Q_{lhv} R}((NMEP^* - (p_{im}^y - p_{em}))V_d - (\beta_1 p_{im}^y + \beta_0)c_1(1 + c_2)) \tag{4.20}$$

where the constraints $NMEP = NMEP^*$ and $\theta_{50} = \theta_{50,S}^*$ have been imposed. Again it is easy to see how this equation simplifies when p_{ivc} is approximated $\approx p_{im}$ by setting $\beta_1 = 1, \beta_0 = 0$.

The θ_{sp} input comes from a direct inversion of the model's θ_{50} correlation. The SI-HCCI transition strategy of Sec. 4.1.3 assumes that the SI mode operates with a low lift intake cam,

and so the result will be derived for the reparameterized θ_{50} correlation in Appendix A.1 which is developed for low lift intake SI operation. Choosing the coefficients

$$A_2 = a_2 \tag{4.21}$$

$$A_1 = a_3 \tag{4.22}$$

$$A_0 = a_1 m_f + a_4 \theta_{evc}^2 + a_5 \theta_{evc} + a_6 \lambda'^2 + a_7 \lambda' + a_8 - \theta_{50,S}^* \tag{4.23}$$

where a_i represent parameters in the θ_{50} correlation Eq. (A.4), the correlation can be arranged into a quadratic function of spark timing

$$A_2 \theta_{sp}^2 + A_1 \theta_{sp} + A_0 = 0 \tag{4.24}$$

whose solution gives $\theta_{50} = \theta_{50,S}^*$. The maximum root (in units of aTDC) is chosen as the correct root because inspection shows that the minimum root occurs unreasonably early spark timings after the quadratic dependence on θ_{sp} shifts inflection. Note that to carry out this calculation, λ' must first be calculated using measured inputs in Eq. (A.5) which also depend on Eqs. (2.37), (2.38). Also note that the θ_{sp} input is calculated after the m_f input due to the dependence of the θ_{50} correlation on m_f.

While the model inverse-based control laws employed here are advantageous for immediate compensation of disturbances and retaining accuracy of the full nonlinear model, they still lack a direct means to account for modeling error. Direct output feedback control for compensation of model errors becomes difficult for the m_f control loop, because its output variable can change back and forth between $NMEP$ and λ during the transition. Also, the transport delay and sensor dynamics of the λ measurement are almost as long as the entire SI phase of the transition. For the θ_{sp} control loop, on the other hand, direct output feedback compensation is more readily implemented, given that the input-output coupling is solely to θ_{50} which is available on a cycle by cycle basis through in-cylinder pressure measurements. Despite this fact, in the control architecture presented here, no measures were taken to apply $\theta_{sp} \rightarrow \theta_{50}$ output feedback compensation. The reason is that in the SI phase of the SI-HCCI transition, the transient in the in-cylinder conditions was generally observed to be fairly mild, so that a wide margin of error was allowable for the $\theta_{sp} \rightarrow \theta_{50}$ without the combustion experiencing any significant deleterious effects. The main concern for the accuracy of the spark timing control will instead come in the HCCI-SI direction, where the θ_{50} reference to the spark timing control will become time-varying as will be discussed in Ch. 6. In this case, efforts at implementing direct cylinder pressure output feedback for the spark timing gave poor results, because the feedback design was chosen following the internal model control scheme which will shortly be proposed for HCCI combustion control in Sec. 4.3.2. This design could not respond quickly enough to the rapid time variation in the spark timing's θ_{50} reference trajectory.

However, the opportunity still exists to apply a standard output feedback compensator architecture which is additive with the spark timing model-inverse control calculation, e.g. a PI controller whose input command is added to the model-inverse command for a simple example. Exploring this kind of design option is an open opportunity for future work. For the control architecture of this dissertation, measurements will be used in the SI phase combustion control to attenuate model error in an adaptive online parameter update scheme, instead of for direct output compensation. The mentioned parameter update scheme will be the subject of Ch. 5.

4.2.4 Cam Switching Logic and the Final SI Cycle

The dominant factor responsible for initiating HCCI is the EVC timing, as it determines the trapped residual which is the main thermal actuator to enable auto-ignition. Hence, the decision to switch the exhaust cam profile Λ^{cam} to low lift exhaust and engage HCCI is based on the simple logic of θ_{evc} being within some window δ_{evc} of θ_{evc}^{swch}. The tolerance δ_{evc} is tuned to account for the delay in the cam profile switching mechanism, which for the experimental two-stage cam mechanism is on the order of 1-2 cycles.

When the decision to switch to HCCI occurs, several other modifications are made to ease the transition to ease the first HCCI cycles. One is to command the throttle to wide-open in advance of the cam switching time, following the actuator strategy depicted in Fig. 4.4. This is done by setting $\bar{\theta}_t = 100$ when there are N_{pre}^{WOT} time steps left before the first low lift breathing event, where N_{pre}^{WOT} is a calibration parameter. Additionally, the m_f control is modified to bypass the calculation of m_f^τ and exclusively track a user defined AFR set point λ^{PS}, which enables leaning of the final SI cycle for reduced exhaust temperature and torque compensation of the shifting EVO timing. The λ^{PS} value must be balanced with catalyst oxygen fill-up, however.

4.2.5 Controller Tuning Variables

To summarize the calibration requirements for the SI phase controller, the controller tuning variables are collected in Table 6.4. The Table clearly shows that calibration variables include only a handful of gains and set points, as opposed to entire actuator sequences. Moreover, many of the set points are intuitive to tune and fall in a small feasible range, e.g. $N_{pre}^{WOT} \in \{0, 1, 2, 3, 4, 5\}$, $\lambda^{rich} \in [.95, 1]$, $\lambda^{lean} \in [1, 1.05]$, etc. It is reasonable to assume that the $\theta_{50,S}^*$ and θ_{ivo}^* set points can be taken from the baseline engine calibration, which reduces the number of tuning variables even further.

Type	Symbol	Description
Gains	$k_t,\ n_t,\ p_t$	Gain, zero, and pole of throttle controller
Set Points	θ_{evc}^{swch}	θ_{evc} at HCCI switch point
	N_{pre}^{WOT}	Number of time steps prior to cam switch that throttle is commanded open
	λ^{PS}	λ set point for lean final SI cycle
	$\lambda^{rich}/\lambda^{lean}$	Rich/lean λ bounds
	$\theta_{50,S}^{*}$	θ_{50} set point in SI
	θ_{ivo}^{*}	θ_{ivo} set point for optimal low lift breathing
	δ_{evc}	θ_{evc} tolerance for switching to HCCI

Table 4.2: Tuning variables of SI phase controller.

4.3 HCCI Phase Controller

4.3.1 Control Problem Overview

The HCCI phase of the SI-HCCI transition presents the problem of recovering from an unfavorable initial condition to reach a desirable operating point while mitigating disturbances to the performance variables throughout. The main unfavorable aspects of the initial condition are a higher exhaust temperature and later EVC timing than any value that can be reached in nominal HCCI operation. For the first few cylinders entering HCCI, the intake manifold pressure may be subatmospheric as well due to air path dynamics, even though the throttle is opened prior to to switching to HCCI (see Sec. 4.2.4. While the HCCI phase carries out, the controller should target two main objectives, based on the performance criteria in Sec. 1.1.3:

- Deviations of the engine torque from the driver demand should be minimized as per performance objective 1.
- Combustion phasing should be kept late enough to minimize pressure rise rate excursions beyond the desired threshold and early enough to avoid combustion instability/misfire based on performance objectives 1 and 2. Misfire can also lead to unacceptably high hydrocarbon emissions and violate perforamnce objective 2.

Note that no AFR objective is specified because it is assumed that the HCCI AFR is always lean, though in general the controller should prevent rich AFRs in HCCI should such conditions arise.

As depicted in Fig. 4.4, when HCCI is engaged, the throttle is commanded wide-open and the spark timing is placed very late so as not to interact with combustion, eliminating u_t and θ_{sp} from the set of control inputs. Moreover, θ_{ivo} is kept constant at the optimal breathing condition θ_{ivo}^{*} to which it was commanded in the SI phase of the transition, and so it too requires no control consideration. On the other hand, the SOI timing, which was unused in SI, now becomes and important actuator. Additionally, the combustion model from Sec. 2.4 now involves states for cycle to cycle couplings, which must be considered in model-based control laws.

Considering the changes to the control objectives, control inputs, and model topology in the HCCI phase of the transition, the control problem is formulated according to the logic in Table 4.3.

Torque and combustion phasing are taken as performance variables to be tracked to a specified reference and are again characterized by $NMEP$ and θ_{50}, respectively. The feedback variables y now include $NMEP$ and θ_{50}, which are assumed to be available from an in-cylinder pressure measurement. These variables will be used in the HCCI phase for output feedback control and observer-based estimation of the combustion model states of blowdown temperature T_{bd}, burned gas fraction b_{bd}, and fuel mass fraction f_{bd}, as these cannot be measured. The input saturation limits for u_{evc} now change to represent the range of feasible timings with the low lift exhaust profile. The lower saturation limit of θ_{soi} is allowed as late as 180° bTDC on cycle *HCCI 0* to compensate for the high residual temperature carried over from SI; this was found to have minor but non-negligible effect on retarding the combustion phasing on the first HCCI cycle, which may be due to the very high recompression temperature carried over from SI that was explored in Sec. 3.1 amplifying reaction rates with fuel pyrolysis or reforming. To prevent potential emissions issues associated with late injection and reduced time for homogeneous mixing, the θ_{soi} late saturation limit is fixed at 280° bTDC on all other cycles besides *HCCI 0*, where its authority on θ_{50} tends to diminish in nominal HCCI operation. This extension of the lower θ_{soi} saturation limit on cycle *HCCI 0* conveys that θ_{soi} input constraints are a major concern in the HCCI phase of the transition in that they limit the ability of θ_{soi} to compensate for disturbances to combustion phasing.

Control Inputs	$u = \begin{bmatrix} u_{evc} & m_f & \theta_{soi} \end{bmatrix}^T$
Feedback Variables	$y = [NMEP \;\; \theta_{50} \;\; p_{im} \;\; T_{im} \;\; \theta_{ivo} \;\; \theta_{evc} \;\; N_{eng}]^T$
Performance Variables	$w = \begin{bmatrix} NMEP & \theta_{50} \end{bmatrix}^T$
λ Rich Bound	$\lambda > \lambda_{min}$
Reference Commands	$r = \begin{bmatrix} NMEP^* & \theta^*_{50,H} \end{bmatrix}^T$
Input Lower Bounds	$u_{low} = \begin{bmatrix} -120 & 5 & 180/280 \end{bmatrix}^T$
Input Upper Bounds	$u_{high} = \begin{bmatrix} -20 & 50 & 390 \end{bmatrix}^T$
Model States	$x = \begin{bmatrix} p_{im} & \theta_{evc} & \dot{\theta}_{evc} & T_{bd} & b_{bd} & f_{bd} \end{bmatrix}^T$

Table 4.3: Control problem formulation for HCCI phase of SI-HCCI transition.

A block diagram of the control architecture for the HCCI phase of the SI-HCCI transition is shown in Fig. 4.7, where $\hat{x}_c = \begin{bmatrix} \hat{T}_{bd} & \hat{b}_{bd} & \hat{f}_{bd} \end{bmatrix}$ denotes estimates of the combustion model states. Notice in the diagram that θ_{evc} is governed by a simple step command to a set point as in the SI phase of the transition. The symbol θ^*_{evc} denotes the nominal HCCI θ_{evc} set point for the given speed and load. The logic behind this step command is to quickly advance the EVC timing to its HCCI set point after cycle *HCCI 0*, in order to increase trapped residual to compensate for the fast decay of exhaust temperature on the first few HCCI cycles. A pre-step factor N^{EVC}_{pre} is included to allow the step command to be issued prior to switching to HCCI to give the EVC timing a "head start" in this regard. Given the simplicity of the EVC step command based control, the remainder of the discussion focuses on the combustion control.

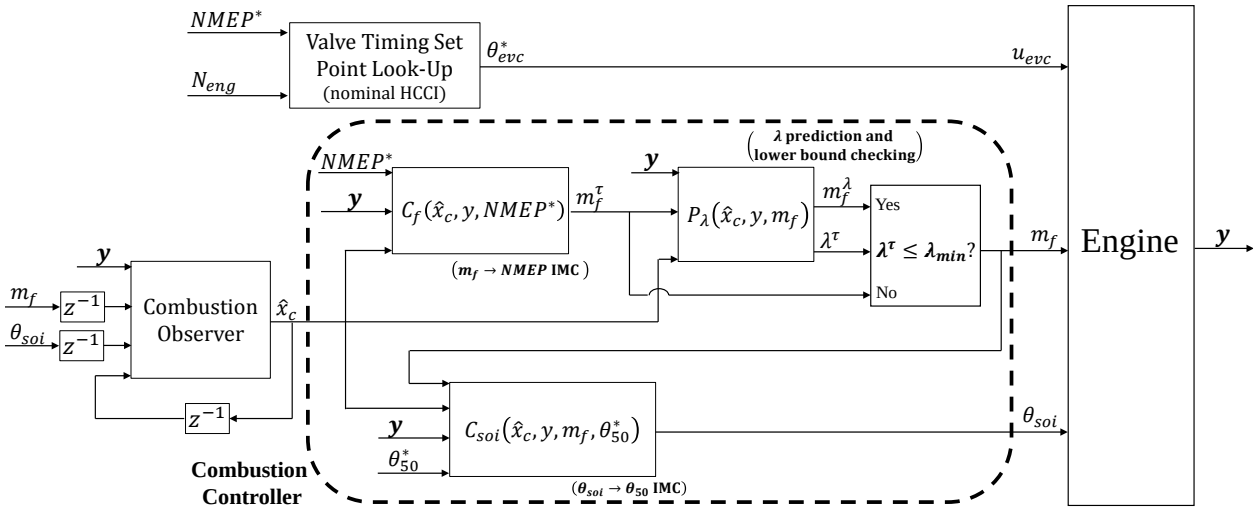

Figure 4.7: Block diagram of controller for HCCI phase of the transition. Variable names are as defined in Table 4.3 with x_c representing combustion states. P blocks indicate calculations using the plant model, and C blocks indicate output feedback controllers.

4.3.2 Combustion Control

The overall architecture of the combustion control is:

- m_f tracks $NMEP = NMEP^*$ through a nonlinear internal model controller assuming $\theta_{50} = \theta^*_{50,H}$. If the required fuel quantity for $NMEP = NMEP^*$ causes $\lambda < \lambda_{min} \approx 1$, the fuel is calculated to fulfill $\lambda = \lambda_{min}$.
- θ_{soi} tracks $\theta_{50} = \theta^*_{50,H}$ through a nonlinear internal model controller

Like the SI phase, the combustion control architecture for the HCCI phase is based on relative degree 0 nonlinear model inverse calculations. The main difference is that corrective combustion output feedback for attenuation of model error is incorporated through the internal model control (IMC) structure. Inclusion of combustion output feedback is more prudent for the HCCI phase because the combustion is more sensitive than SI combustion so that modeling errors have a larger effect, and in general the HCCI phase experiences a more severe transient than the SI phase with the strategy of Sec. 4.1.3 so that corrective output feedback compensation can have a greater impact. Additionally, combustion output feedback control is easier to implement for the HCCI fuel controller than for the SI counterpart, as the lower λ bound is rarely encountered and so the output can be taken to be solely $NMEP$. Lastly, since HCCI is the destination mode of the transition, steady-state tracking and disturbance attenuation become more pertinent than for the SI phase, which are aided by combustion output feedback.

The IMC structure by which combustion output feedback is incorporated is depicted in general form in Fig. 4.8. In the diagram, P represents the true plant and $\tilde{P}$ the modeled approximation, while $Q(z)$ represents a linear low pass filter included to keep the inversion $\tilde{P}^{-1}$ causal. The basic

idea behind the controller structure is that when the model is perfect, $\tilde{P} = P,\ \tilde{y}_{IMC} = y_{IMC}$, then the output feedback does nothing and the controller is left to perfectly invert the plant model. When $\tilde{P} \neq P,\ \tilde{y}_{IMC} \neq y_{IMC}$, then the output feedback modifies the reference signal for the inversion until the measured output tracks the predicted output. This structure was chosen because it only intervenes with corrective output feedback when it detects a model prediction error, so that if the model inverse calculations are ideal and generate outputs that are close to the expected value, the output feedback does not induce additional control effort. This was found to be especially helpful for combustion phasing control on the first few HCCI cycles of SI-HCCI transitions, where combustion phasing often became early due to high exhaust temperature, even with a saturated θ_{soi} command. Because the model prediction of IMC acknowledged an expected early θ_{50} timing on these cycles, unwanted control effort was not generated which could interfere with the model inverse cancellation of disturbances. The IMC structure also offers several favorable theoretical properties, such as guaranteed zero-offset steady-state tracking and closed-loop stability within a sufficient model error tolerance [66]. A technical note is that the low pass filter $Q(z)$ is not strictly necessary to keep the control system causal because of its relative degree 0 nature, however a first order low pass filter is still included in order to smooth the controller response and reduce sensitivity to noise.

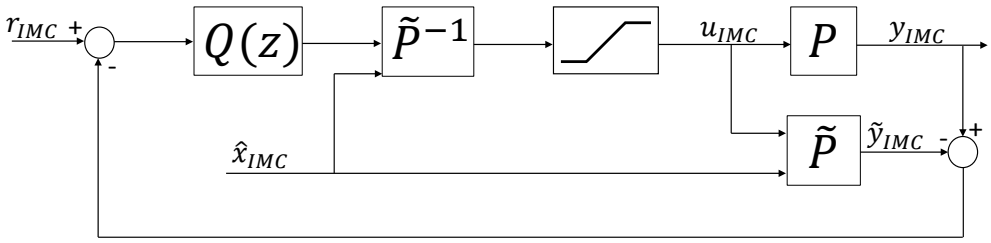

Figure 4.8: Diagram of IMC structure. $Q(z)$ represents a linear low pass filter, and P and $\tilde{P}$ represent the true and controller model of the plant.

The model inverse calculation for the m_f IMC loop is derived from an inversion of the HCCI torque model with respect to fuel using the measured intake conditions and valve timings and estimated combustion states, following a similar procedure to that for m_f^τ in the SI phase controller. The equation for the gross cycle work is given by Eq. (2.59), and the constraint equations $NMEP = NMEP^*$ and $\theta_{50} = \theta_{50,H}^*$ are imposed. The main difference in solving for m_f is caused by the appearance of the combined thermal and combustion efficiency η_λ in Eq. (2.92), so that the equivalent of Eq. (4.19) takes the form

$$W_{cig} = c_1 p_{ivc} + c_2 (c_1 p_{ivc} + \frac{m_f Q_{lhv} R}{c_v V_{cmb}} \frac{a_{\eta 1} \lambda_c + a_{\eta 2}}{\lambda_c + a_{\eta 3}}) \tag{4.25}$$

where $a_{\eta i},\ i = 1, 2, 3$ are coefficients in the η_λ expression (2.93) and all intermediate quantities b_i, c_i are as defined in Sec. 4.2.2. Evaluating m_a and m_r with the current state estimates and

measured quantities and substituting in for λ_c, it can be shown that Eq. (4.25) reduces to a quadratic polynomial in m_f

$$B_2 m_f^2 + B_1 m_f + B_0 = 0 \tag{4.26}$$

with the following coefficients

$$B_2 = a_{\eta 2} \tag{4.27}$$

$$B_1 = \frac{a_{\eta 1}(m_a + m_r)}{AFR_s} - \frac{d_2 a_{\eta 3}}{d_1} \tag{4.28}$$

$$B_0 = -\frac{d_2(m_a + m_r)}{d_1 AFR_s} \tag{4.29}$$

where

$$d_1 := \frac{Q_{lhv} R V_{cmb} (\theta_{50}^*)^{n_c - 1}}{c_v p_{ivc} V_{ivc}^{n_c}} \tag{4.30}$$

$$d_2 := \frac{(NMEP^* - P\bar{M}EP)V_d - c_1 p_{ivc}}{c_2 b_1 p_{ivc}} - 1 \tag{4.31}$$

and hence can be readily solved for m_f with p_{ivc} obtained from the measured p_{im}. The maximum root of the quadratic equation is selected, as the minimum root tends to be negative which is not physical.

Note that to maintain the decentralized m_f/θ_{soi} structure, the assumption that the θ_{soi} controller maintains $\theta_{50} = \theta_{50,H}^*$ is necessary to decouple the torque from the combustion phasing. This is a good assumption for most of the HCCI phase of the transition, however its validity can weaken on cycle *HCCI 0* of the transition and possibly a few thereafter due to high residual temperatures advancing the combustion phasing beyond the authority of θ_{soi} to compensate. Such early combustion phasing can cause a reduction in torque if the m_f controller assumes $\theta_{50} = \theta_{50,H}^*$. For this reason, the combustion phasing decoupling assumption is modified to $\theta_{50} = \theta_{50,f}^0$ on cycle *HCCI 0*, where $\theta_{50,f}^0$ is tuned to be earlier than $\theta_{50,H}^*$ to alert the fuel control loop to compensate for the effect on the torque. On all other cycles the decoupling assumption remains unchanged.

The model inverse calculation for the θ_{soi} IMC loop is derived by solving for the θ_{soi} timing to make the Arrhenius threshold of the HCCI combustion model perfectly match the integrated Arrhenius rate when $\theta_{50} = \theta_{50,H}^*$. The calculation begins by first solving Eq. (2.91) for the SOC timing that results in the reference $\theta_{50,H}^*$,

$$\theta_{soc}^* = (\theta_{50} - a_{soc,0})/a_{soc,1} \tag{4.32}$$

where $a_{soc,i}$ come from Eq. (2.91). The Arrhenius rate integral in Eq. (2.87) is then evaluated up to θ_{soc}^* using the p_{ivc} and T_{ivc} values estimated from the current state estimates and measurements.

This gives the value of the Arrhenius threshold to perfectly match the desired ignition timing for the current estimates of the in-cylinder conditions, K^*_{th}:

$$K^*_{th} = \int_{\theta_{ivc}}^{\theta^*_{soc}} \frac{1}{\omega} p_c(\theta)^{n_p} e^{\left(\frac{-E_a}{RT_c(\theta)}\right)} d\theta \tag{4.33}$$

where p_c and T_c are evaluated with Eq. (2.89). Finally, the appropriate θ_{soi} value to yield $K_{th} = K^*_{th}$ is solved from the Arrhenius threshold correlation,

$$\theta_{soi} = \frac{K^*_{th} - a_{02}\lambda_r^2 - a_{01}\lambda_r - a_{00} - a_T T_{rc}}{a_{12}\lambda_r^2 + a_{11}\lambda_r + a_{10}} \tag{4.34}$$

where the slightly simplified Arrhenius threshold correlation of the reparameterized model for the replica engine Eq. (A.9) has been used, because the SI-HCCI control experiments are carried out on the replica engine.

Note that the evaluation of K^*_{th} in Eq. (4.33) requires iteration and is thus computationally intensive. To facilitate real-time implementation, p_{ivc} and ω are factored out of the Arrhenius integral to give

$$\frac{K^*_{th}\omega}{p_{ivc}^{n_p}} = \int_{\theta_{ivc}}^{\theta^*_{soc}} \left(\frac{V_{ivc}}{V(\theta)}\right)^{n_c n_p} e^{\left(\frac{-E_a}{RT_c(\theta)}\right)} d\theta \tag{4.35}$$

since p_{ivc} and N_{eng} are assumed constant during one cycle. The right-hand side of this equation can be solved as a function of T_{ivc} and θ^*_{soc} (neglecting the impact of IVC timing) and stored in a two-dimensional look-up table. The term $\frac{K^*_{th}\omega}{p_{ivc}^{n_p}}$ can then be solved for K^*_{th}, hence bypassing the iterative calculation in real-time.

Given that the HCCI combustion model is equipped with cycle to cycle dynamics, the stability of the combustion control is of concern, as opposed to the SI combustion model which contains no dynamics and hence cannot be unstable. To check the stability of the HCCI internal model combustion control, a linear analysis is performed at several operating conditions which span the load range of HCCI on the experimental engine at the parameterized engine speed of 2000 RPM. The analysis is carried out on a single input-single output basis, neglecting cross couplings between the $\theta_{soi} \rightarrow \theta_{50}$ and $m_f \rightarrow NMEP$ loops. To corroborate the validity of the linear analysis, the output and state response of the linearized model about one considered operating point is compared to the response of the full nonlinear model for moderate input steps over a range of 30° θ_{soi} and 1 mg m_f in Fig. 4.9.

Being that the IMC structure is always stable when the controller model matches the true plant, error is introduced between the approximate model $\tilde{P}$ and true plant model P in the IMC diagram 4.8. The introduced error is based on the difference between the baseline combustion model parameters, and those obtained after application of an adaptive parameter update law in engine experiments, which will be covered in Chapter 5. The error thus represents a parametric uncertainty,

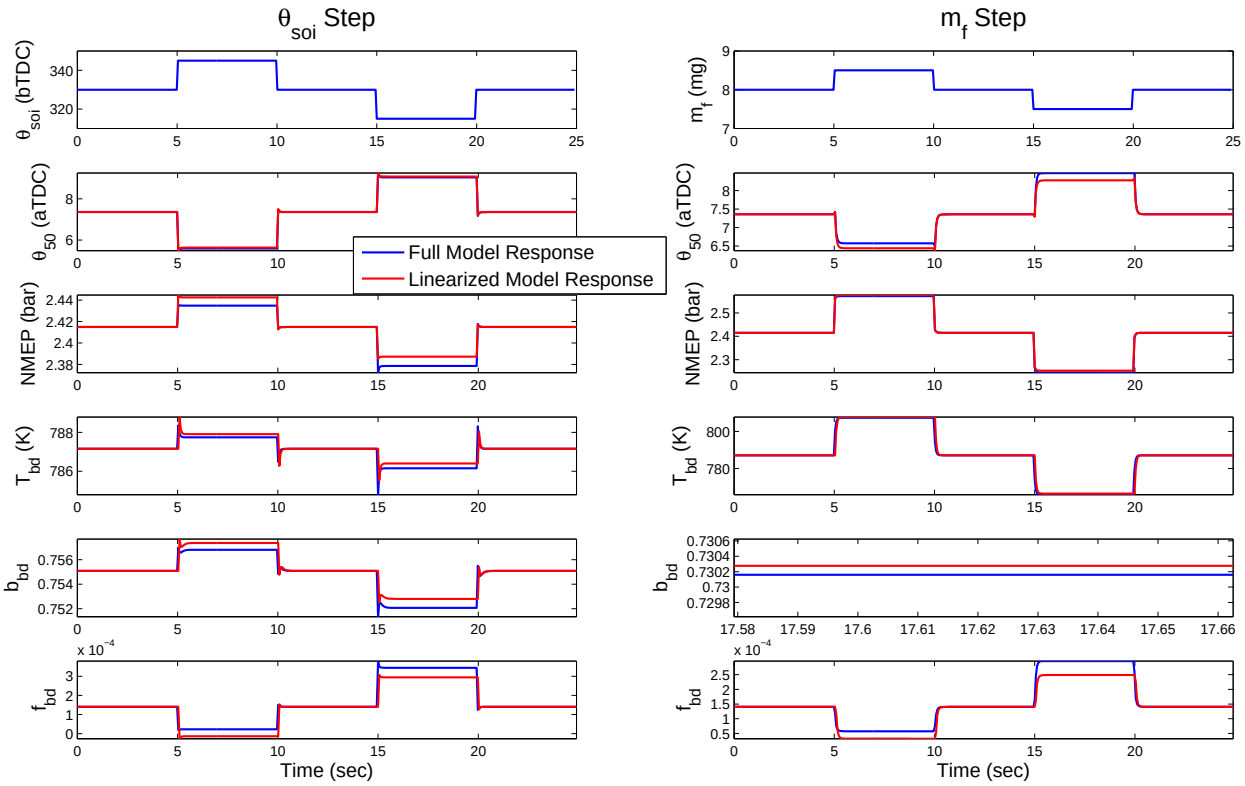

Figure 4.9: Linearized versus full nonlinear HCCI model input and state responses for steps of θ_{soi} (left) and m_f (right).

as opposed to a structural uncertainty. To analyze the stability of the perturbed plant/controller model system, the open-loop transfer function of the IMC structure in Fig. 4.8 is formed using the linearized models as

$$L(z) = Q(z)\tilde{P}^{-1}(z)(P(z) - \tilde{P}(z)) \tag{4.36}$$

where $P(z)$ and $\tilde{P}(z)$ are the linearized true and controller plant models, and $Q(z) = \frac{1-p_Q}{z-p_Q}$ is the first order IMC filter. The stability of the closed-loop system can then be analyzed by inspection of the frequency response of $L(z)$. Note that the values of $p_Q = 0.85$ for the $\theta_{soi} \rightarrow \theta_{50}$ loop and $p_Q = 0.8$ for the $m_f \rightarrow NMEP$ loop which were used in experimental implementation were chosen to form the respective open-loop transfer functions. Fig. 4.10 plots the frequency response of $L(z)$ for both the $\theta_{soi} \rightarrow \theta_{50}$ loop (top) and $m_f \rightarrow NMEP$ loop (bottom) for low (left), mid (center), and high (right) load linearization points. As can be seen, for the given plant/controller model perturbance, the stability margins of the control loops are very generous. This suggests that a significantly larger plant/controller model mismatch is tolerable by the controller, which is desirable for stability robustness. However, the effect of the combustion state estimator was left out of the

analysis, which can lead to significant reductions in stability margins. Structural uncertainties were also not considered. Thus, while the analysis method here displays encouraging results for controller robustness to basic parametric model uncertainty, further analysis would be necessary to definitively characterize the controller stability robustness.

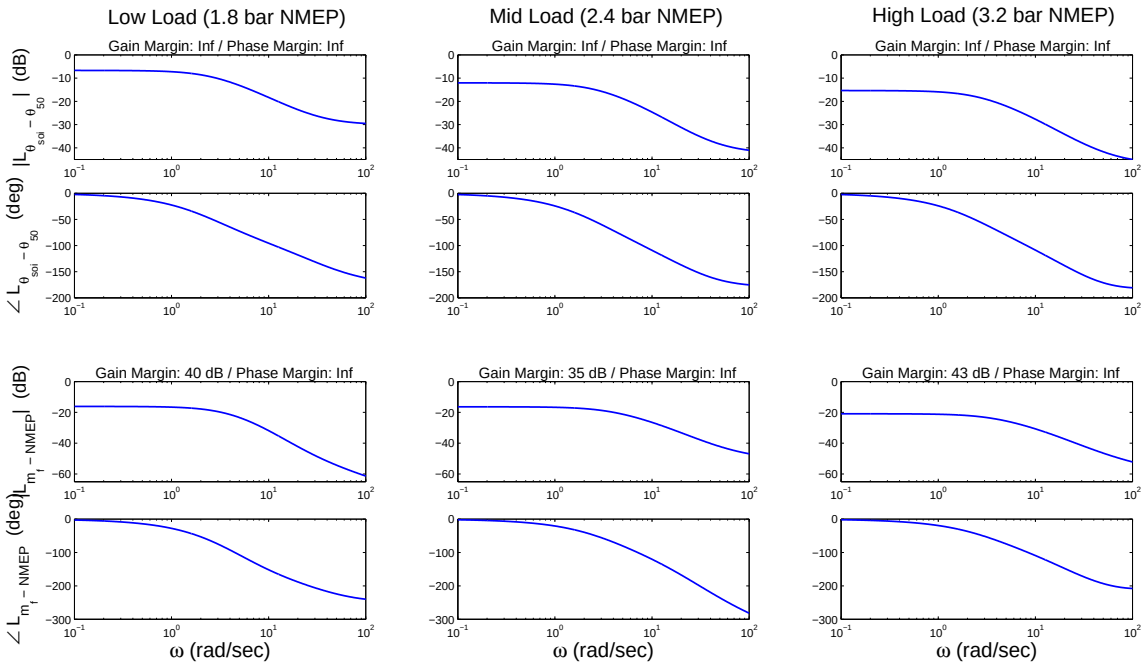

Figure 4.10: Frequency response of linearized IMC open-loop transfer function at low (left), mid (center), and high (right) load linearization points. Frequency response for $\theta_{soi} \rightarrow \theta_{50}$ open-loop transfer function shown in upper two subplots; Frequency response for $\theta_{soi} \rightarrow \theta_{50}$ open-loop transfer function shown in lower two subplots.

4.3.3 Combustion State Estimator

The dependence of the HCCI combustion control laws given in Sec. 4.3.2 on the HCCI model in-cylinder temperature and composition conditions indicates that combustion model states T_{bd}, b_{bd}, f_{bd} must be available to carry out the controller calculations. Because these states represent properties of the in-cylinder gases, they are not directly measurable, and so an observer is included for their estimation. The overall structure of the observer is to use the full nonlinear model in the prediction step of the estimation, while keeping a linear output injection

$$\hat{x}_c(k|k-1) = f(\hat{x}_c(k-1|k-1), u(k-1), y(k-1)) \tag{4.37}$$

$$\hat{x}_c(k|k) = \hat{x}_c(k|k-1) + L(w(k) - \hat{w}(k|k-1)) \tag{4.38}$$

where f represents the dynamics of the nonlinear combustion model, and L is the observer gain. Note that the combustion performance outputs w are used in the output injection as opposed to the entire output vector y defined in Table 4.3. A block diagram of the observer is shown in Fig. 4.11.

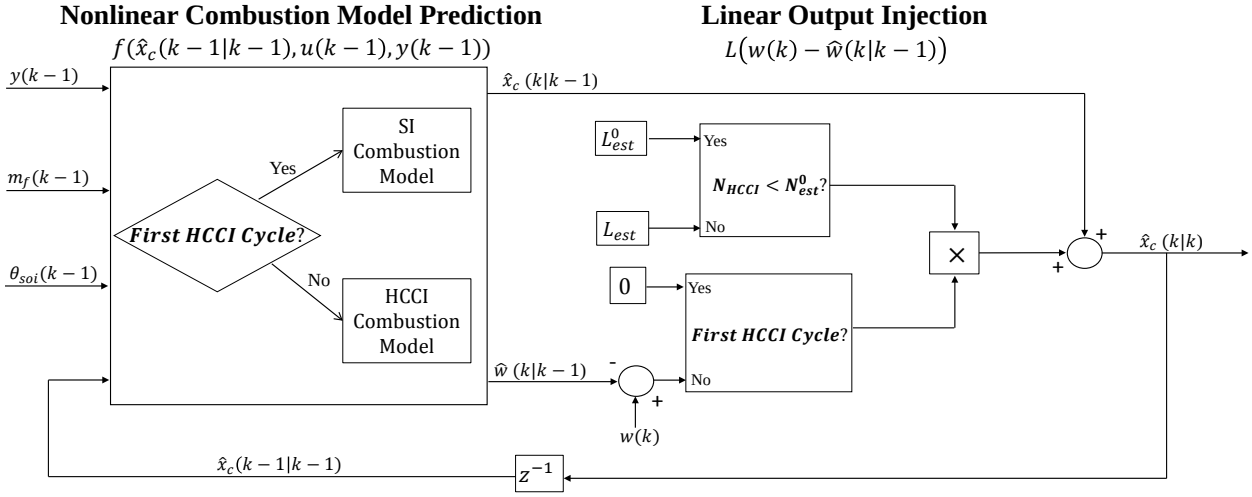

Figure 4.11: Diagram of HCCI combustion state estimator.

The idea behind the observer structure is that when first switching to HCCI, little combustion feedback information for the HCCI mode is accrued until several cycles elapse, starting from *HCCI 0* where there is none at all. Hence the model predictions are very important, and so the full nonlinear model is employed to carry out the prediction step for improved accuracy over a linearized prediction model. The output injection is kept linear mainly for ease of implementation, and is tuned with linear Kalman filter methodology to balance the trade off between process noise and measurement noise which both play an important role for the HCCI mode. Given the three combustion states and two combustion outputs, the Kalman filter covariance matrices have dimension $W_{est} \in \mathbb{R}^{3\times3}$ for process noise and $V_{est} \in \mathbb{R}^{2\times2}$ for measurement noise. Note that this simpler nonlinear prediction - linear output injection design was compared in SI-HCCI transition experiments with a more sophisticated unscented Kalman filter (UKF) design, and it was found that both designs produced similar output injection profiles and overall state estimates. Hence, experiments indicated that there was not much to be gained from the more computationally intensive UKF, and so the simpler design was kept.

The state estimation structure also includes several logical decisions as is apparent from Fig. 4.11. The first of these logical actions concerns the estimation on cycle *HCCI 0*, where the exhaust gas states are given not by the HCCI model, but by the SI model. If on cycle *HCCI 0*, the observer executes the SI combustion model to generate the prediction step estimates $\hat{x}_c(k|k-1)$, which is possible without any prior $\hat{x}_c$ estimates due to the static nature of the SI model. Additionally, the output injection is set to 0, because HCCI combustion feedback is not yet available ($w(k)$ comes

from SI). The last logical action involves switching of the observer gains between the values L_{est} and L^0_{est}, which is included as an optional design modification. The motivation for this modification is that, during the first few HCCI cycles, there is a large transient in the combustion dynamics with strong deterministic features. Hence the deterministic response of the system far outweighs stochastic disturbances from noise, and so measurements can be trusted more closely allowing for a higher observer gain. The observer gain L^0_{est} for the first N^0_{est} cycles is thus tuned to be more aggressive than the nominal observer gain L_{est}. In the experiments of this paper, L^0_{est} is generated simply by reducing the variance of the θ_{50} measurement in the Kalman filter V_{est} matrix. The logical implementation of the two observer gains corresponds a simple switch that activates the L^0_{est} gain if the number of cycles in HCCI N_{HCCI} is less than the pre-specified threshold N^0_{est}, chosen to be 5 in all cases.

4.3.4 Controller Tuning Variables

As was done for the SI phase controller, the tuning variables of the the HCCI phase controller are collected to convey calibration requirements and displayed in Table 4.3.4. As with the SI phase controller, the HCCI phase controller calibration involves tuning only several gains and set points, and again multiple set points are constrained to a small and intuitive tuning set (e.g. $N^{evc}_{pre} \in \{0,1,2,3,4\}$, $\theta^0_{50,f} \in [-10,0]$, $\lambda_{min} \in [1,1.05]$, etc.). Also, it is reasonable to assume that the nominal set points for HCCI EVC timing and θ_{50} θ^*_{evc} and $\theta^*_{50,H}$ come from the baseline engine calibration, in which case these variables need not be included in the HCCI phase controller calibration.

Type	Symbol	Description
Gains	p_f/p_{soi}	Pole of fuel/spark IMC filter
	$W_{est}, /V_{est}$	Kalman filter covariance matrices for combustion state observer
	$W^0_{est}, /V^0_{est}$	Kalman filter covariance matrices for optional more aggressive observer on first several HCCI cycles
Set Points	θ^*_{evc}	Nominal HCCI θ_{evc} set point
	N^{evc}_{pre}	Number of time steps prior to cam switch the θ_{evc} is commanded to θ^*_{evc}
	$\theta^*_{50,H}$	θ_{50} set point in HCCI
	$\theta^0_{50,f}$	Assumed θ_{50} in fuel IMC on cycle *HCCI 0*
	λ^{min}	Lower λ bound for lean HCCI operation

Table 4.4: Tuning variables of HCCI phase controller.

4.4 Experimental Results

The combined SI-HCCI control architecture described in Secs. 4.2, 4.3 is implemented on the second instance of the experimental SI/HCCI engine which was used to generate the transient data in Sec. 3.3. As noted in Sec. 3.3 and Appendix A, this second engine has the same geometry as in Table 2.1 but with a slightly modified compression ratio of 11.45:1. The reparameterized SI/HCCI combustion models based on the data from the replica engine given in Appendix A are used in the controller's model-based calculations. The controller is implemented using an ETAS ES910 rapid prototyping module to communicate with the engine control unit (ECU). The fuel used to carry out the mode transition experiments is a 93 anti-knock index (AKI) 10% ethanol pump gasoline. Because of its generic nature, the properties for the specific fuel batch used in the experiments could not be obtained; however, some properties for a similar batch of 93 AKI pump gasoline are listed in Table 4.4 which can be expected to be at least close to those of the experimental fuel batch. Note that no value for the sensitivity of the fuel was given; being that the fuel is gasoline, it is likely that its sensitivity is close to 8. In the SI-HCCI transition experiments, two of the four cylinders displayed unreasonable torque and AFR responses in HCCI mode (e.g. increases in indicated torque accompanied by decreases in AFR for constant fueling), which indicated possible fuel metering errors and/or leakage of lubricant oil into these cylinders. The responses of these two anomalous cylinders are omitted in the following results.

Fuel Property	**Value**
Specific Gravity	0.7468
Net Heating Value	41.94 MJ/kg
Carbon Weight %	82.31 %
Hydrogen Weight %	13.75 %
Oxygen Weight %	3.94 %
Stoichiometric Air-Fuel Ratio (CH-based)	14.77
Stoichiometric Air-Fuel Ratio (CHO-based)	14.02
Anti-Knock Index	93

Table 4.5: Properties of 93 AKI pump gasoline used as fuel in SI-HCCI transition experiments.

The first experimental SI-HCCI mode transition takes place at an intermediate HCCI load of 2.4 bar NMEP at 2000 RPM and is displayed in Fig. 4.12. The presented cylinders correspond to the first and second of the four to fire on cycle *HCCI 0*, which serves as a limiting case because the intake manifold pressure dynamics have less time to reach atmospheric levels than for the third and fourth cylinders. The first and second cylinders to enter HCCI are referred to as cylinder $H1$ and cylinder $H2$, respectively. Continuous air path valve and output responses are interpolated to be plotted versus cycle along with the discrete combustion input/output responses. As stated in Sec. 4.2.1, the mode transitions are carried out starting after the intake cam has been switched to

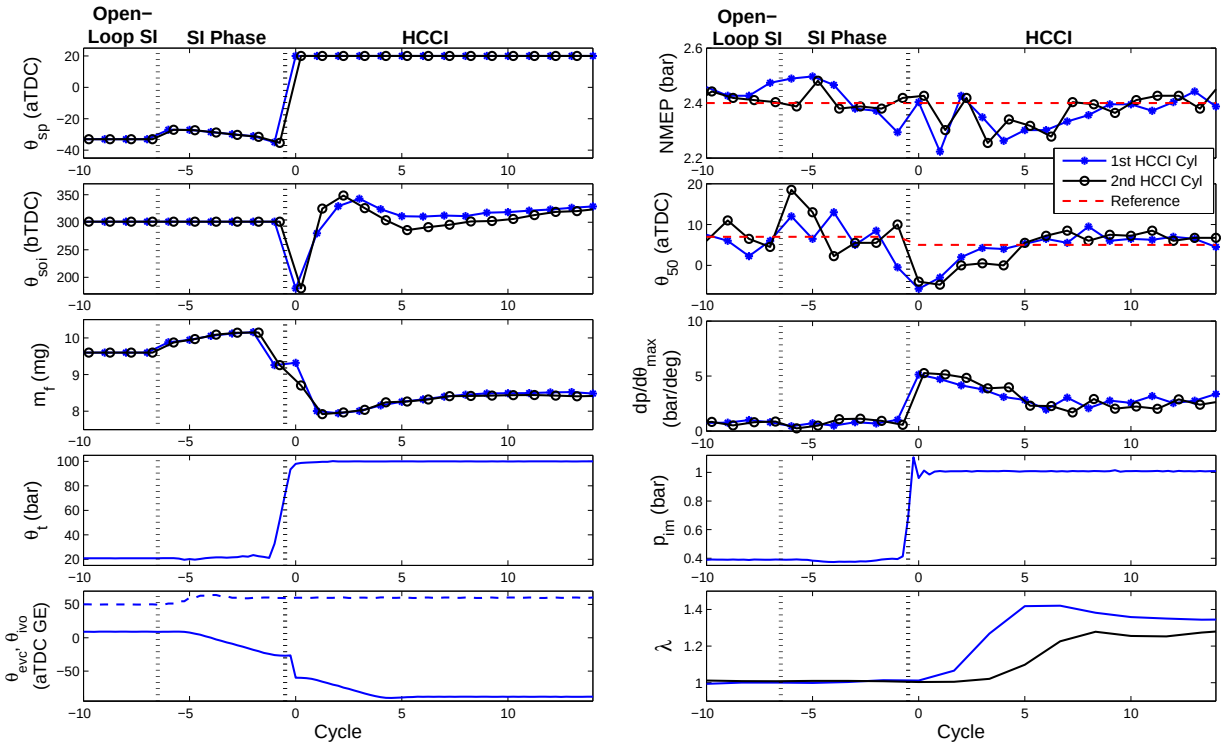

Figure 4.12: Controlled SI-HCCI transition at mid load HCCI at 2000 RPM. Inputs shown in left column and outputs shown in right column. The first and second cylinders to enter HCCI are referred to as $H1$ and $H2$, respectively.

low lift at the beginning of the SI phase, which is designed for NVO and so gives late θ_{ivo}.

The most notable change in the SI phase of the transition in Fig. 4.12 is the advancing of the EVC timing from its nominal SI set point of 9° aTDC to the θ_{evc}^{swch} set point, which is chosen at 23° bTDC for this condition. The disturbance caused by the shift of EVC timing causes the throttle to respond first by slightly closing and then slightly opening relative to its nominal position, as the EVC timing passes through inflection point between rebreathing and trapping residual that is around TDC. Throughout this adjustment, the fuel quantity rises to account for the torque disturbance caused by the earlier EVC timing and hence earlier EVO timing reducing the length of the expansion stroke, while respecting the AFR bounds outlined in Sec. 4.2.1 (here chosen to be [0.97, 1.03]). It can be seen that the $NMEP$ stays close to its reference and λ deviation from stoichiometric is minimal for both cylinders, which suggests that the throttle and fuel control perform adequately. Note though that the exhaust oxygen sensors have strong low pass filtering characteristics, and so λ deviations may be larger than they appear in Fig. 4.12. The spark timing control allows some errors in the θ_{50} response, most notably with late θ_{50} for cylinder $H2$ at the beginning and early θ_{50} for cylinder $H1$ towards the end. However, SI combustion is more robust to perturbations in

θ_{50} than is HCCI, and so the effect on the torque response is minimal.

When cycle *HCCI 0* is approached, the throttle is commanded wide-open, giving a rapid rise in intake manifold pressure. The spark is placed very late so as not to interact with combustion, and the EVC timing jumps by the high lift - low lift cam offset (see Fig. 2.2) as the exhaust cam switches to low lift and HCCI engages. Upon entering HCCI, u_{evc} is stepped to the nominal HCCI set point θ^*_{evc} and so θ_{evc} advances. The λ measurements rise lean, with a slower rise in cylinder $H2$ potentially due to differences in oxygen sensor dynamics and transport delay, or cylinder to cylinder fuel injector offsets. On cycle *HCCI 0*, the combustion controller places θ_{soi} at the extended lower saturation limit of 180° bTDC in anticipation of the high SI exhaust temperature advancing combustion phasing. However, θ_{50} is still very early on cycle *HCCI 0*, signifying that the exhaust temperature effect is outside the authority of θ_{soi} to compensate, despite that the EVC timing that is $\approx 25°$ later than the nominal HCCI set point. Due to the tuning factor $\theta^0_{50,f}$ (here chosen $= -6°$ aTDC), the fuel controller anticipates the early θ_{50} and injects a larger quantity, so that the torque is minimally affected on cycle *HCCI 0*. However, θ_{50} is again early on cycle *HCCI 1* which the fuel controller does not anticipate, and so a torque reduction results. The SOI controller makes the optimal response to this early θ_{50} for cylinder $H1$ by placing θ_{soi} at its nominal late saturation limit of 280° bTDC, though for cylinder $H2$ the controller advances θ_{soi} past the saturation limit. Cylinder $H2$ θ_{50} is more advanced than that of $H1$ over the next few HCCI cycles as well. Further inspection of the controller response data suggests that the more advanced θ_{soi} timing for cylinder $H2$ than $H1$ over the first few HCCI cycles is primarily due to a difference in cylinder air mass and temperature estimation on cycle *HCCI 0*, which carries over to the next few HCCI cycles due to the model's temperature and composition states. This difference is caused by cylinder $H1$ being predicted to have a lower air mass and hence higher temperature on cycle *HCCI 0* because it occurs earlier in the cycle when the intake pressure has not risen as much. The controller thus predicts an earlier θ_{50} for cylinder $H1$ than $H2$, resulting in a later θ_{soi} timing for $H1$. Other effects which may cause the θ_{50} of cylinder $H2$ to retard more slowly than that of $H1$ include potentially higher estimation error for $H2$ and cylinder to cylinder variability, because a single set of control model parameters is used for all cylinders and cylinder $H2$ is often observed to knock more readily than $H1$.

Despite some imperfections in the combustion controller, the $NMEP$ stays close to its reference value throughout the transition, with a peak deviation ≈ 0.18 bar NMEP (8%). Peak pressure rise rates $dp/d\theta_{max}$ are higher on the first few HCCI cycles due to earlier combustion phasing, though they remain within the preferred steady-state limit of 6 bar/degree, and so are more than acceptable for the short HCCI transient period. The mode transition is thus largely successful.

To demonstrate the ability of the controller to generalize to multiple conditions, it is exercised to carry out SI-HCCI mode transitions near the low load (≈ 1.8 bar NMEP) and high load (≈ 3.2 bar NMEP) HCCI limits at 2000 RPM on the experimental engine. In the high load case, cylinder

$H2$ began experiencing problems with runaway knocking and unreasonable AFR/torque responses which were uncorrelated with the fuel command in HCCI, which are hypothesized to be influenced by carbon deposit build up in the cylinder based on boroscope investigations. This cylinder could not be operated safely in HCCI with the necessary fuel quantity for the high load condition, and so its response is omitted in this case.

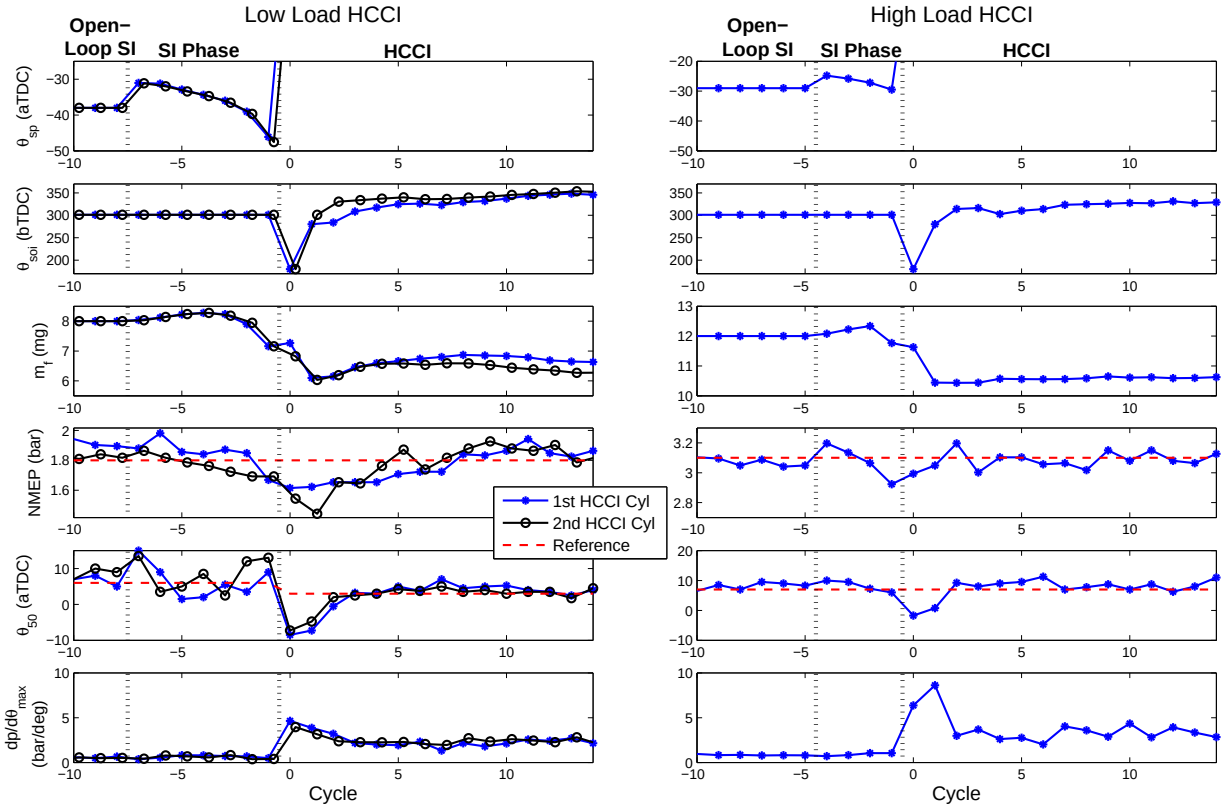

Figure 4.13: Controlled SI-HCCI transition experimental results across the HCCI load regime at 2000 RPM. Left: Low load of 1.8 bar NMEP Right: High load of 3.1 bar NMEP. The first and second cylinders to enter HCCI are referred to as $H1$ and $H2$, respectively.

Summary experimental results for the low load (left) and high load (right) SI-HCCI transition conditions are presented in Fig. 4.13, where the top three subplots show the combustion inputs and bottom three subplots show the combustion outputs. The θ_{sp} axis is enlarged to show more detail, omitting the late placement of θ_{sp} in HCCI. The plots show that several main features of the actuator trajectories remain common through each condition, with the spark timing advancing and fuel increasing throughout the SI phase, and the SOI timing retarding at the start of the HCCI phase and eventually advancing. However, the absolute values of the actuator trajectories vary significantly from case to case, which the controller is able to deduce automatically through model-based calculations. The θ_{50} follows a similar response in all cases, starting early and retarding to the reference in a few cycles. In the high load case, the early initial HCCI cycles $dp/d\theta_{max}$ to

rise above the desired 6 bar/degree threshold, which is not favorable but acceptable for a the short transient period given that the threshold is only exceeded by ≈ 2.5 bar/degree for one cycle. Such pressure rise rate excursions are difficult to avoid in SI-HCCI transitions near the upper HCCI load limit where fuel quantity is high. The early θ_{50} on the first few HCCI cycles also causes a torque reduction, which is minimal in the high load case but larger in the low load case, most likely because θ_{50} is advanced to a greater extent in the low load case. The maximum $NMEP$ reduction in the low load case occurs over the first two HCCI cycles and reaches ≈ 0.2 bar $= 11\%$ for cylinder $H1$ and ≈ 0.35 bar $= 19\%$ for cylinder $H2$. It can be seen that in terms of absolute values, the maximum reduction is not very much worse than other cases, however because of the lower load reference the disturbance is larger on a percentage basis. After the first two HCCI cycles, the $NMEP$ is increased to within $\approx 8\%$ of the reference value, however takes several more cycles to converge to the reference. While this amount of error in the torque response may still be passable for drivability, it can be said that it is the least desirable of all cases examined.

One obvious potential reason for the weaker torque tracking at low load is higher error in the HCCI torque model at the low load operating condition (which has fuel quantity outside the range of parameterized conditions). The gradual increase of m_f after the start of the HCCI phase in Fig. 4.13 supports this hypothesis, as it signals that the IMC output feedback is increasing m_f to compensate for model error. While the output feedback is able to attenuate the model error after several cycles, higher model accuracy would be preferable to minimize the chance of the error occurring. An online adaptation scheme which aids in attenuating such model error will be developed later [67]. Another, more subtle possible reason is that the EVC timing at the SI-HCCI switch point θ_{evc}^{swch} was tuned too early for the low load condition, which caused θ_{50} to advance even earlier on the first few HCCI cycles than in other cases.

To gauge the repeatibility of the SI-HCCI mode transition experiments, a repeated trial was carried out at each of the previously presented operating conditions, without any modifications to the controller calibration. The results are depicted in Fig. 4.14 for the low load (left), mid load (center), and high load (right) cases. Observing the plots, it can be seen that, although the trajectories do not follow the same path on a cycle by cycle basis as in the original trials, the overall qualitative behavior and general controller performance is similar. This is characterized by satisfactory torque and combustion phasing tracking in the SI mode, and early combustion phasing and amplified pressure rise rates along with a mild torque disturbance during the first few HCCI cycles. The peak torque deviations maintain similar levels, with values of 18%, 9%, and 7% in the low, mid, and high load cases, where the trend of the lowest load case having the largest torque deviation is again observed. Some slightly less favorable aspects relative to the original trials can be seen in the high load case, where the torque decreases by nearly the peak deviation amount for three cycles, and the pressure rise rate on cycle *HCCI 1* is slightly higher than in the original case. However, overall effect of these differences on performance is likely to be negligible, given that the

peak torque deviation is already minimal and the reduced torque cycles are interspersed with cycles of good torque tracking, and also that the increased pressure rise rate is only slightly higher for one cycle. One other noticeable difference between the repeat and original runs appears in the mid load on cycle *HCCI 2* for cylinder$H2$, where the θ_{50} suddenly advances. The increase in torque which accompanies the advanced θ_{50} suggests that the effect is related to the anomalous behavior exhibited by cylinder $H2$ at high loads, where torque could increase without stimulus from the fuel command. This anomalous behavior may have surfaced to a minor extent on cycle *HCCI 2* at this mid load condition. However, given the small impact of such behavior at mid loads, the overall performance in terms of torque tracking and pressure rise rate remains minimally affected for the repeated trial.

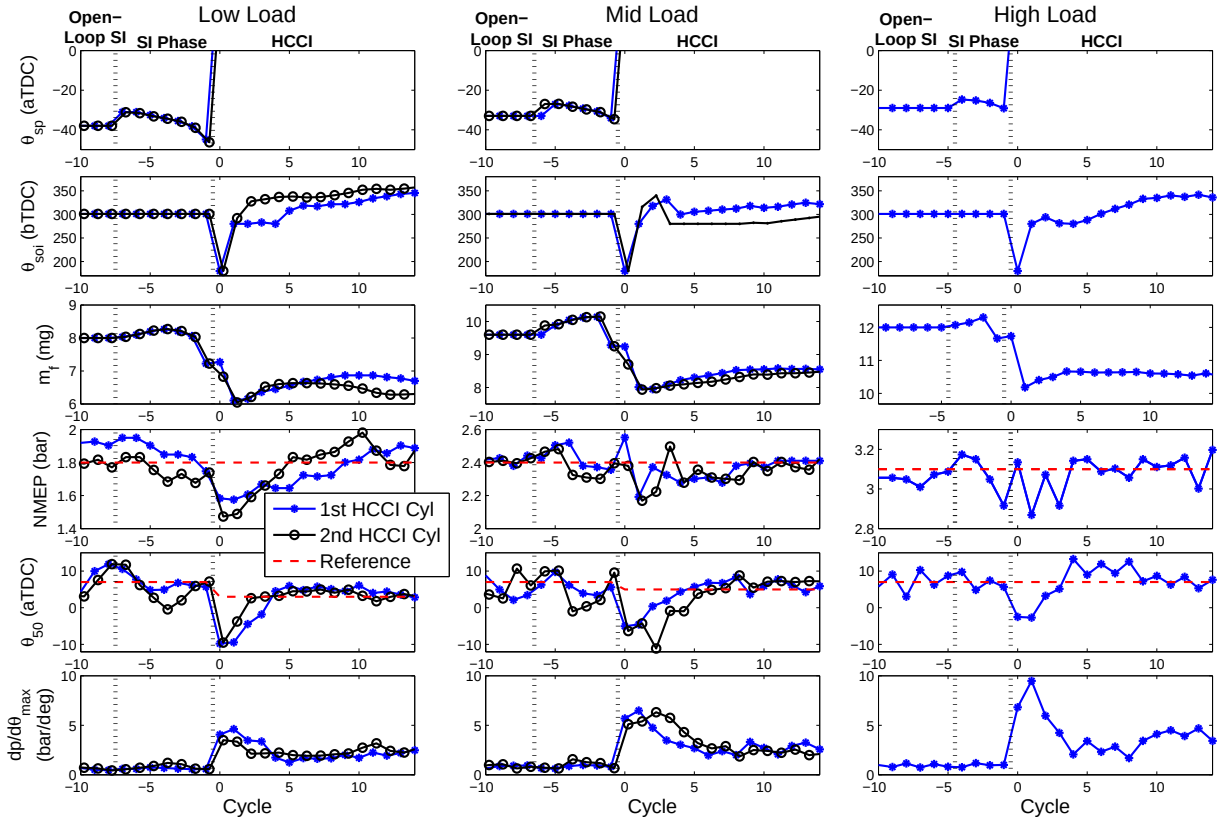

Figure 4.14: Repeated SI-HCCI mode transition experiments at 2000 RPM. Left: Low load of 1.8 bar NMEP. Center: Mid load of 2.4 bar NMEP. Right: High load of 3.1 bar NMEP.

4.4.1 Calibration Effort

To convey the effort involved in calibration of the SI-HCCI transition controller, all tuning variable values for the both the SI and HCCI phases of the presented mode transition experimental results

are listed in Table 4.4.1. The table separates the tuning variables which remained constant across all experimental conditions from those which were varied, as the adjustment of calibration variables by operating condition may present significantly more calibration effort. Those calibration variables which can be assumed to be specified by the baseline engine calibration as necessary for nominal SI and HCCI mode control are also placed in a separate category. Looking over the list of variables, it can be seen that there are 20 variables in total which must be tuned, where the variables which are included in the baseline calibration have been left out of the count. The number 20 is based on the fact that the Kalman filter covariance matrices W_{est} and V_{est} include 3 and 2 tuning elements, respectively, and that the faster Kalman gain is obtained by simply reducing the θ_{50} variance in the matrix V_{est}^0 and leaving all other estimator tuning parameters costant. Three of these 20 elements are trivially easy to tune, referring to $\lambda^{rich}, \lambda^{lean}, \lambda^{min}$, which will always be within some small margin of stoichiometric. Additionally, only four of the 20 tuning variables are adjusted by operating condition in the SI-HCCI transition experiments, and of these four θ_{evc}^{swch} is the main factor influencing the smoothness of the transition with the other three variables being adjusted only with minor tweaks. The experimental results thus show that the controller generalizes across the nearly the full load range of HCCI combustion at 2000 RPM on the experimental engine with adjustments made only to one major and three minor calibration variables.

It is difficult to draw a quantitative comparison between the calibration effort of the proposed model-based feedback control scheme and that of open-loop experimental approaches in the literature, as the details of the input sequence tuning for SI-HCCI transitions are not clear in many experimental works. In the most extreme case, each control input command at every control action can be considered as a calibration variable, i.e. every point in the open-loop input sequence is a separate calibration variable. For the air path actuators, this can amount to a very large number of calibration parameters if considered on the same basis as the model-based feedback control scheme, which operates the air path actuators on a 10 msec sample time giving six calibration variables per cycle at 2000 RPM for each air path control input. However, for simplicity it is assumed that the air path inputs in an open-loop scheme can be commanded on a cycle-cycle basis similar to the combustion inputs. Roughly assuming a five cycle duration for the SI phase of the transition, which is around average for the experimental SI-HCCI trials, and also a five cycle transient phase after switching to HCCI mode, this amounts to 5 inputs $\times$ 5 cycles = 25 calibration variables in the SI phase, and 3 inputs $\times$ 5 cycles = 15 calibration variables in the HCCI phase, for a total of 40 calibration variables.

In a practical open-loop SI-HCCI mode transition method, simplifications to the approach of treating all control actions as calibration variables are likely to be made so that the number of calibration variables is not as high as 40. Some such simplifcations are already suggested in the proposed model-based feedback control structure, wherein the valve timing commands were governed by simple step inputs, which reduces the 5 calibration variable sequence to a one calibration variable

Variable	Low Load	Mid Load	High Load	Dependence
k_t	50	...	...	Constant w/ Operating Condition
n_t	0.97	...	...	
p_t	0.91	...	...	
N_{pre}^{WOT} (time steps)	4	...	...	
$\lambda^{rich}/\lambda^{lean}$	0.97/1.03	...	...	
δ_{evc} (CAD)	8	...	...	
p_f	0.8	...	...	
p_{soi}	0.85	...	...	
W_{est}	diag[5 .02 10^{-6}]	...	...	
V_{est}	diag[0.8 0.05]	...	...	
W_{est}^0	W_{est}	...	...	
V_{est}^0	diag[0.1 0.05]	...	...	
λ^{min}	1.05	...	...	
θ_{evc}^{swch} (aTDC GE)	-40	-23	-14	Vary w/ Operating Condition
N_{pre}^{evc} (cyl steps)	2	2	3	
λ^{PS}	1	1.05	1.05	
$\theta_{50,f}^0$ (aTDC)	-9	-6	-3	
$\theta_{50,S}^*$ (aTDC)	7	...	...	Baseline Calibration
θ_{ivo}^* (aTDC GE)	60	...	...	
θ_{50}^H (aTDC)	3	5	7	
θ_{evc}^* (aTDC GE)	-101	-89	-79	

Table 4.6: Tuning variable values for SI-HCCI transition controller.

set point, and so reduces the number of calibration variables from 40 to 28. Another simplification that was apparent in the approach of [21] was to tune the HCCI fuel command to be constant after the first HCCI cycle, which reduces the 5 cycle sequence to a 2 cycle sequence, which can drop the number of calibration variables to 25. Other such simplifications may also exist which can reduce the number of calibration variables even further.

In comparison of the number of calibration variables to open-loop methods, the number that should be used for the proposed model-based feedback control scheme is 18, given that the variables N_{pre}^{WOT} and δ_{evc} are used for planning the throttle opening and cam switch timing which must also be done for open-loop schemes. Additionally, 3 of these 18 variables are trivially easy to tune, as already noted. However, comparison purely on the basis of the number of calibration variables can be misleading, in that the variables may become more time intensive to calibrate without the presence of model-based feedback control. Take for example the tuning of the EVC timing at the SI-HCCI switch point, θ_{evc}^{swch}, which must be calibrated both in the proposed model-based feedback scheme and in any open-loop sequence type method. With the proposed model-based feedback control scheme, θ_{evc}^{swch} is relatively straightforward to tune, in that its value can be freely

adjusted and the model-based controller takes the necessary actions to ensure adequate conditions at the SI-HCCI switch point, e.g. keeping the torque close to the reference, keeping the mixture stoichiometric, etc. Therefore several different values can be iterated through very quickly for a fast tuning. However, if all inputs are applied in open-loop, then everytime a new θ_{evc}^{swch} is tested, the calibrator must manually deduce the necessary values of the other inputs to give adequate conditions at the SI-HCCI switch point, and so trial and error tuning of the θ_{evc}^{swch} value can take substantially longer. Another point to make is that the gains and set points of the model-based feedback control scheme may be more intuitive to tune than specification of actuator sequences on a cycle by cycle basis, since they have a simpler interpretation (e.g. higher gain $\rightarrow$ faster response) and generate the input command profile automatically.

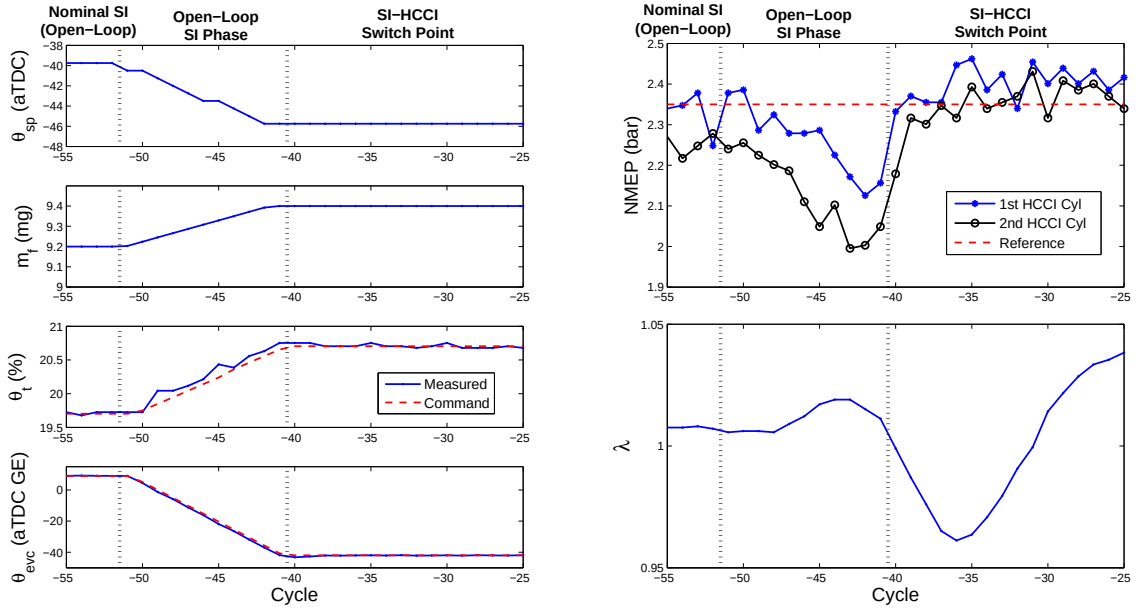

Figure 4.15: Data from open-loop SI-HCCI transition wherein all input commands are specified through a linear ramp from the nominal SI condition to the SI-HCCI switch point in the SI phase of the transition, for examination of efficacy of simple open-loop actuator profiles.

One other possible simplification to open-loop scheduled sequences which should be noted is to specify the shapes of the actuator profiles (e.g. a ramp) as opposed to cycle by cycle trajectories, in which case only the actuator profile shape and ending point of the profile must be selected for each actuator. While it is unclear from the literature if such an approach has ever had success, an observation can be made from the open-loop SI-HCCI transition sequences used for transient model validation in Chapter 3, where the SI phase of the SI-HCCI transition was carried out with simple ramp inputs for all actuators. This part of the transient was not shown in Chapter 3 because it was not the focus of the model validation, and so it is depicted for one example open-loop

SI-HCCI transition in Fig. 4.15. As can be seen, all actuators are ramped from their nominal SI condition to the SI-HCCI switch point condition. Throughout this transient, a moderate torque reduction and AFR fluctuations occur over several cycles, giving significantly worse performance than any of the previously examined closed-loop SI-HCCI transitions in the SI phase. While not constituting a definitive conclusion that simple actuator trajectories for SI-HCCI open-loop sequence are unnacceptable, the data at least cautions that more sophisticated open-loop mode transition actuator profiles may be necessary to attain satisfactory performance, while will again increase calibration time.

One last point needs to be made when considering the calibration effort of the proposed model-based controller against an open-loop mode transition method. While it was stated that simplifications may exist which can reduce the number of calibration variables of open-loop mode transition methods, in any method where the actuator commands are specified by open-loop sequences, most if not all calibration variables of the controller are required to change between operating condition. As was previously mentioned, for the proposed model-based feedback control scheme, only one major and three minor variables were adjusted between operating points. Thus, from the stand point of scheduling the SI-HCCI transition controller across the feasible HCCI range, the ability of the model-based feedback controller to generalize to many operating conditions with minimal tuning can be expected to significantly reduce calibration effort relative to an open-loop method.

Chapter 5

Online Parameter Adaptation for Improved Model-Based Combustion Control in SI/HCCI Transitions

In Ch. 4, a model-based feedback control architecture for SI-HCCI transitions was developed which was shown to generalize to several operating conditions with minimal calibration. A major component which contributes to the controller generality are the nonlinear model-based calculations using the SI and HCCI combustion models. The model-based calculations are especially important given the nature of SI/HCCI mode transitions, wherein a large state and input transition occurs in a very short time. Direct output feedback control thus has a limited window over which to empirically compensate for errors during several key transient cycles, so that the model-based calculations must make up a large portion of the control input. This is most obvious in the HCCI phase of the transition, where upon entry, no HCCI combustion feedback is yet available, and so the control input is determined entirely through model predictive calculations. The model on which the control architecture is built was shown to fit a wide range of SI and HCCI data in Secs. 2.3.3 and 2.4.2, however model accuracy may decrease as the engine ages and conditions are extrapolated outside those in the model parameterization. Additionally, cylinder to cylinder and engine to engine variability is not accounted for in the model parameterization.

This Chapter aims to improve performance and robustness of the model-based control architecture of [65] by using transient SI/HCCI transition feedback to tune the combustion model parameters in online operation with an adaptive parameter update scheme. The controller thus makes use of transient data not only for immediate corrective output feedback action, but for improving the model-based control input calculations for successive transitions. The adaptive scheme is developed from the standpoint of being used in the control architecture of Ch. 4 for SI-HCCI transitions, however it will be seen in Ch. 6 that the scheme also is helpful in HCCI-SI transitions without any modifications to the development made in this chapter. In the SI-HCCI direction of the mode transition, the adaptive method for the residual gas correction factor from Sec. 3.2.1 is employed on the first HCCI cycle *HCCI 0*, while for all other cycles a new method is developed which involves linear least squares updating of the torque and combustion phasing models. In what follows, the

adaptive methodology is described, and experimental examples are given which show the effect of the parameter adaptation on the controller response.

5.1 Parameter Adaptation Method

5.1.1 Overview

The online parameter update method focuses on the combustion phasing and torque calculations of the SI and HCCI combustion models, which play a central role in all of the model-based calculations of the controller in Ch. 4 for both SI and HCCI mode (including the p_{im} reference derivation). The parameter update problems will be formulated in the linear parameteric model framework where the model estimate $\tilde{z}$ of the quantity z can be expressed as

$$\tilde{z} = a^T \Phi \tag{5.1}$$

where a is the parameter vector and Φ is the regressor vector. This allows standard linear parameter update laws to be used [64], which are easy to implement and favorable for real-time calculations.

All parameter update laws follow the recursive least squares with forgetting factor algorithm, which is chosen because of its desirable convergence and optimality properties [64]. The algorithm is reproduced here for convenience:

$$a(m) = a(m-1) + G(m)(z(m) - \tilde{z}(m)) \tag{5.2}$$

$$G(m) = P(m-1)\Phi(m)(\beta + \Phi^T(m)P(m-1)\Phi(m))^{-1} \tag{5.3}$$

$$P(m) = (I - G(m)\Phi^T(m))P(m-1)/\beta \tag{5.4}$$

where m is the update time index and β is a forgetting factor. The basis function matrix P of the recursive least squares algorithm is initialized at $10^{-3}I$ for torque adaptation laws and $10^{-2}I$ for combustion phasing adaptation laws, where these values were tuned in simulation to give some but not too much sensitivity in the first several parameter updates. The combustion phasing update laws are implemented using normalized regressor variables of the form

$$n_x = \frac{x - x_{min}}{x_{max} - x_{min}} \tag{5.5}$$

which vary from 0 to 1 as the physical variable x varies between some reasonable maximum and minimum values. This was done for combustion phasing but not torque parameter update laws because the combustion phasing parameterizations involve more variables with a wider span of units, as will be seen.

When a mode transition commences, parameter updates are executed after feedback is obtained from each subsequent cycle. The adaptation is turned off after a certain number of cycles elapse after the destination mode is reached, chosen to be ten for all cases. After each update, the parameters are then used immediately in the following cycle model-based control calculations, creating an indirect adaptive control architecture. Note that for all control loops, the model predicted quantity $\tilde{z}$ that is necessary for parameter updating is easy to generate from its corresponding model inverse calculation by simply running the calculation forward with the solved control input.

5.1.2 SI Model Adaptation

Torque Model

The torque model adaptation focuses on the model's $NMEP$ prediction. Because the $NMEP$ calculation in the SI model of Sec. 2.3 is largely based on simplified physics of polytropic compression and expansion work, there are few parameters in the baseline model which lend themselves to $NMEP$ adaptation. For this reason, the $NMEP$ adaptation is carried out by introduction of correction parameters which depend on important influencing factors for the torque:

$$\Delta_{\tau,S} = NMEP - \tilde{NMEP} \tag{5.6}$$

$$\tilde{\Delta}_{\tau,S} = a_{\tau,S}^T \Phi_{\tau,S} \tag{5.7}$$

$$\Phi_{\tau,S} = \begin{bmatrix} m_f & V_{cmb}^2 & V_{cmb} & 1 \end{bmatrix}^T \tag{5.8}$$

where $\Delta_{\tau,S}$ and $\tilde{\Delta}_{\tau,S}$ are the actual and predicted errors in the SI $NMEP$ calculation. The parameterization for the estimated prediction error $\tilde{\Delta}_{\tau,S}$ is based on the fact the torque is normally a strong function of fuel quantity, and rolls off with a nonlinearly increasing slope as combustion departs from MBT timing. V_{cmb} is meant to capture this nonlinear dependence of torque on combustion phasing based on the logic in [49] and is expressed in units of $\text{dm}^3 \times 10$ when m_f is in milligrams, to keep the regressors on the same order of magnitude. The V_{cmb} terms are included mostly for disambiguation in the SI-HCCI controller, so that in the event that a θ_{50} far from MBT occurs, the controller can detect a torque reduction due to non-ideal combustion phasing, rather than incorrectly attributing the effect to fuel quantity. The V_{cmb} terms will become more important for control in the HCCI to SI direction, which will be covered in Ch. 6.

Combustion Phasing Model

The SI combustion phasing model is adapted by direct update of the model's θ_{50} correlation. The θ_{50} correlation of the reparameterized model in Appendix A is used since the experimental adaptation

results of Sec. 5.2 are generated with the replica engine to which the model is reparameterized,

$$\tilde{\theta}_{50} = a_{50}^T \Phi_{50} \tag{5.9}$$

$$\Phi_{50} = [n_f \;\; n_{sp}^2 \;\; n_{sp} \;\; n_{evc}^2 \;\; n_{evc} \;\; n_{\lambda'}^2 \;\; n_{\lambda'} \;\; 1]^T \tag{5.10}$$

$$n_f = \frac{m_f - 5}{20 - 5}, \quad n_{sp} = \frac{\theta_{sp} - (-60)}{0 - (-60)} \tag{5.11}$$

$$n_{evc} = \frac{\theta_{evc} - (-50)}{15 - (-50)}, \quad n_{\lambda'} = \frac{\lambda' - 1}{2 - 1} \tag{5.12}$$

The maximum and minimum normalization limits are chosen based on physical reasoning for the feasible range of the corresponding variable in the SI phase of the transition.

5.1.3 HCCI Model Adaptation

Residual Gas Temperature Correction: SI-HCCI Transition First HCCI Cycle

Based on the inspection in Sec. 3.1, any error in the combustion phasing prediction on cycle *HCCI 0* of an SI-HCCI transition is attributed to the high SI exhaust temperature and low residual mass pushing the model's charge mass and temperature calculation far outside the nominal HCCI range. Cycle *HCCI 0* is thus distinct from all other HCCI cycles, where combustion phasing error will be attributed directly to error in the Arrhenius combustion phasing correlation. This policy is chosen following the results of Sec. 3.1, which suggest that the strongest source of error on cycle *HCCI 0* is in the excursion of the thermodynamic state far outside the nominal HCCI range, while for the remainder of the cycles error is mostly due to nominal model error. The combustion phasing error on cycle *HCCI 0* is captured by the residual gas temperature correction factor k_r introduced in Sec. 3.1.3, and the same method as in Sec. 3.2.1 is applied to backtrack from the measured θ_{50} to the necessary k_r value for the parameter adaptation. The Arrhenius integral inversion involved in this method is carried out using the Arrhenius tabulation explained in Sec. 4.3.2 which allows execution in real-time. For the range of conditions examined, k_r is parameterized as a linear function of θ_{evc} as in Sec. 4.3.2,

$$\tilde{k}_r = a_{kr}^T \Phi_{kr} \tag{5.13}$$

$$\Phi_{kr} = \begin{bmatrix} \theta_{evc} & 1 \end{bmatrix}^T \tag{5.14}$$

Note that on cycle *HCCI 0* during an SI-HCCI transition no parameter updates are executed other than the residual temperature correction, and on all other cycles the residual temperature correction update is deactivated.

Torque Model

Similar to the SI case, the HCCI $NMEP$ calculation in the model of Sec. 2.4 mainly comes from simplified physics, with the exception of the combined thermal/combustion efficiency factor η_λ. However, this factor is not convenient for use for adapting the torque model to match transient data, because it only accounts for the dependency of $NMEP$ on AFR and nothing else. Thus the adaptation of the HCCI torque model is carried out following the same approach as in the SI case, where corrective parameters are introduced to account for error in the $NMEP$ prediction:

$$\Delta_{\tau,H} = NMEP - \tilde{NMEP} \tag{5.15}$$

$$\tilde{\Delta}_{\tau,H} = a_{\tau,H}^T \Phi_{\tau,H} \tag{5.16}$$

$$\Phi_{\tau,S} = \begin{bmatrix} m_f & 1 \end{bmatrix}^T \tag{5.17}$$

where $\Delta_{\tau,H}$ and $\tilde{\Delta}_{\tau,H}$ are the actual and predicted errors in the HCCI $NMEP$ prediction. The dependence of the torque error is simplified to be a function of fuel only, because combustion phasing is typically constrained to a smaller window in HCCI than SI and so deviations of θ_{50} from the optimal cannot be as large. As is apparent from the SI-HCCI transitions of Sec. 4.4, the validity of this simplification can weaken on the first several HCCI cycles of the transition due to early combustion phasing caused by high exhaust temperatures. However, the torque model is not updated on the first HCCI cycle *HCCI 0* where only the k_r adaptation executes, which is often the point of earliest combustion phasing. A few early cycles may follow *HCCI 0* which may not be captured properly with the simplified $\tilde{\Delta}_{\tau,H}$ parameterization, however the simplified method was still found to provide notable improvements in torque control.

Combustion Phasing Model

As previously stated, error in the HCCI combustion phasing model on all cycles other than *HCCI 0* is attributed to the model's Arrhenius correlation Eq. 2.87. This correlation is not straightforward to work with for developing a linear parameter update method, since the integrated Arrhenius rate creates a nonlinear and implicit function. However, it can be noted that many of the dependencies in the Arrhenius correlation are parameterized into the Arrhenius threshold K_{th}, which is an explicit expression that is linear in the parameters. The combustion phasing model update is thus carried out targeting the parameters of the Arrhenius threshold, while leaving the parameters n_p and E_a which are inside the nonlinear and implicit Arrhenius integral unchanged. Note that the correlation for the Arrhenius threshold K_{th} is taken from Eq. (A.9) for the reparameterized model in Appendix A for the replica experimental engine, since experiments with the proposed adaptive scheme are carried out on this replica engine. A term to capture variation of in-cylinder temperature is augmented to the

Arrhenius threshold, since the dependence of the Arrhenius correlation on in-cylinder temperature enters through the Arrhenius integral and so is inaccessible

$$K_{th}^{*} = \int_{\theta_{ivc}}^{\theta_{soc}^{*}} \frac{1}{\omega} p_c(\theta)^{n_p} e^{\left(\frac{-E_a}{RT_c(\theta)}\right)} d\theta \tag{5.18}$$

$$\theta_{soc}^{*} = (\theta_{50} - a_{soc,0})/a_{soc,1} \tag{5.19}$$

$$p_c(\theta) = p_{ivc}\left(\frac{V_{ivc}}{V(\theta)}\right)^{n_c}, \quad T_c(\theta) = T_{ivc}\left(\frac{V_{ivc}}{V(\theta)}\right)^{n_c-1} \tag{5.20}$$

$$\tilde{K}_{th} = a_{th}\Phi_{th} \tag{5.21}$$

$$\Phi_{th} = \left[n_{\lambda_r}^2 n_{soi} \;\; n_{\lambda_r} n_{soi} \;\; n_{soi} \;\; n_{\lambda_r}^2 \;\; n_{\lambda_r} \;\; n_{T_{rc}} \;\; \frac{1}{T_{ivc} - T_{ivc}^{min}} \;\; 1\right]^T \tag{5.22}$$

$$n_{\lambda_r} = \frac{\lambda_r - 0}{1 - 0}, \quad n_{soi} = \frac{\theta_{soi} - 280}{390 - 280}, \quad T_{rc} = \frac{T_{rc} - 600}{1000 - 600} \tag{5.23}$$

where θ_{soc}^{*} is the start of combustion timing to match the measured θ_{50}. Eqns. (5.18)-(5.20) convey that the Arrhenius threshold K_{th}^{*} to perfectly match the measured θ_{50} is obtained by inverting the θ_{soc} to θ_{50} linear fit (5.19) and then running the Arrhenius integration up to the desired θ_{soc}^{*} with the estimated pressure and temperature. K_{th}^{*} then takes the place of the "measured" output which the model prediction $\tilde{K}_{th}$ tries to approximate, with a normalized parameterization that follows the same form as in Eq. (A.9) with an augmented term for T_{ivc}. The hyperbolic dependence on T_{ivc} is chosen to approximate the profile of the full Arrhenius correlation, which tends to have a nonlinearly increasing slope as T_{ivc} decreases and misfire conditions are approached. The T_{ivc}^{min} shift factor is chosen near the lower range of feasible T_{ivc} values to increase the sensitivity of the hyperbolic dependence in that region, but still outside the feasible T_{ivc} range to avoid dividing by zero. Note that the Arrhenius integration in Eq. (5.18) is evaluated using the look-up table method described in Sec. 4.3.2 to faciliate real-time execution of the adaptive law.

5.2 Experimental Results

The effects of the SI and HCCI parameter update methods described in Sec. 5.1 are examined in the SI-HCCI direction of the mode transition by augmenting the update methods to tune the parameters of the baseline SI-HCCI transition controller from Ch. 4 in online operation. The adaptive experiments are carried on the replica experimental engine from Appendix A, which also served as the experimental apparatus for the baseline controller of Ch. 4. The experimental conditions are perturbed from those in the baseline controller results of Sec. 4.4 in that a different fuel batch is used, which is a reference type fuel without any ethanol content as opposed to the 10% ethanol pump gas of Sec. 4.4. The fuel is of type Corrigan UTG 96, whose properties are listed in

Table 5.2. Despite that both the reference and pump fuel batches have the same AKI, daily check points and general SI-HCCI mode transition experimental observations indicate that reference fuel tends to increase engine knocking relative to the original pump gas. The cause for this result could not be discerned from the given information, which did not include the research and motor octane number of the pump gas, or detailed information about the pump gas aromatics, olefins, etc. One reason could be that the ethanol in the pump gas somehow provides better anti-knock properties, and/or slows the rate of coking in the combustion chamber which will reduce deposit formation and the associated combustion advancing effects. In any case, the performance of the baseline SI-HCCI transition controller from Chapter 4 suffers in some experimental trials due to higher knocking, but it will be seen that the parameter adaptation is able to restore performance and even surpass the baseline results in Sec. 4.4 in most cases. As in Sec. 4.4, the responses of two of the four cylinders which elicit anomalous torque and AFR responses are omitted.

Fuel Property	**Value**
Specific Gravity	0.744
Vapor Pressure	9 psi
Net Heating Value	42.90 MJ/kg
Carbon Weight %	86.4 %
Hydrogen Weight %	13.6 %
Oxygen Weight %	0 %
Stoichiometric Air-Fuel Ratio (CH-based)	14.77
Anti-Knock Index	93
Sensitivity	7.9

Table 5.1: Properties of Corrigan UTG 96 gasoline used as fuel in adaptive SI-HCCI transition experiments.

5.2.1 Successive Adaptations at One Operating Condition

The parameter adaptation is carried out in the simple case where successive SI-HCCI transitions are repeated at single intermediate load operating condition at 2000 RPM with parameter updating active during all trials. A total of 16 SI-HCCI trials are run with the forgetting factor of the recursive least squares update tuned to an aggressive value of 0.94 to expedite convergence, which is acceptable given the constant operating condition. The first experimental result compares SI-HCCI transition responses prior to any parameter updating and after the adaptive trials complete at the constant operating condition to illustrate the major effects of the adaptation. Fig. 5.1 plots the responses before (left) and after (right) adaptation, where combustion inputs (top three rows) and outputs (bottom three rows) are shown since the adaptation is concerned with the combustion model. The θ_{sp} input is zoomed in upon to show more detail in the SI phase; in the HCCI phase, it

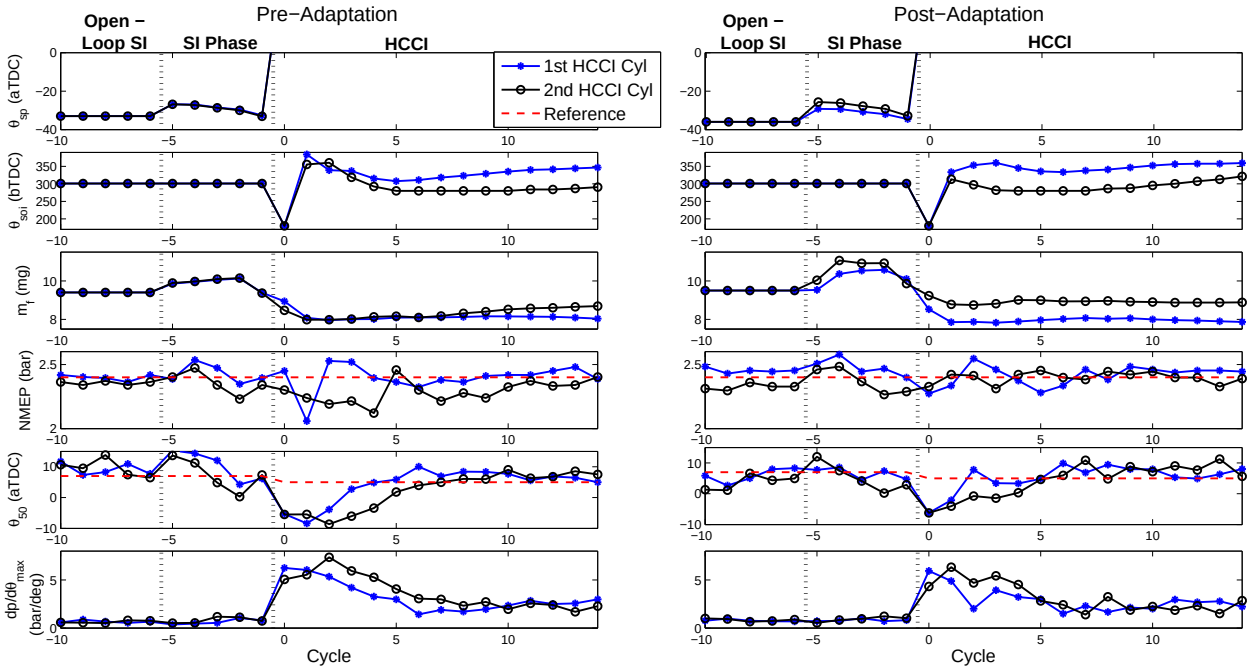

Figure 5.1: SI-HCCI mode transitions before (left) and after (right) successive adaptations at an intermediate HCCI load operating condition. The first and second cylinders to enter HCCI are referred to as $H1$ and $H2$, respectively.

is placed aTDC as in Sec. 4.4. The displayed responses correspond to the first and second cylinders to enter HCCI, which are referred to as cylinder $H1$ and $H2$, respectively, as in Sec. 4.4.

Observing the pre-adaptation responses in Fig. 5.1, it can be seen that minor errors are present in the SI phase of the transition associated with late θ_{50} for cylinder $H1$ and slight reductions in $NMEP$ for cylinder $H2$, though the effects are not that significant. However, when the HCCI phase commences, the controller makes significant errors in advancing θ_{soi} on the 2-3 cycles following *HCCI 0*, which amplifies early combustion phasing on these cycles and contributes to reductions in $NMEP$. Additionally, the torque output of cylinder $H2$ tends to be lower than $H1$ for a given fuel quantity, so that the $NMEP$ of this cylinder remains low for multiple cycles after entering HCCI. These errors are compensated by the IMC output feedback, however several cycles must elapse before the output feedback can fully attenuate the errors because the bandwidth of the controller cannot be arbitrarily high.

After the combustion model parameters are adapted, the problems displayed in the baseline controller responses are for a large part inherently attenuated by the model-based calculations. The θ_{sp} command for cylinder $H1$ is advanced relative to $H2$, giving a θ_{50} response in SI which stays closer to the reference. The $NMEP$ dip of cylinder $H2$ in SI is kept to a lesser extent as

well. In HCCI, the θ_{soi} command is not as advanced on the first few cycles following *HCCI 0*, most notably for cylinder $H2$. This causes θ_{50} to retard to its reference more readily after cycle *HCCI 0*, which has positive effects for the $NMEP$ and $dp/d\theta_{max}$ responses. Additionally, the m_f command for cylinder $H2$ is increased relative to $H1$, which mitigates the excursion of cylinder $H2$ $NMEP$ below the reference that was observed in the pre-adaptation response. The adaptation thus enables errors to be immediately compensated by improving the model predictions, giving performance benefits during the cycles where direct output feedback would otherwise be adjusting to cancel the errors. A last important comment is that the input trajectories for cylinders $H1$ and $H2$ are further apart than they are prior to adaptation, which is due to the fact that the baseline model is parameterized with a single set of coefficients. Differences in the cylinder's input trajectories in the baseline controller are thus only caused by corrective output feedback and differences in measured disturbance quantities (valve timing, intake pressure, etc.) between the cylinders, and the measured disturbances tend to be similar for both cylinders given that they are next to each other in firing order. The adaptation is carried out on a per cylinder basis, allowing each cylinder to be parameterized by its own set of coefficients and so inherently compensating for cylinder to cylinder variability.

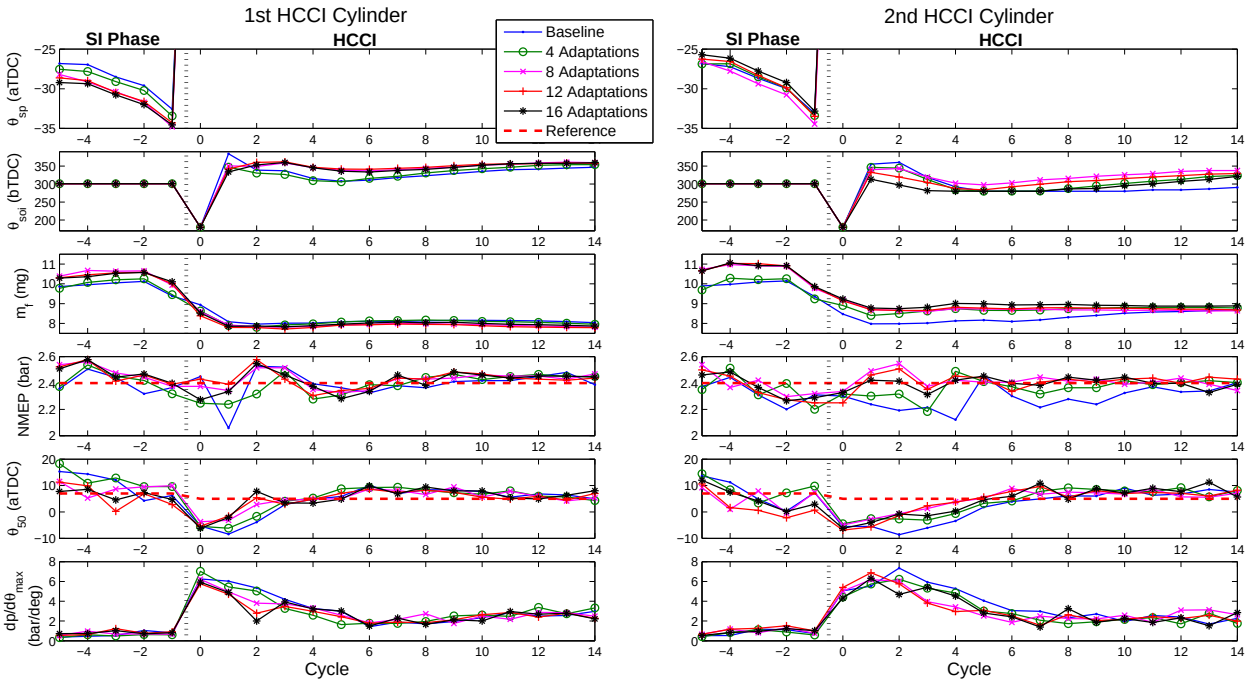

Figure 5.2: Successive SI-HCCI mode transition trials at an intermediate HCCI load operating condition with adaptation active. The first and second cylinders to enter HCCI are referred to as $H1$ and $H2$, respectively.

For a more detailed view of how the parameter adaptation changes the controller response,

Fig. 5.2 plots the input/output responses at the condition of Fig. 5.1 for several intermediate instances throughout the 16 adaptive trials. Separate plots are given for cylinder $H1$ (left) and $H2$ (right) because the adaptation occurs on a per cylinder basis. Moving from the blue dot lines to the black starred lines shows how a given trajectory changes with increasing adaptations. Observing the θ_{sp} and m_f input trajectories, a clear trend can be seen of advancing θ_{sp} on cylinder $H1$ and increasing m_f on cylinder $H2$ to compensate for the late SI θ_{50} of cylinder $H1$ and lower $NMEP$ of cylinder $H2$. The m_f command also increases slightly in SI for cylinder $H1$, though the change to the $NMEP$ response is minor. Cylinder $H2$'s θ_{sp} command does not appear to have significant error as its variation with increasing adaptations seems mainly influenced by noise. Generally speaking, the θ_{sp} and m_f input trajectories tend to converge within a small tolerance after eight adaptations. The θ_{soi} trajectory, however, shows more significant variation as the adaptation progresses beyond eight trials, mainly in the first few HCCI cycles. As θ_{50} tends to be early on these cycles, θ_{soi} continues to retard with increasing adaptive trials, most notably on cycle *HCCI 1* where the θ_{soi} retards by 17° for cylinder $H1$ and 27° for cylinder $H2$ between eight and sixteen trials. After cycle *HCCI 1*, cylinder $H1$'s θ_{soi} command is actually later for the zero and four adaptation cases, which is most likely due to the IMC feedback retarding θ_{soi} by a greater amount due to the earlier θ_{50} on cycle *HCCI 1* these cases. θ_{50} retards towards the reference, though to a lesser degree on cycle *HCCI 2* for the zero and four adaptation cases than in the more advanced adaptive cases, which may be influenced by the cyclic coupling to the previous HCCI cycles which tend to have slightly higher fuel mass in the zero and four adaptation cases. The θ_{50} response of cylinder $H2$ is slower to retard to the reference value than that of cylinder $H1$, which is reasonable given that this cylinder tends to have earlier combustion phasing and higher knocking in general. This promotes a more dramatic retarding effect on the θ_{soi} trajectory with increasing adaptations, to the point where after sixteen adaptations cylinder $H2$'s θ_{soi} command is close to the nominal 280° bTDC θ_{soi} saturation immediately after cycle *HCCI 0*. This gives a general trend of faster retarding θ_{50} and reduced pressure rise rates on the cycles following *HCCI 0*, however even with the much later θ_{soi} at higher degrees of adaptation the θ_{50} still takes several more cycles to retard to the reference than for cylinder $H1$ due to the cylinder to cylinder variability.

Further information on the effect of the adaptation can be obtained by viewing how the model parameters change in the sequential adaptative trials. It is difficult to interpret the trajectories of the parameters based on their absolute values, as the parameterization is empirical and so absolute values may have little physical meaning. However, some information may still be drawn by observing the relative magnitudes and directionality of the parameter changes.

The first set of parameters that are examined are those of the SI combustion model, which are portrayed in Fig. 5.3 for the combustion phasing (left) and torque (right) correlations at discrete instances throughout the adaptive trials of Fig. 5.2. Given that the number of parameters for the SI θ_{50} correlation is high (see Eq. (5.10)), the figure focuses on the parameters for several key

dependencies within the correlation, to see how the sensitivity of the correlation to each of these changes; note that the parameters for the corresponding second order terms of each dependence followed a similar trajectory. Also, the parameter for the bias term in the torque correlation is not shown because it was unfortunately not recorded.

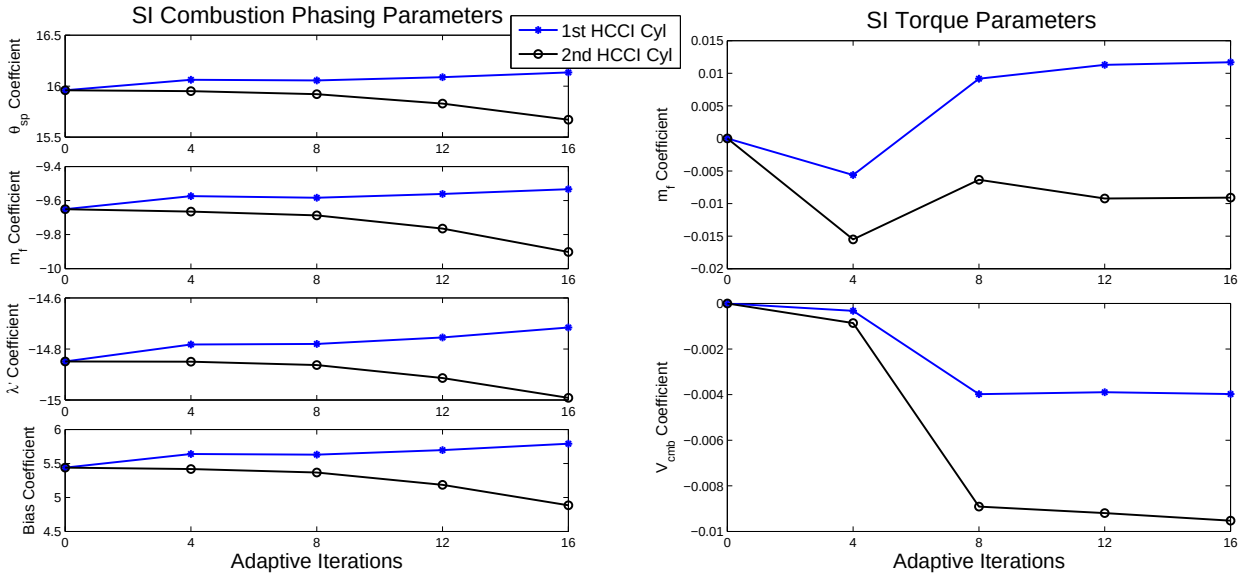

Figure 5.3: SI combustion phasing (left) and torque (right) model parameter variation with succesive SI-HCCI adaptations. The first and second cylinders to enter HCCI are referred to as $H1$ and $H2$, respectively.

Observing the combustion phasing parameter trajectories in Fig. 5.3, it can be seen that the parameters for the cylinder $H1$ tend to increase with successive adaptations, while the parameters of cylinder $H2$ tend to decrease. This is to be expected given that cylinder $H2$ was typically found to have earlier combustion phasing that $H1$. For both the cylinder $H1$ and $H2$ parameters, one attribute that stands out is that the trajectories for all parameters tend to follow the same shape, and the final values are not very far from the initial values on a percentage basis. The highest percentage change occurs for the bias parameter, which shifts by approximately 5% for cylinder $H1$ and 10% for cylinder $H2$. These observations suggest that the adaptation did not change the sensitivities of the θ_{50} regression to individual regressors much, but rather acted mostly to shift the correlation in one direction or the other by acting as a bias or scaling gain. Further experiments with different initial conditions and a wider set of operating conditions are necessary to confirm this hypothesis, but if such behavior is consistently observed in implementation, then it may be possible to simplify the adaptive parameterization for the SI θ_{50} regression to a simple gain or bias term. A last observation is that, after16 adaptive trials, the θ_{50} parameters do not appear to have settled to a steady-state value. It is unclear whether or not the parameters eventually converge to a steady value

without having experimental data which continues the successive adaptations to a higher number of trials. However, simulation investigation suggests that under idealized conditions, the parameter estimates could diverge after a large number of adaptive iterations, due to an implementation issue which was not addressed in the basic recursive least squares parameter update (5.2) - (5.4). However, the simulation results indicate that divergence of the parameters and resulting deleterious effects on controller performance only become significant after 50 or more adaptive iterations, so that the presented experimental results with 16 or less adaptation iterations still convey the positive effects of the adaptation without being distorted by problems of parameter divergence. This topic will be discussed in detail in the following subsection.

Moving now to the torque parameter trajectories in Fig. 5.3, it can be seen that again the relative difference between parameters of cylinders $H1$ and $H2$ matches the observations from the experiment, where cylinder $H2$ was typically observed to produce a lower torque than $H1$ for a given fuel command and so has lower (more negative) parameter values. Note that the parameters for both the first and second order V_{cmb} term followed the same shape of trajectory, and so only the first order term is shown for brevity. Returning to the topic of parameter convergence, it appears that the torque model parameters stay much closer to a steady value after 8 adaptive trials than was observed with the combustion phasing parameters. One simple possible reason for this behavior is that the initial values of the torque parameters may not be as far away from the final values to which they would converge over a large number of iterations as the combustion phasing parameters. Another reason may be that the torque model contains a lower number of parameters than the combustion phasing model, so that the torque parameters can be identified with a lesser degree of excitation. Thus, as mode transition trials are repeated and similar input and output signals emerge on each trial, causing parameter excitation to weaken, the torque model parameters remain more readily estimable than the combustion phasing parameters.

The discussion now moves on to consider the trajectories of the HCCI model parameters throughout sequential adaptations, which are plotted for the combustion phasing (left) and torque (right) correlations in Fig. 5.4. As with the SI combustion phasing parameters, only the number of parameters in the HCCI combustion phasing correlation is high, and so the figure focuses on a reduced set of parameters to show how key dependencies within the combustion phasing correlation change with successive adaptations. Observing these combustion phasing parameter trajectories, once again the cylinder individual trajectories comply with experimental findings, in that the parameters of cylinder $H2$ become more lower (more negative) than those of $H1$, giving a lower threshold for combustion and earlier combustion phasing. It can also be seen that, in general, cylinder $H2$'s parameters change to a much larger degree than those of cylinder $H1$, which is most likely due to the much higher ringing observed with this cylinder in HCCI making it's mismatch with the baseline parameterization greater. Observing the shapes of the parameter trajectories, it is apparent that, unlike the SI combustion model, different dependencies within the model take

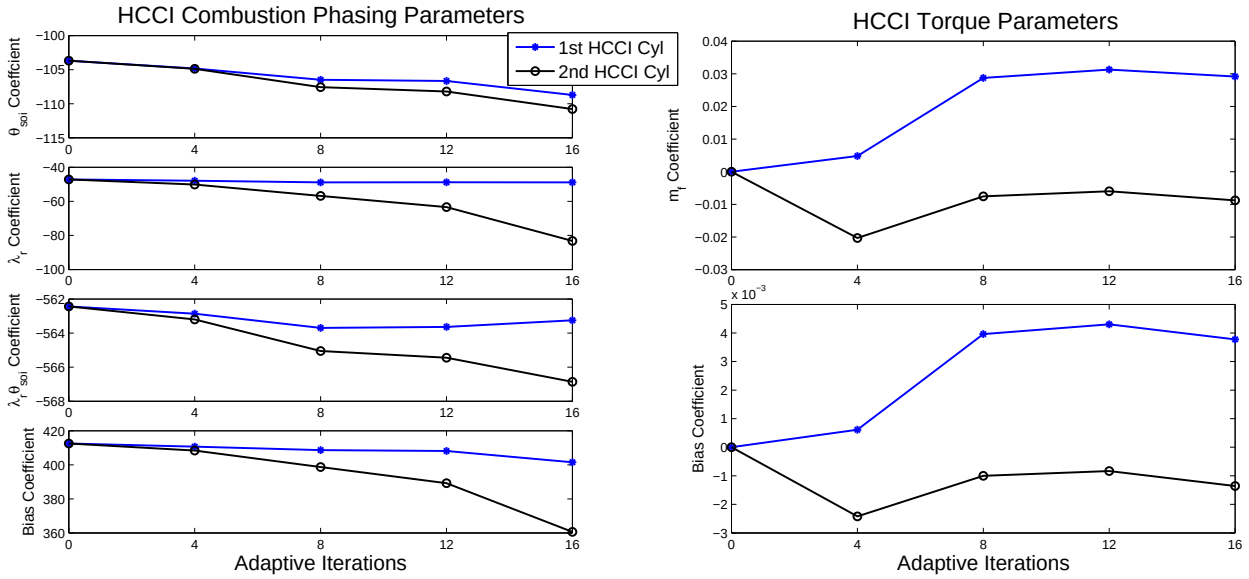

Figure 5.4: HCCI combustion phasing (left) and torque (right) model parameter variation with succesive SI-HCCI adaptations. The first and second cylinders to enter HCCI are referred to as $H1$ and $H2$, respectively.

different parameter paths throughout the adaptation. For cylinder $H1$, the θ_{soi} dependence follows a mostly decreasing trend, while the λ_r dependence remains relatively flat with minor fluctuations. For cylinder $H2$, the λ_r dependence follows a more strongly decreasing trend than the θ_{soi} dependence, and changes by a much greater extent on a percentage basis overall. Moreover, the parameter for the cross coupling term $\lambda_r\theta_{soi}$ tends to follow the same trend as the λ_r dependence for cylinder $H1$, but for cylinder $H2$ it follows a trend closer to the θ_{soi} dependence. It thus appears that during the adaptative iterations, the combustion phasing correlation is adjusted on a regressor-individual basis, to change the sensitivities of the correlation to different regressors. This is in contrast to the behavior of the SI combustion phasing correlation, which seemed to be mainly affected through a constant offset or scaling type adjustment. This result suggests that, for the HCCI combustion phasing correlation, the higher order parameterization with multiple regressor dependencies is advisable.

One other facet of the HCCI combustion phasing parameter trajectories in Fig. 5.4, which is in common with the SI combustion phasing correlation, is that again most parameters do not seem to be converging to a steady-state at the end of the adaptive trials. However, as stated for the SI combustion phasing correlation, simulations suggest that parameter divergence is not an issue for the low number of iterations considered in the successive adaptation experiments. It is lastly noted of Fig. 5.4 that the torque parameter trajectories exhibit similar behavior to those of the SI model, being lower for cylinder $H2$ and appearing to converge more closely to a steady value after 8

adaptive iterations.

In regard to the behavior of the parameters in the expression for the adaptive residual correction factor k_r, the experimental results suggested a lack of sufficient excitation to identify the two parameters set out in the basis function of Eq. (5.14). This manifested as a noticeable change in one of the basis function parameters, and a minute and negligible change in the other. Considering that the k_r adaptive method only operates on cycle *HCCI 0*, and that the operating condition was not changed, this result makes sense because the k_r adapation was essentially being carried out on the same data point over and over again (within stochastic variations). To truly identify the k_r correlation when more than one parameter is used, future experiments must execute the adaption at as least as many operating conditions as there are parameters in the k_r correlation (here two).

Numerical Investigation of Closed-Loop Stability in Successive Adaptations

It was seen in the combustion phasing parameter trajectories of the successive adaptation experiments that after 16 trials, most parameters did not appear to converge to a steady value. This raise the question of whether or not the estimated parameters of the adaptive scheme will converge in the limit, and if they do not if the closed-loop control system remains stable. Though it was noted in Sec. 4.3.2 that the SI combustion controller is inherently stable and that HCCI combustion controller displayed strong stability margins in the presence of parametric error, the stability of the full closed-loop system with recursive parameter updating in the loop is still not ensured by these facts.

Given the nonlinearities introduced by the use of recurisvely updated model parameters to drive the control input calculation (which still appear when individual components are linearized) and the high dimensionality introduced by adding dynamics to multiple parameters, analytical determination of the system stability is difficult. For this reason, a numerical study is carried out, where the full closed-loop SI-HCCI transition controller with adaptive parameter updating is simulated in consecutive mode transitions. The simulation mimics the scenario of the successive adaptations considered in the previously presented experimental results, in that the true plant model is set with parameter values from the end of the successive adaptive trials, while the controller model is set with the baseline parameters. A similar operating condition and forgetting factor are used as well. The post-adaptation parameters are taken from cylinder $H2$, which represents a greater plant model perturbation as cylinder $H2$'s parameters had a more substantial change during adaptation than those of cylinder $H1$. The goal of the simulation is then to investigate, over a large number of iterations, if the controller remains stable and if the estimated parameters converge to a steady value, and if so does this steady value match the true plant parameters.

Fig. 5.5 plots the results of the closed-loop SI-HCCI transition adaptive simulations by showing example parameter trajectories for each adapted correlation with successive adaptations. As can be

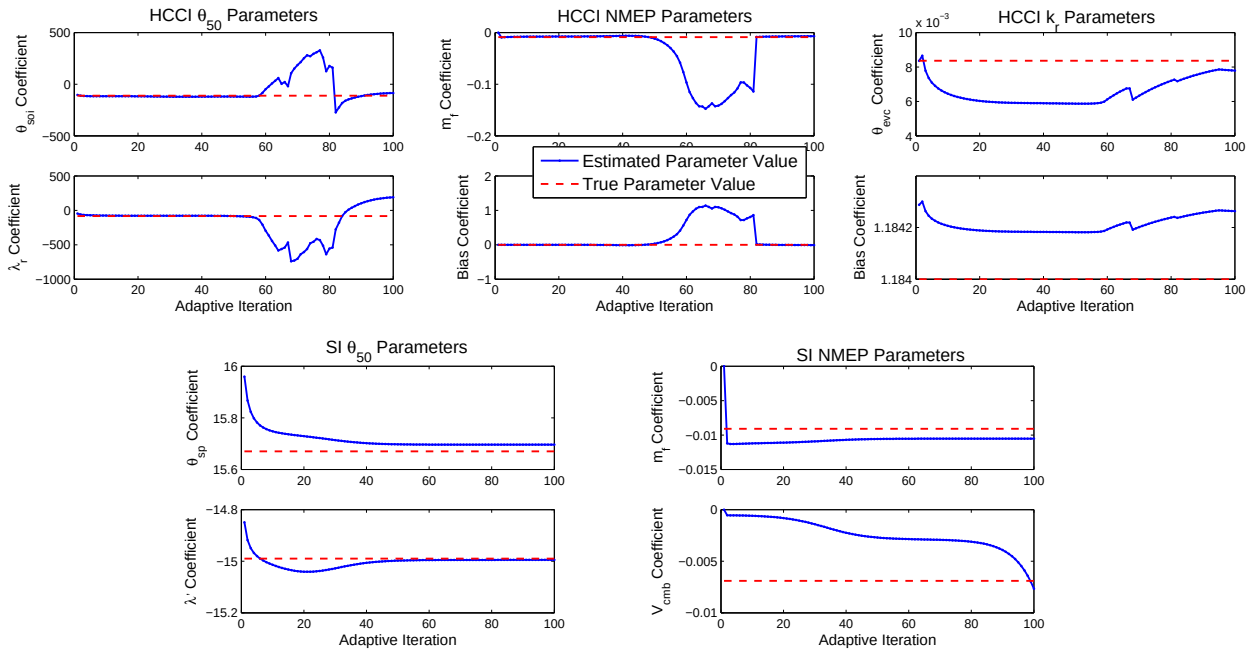

Figure 5.5: Parameter trajectories for each adaptive model correlation in simulation of successive closed-loop SI-HCCI adaptive trials for the baseline recursive least squares algorithm. HCCI model correlations shown in upper two subplots; SI model correlations shown in bottom two subplots. Forgetting factor kept at value of 0.94 from successive adaptation experiments.

seen, when starting the adaptive iterations, the parameters tend to shift by some reasonable amount towards the true plant value, and from there taper off with a slight drift after 15 or so adaptive iterations. However, as the number of adaptive iterations continues to increase, some parameters, most notably in the HCCI model, start to diverge tremendously from their starting value, and also the true plant value. These parameters then go through a period of very large fluctuations, before settling back down to more reasonable values where they then continue to drift slightly. The simulation thus predicts that the parameter estimates of the closed-loop adaptive system can become unstable when a high number of adaptive iterations is carried out at a fixed operating point.

To obtain an idea of how the controller response changes as the parameter estimates shift and eventually diverge during the successive adaptive trials, Fig. 5.6 plots the time histories of important inputs and outputs of the closed-loop simulation at several instances throughout the adaptive iterations. As can be seen, when starting from the baseline parameters with 0 adaptive iterations, the controller response contains errors in the torque and combustion phasing tracking, with the NMEP dropping significantly below the reference in both the SI and HCCI phases, and the θ_{50} having undesirable early excursions for several cycles after cycle *HCCI 0*. After 15 adaptive iterations, most of these negative effects are cancelled out by the controller learning the modeling error. The

torque remains close to its reference in both the SI and HCCI phases, save for an inevitable slight increase on cycle *SI -1* due to a shift of the EVO timing from the cam switch, and the θ_{50} tracks an essentially flat line besides cycle *HCCI 0* where the high exhaust temperature makes early combustion phasing difficult to avoid. The controller thus obtains nearly perfect response, with very little overall deviation in the outputs from their references. Examination of simulation results as the number of adaptive iterations increases past 15 shows that the controller tends to reproduce a similar near-perfect response, but as the number of adaptive iterations becomes very high and the diverging parameter region is entered, fluctuations start to arise in the controller commands. These fluctuations culminate on the 82nd adaptive iteration, where the command inputs wildly jump to extreme values in the HCCI mode, leading to very bad performance as depicted in Fig. 5.6.

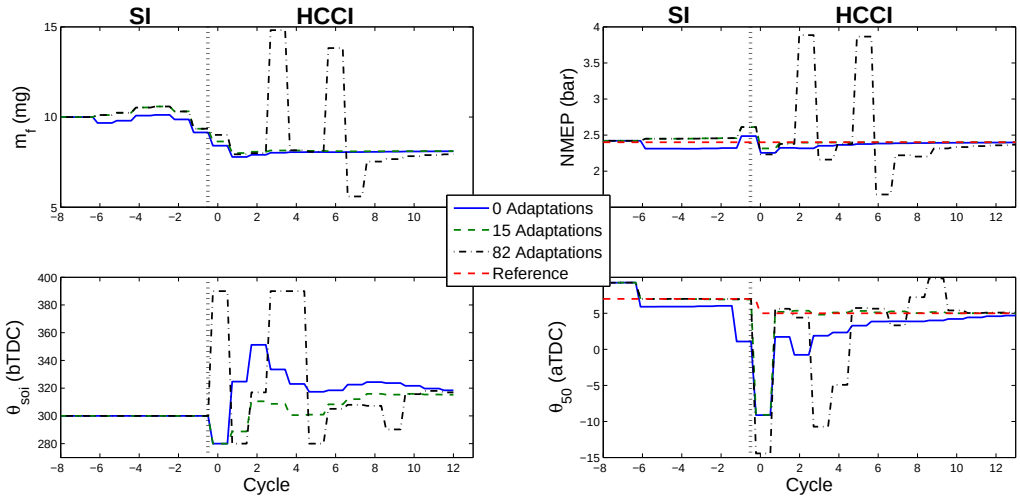

Figure 5.6: Input (left) and output (right) simulation responses at severeal instances throughout successive closed-loop SI-HCCI adaptive trials with baseline recursive least squares algorithm. Forgetting factor kept at value of 0.94 from successive adaptation experiments.

To gain insight into the source of the adaptive parameter divergence and resulting degradation of controller performance, Fig. 5.7 shows how the condition number of each correlation's recursive least squares P matrix (see Eq. (5.4)) changes throughout the adaptive trials. There is a clear trend that as the number of adaptive iterations becomes large, the condition number of the P matrix grows very large, so that the P matrix becomes very ill conditioned. Note that the P matrix is defined through $P = \left(\sum_{i=1}^{m} \Phi(i)\Phi^T(i)\right)^{-1}$, so that it depends on the time history of the regressor vectors. Thus, if the matrix becomes ill-conditioned, it signifies that the regressor vectors on each adaptive iteration are nearly the same, which can lead to a linearly dependent set of vectors. This is not surprising for a high amount of adaptive iterations, given that the controller attains nearly perfect performance and so essentially just repeats the same ideal trajectory on each iteration. However, because of the exponential discounting of data from the initial phases of the adaptive iteration introduced by the forgetting factor of the algorithm, the regressor vectors begin to become purely

based on the later, more repetitive trials as the number of adaptive iterations becomes high. Thus the regressor vectors that comprise the P matrix become less unique with increasing adaptive trials, causing it to become ill-conditioned. This phenomenon is referred to as estimator wind-up, and can cause instability in recursive least squares updating schemes with exponential forgetting in periods of repetitive control inputs and hence low excitation [64].

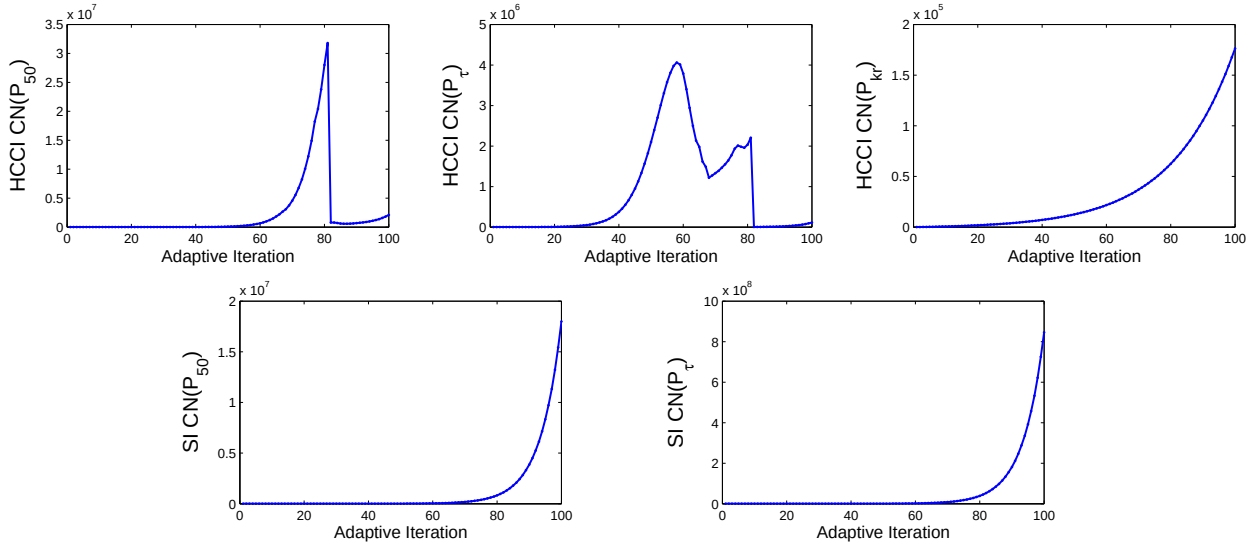

Figure 5.7: P matrix condition number (CN) of baseline recursive least squares algorithm in simulation of successive closed-loop SI-HCCI adaptive trials. Forgetting factor kept at value of 0.94 from successive adaptation experiments.

Given that the experimental implementation of the adaptive parameter estimation consistently experiences stochastic fluctuations, and most likely has a higher order, structural uncertainty as opposed to the simple parametric model uncertainty introduced in simulation, it is likely that parameter excitation will be remain higher in experiment than was experienced in the simulation study which will inhibit estimator wind-up. Additionally, an aggressive forgetting factor of 0.94 was used to expedite the successive adaptation experiments, however in a real world implementation a slower forgetting factor of 0.98 or 0.99 is more advisable, which will also slow the effects of estimator wind-up. Despite these observations, it may still be prudent to take measures to avoid potentially dangerous effects of estimator wind-up, and so a modified recursive least squares algorithm based on a concept called directional forgetting [64] is employed in Appendix D for this purpose. Repeated simulations of successive adaptive iterations with this modified parameter update show that the parameters converge and remain within a small window for a high number of adaptive iterations, and deleterious effects on controller performance are avoided. The converged values of the parameters do not exactly match the true plant values, most likely due to a loss of persistance of excitation as the control input sequence becomes repetitive with increasing adaptive trials, however it is of little

consequence given that the tracking performance of the controller is strong.

The remaining step in examination of the convergence of the parameter adaptation is then to return to experiment and repeat the successive SI-HCCI transition adaptive trials to a higher number of adaptive iterations. This is necessary to ascertain parameter convergence from an experimental standpoint, because the adaptive simulation results suggest that insufficient experimental adaptive iterations were carried out to decisively gauge convergence. The reason is that the number of adaptive iterations for parameter convergence in the simulation tends to be around 15, and the successive adaptation experiments were carried out only to 16 adaptive iterations. Given that the adaptive simulation considered a simple case of parametric uncertainty with a deterministic plant, the convergence time for the parameters in experiment is likely to be much longer given the higher order structural uncertainty and stochastic fluctuations presented by the true plant. For a more thorough experimental characterization of parameter convergence, it may be advisable to carry out at least double the convergence interval for the simulation, or 30 adaptive iterations. In these follow-up experimental trials, it is advisable to use the previously mentioned directional forgetting recursive least squares algorithm to mitigate potential estimator wind-up issues which can interfere with parameter convergence.

5.2.2 Differing Operating Conditions

The results of Sec. 5.2.1 show that the proposed parameter adaptation can yield significant improvements when applied at one operating condition. The effect of the adaptation on the controller response in differing operating conditions is now examined, in the limiting case where the adaptation is conditioned on data only from a single operating condition. That is, the controller parameters are adapted in successive SI-HCCI trials at a single operating condition, and then the controller is taken outside this condition to carry out SI-HCCI transitions without first being adapted at the altered conditions. This emulates the worst case scenario where a driver's behavior tends to favor entry to HCCI in a narrow range of conditions so that the controller adapts mainly in that range, and then the controller is suddenly taken outside that range due to a change in driving pattern. The danger is that the adaptation will "overfit" to a narrow range of conditions so that performance will suffer when these conditions are exited. The operating condition for successive adaptations corresponds to that of Sec. 5.2.1, so that the post-adaptation experimental results that follow are generated using parameter values taken at the end of the adaptive trials in Sec. 5.2.1.

The first set of experimental results considers varying load conditions for the SI-HCCI transition which span the HCCI load range of the experimental engine at 2000 RPM, similar to the low and high load conditions of Sec. 4.4. As in Sec. 4.4, cylinder $H2$ experienced problems with runaway knocking and unreasonable AFR/torque responses in the high load HCCI condition, and so its response is omitted in this case. Figs. 5.8 and 5.9 plot the combustion responses with the baseline

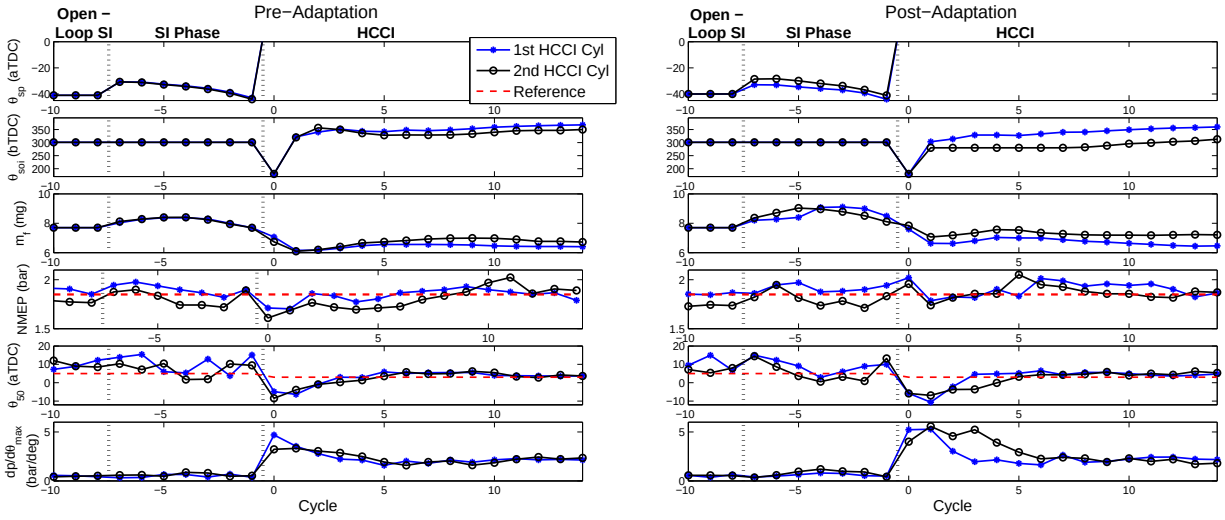

Figure 5.8: SI-HCCI mode transitions near the low load HCCI limit before (left) and after (right) successive adaptations at the operating condition of Sec. 5.2.1.

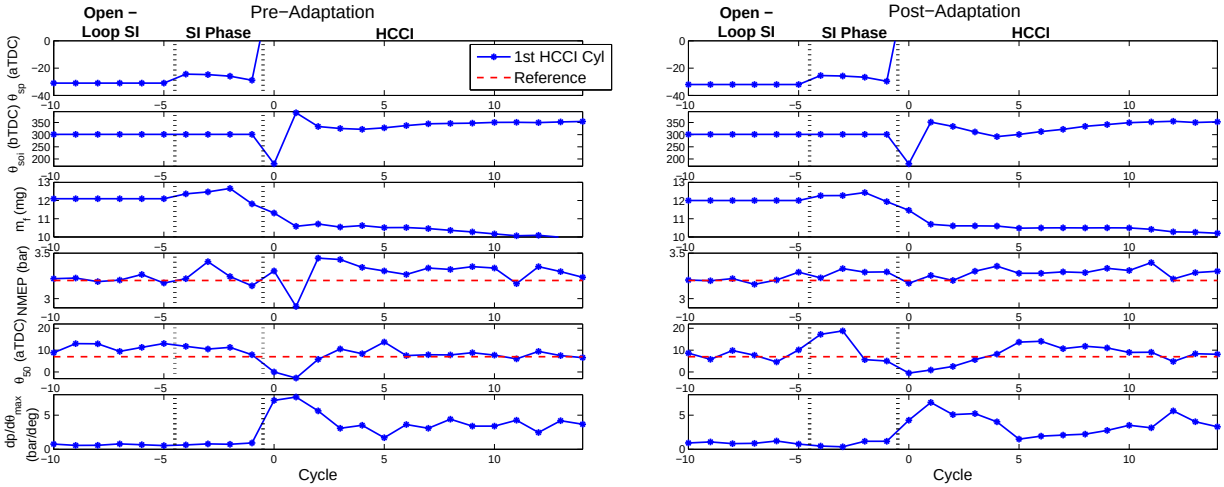

Figure 5.9: SI-HCCI mode transitions near the high load HCCI limit before (left) and after (right) successive adaptations at the operating condition of Sec. 5.2.1.

controller (left) and after adaptation at the operating condition of Sec. 5.2.1 (right) for the low load and high load cases, respectively. The general observation can be made from both plots that the $NMEP$ response appears more favorable after adaptation in all cases. In the low load case, the adapted parameters induce a higher fuel quantity when HCCI is entered, which essentially eliminates the drop in $NMEP$ seen in the baseline controller response for which the IMC feedback must compensate over multiple HCCI cycles. Note however that the higher fuel quantity commanded in

the post-adaptation case appears to contribute to θ_{50} values which are similar or even slightly earlier than the baseline case over the first few HCCI cycles. The post-adaptation controller commands later θ_{soi} than the baseline controller during these cycles to the point of saturating the θ_{soi} command on cylinder $H2$, however the effect on θ_{50} is not great enough to compensate for the higher fuel quantity and so greater $dp/d\theta_{max}$ values result for the post-adaptation controller. While the increased pressure rise rates are not of too great concern because they do not exceed the preferred threshold of 6 bar/degree in this case, the example still shows that it is possible for some performance variables to suffer while others benefit when the parameters are adapted over a small range and the operating condition is then changed. In the high load case, mainly positive results are seen comparing the pre- and post-adaptation responses, with the most notable benefit being the later θ_{soi} commanded on cycle *HCCI 1* in the post-adaptation case. The later θ_{soi} yields a less advanced θ_{50} than in the baseline case, mitigating the torque reduction that results on cycle *HCCI 1* in the baseline case and giving slightly lower $dp/d\theta_{max}$.

The second set of experimental results considers perturbations to the engine speed in a 500 RPM range about the nominally parameterized engine speed of 2000 RPM. Over this RPM range, the controller model has no speed dependent parameterization, with the engine speed only showing up in physical relationships such as the conversion of air flow to trapped mass. As with the high load case previously considered, cylinder $H2$ began experiencing runaway knocking and unreasonable AFR/torque responses at the higher speed perturbed condition, and so its response is omitted in this case. The low and high speed perturbed cases of 1750 RPM and 2250 RPM at the load condition of Sec. 5.2.1 are plotted in Figs. 5.10 and 5.11, respectively. Observation of the plots shows that both the baseline and adapted controller are able to handle the engine speed perturbation without any extreme pitfalls. However, comparison of the pre- and post-adaptation outputs shows that again the responses in the adapted case are predominantly favorable to the baseline. In the low speed perturbed condition, the SI phase $NMEP$ and θ_{50} responses stay closer to their references after adaptation, with the most notable effect being in the attenuation of the $NMEP$ drop and early θ_{50} observed in cylinder $H2$'s baseline response. In the HCCI phase, again the drop in cylinder $H2$'s $NMEP$ over the first several HCCI cycles is mitigated by the higher fuel command of the adapted controller. The θ_{soi} timing is also commanded later for both cylinders to aid in retarding θ_{50} to its reference, which has the greatest impact for cylinder $H1$ on cycle *HCCI 1* where θ_{50} retards significantly further than is seen with the baseline controller. In the high speed perturbed condition, the $NMEP$ and θ_{50} responses stay within a similar vicinity of their reference for both the pre- and post-adaptation cases, and so there is not much difference in this case. However, when HCCI is entered, the adapted controller commands a later θ_{soi} than the baseline controller on cycle *HCCI 1*, which yields a later θ_{50} and keeps the $NMEP$ reduction to a similar level despite that the fuel command is much lower in the adapted case. The lower fuel command of the adapted controller causes significantly less overshoot of the $NMEP$ reference after cycle *HCCI*, and also the

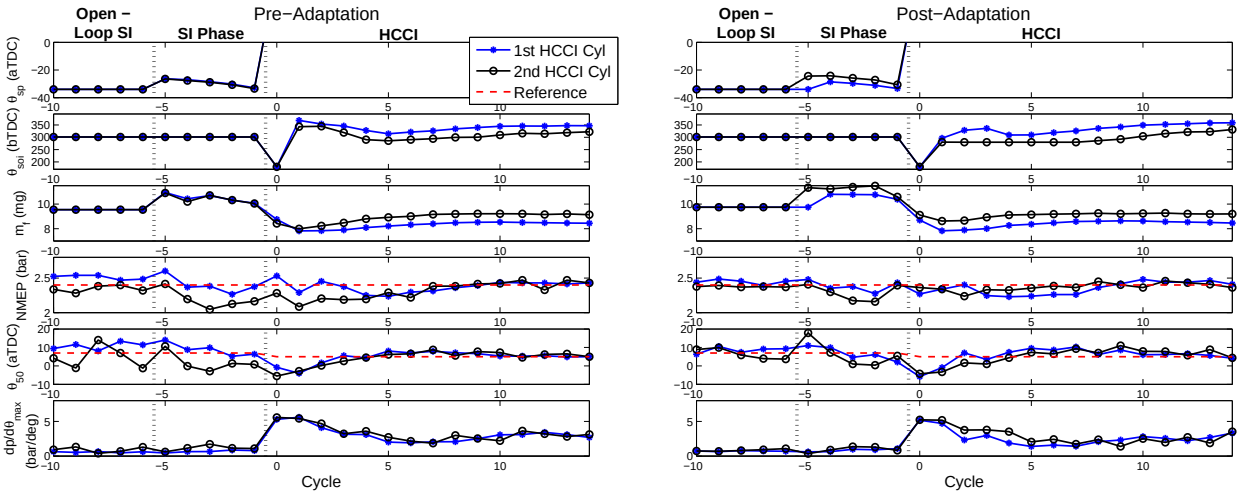

Figure 5.10: SI-HCCI mode transitions with negative 250 RPM speed perturbation before (left) and after (right) successive adaptations at the operating condition of Sec. 5.2.1.

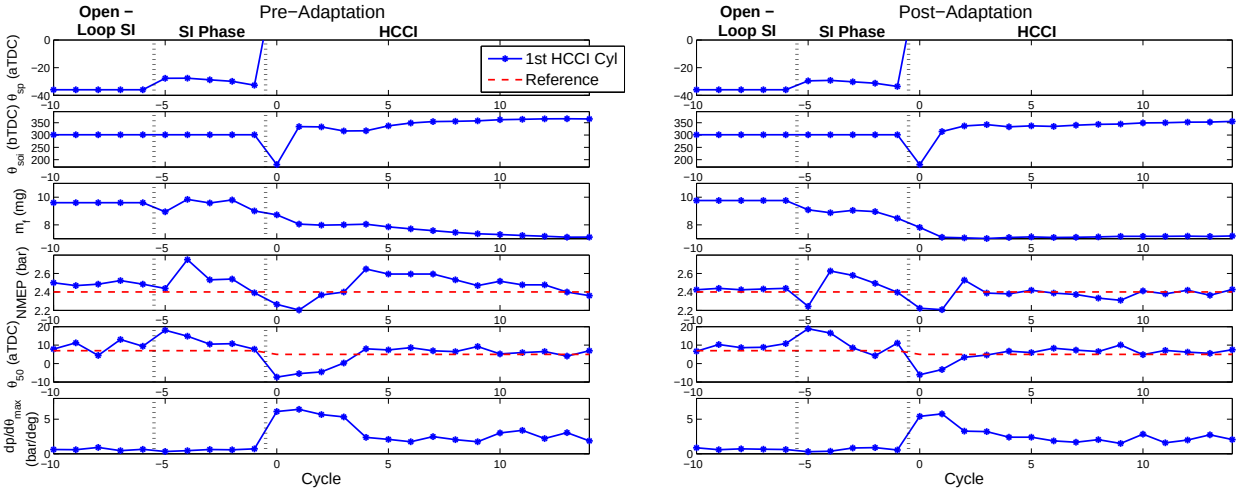

Figure 5.11: SI-HCCI mode transitions with positive 250 RPM speed perturbation before (left) and after (right) successive adaptations at the operating condition of Sec. 5.2.1.

θ_{soi} trajectory more quickly retards θ_{50} to its reference after entering HCCI in the adapted case, giving lower pressure rise rates.

Chapter 6
HCCI-SI Mode Transition Control

This Chapter considers the remaining portion of the SI/HCCI mode transition control problem, the HCCI-SI direction of the transition. The presentation is structured similarly to that of the SI-HCCI control architecture in Chapter 4, first examining the high-level actuator strategy and performance concerns for transitioning from HCCI to SI, and then going onto develop model-based feedback controllers for the HCCI and SI modes and testing them in experiment. The majority of the development is centered around the air path control component, as the HCCI-SI direction of the mode transition presents a more challenging scenario for proper air charge control than does the SI-HCCI counterpart. The combustion control follows largely from the architecture for the SI-HCCI direction, with one major modification necessary to cope with less favorable air path conditions.

The treatment of the HCCI-SI direction is not as extensive as for the SI-HCCI direction in previous chapters in that only the essential components of the mode transition strategy and closed-loop control architecture are given. Transient model validation against HCCI-SI transition data is not considered, and the control architecture is tested in fewer experimental conditions. Additionally, the effect of the parameter adaptation of Ch. 5 is not thoroughly explored, but rather the adaptation is employed at the outset to give better controller functionality and the model parameters are left at that state for all experiments. These less comprehensive aspects are due mainly to time constraints. However, the fundamental control architecture and strategy components presented still take significant strides past previous work, especially considering that all HCCI-SI transition studies in the literature have been purely open-loop, and show encouraging experimental results for an initial proof of concept.

6.1 High-Level Mode Transition Strategy

Following the procedure of the SI-HCCI controller development in Ch. 4, the high level strategy for transitioning from HCCI to SI is first discussed, to define the general paths of the control inputs throughout the transition. As in the SI-HCCI case, a cam switching type strategy is used wherein the mode is abruptly changed through a switch of the exhaust cam profile which induces a drastic change in internal residual quantity. The conceptual differences between this type of strategy and a

cam phasing strategy wherein the internal residual quantity is gradually adjusted through phasing of the exhaust cam instead of an abrupt switch are the same as in the SI-HCCI direction, which was reviewed in Sec. 4.1. For this reason, the cam switching and cam phasing strategies are not compared in detail here. It is simply noted that for whereas for the SI-HCCI direction the cam phasing strategy involved gradual advancing of the EVC timing and opening of the throttle, in the HCCI-SI direction the EVC timing is gradually retarded and throttle closed. The exhaust cam profile is switched to high lift at the end of the transition when the SI mode is reached, as opposed to the SI-HCCI direction where it was switched to low lift at the beginning of the transition. The only study in the literature that appears to have implemented a cam phasing strategy for the HCCI-SI direction of the mode transition is [29], where it was noted that the HCCI-SI direction is more difficult than the SI-HCCI direction with the cam phasing strategy. The reason is that the exhaust temperature is not initially higher so that in-cylinder temperatures are lower when passing through the "unstable area" between HCCI and SI combustion, making it more challenging to stabilize the combustion in the face of the high dilution. The ability of the cam switching strategy to bypass the "unstable area" is thus of great utility, though it will be seen that very unfavorable air path conditions must be passed through in order to do this, which makes HCCI-SI direction more challenging than the SI-HCCI counterpart with cam switching strategies as well.

6.1.1 Considerations for the Cam Switching Strategy

The Problem of Intake Manifold Air Storage

Perhaps the most critical and challenging feature of cam switching type HCCI-SI mode transitions is the difference in intake manifold pressure between HCCI and SI combustion. The reason the intake manifold pressure difference is so critical is that the manifold dynamics are more sluggish when decaying from higher HCCI levels to lower SI levels in an HCCI-SI transition than in the converse situation in an SI-HCCI transition. Fig. 6.1 plots the throttle input alongside the intake manifold pressure measurement during an experimental HCCI-SI transition to illustrate this point. The SI mode begins at cycle 0, denoted *SI 0*, following the dual convention to that used in SI-HCCI transitions in Chapters 4 and 5. The response is shown focusing on the instant where SI mode engages to observe the characteristics of the intake manifold dynamics, and the details of the how the transition is carried out and the controller design are left for later sections. Notice in the plot that although the throttle is commanded nearly fully closed (with a 2% saturation margin) one half cycle prior to the first SI cycle and held there for ≈ 2 cycles, there is still a 1.5-2 cycle decay time wherein the intake manifold pressure is significantly higher than the steady-state SI value at the given load. This is in contrast to the SI-HCCI p_{im} response shown in Fig. 4.12, wherein p_{im} is increased from ≈ 0.4 bar to 1 bar in roughly 20-30 milliseconds (1/3-1/2 cycle at 2000 RPM).

Efforts to command the throttle closed even sooner than in Fig. 6.1 to give a faster reduction in p_{im} were unsuccessful due to adverse effects on the HCCI combustion mode.

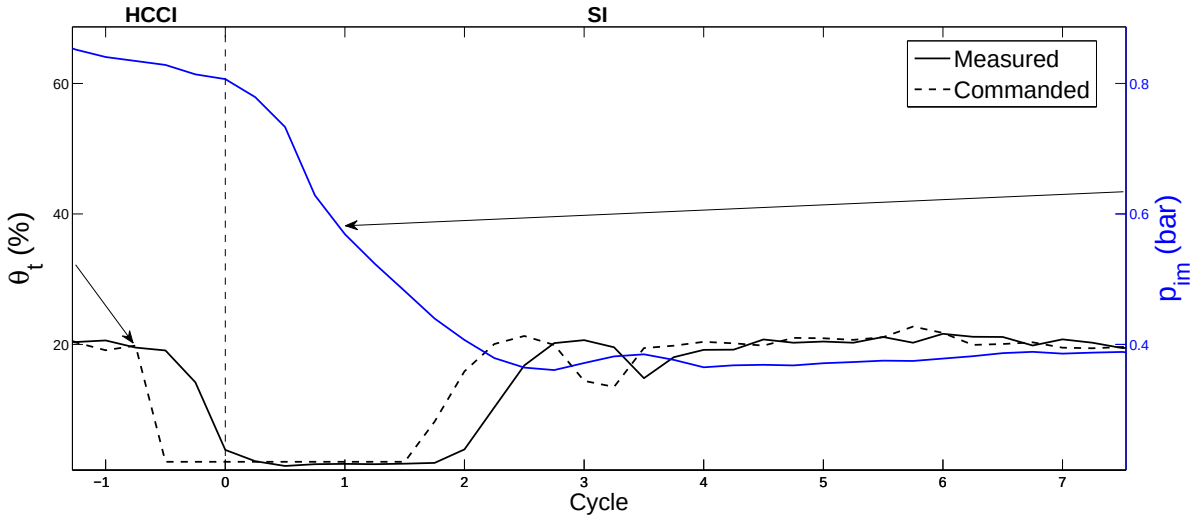

Figure 6.1: Data from an experimental HCCI-SI transition at 2000 RPM illustrating the time required for the intake manifold pressure to reduce to SI levels even with very aggressive throttle control. Continuous air path variables interpolated to be plotted versus engine cycle.

The large discrepancy between the intake manifold pressure response time when opening the throttle in an SI-HCCI transition and closing the throttle in an HCCI-SI transition is most likely due to the fact that when opening the throttle, there is essentially an infinite reservoir of air upstream of the intake manifold and so pressure can be built very fast. When closing the throttle, however, there is a given mass of air stored in the intake manifold, and that mass must be expelled by being pumped into the cylinders before a steady-state condition can be reached, which takes significantly more time. The reason this increased intake manifold pressure in SI is so problematic is that the SI AFR cannot stray too far from stoichiometric for emissions reasons. This is especially important during HCCI-SI transitions, where the exhaust catalyst may be saturated with oxygen from lean HCCI operation and so loses the ability to convert NOx [63]. The high air flow caused by the high intake pressure thus necessitates a large quantity of fuel to be injected, which can cause the engine torque output to greatly exceed the reference and interfere with drivability. Coping with this high intake pressure on the first several SI cycles is the most critical aspect of cam switching HCCI-SI mode transitions.

SI Fuel Injection Strategies for Compensation of Air Storage

The problem of intake air storage in the HCCI-SI direction of the mode transition has been witnessed in previous experimental studies. In cases where a fully flexible valve actuation device was available [20–22], the problem could be dealt with relatively straightforwardly through selection of the valve events and lifts to give appropriate air flow for stoichiometric SI combustion even with an atmospheric intake pressure. However, with the use of more practical two-stage cam and VVT hardware [23–28], the valve events and lifts cannot be adjusted as quickly and are limited in their range, motivating other measures to be taken via the fuel injection strategy. All the previous studies [23–28] employ the tactic of leaning the mixture when entering the SI mode by using a lower fuel quantity which is appropriate for operation in the HCCI load region (see Fig. 1.1), instead of increasing the fuel quantity as necessary to maintain a stoichiometric AFR with the higher air flow. The torque can thus be maintained near the target low load value by virtue of the lower fuel quantity. Some studies experience difficulties with partial burning/misfire and consequent large torque fluctuations when leaning the mixture in this manner, due to the high air dilution obstructing flame propagation [23, 25, 27, 28]. Others though are able to circumvent this problem using stratified fuel injection, which forms a locally rich area around the spark plug and aids the burn process [24, 26].

While combining the methods of lean AFR and stratified fuel injection appears capable of maintaining satisfactory torque regulation in the face of the high intake pressure and air flow during the initial cycles of the SI phase of the HCCI-SI transition, this strategy is not considered as a viable option here. The reason is that the degree of leaning must be high due to the large discrepancy in intake pressure, which promotes high NOx generation and leads to unburnt oxygen in the exhaust. These issues are especially critical for HCCI-SI transitions because the catalyst oxygen storage is charged while in lean HCCI operation, so that when switching back to SI operation, the catalyst NOx conversion efficiency may be very low [63]. A high NOx generation in the cylinder thus leads to very high tailpipe NOx emissions. NOx measurements during an HCCI-SI transition with lean SI operation can be seen in [24]. Furthermore, the excess oxygen in lean SI exhaust contributes even more to the catalyst oxygen storage, so that the catalyst may be rendered ineffective at converting NOx for an even longer period of time after switching from HCCI to SI.

In this dissertation, the contrary SI fuel injection strategy to those in [23–28] is taken; the AFR is commanded slightly rich when entering SI in an HCCI-SI transition, in order to mitigate NOx emissions and also deplete the catalyst oxygen storage through unburnt hydrocarbons in the exhaust. Fuel quantity is thus very high when first entering SI due to the intake air storage phenomenon, which makes torque regulation very difficult. The problem is approached by adjusting the valve timings and using aggressive throttle control to restrict air flow when entering the SI mode, while retarding the spark timing to compensate for the higher fuel quantity through non-optimal combustion phasing. Note that this retarded spark timing may also reduce NOx generation due

to lower burn temperatures, though an emissions study is necessary to truly see the effect. As will be seen, though, the degree of spark retard must be very high to reduce the torque to the appropriate levels, giving more cyclic variability and less precise torque control overall than the SI-HCCI direction of the mode transition. This is the main drawback of the cam switching HCCI-SI transition strategy.

Throttling Down the HCCI Mode

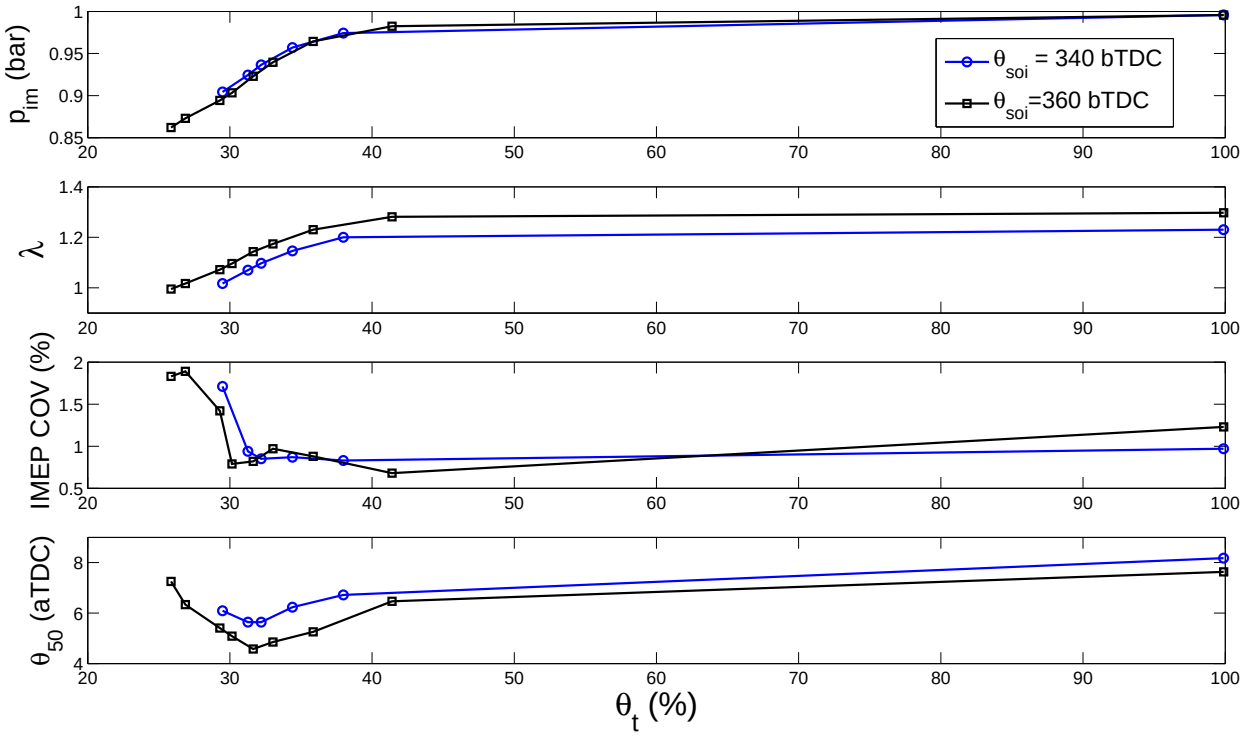

Figure 6.2: Steady-state throttle sweeps in HCCI mode for two different injection timings depicting the loss in combustion stability as HCCI becomes throttled.

Given the problem of intake air storage and undesirably high intake pressure when entering SI during an HCCI-SI transition, it is logical to throttle the intake flow while still in HCCI mode prior to switching to SI, so that the SI mode commences with a lower p_{im} initial condition. Though it is preferable to throttle the HCCI intake pressure down as close to nominal SI levels as possible, difficulty was found in significantly throttling the HCCI mode with respect to combustion stability. To illustrate this difficulty, Fig. 6.2 plots results from steady-state throttle sweeps in HCCI mode for two injection timings with all other quantities fixed. Note that the large jump from $\theta_t = 100\%$ to $\theta_t \approx 40\%$ is present because of the saturating nature of the throttle flow area, which causes the

throttle opening to have little effect after $\approx 40\%$ at 2000 RPM. The top two subplots show the expected trends that as throttle is closed, intake pressure and AFR (hence flow rate) decrease. The third subplot shows a less obvious trend, which is that as the HCCI combustion becomes more and more throttled, cyclic variability and torque oscillations as characterized by the IMEP COV sharply increase. This increase in cyclic variability prevented the further throttle closure in the sweeps, as misfire became eminent. The bottom subplot of θ_{50} confirms that this loss of combustion stability is not simply due to late combustion phasing, because even at the most throttled points, the θ_{50} values are earlier than with the throttle wide-open. The data thus suggests that there is some effect imposed by throttling the HCCI combustion which deteriorates combustion stability in a sharply nonlinear manner. One potential source of combustion instability could be the AFR approaching stoichiometric, around which point the sensitivity of combustion phasing to injection timing varies strongly with the AFR affecting the amount of oxygen available for recompression chemical reactions, so that cycle to cycle differences in AFR may have a large impact on combustion. Experimentation with the EVC timing during throttle closure supports this hypothesis, in that the throttle could be closed further without combustion instability at later EVC timings, which increase the AFR further into the lean regime. Another potential source is the lower intake pressure causing lower pressure in the cylinder and introducing variability into the chemical reaction rate that governs the auto-ignition timing. Though the cause of the combustion instability upon throttling is not certain, the implication on the HCCI-SI mode transition strategy is certain; that intake pressure cannot be reduced to near-SI levels while in HCCI mode, so that a significant gap in intake pressure will still be present upon switching to SI.

As noted above, the EVC timing was found to have an impact on how far the HCCI combustion could be throttled, with later EVC timings allowing greater throttling. This result may suggest that the optimal strategy is to retard the EVC timing as far as possible while in HCCI mode prior to switching to SI. There is, however, a trade-off in the placement of the EVC timing with which to switch to SI; as was shown in Fig. 4.2, earlier EVC timing in SI mode restricts the cylinder air flow for a given intake pressure. Thus, a later EVC timing while in HCCI will result in greater air induction for a given intake pressure when the exhaust cam is switched to high lift and SI is engaged. This is because the high lift and low lift cams are linked through a constant crank angle offset as reviewed previously (see Fig. 2.2). Additionally, it was found that the EVC timing is also limited in how far it can be retarded in the HCCI mode, with very late EVC timings leading to combustion instability due to lower in-cylinder temperature, even when trying to compensate with advanced spark and injection timing and throttle coordination. The choice of EVC timing for switching from HCCI-SI must take into account the trade-off between lower intake pressure and higher air flow when entering SI mode and respect the late limit on EVC timing for combustion stability.

6.1.2 Walkthrough of HCCI-SI Transitions with Chosen Strategy

Based on the considerations discussed in Sec. 6.1.1, the high-level actuator trajectories for the cam switching HCCI-SI mode transition strategy are defined in Fig. 6.3. As in the SI-HCCI direction of the transition, the intake cam is left in low lift for the duration of the mode transition transient, and is switched back to high lift at the end of the transition when nominal SI operation resumes. The reason for this decision is motivated by calibration simplicity given the minor impact of the high lift versus low lift intake cam discussed in Sec. 4.1.2. The intake cam switch can be accomplished with minimal effect on the engine flow rate for a significant range of intake valve timings, so that no compensation for the switch with other actuators is taken.

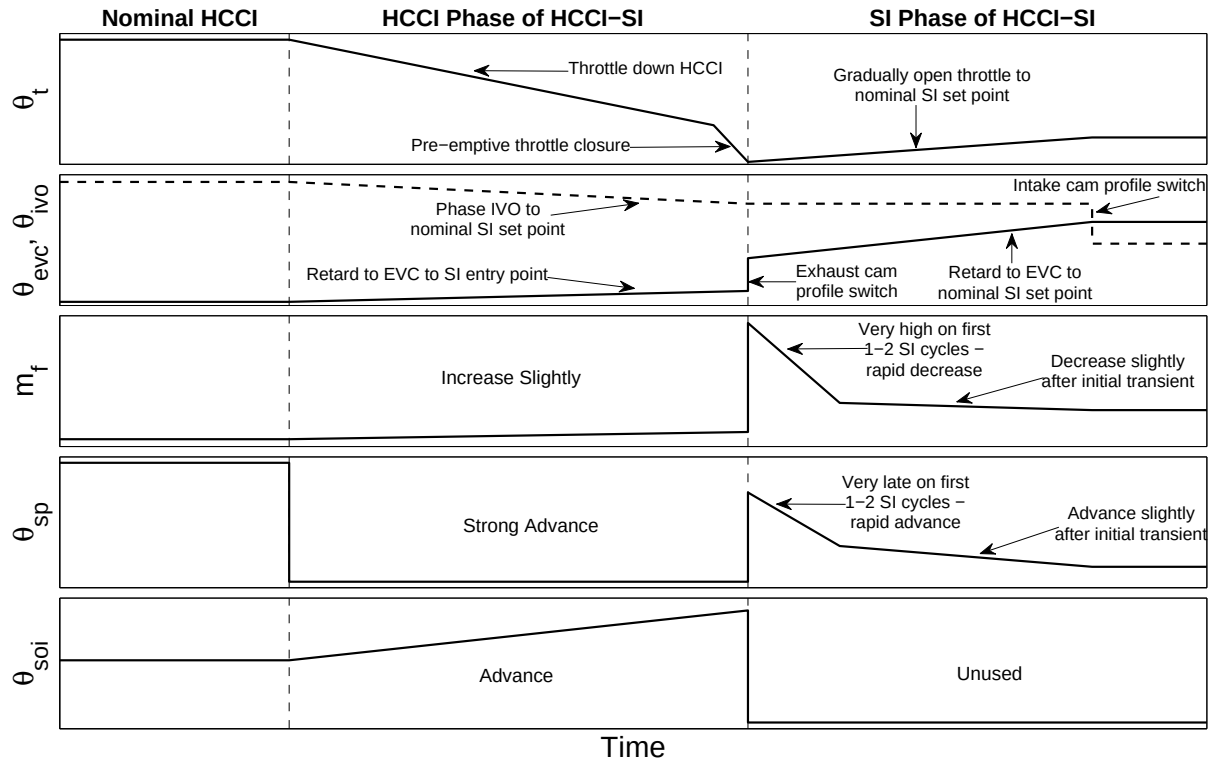

Figure 6.3: Representative depiction of high-level actuator trajectories for cam switching HCCI-SI transition strategy. θ_{soi} shown with reference to bTDC; all other timings shown with reference to aTDC.

The HCCI phase of the HCCI-SI transition is characterized by a significant reduction of the throttle opening to decrease the intake pressure for entry into SI as motivated in Sec. 6.1.1, along with an EVC timing which tends to retard from the nominal HCCI set point at the given load. The throttle reduction is large relative to the 100% nominal opening because of the inherent saturation in the throttle's effect on air flow above 40-50% opening at middle engine speeds. The EVC timing will tend to retard to keep the AFR in the lean regime as the throttle is closed by reducing trapped

residual and allowing more air to enter the cylinder, in order to avoid problems with combustion stability upon throttling noted in Sec. 6.1.1. As stated, though, the EVC placement must be chosen to balance the trade-off between stronger throttling while in HCCI with air flow restriction when SI is entered, so that the degree of EVC retard may be small in HCCI conditions which already have a high AFR.

Throughout the closure of the throttle and phasing of the EVC, the combustion actuators take several actions to compensate for the effects of the air path actuators on the in-cylinder conditions. The fuel mass tends to increase slightly as necessary to maintain constant torque, given the increased pumping loss from throttling the intake and also the lower air dilution which can reduce the mixture's ratio of specific heats and give less expansion work. In light of the combustion stability issues observed upon throttling HCCI in Sec. 6.1.1, the injection timing tends to advance in an effort to bring the combustion phasing earlier where cyclic variability is mitigated. Also to assist in this regard, the spark timing is placed very advanced during the HCCI phase of the transition. While having a smaller effect in HCCI mode due to the high dilution obstructing flame propagation, spark advance was still found to allow further throttling/later EVC timings to be achieved than when the spark did not interact with combustion.

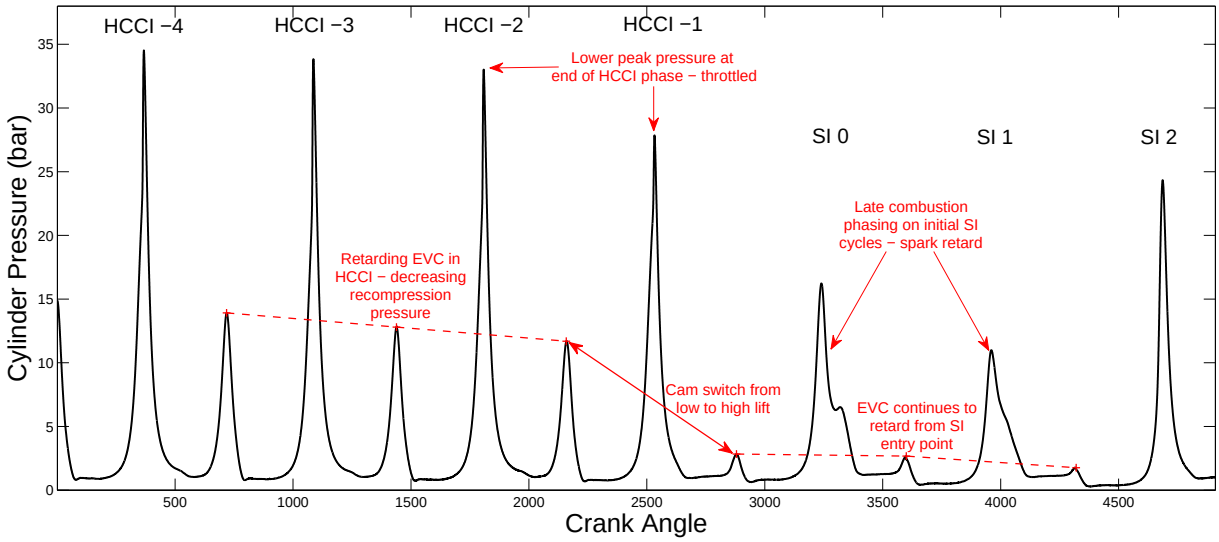

Figure 6.4: In-cylinder pressure data from a cam switching HCCI-SI mode transition illustrating the changes in combustion features over the course of the transition.

When the HCCI-SI switch point is reached, a pre-emptive command for closure of the throttle is issued slightly prior to the exhaust cam switch from low to high lift, in order to lead the manifold and actuator dynamics in decreasing the intake pressure in the SI phase of the transition. However, the pre-emptive closure cannot be issued too far prior to the start of the SI mode without adversely

affecting the HCCI combustion, so that when the SI mode engages, the intake manifold pressure is still high. The high intake pressure tends to require a large increase in the fuel quantity to keep the mixture stoichiometric or slightly rich as set out in Sec. 6.1.1, which also requires the spark timing to be very retarded to prevent the torque from spiking upwards too far. The fuel quantity and spark timing rapidly return to values close to those in nominal SI operation as the manifold pressure drops over the first 1-2 SI cycles, and the throttle is gradually returned to its nominal SI set point. From this point on, the main transient aspect corresponds to the EVC timing being phased from the early value upon entering SI to the nominal SI condition that is aTDC. Through this portion of the transition, the fuel quantity tends to decrease slightly as the EVC is phased to a more optimal position for SI fuel economy, and the spark tends to retard as the in-cylinder residual is reduced. The transition is ended when the intake cam switches back from low to high lift to resume standard SI operation.

6.2 HCCI Phase Controller

6.2.1 Control Problem Overview

The goal of the HCCI phase of the HCCI-SI transition strategy covered in 6.1.2 is to throttle down the HCCI combustion while adjusting the EVC timing to an appropriate position for switching to SI. During this transient, there are three main control objectives to consider, based on the performance objectives in Sec. 1.1.3:

- Deviations of the engine torque from the driver demand should be minimized as per performance objective 1.
- The combustion phasing should be kept as advanced as possible without inducing excessive pressure rise rates while the throttling down the HCCI combustion and retarding EVC, to promote better combustion stability and combat the issues observed in Sec. 6.1.1. This is motivated by performance objective 3, but also relates to performance objectives 1 and 2 in that partial burns and misfires from unstable combustion can reduce the torque output and give increased hydrocarbon emissions.
- The HCCI-SI switch point should be reached as quickly as possible as per performance objective 4.

It should be noted that although the spark timing is included in the strategy of Sec. 6.1.2 to aid the second control objective above, θ_{sp} is not considered as a control input because the HCCI model developed in Sec. 2.4 does not account for effects of spark assist on auto-ignition. Instead, the spark timing will be placed at a very advanced constant set point and treated as a disturbance to the nominal HCCI combustion phasing controller. The reason that this simple approach is valid is that the intention of using the spark timing in the HCCI phase is to advance combustion to help stabilize it as much as possible, allowing for higher throttling, which is achieved when spark timing is at its max advance.

Control Inputs	$u = \begin{bmatrix} u_t & u_{evc} & u_{ivo} & m_f & \theta_{soi} \end{bmatrix}^T$
Feedback Variables	$y = [NMEP \;\; \theta_{50} \;\; p_{im} \;\; T_{im} \;\; \theta_{ivo} \;\; \theta_{evc} \;\; \theta_t \;\; N_{eng}]^T$
Performance Variables	$w = \begin{bmatrix} NMEP & \theta_{50} \end{bmatrix}^T$
λ Rich Bound	$\lambda > \lambda_{min}$
Reference Commands	$r = \begin{bmatrix} NMEP^* & \theta^E_{50,H} & \lambda^* \end{bmatrix}^T$
Input Lower Bounds	$u_{low} = \begin{bmatrix} -120 & 5 & 180/280 & 0 \end{bmatrix}^T$
Input Upper Bounds	$u_{high} = \begin{bmatrix} -20 & 50 & 390 & 100 \end{bmatrix}^T$
Model States	$x = \begin{bmatrix} p_{im} & \theta_t & \dot{\theta}_t & \theta_{evc} & \dot{\theta}_{evc} & \theta_{ivo} & \dot{\theta}_{ivo} & T_{bd} & b_{bd} & f_{bd} \end{bmatrix}^T$

Table 6.1: Control problem formulation for HCCI phase of HCCI-SI transition.

Considering the stated control objectives in conjunction with the strategy outlined in Sec. 6.1.2 and the model in Ch. 2, the control problem is formulated following the logic in Table 6.1. Given that throttling the intake is a significant constituent of the HCCI phase of the transition, the control input suite expands from that in the SI-HCCI direction to include u_t, and the state description expands to include the throttle actuator dynamics. The IVO input and actuator dynamics states are also added in order to allow the intake timing to be phased prior to entry to SI, however the IVO timing will not be an important concern in the transition. As with the SI-HCCI direction, the torque and combustion phasing control objectives are treated through tracking of $NMEP$ and θ_{50} references, respectively, though now a modified θ_{50} reference $\theta^E_{50,H}$ is used. The symbol θ^E_{50} is intended to show that the θ_{50} reference can be placed earlier than the nominal θ_{50} reference $\theta^*_{50,H}$ in order for the controller to target earlier combustion phasing and improve combustion stability as per the defined control objectives. θ^E_{50} must not be chosen so early as to induce excessive pressure rise rates, however. In addition to the previously considered $NMEP$ and θ_{50} references, an AFR reference λ^* is now introduced. The purpose of the AFR reference is to ensure that the throttle regulates the cylinder air charge such that the intake pressure and cylinder air flow are in a reasonable range as EVC is phased to its HCCI-SI switch point throughout the HCCI phase. If the air flow is too high and $\lambda >> \lambda^*$, then the in-cylinder temperature can become low and lead to late combustion phasing, and additionally the intake pressure will not be reduced as much as possible for the switch to SI. If the air flow is too low and $\lambda << \lambda^*$, then the problems with combustion instability observed in throttle sweeps of Sec. 6.1.1 as the AFR approaches stoichiometric can arise. Control input saturation limits are listed for completeness, though they are the same as in Ch. 4. The salient difference to acknowledge is that, while the lower saturation limit of θ_{soi} was critical for the SI-HCCI direction to reduce ringing, now the upper saturation limit is critical as it bounds the ability of θ_{soi} to stabilize the combustion.

Now that the throttle plays a significant role in the HCCI mode, the air path control problem is not as basic as in the SI-HCCI direction, where the throttle was simply commanded wide-open. The control architecture thus contains a more detailed air path control component, while the combustion

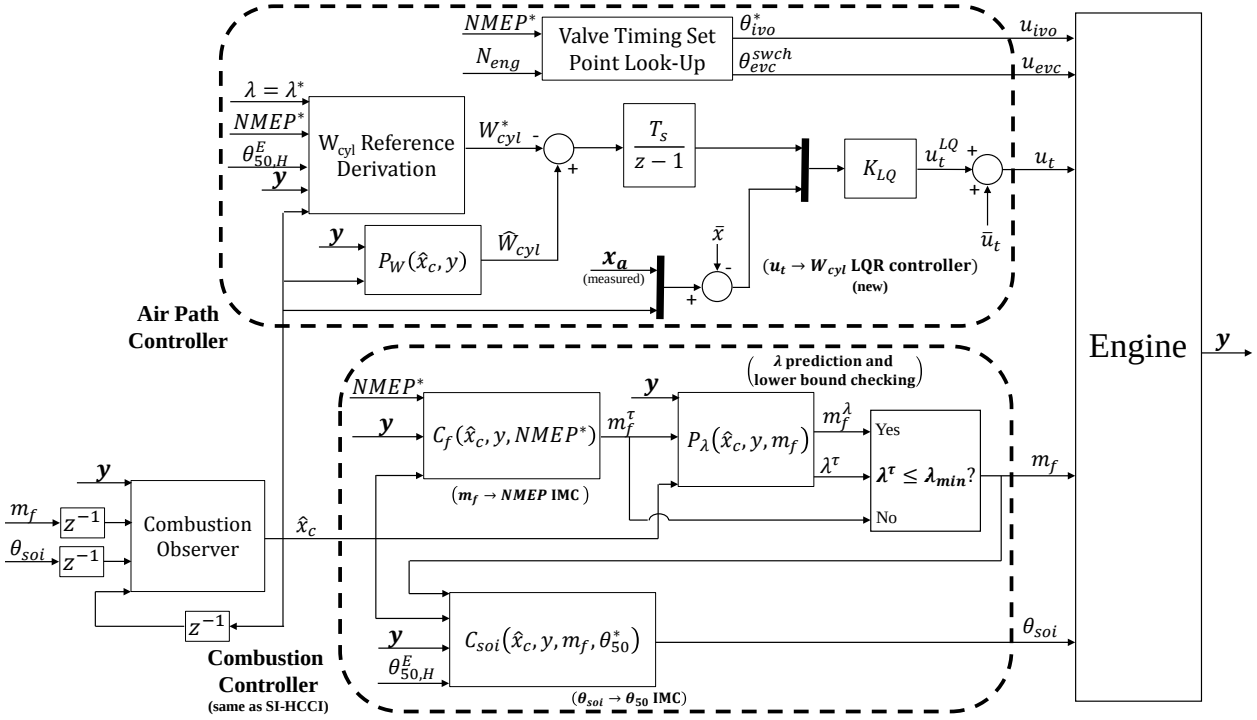

Figure 6.5: Block diagram of controller for HCCI phase of the transition. Variable names are as defined in Table 6.1. P blocks indicate calculations using the plant model, and C blocks indicate output feedback controllers.

control follows the same design as in the SI-HCCI direction. The combustion control is not changed because the motivating factors for its structure remain intact for the HCCI-SI direction; a large transient occurs over a short amount of time and the combustion control loops are relative degree 0, so that model inverse calculations can compensate for disturbances before they occur without any dynamics, and IMC output feedback can help attenuate model error. An added benefit can be attained if the same combustion control structure is used in HCCI mode prior to initiating the HCCI-SI transition, as the IMC feedback will have already adjusted to cancel the model error, so that modeling error biases will be accounted for at the start of the transition. Note though that this added bonus is not assumed to be available in the development or validation, however. The air path and combustion control are integrated in the same way as the SI phase of the SI-HCCI transition, where the air path control executes on a time synchronous sample loop and the combustion control executes on a cycle synchronous sample loop. A block diagram of the control architecture for the HCCI-SI transition is shown in Fig. 6.5, with the combustion control architecture reproduced for convenience. Given that the combustion control is unchanged from the SI-HCCI direction, only the air path control is explained in what follows.

6.2.2 Air Path Control

The overall architecture of the air path control is:

- u_{ivo} is stepped to the set point θ^*_{ivo} which is determined from the nominal SI set point at the given operating condition, which is assumed to be available from a look-up table in engine speed.
- u_{evc} is ramped to the set point θ^{swch}_{evc}, which is calibrated to give a favorable starting condition for the air path when the exhaust cam is switched to high lift and SI mode engages. It is stored in a look-up table versus engine speed and load.
- u_t is commanded through a LQR feedback controller with gain K_{LQ} to track a time-varying reference cylinder flow rate W^*_{cyl}.
- The reference W^*_{cyl} is derived from a model-based calculation to achieve $\lambda = \lambda^*$ with the constraints $NMEP = NMEP^*$ and $\theta_{50} = \theta^E_{50,H}$ with one step look-ahead valve timing disturbances.

The intake and exhaust valve timing control in the HCCI phase of the HCCI-SI transition is treated in essentially the same way as in the SI phase of the SI-HCCI transition. The major feature is that the EVC timing is adjusted to some set point θ^{swch}_{evc} which is calibrated for favorable (or perhaps least unfavorable) entry in SI. The selection of θ^{swch}_{evc} must be based on the trade-off discussed in Sec. 4.1.2, with later θ^{swch}_{evc} allowing further throttling and greater intake manifold pressure reduction prior to entering SI, but also imposing a later EVC timing when the SI mode begins, allowing more air flow. Because the effect of θ_{evc} on the air path and combustion is so strong in HCCI mode, a ramp interval N^{EVC}_{ramp} is introduced over which u_{evc} is linearly interpolated to θ^{swch}_{evc}, to allow θ_{evc} to more gradually approach θ^{swch}_{evc}. This is not as preferable as a step input for u_{evc}, which would approach θ^{swch}_{evc} the fastest and hence shorten the duration of the HCCI phase following the control objective listed in Sec. 6.2.1. However, the more gradual EVC profile was found to yield better performance in giving the throttle more time to move from its nominal 100% position to the 30-40% range where it has authority, and in general slowed down the EVC disturbance to the air path and combustion giving a gentler transient.

Throughout the motion of the valve timings to their HCCI-SI switch points, the throttle is tasked with regulating the cylinder air flow to maintain the AFR at the λ^* set point introduced in Sec. 6.2.1. The method by which this is done involves the W_{cyl} reference derivation and LQR throttle feedback controller depicted in Fig. 6.5. These controller components are explained in the following subsections.

W_{cyl} Reference Derivation

For higher loop bandwidth, it is desirable to convert the setpoint λ^* into something more readily trackable by the throttle, since tracking λ directly necessitates uses of the exhaust oxygen sensors which have a very large transport delay and sensor dynamics relative to the short duration of the HCCI phase of the HCCI-SI transition. An obvious first choice is the intake manifold pressure,

which was used as a reference for the throttle controller in the SI phase of the SI-HCCI transition. However, when significant throttling and EVC phasing occurs in the HCCI phase of the transition, the reference for intake manifold pressure exhibits significant time variation, making it harder to track than in the SI phase of the SI-HCCI transition where the degree of variation was smaller. For this reason, the choice is made to convert the λ^* reference into a cylinder flow rate reference W^*_{cyl}, since the cylinder flow rate for a given AFR changes much less throughout the HCCI phase because the fuel and so air mass do not need to change much. The W^*_{cyl} reference can be thought of as a nonlinear transformation on an intake manifold pressure reference, which takes other measured variables and state dependencies into account to arrive at a set point with less time variation. Indeed, if the predicted cylinder flow rate $\hat{W}_{cyl}$ perfectly tracks W^*_{cyl} in Fig. 6.5, then the measured p_{im} will perfectly track the required value to achieve $\lambda = \lambda^*$, because there is a one-to-one mapping between p_{im} and W_{cyl} for a given set of measured variables and state estimates.

The method to derive the reference W^*_{cyl} drives the last point home. W^*_{cyl} is derived by first solving for the intake pressure to give $\lambda = \lambda^*$, and then converting this value to a required cylinder flow rate using the model's air charge calculations. This approach is taken to simplify the calculations, because the IVC pressure p_{ivc} appears much more throughout the model equations than does W_{cyl} or m_a, and so it is easier to substitute for W_cyl in terms of p_{ivc} than the other way around. As with the throttle reference calculation in the SI phase of the SI-HCCI transition, the valve timings used to derive the W_{cyl} reference are propagated one time step into the future with the discretized actuator dynamics model (4.1).

The principle behind the derivation of W^*_{cyl} is the same as that for the p^*_{im} derivation for the SI phase of the SI-HCCI transition in Sec. 4.2.2; the combustion model is inverted under constraints for torque, combustion phasing, and AFR tracking, $NMEP = NMEP^*$, $\theta_{50} = \theta^E_{50,H}$, and $\lambda = \lambda^*$. Again the derivation starts from the model's gross work relation, which is given in reduced form for the HCCI combustion model in Eq. (4.25). The problem in this equation is the efficiency factor η_λ which is a function of λ_c, and so introduces higher order dependencies on the intake pressure and air charge. If dealt with by direct substitution of the equations for the fresh and residual air mass (2.79), (2.71), it can be shown that the resulting equations contain a third order polynomial dependence on p_{ivc}, which is difficult to solve. In order to bypass this difficulty, an approximation is made where the in-cylinder AFR λ_c is roughly correlated to the exhaust AFR λ through a linear function,

$$\lambda_c^{fit} \approx a_{\lambda 1}\lambda + a_{\lambda 0}. \tag{6.1}$$

The fit of λ_c versus λ for the experimental HCCI actuator sweep data of Appendix A is shown in Fig. 6.6. Note that the range of λ is constricted between 1 and 1.2 for a better fit in this range, because it is likely that the set point λ^* will be tuned within these limits.

With the approximation in Eq. (6.1), η_λ can be trivially evaluated under the constraint $\lambda = \lambda^*$

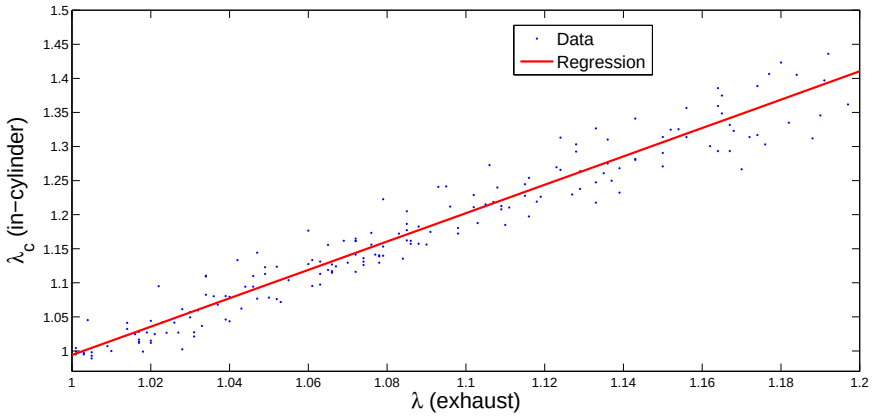

Figure 6.6: Linear approximation of λ_c versus λ HCCI actuator sweep data of Appendix A. Note that only $\lambda \in [1, 1.2]$ is considered.

by substituting $\lambda = \lambda^*$ into Eq. (6.1) and then that result into Eq. (2.93). Then substituting

$$m_f = \frac{m_a^{in}}{AFR_s\lambda^*} \tag{6.2}$$

which also follows from the constraint $\lambda = \lambda^*$ into Eq. (4.25), the equation becomes

$$W_{cig} = c_1 p_{ivc} + c_2(c_1 p_{ivc} + \frac{\frac{m_a^{in}}{AFR_s\lambda^*} Q_{lhv} R}{c_v V_{cmb}} \eta_\lambda^{fit}) \tag{6.3}$$

where η_λ^{fit} is evaluated from Eq. (2.93) using λ_c^{fit} and the intermediate quantities c_1 and c_2 are as defined in Eq. (4.6). Note V_{cmb} is evaluated at $\theta_{50,H}^E$ as per the listed constraints. Defining

$$c_{3H} := \frac{Q_{lhv} R \eta_\lambda^{fit}}{c_v V_{cmb}} \tag{6.4}$$

and substituting into Eq. (6.3) along with the expression (2.79) for m_a^{in},

$$W_{cig} = c_1 p_{ivc} + c_2(c_1 p_{ivc} + c_{3H} \frac{a_{1a} p_{ivc} V_{ivc} - m_r T_r + a_{2a}}{T_{im} AFR_s \lambda^*} \tag{6.5}$$

where a_{1a} and a_{2a} come from Eq. (2.79) and the simplification $(m_r + m_f) \approx m_r$ has been made with minimal error to avoid introducing another m_f dependency which has already been eliminated. Finally, defining

$$c_{4H} := T_r + T_{im} AFR_s \lambda^* \tag{6.6}$$

and substituting into Eq. (6.5) with $W_{cig} = (NMEP - P\bar{M}EP)V_d$ from Eq. (2.99), p_{ivc} can be

isolated due to the linear dependence, which can be shown to result in

$$p^*_{ivc} = \frac{c_{4H}(NMEP^* - P\bar{M}EP)V_d/(c_2c_{3H}) + m_rT_r - a_{a2}}{a_{a1}V_{ivc} + c_{4H}(c_1 + b_1c_2)/(c_2c_{3H})} \tag{6.7}$$

where b_1 is as defined in Eq. (4.3), and the expressions for m_r and T_r must be evaluated with the HCCI model equations with the given state estimates and measured quantities. This gives the required p_{ivc} to satisfy the constraints $NMEP = NMEP^*$, $\theta_{50} = \theta^E_{50,H}$, and $\lambda = \lambda^*$. Note that this is equivalent to solving for a reference intake manifold pressure since p_{ivc} and p_{im} are linearly related in the model of Sec. 2.4 and are exactly the same in the reparameterized model of Appendix A. Now p^*_{ivc} is transformed to a cylinder flow rate reference using Eqs. (2.79) and (2.37),

$$m_a^{in*} = \frac{1}{T_{im}}\left[a_{1a}p^*_{ivc}V_{ivc} - m_rT_r + a_{2a}\right] \tag{6.8}$$

$$W^*_{cyl} = \frac{m_a^{in*}N_{eng}}{120N_{cyl}} \tag{6.9}$$

and the derivation is complete.

LQR Throttle Controller

While the throttle control in the SI phase of the SI-HCCI mode transition was addressed with a simple lead filter, the control problem in the HCCI phase of the HCCI-SI direction presents considerably more difficulty. The disturbance induced by the phasing of the exhaust cam has a stronger effect due to the higher sensitivity of the HCCI mode to combustion phasing, and the transition in the intake pressure is larger. Additionally, in the HCCI mode, the combustion is much more sensitive to the thermodynamic state in the cylinder, on which the intake air flow has a strong effect. This is especially important given the reduced combustion stability which can occur during throttling which was observed in Sec. 6.1.1, which implies that errors in the in-cylinder conditions caused by inappropriate air flow have a greater chance of causing combustion abnormalities. For these reasons, a moderately more sophisticated throttle control design is pursued here.

The chosen design methodology for the $u_t \rightarrow W^*_{cyl}$ controller is LQR with an augmented integrator for set point tracking. The LQR methodology allows higher order, linear quadratic optimal controllers to be synthesized while requiring tuning of only a few intuitive cost function weighting parameters. The main drawback of LQR over simpler designs such as lead-lag and PI is that it requires knowledge of the system state. However, this does not arise as a problem for the $u_t \rightarrow W^*_{cyl}$ system, however, as all air path states are measured, and the combustion states are already estimated via the observer developed in Sec. 4.3.3. Additionally, for the SISO $u_t \rightarrow W^*_{cyl}$ structure with integral tracking, the tuning of the LQ weighting matrices becomes extremely simple

in that only one input weight and one output weight are present, so only their ratio need be tuned. Note that because the combustion states are estimated with a Kalman filter design, strictly speaking the controller classifies as LQG, however the estimator is unchanged from its structure in Sec. 4.3.3 and so is not considered part of the air path controller.

A potential caveat with the LQR state feedback structure for the HCCI mode is the problem of differing sample times between the air path and combustion states, with the air path states defined on a 10 msec time synchronous loop and the combustion states defined on a quarter cycle loop which can update at any sample time between 10-20 msec within the HCCI speed regime. Also, the combustion states vary from one cylinder to the next, which may introduce variability in the state feedback time sequences. Inspection shows that the only combustion state which has a considerable impact on the W_{cyl} output is T_{bd}, and the effect is secondary compared with the air path states of p_{im} and θ_{evc}. This makes physical sense given that it affects the temperature and so pressure of the residual gas. Throughout the HCCI phase of the transition, it is assumed that the T_{bd} state estimate changes gradually without any extreme jumps, because the main impact on the in-cylinder conditions are through the movement of the EVC and throttle which are inherently gradual due to actuator dynamics and the EVC ramp interval. With a gradual T_{bd} change, it is reasonable to assume that differences in the T_{bd} estimate within the sample time offsets of the time synchronous and crank synchronous loops and between cylinders has a negligible effect on the throttle control, especially because the effect of T_{bd} on W_{cyl} is smaller than that of p_{im} and θ_{evc}. The combustion state estimates are thus taken at their most recent estimates for the most recent cylinder for feedback to the LQR throttle control. As will be seen in Sec. 6.4, throttle control input commands with this convention remain smooth and devoid of chattering.

The LQR design is based on a linearized and discretized state space representation of the SISO system

$$x_t^{k+1} = Ax_t^k + b_t u_t^k \tag{6.10}$$

$$W_{cyl}^k = c_W x_t^k \tag{6.11}$$

where the input and output vectors b_t and c_W are unique to the throttle input and air flow output, respectively, and the state vector for the control problem x_t is defined as the concatenation of the air path state measurements x_a and the combustion control state estimates $\hat{x}_c$

$$x_t := \begin{bmatrix} x_a & \hat{x}_c \end{bmatrix}^T \tag{6.12}$$

$$x_a := \begin{bmatrix} p_{im} & \theta_t & \dot{\theta}_t & \theta_{evc} & \dot{\theta}_{evc} \end{bmatrix}^T \tag{6.13}$$

where $\hat{x}_c$ is as defined in Sec. 4.3. The states for the IVO timing have been dropped from x_a due to their minimal influence when the low lift intake cam is in place. The linearization is carried out in

a throttled HCCI condition where throttle is closed to the range of $\approx$ 25-35% where the throttle orifice profile is roughly linear profile, making the assumption of linearity more valid.

For reference tracking, an integrated output error state is augmented to the system

$$q_W^k = \sum_{i=0}^{k} (W_{cyl}^i - W_{cyl}^{i*}) T_s = q_W^{k-1} + (c_W x_t^k - W_{cyl}^{k*}) T_s \tag{6.14}$$

where the simple forward Euler integration can be reduced to the depicted first order difference equation. Augmenting this difference equation to the baseline system gives

$$\begin{bmatrix} x_t^{k+1} \\ q_w^{k+1} \end{bmatrix} = \begin{bmatrix} A & 0 \\ T_s c_W & 1 \end{bmatrix} \begin{bmatrix} x_t^k \\ q_W^k \end{bmatrix} + \begin{bmatrix} b_t \\ 0 \end{bmatrix} u_t^k + \begin{bmatrix} 0 \\ -T_s I \end{bmatrix} W_{cyl}^{k*} \tag{6.15}$$

$$W_{cyl}^k = \begin{bmatrix} c_W & 0 \end{bmatrix} \begin{bmatrix} x^k \\ q_W \end{bmatrix} \tag{6.16}$$

Defining

$$A_{aug} := \begin{bmatrix} A & 0 \\ T_s c_W & 1 \end{bmatrix} \tag{6.17}$$

$$B_{aug} := \begin{bmatrix} b_t \\ 0 \end{bmatrix} \tag{6.18}$$

$$C_{aug} := \begin{bmatrix} c_W & 0 \end{bmatrix} \tag{6.19}$$

a standard LQR solution can be applied to the augmented system, penalizing only the augmented output error state as this is the only state which is intended to be tracked to 0,

$$Q_t = \text{diag}[0_{8\times 8}, q_W], R_t = r_t \tag{6.20}$$

where $q_W > 0$ and $r_t > 0$ are scalar. The resulting gain K_{LQ} is applied to the augmented state vector to determine the LQ throttle command

$$u_t^{LQ} = -K_{LQ} \begin{bmatrix} x_t^k \\ q_w^k \end{bmatrix} \tag{6.21}$$

The control law is implemented as shown in the air path control block of Fig. 6.2, where the state linearization point $\bar{x}$ is subtracted off of the state feedback x_t before execution of the control law, and the control input linearization point $\bar{u}_t$ is added back into control input afterwards.

6.2.3 Cam Switch Logic and the Final HCCI Cycle

Considering that the same structure of defining an EVC set point at the mode switch boundary condition as in the SI-HCCI direction is also used in the HCCI-SI direction, the logic for determining when to switch the exhaust cam and change combustion modes is kept the same. The exhaust cam is switched to high lift to engage SI combustion when θ_{evc} is within some window δ_{evc} of θ_{evc}^{swch}, where δ_{evc} is kept at the same value as in the SI-HCCI direction. This logic can be viewed in control block diagram form in the SI phase of the SI-HCCI transition in Fig. 4.6; it is not reproduced in the HCCI-SI control block diagram in Fig. 6.5 because of it's extreme simplicity. Also similar to the SI-HCCI direction, a throttle pre-step factor N_{pre}^{CT} is included to give the throttle a "head start" prior to the entry into SI mode to compensate for actuator and manifold dynamics. The difference is that, whereas the throttle was stepped open in the SI-HCCI direction, in the HCCI-SI direction it is stepped closed (with a 2% saturation margin for safety) in order to promote intake manifold pressure discharge as set out in the strategy of Sec. 6.1.2.

Type	Symbol	Description
Gains	$\frac{q_W}{r_t}$	Ratio of output to input weight in throttle LQR controller
Set Points	θ_{sp}^{adv}	Set point for constant spark advance to help stabilize combustion
	θ_{evc}^{swch}	θ_{evc} at SI switch point
	N_{ramp}^{evc}	Number of cycles over which EVC command is linearly interpolated to θ_{evc}^{swch}
	N_{pre}^{CT}	Number of time steps prior to cam switch that throttle is commanded closed
	$\theta_{50,H}^{E}$	Adjusted early θ_{50} reference in HCCI
	λ^*	λ reference in HCCI
	λ^{min}	Lower λ bound for lean HCCI operation

Table 6.2: Tuning variables of HCCI phase controller.

6.2.4 Controller Tuning Variables

As in previous sections, the tuning variables for the controller for the HCCI phase of the HCCI-SI transition are collected here to clarify calibration requirements. Those calibration variables which are in common with the SI-HCCI direction are not repeated, as they are assumed to already be specified for the SI-HCCI controller. Note though that λ_{min} is listed again, as it may be tuned higher than in the SI-HCCI direction to maintain greater stability upon throttling. As before, only a small number of calibration parameters are present, with many setpoints constrained to small and intuitive sets (e.g. $N_{ramp}^{evc} \in \{0,1,2,3,4,5\}$, $N_{pre}^{CT} \in \{0,1,2,3,4,5\}$, $\lambda^* \in [1, 1.2]$, $\theta_{50,H}^{E} \in [\theta_{50,H}^{*} - 5, \theta_{50,H}^{*}]$, etc.).

6.3 SI Phase Controller

6.3.1 Control Problem Overview

The control problem for the SI phase of the HCCI-SI transition is similar to that of the HCCI phase of the SI-HCCI transition in that the system is initialized at a very unfavorable condition, and must recover from this condition while preventing excessive disturbances to the performance outputs. The difference is that the dominant unfavorable aspects of the initial condition are associated with the air path and the problem of intake manifold air storage, whereas in the SI-HCCI direction they were associated with the combustion as influenced by high exhaust temperature and very late EVC timing. While returning from this disadvantageous initial condition to a nominal SI operating point, there are three main control objectives to consider, based on the performance objectives in Sec. 1.1.3:

- Deviations of the engine torque from the driver demand should be minimized as per performance objective 1.
- The AFR should not be allowed to become lean, where NOx generation is high and excess oxygen in the exhaust contributes to the catalyst oxygen storage. This is motivated by performance objective 2 in that the catalyst oxygen storage will often be filled during lean HCCI combustion, so that the catalyst loses the ability to convert NOx [63]. The mixture can however be enriched, to reduce NOx generation and also assist in depletion of the catalyst oxygen storage to return NOx conversion functionality.
- The EVC timing should be retarded to its nominal SI set point as quickly as possible to minimize fuel economy losses as per performance objective 4.

Notice that, unlike the SI phase of the SI-HCCI direction, no objective relating to maintaining combustion phasing near MBT timing is listed. This is because in the SI-HCCI direction, the SI combustion starts from a nominal operating point where the air path conditions are such that stoichiometric fuel amount can be injected while maintaining $\theta_{50} = \theta_{50}^{MBT}$ without causing significant deviation of the torque from its reference. When entering SI in the HCCI-SI direction, however, injecting the stoichiometric fuel amount can cause a very large disturbance to the torque if the combustion phasing is held at MBT, given the high intake pressure and hence trapped air mass which necessitates a high quantity of fuel to be injected. In order to simultaneously satisfy the first and second objectives listed above, it thus becomes necessary to phase θ_{50} significantly away from its optimal timing to reduce the torque output, as noted in Sec. 6.1.1.

Based on the stated control objectives and considerations in Sec. 6.1.1 along with the model in Ch. 2, the control problem for the SI phase of the HCCI-SI transition is formulated according to the logic in Table 6.3. The input vector is nearly the same as that in the SI phase of the SI-HCCI transition, with the minor change that the IVO timing input is removed because IVO is held at its nominal set point θ_{ivo}^{*} to which it is adjusted prior to entering SI. The performance variables change to eliminate consideration of θ_{50}, as now it will be allowed to float in order to track the torque reference while preventing lean operation. The λ bounds remain in place but are constricted to lower values in order to ensure that the mixture is always stoichiometric or slightly rich. The

remainder of the formulation remains the same as for the SI phase of the SI-HCCI direction.

Control Inputs	$u = \begin{bmatrix} u_t & u_{evc} & m_f & \theta_{sp} \end{bmatrix}^T$
Feedback Variables	$y = \begin{bmatrix} p_{im} & T_{im} & \theta_{ivo} & \theta_{evc} & N_{eng} \end{bmatrix}^T$
Performance Variables	$w = \begin{bmatrix} NMEP & \lambda \end{bmatrix}^T$
Reference Command	$r = NMEP^*$
λ Output Bounds	$\lambda^{lo} \leq \lambda \leq \lambda^{hi}$
Input Lower Bounds	$u_{low} = \begin{bmatrix} 0 & -85 & 5 & -60 \end{bmatrix}^T$
Input Upper Bounds	$u_{high} = \begin{bmatrix} 100 & 15 & 50 & 50 \end{bmatrix}^T$
Model States	$x = [p_{im} \;\; \theta_t \;\; \dot{\theta}_t \;\; \theta_{evc} \;\; \dot{\theta}_{evc} \;\; \theta_{ivo} \;\; \dot{\theta}_{ivo}]^T$

Table 6.3: Control problem formulation for SI phase of HCCI-SI transition.

A block diagram of the control architecture based on the above control problem formulation for the SI phase of the HCCI-SI transition is shown in Fig. 6.7. Notice that several additional elements are now present compared to the SI-HCCI direction, including a more elaborate multi-input air path controller for the throttle and EVC timing, and a secondary θ_{50} reference generation for the spark timing based on torque tracking requirements. These elements were added as necessary to meet the control objectives in the presence of the more extreme conditions during the SI phase of the HCCI-SI transition. As before, the control architecture is split into a time synchronous air path control component and a crank synchronous combustion control component. In what follows, both the air path and combustion control will be explained, focusing on the new elements which were not present in the SI-HCCI direction.

6.3.2 Air Path Control

The overall architecture of the air path control is:

- u_t and u_{evc} are commanded through a two-input speed-gradient controller to a time-varying reference cylinder flow rate W^*_{cyl} while also targeting fast convergence of the EVC timing to its nominal SI set point θ^*_{evc}.
- The reference W^*_{cyl} is derived from a model-based calculation to achieve $NMEP = NMEP^*$ under the constraints $\lambda = 1$ and $\theta_{50} = \theta^*_{50,S}$ with one step look-ahead valve timing disturbances, following the same procedure as for the p^*_{im} derivation in the SI-HCCI direction.

The large discrepancy in intake pressure at the initiation of the SI phase of the HCCI-SI direction poses a very difficult control problem for the air path actuators. In one respect, it is desirable to aggressively throttle the intake to give a fast reduction in intake manifold pressure, however a fast intake manifold pressure reduction can induce a large overshoot when the intake pressure reaches nominal SI levels and cause a reduction in torque. Additionally, coordination of the EVC timing with the throttle becomes much more important than in the SI-HCCI direction, in that the EVC timing's ability to obstruct air flow at advanced positions should be leveraged in order to reduce the inducted air quantity while the intake manifold pressure is high. However, once the intake manifold

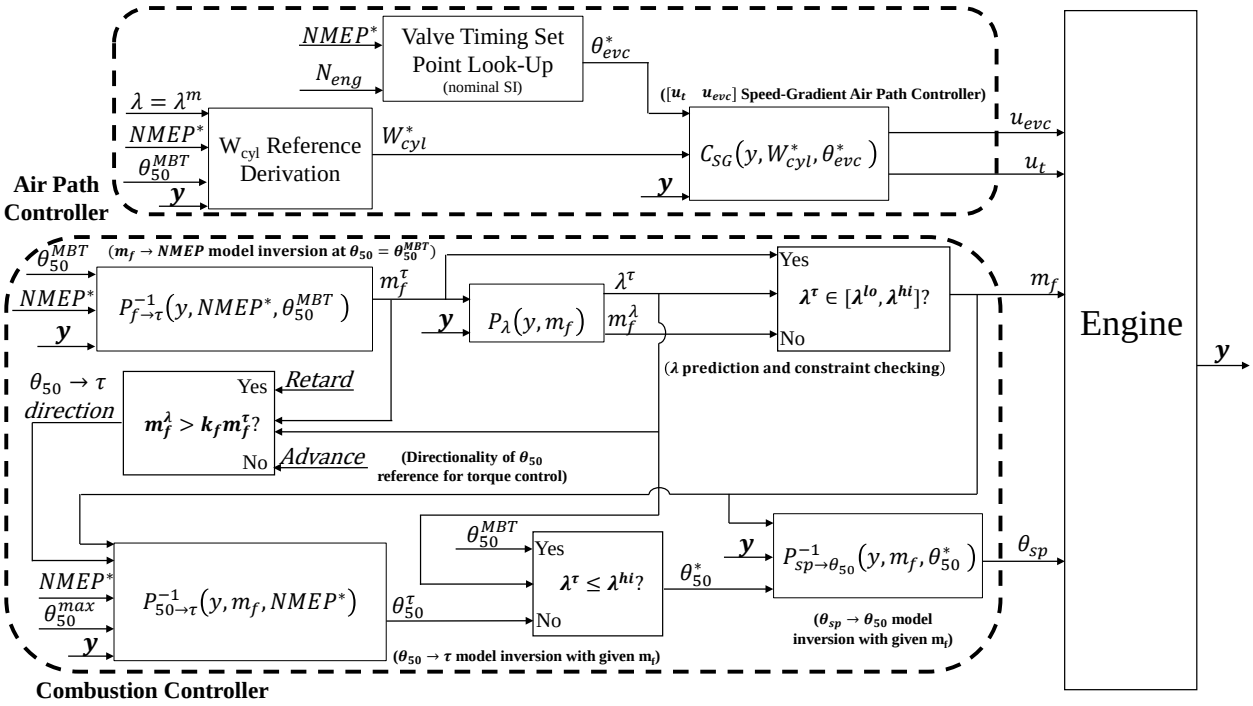

Figure 6.7: Block diagram of controller for SI phase of the transition. Variable names are as defined in Table 6.3. P blocks indicate calculations using the plant model, and C blocks indicate output feedback controllers.

pressure sufficiently reduces, the EVC timing should approach its optimized SI set point as quickly as possible as per the control objectives listed in Sec. 6.2.1.

Given the difficulty of the air path control problem in the SI phase of the HCCI-SI transition, a more elaborate control design method than those of previous chapters known as Speed-Gradient Control (SGC) is employed to address the problem. The SGC method takes into account the plant nonlinearities, which are significant in the conditions passed through in the SI phase of the HCCI-SI transition given the strong variation in the EVC gain to intake pressure and flow at advanced timings (see Fig. 4.2) and also in the throttle gain at low throttle openings ($<\approx 10\%$). Additionally, SGC is an optimal control method so that it inherently addresses the control allocation problem in MIMO control topologies, and is intuitive to tune through LQR-like cost function weights. The downside of SGC is that it is tailored for systems which take a certain form to which the air path control problem in the SI phase of the transition does not exactly conform, which requires additional considerations which increase mathematical and computational complexity.

To explain the SGC control design, an overview of the SGC method is first given and then the procedure to apply it to the air path control problem in the SI phase of the transition is described. The overview of the SGC method is modified after the description in [68], and is simplified in that

no integral term is considered as it was not included in the control design here. Consider a nonlinear system

$$\dot{x} = f(x, u) \tag{6.22}$$

where the control input u is to be chosen to track the state x to some desired state x_d. Let the control input be divided into a feedforward term u_d and a feedback term u_p,

$$u = u_d + u_p \tag{6.23}$$

where the u_d attains $x = x_d$ at steady-state, $f(x_d, u_d) = 0$, and the feedback term is to be determined by the SGC design method. The idea behind the SGC method is to minimize a cost function in terms of the state and control effort over a one-step ahead predicted time interval Δt,

$$J = Q(x(t + \Delta t)) + \frac{1}{2} \int_t^{t+\Delta t} u_p(\tau)^T \Pi^{-1} u_p(\tau)\, d\tau \tag{6.24}$$

where Q is some function of the state intended to penalize the error between x and x_d, and $\Pi > 0$ is a square weighting matrix. One straightforward choice for Q is $Q = (x - x_d)^T S(x - x_d), \quad S > 0$. To obtain a more tractable optimization problem, the SGC method simplifies the one-step ahead prediction with a simple forward Euler approximation

$$Q(x(t + \Delta t)) \approx Q(x(t)) + \frac{\partial Q}{\partial x}(x(t)) f(x(t), u(t)) \Delta t \tag{6.25}$$

$$\int_t^{t+\Delta t} u_p(\tau)^T \Pi^{-1} u_p(\tau)\, d\tau \approx u_p(\tau)^T \Pi^{-1} u_p(\tau) \Delta t \tag{6.26}$$

reducing the cost function to

$$J = Q(x(t)) + \frac{\partial Q(x(t))}{\partial x} f(x(t), u(t)) \Delta t + \frac{1}{2} u_p(t)^T \Pi^{-1} u_p(t) \Delta t \tag{6.27}$$

The control law for u_p is then found by minimizing this cost function with respect to u_p.

To apply the SGC method to the SI phase air path control problem, a change of state variables is first made to replace the p_{im} state by W_{cyl}, in order allow W_{cyl} to be tracked as a performance output. This is necessary because the SGC optimization is carried out with respect to the state and so W_{cyl} must be a state if it is to be considered for tracking. W_{cyl} is taken as a performance output in place of p_{im} as in the air path control of the HCCI phase of the transition, which is motivated by the same reasoning that the reference W_{cyl} changes less throughout the air path transient than does the reference p_{im}, but more so by the inclusion of the EVC timing in the control design. The reason is that the EVC timing has a conflicting effect on W_{cyl} versus p_{im}; retarding EVC reduces p_{im}, but allows more air flow into the cylinders so increases W_{cyl}. Thus, if p_{im} is taken as a performance output and the goal is to reduce p_{im} as quickly as possible after switching to SI, this will result in

immediate retard of the EVC timing which will increase flow rate and counteract the controller's intention. Directly considering W_{cyl} as a performance output bypasses this confusion.

The state equation for W_{cyl} is found by differentiating the SI model's flow rate regression with respect to time. The reparameterized model in Appendix A is used because it is regressed in low lift intake SI operation, which is the focus of the strategy in Sec. 6.1.2,

$$W_{cyl} = \alpha_1(\theta_{evc})p_{im} + \alpha_0(\theta_{evc})$$
$$\alpha_1 = a_{w1}\theta_{evc}^2 + a_{w2}\theta_{evc} + a_{w3}, \quad \alpha_0 = a_{w4}\theta_{evc}^2 + a_{w5}\theta_{evc} + a_{w6} \tag{6.28}$$

where the fitting coefficients have been labeled as $a_{wi}, \quad i = 1, ..., 6$ for simplicity in the following derivation. Differentiating this equation with respect to time gives

$$\dot{W}_{cyl} = \left(\frac{\partial \alpha_1}{\partial \theta_{evc}} p_{im} + \frac{\partial \alpha_0}{\partial \theta_{evc}}\right)\dot{\theta}_{evc} + \alpha_1 \dot{p}_{im} = (\alpha_{1,e} p_{im} + \alpha_{0,e})\dot{\theta}_{evc} + k_{im}(W_t - W_{cyl}) \tag{6.29}$$

$$\alpha_{1,e} := \frac{\partial \alpha_1}{\partial \theta_{evc}} = 2a_{w1}\theta_{evc} + a_{w2}, \quad \alpha_{0,e} := \frac{\partial \alpha_0}{\partial \theta_{evc}} := 2a_{w4}\theta_{evc} + a_{w5} \tag{6.30}$$

where $\dot{p}_{im}$ has been substituted for using the expression for isothermal manifold dynamics (2.4) with $k_{im} := \frac{RT_{im}}{V_{im}}$ and the quantities $\alpha_{i,e} := \frac{\partial \alpha_i}{\partial \theta_{evc}}$ have been defined for convenience. It can be seen that the equation (6.29) can be expressed completely in terms of W_{cyl} and the other model states using $p_{im} = \frac{W_{cyl} - \alpha_0}{\alpha_1}$ to eliminate all occurences of p_{im}. The state vector for the SGC design is then

$$x_{SG} := \begin{bmatrix} W_{cyl} & \theta_t & \dot{\theta}_t & \theta_{evc} & \dot{\theta}_{evc} \end{bmatrix}^T \tag{6.31}$$

where the IVO timing has been dropped from the state description due to its minimal influence. The design will be carried out using both throttle and EVC as control inputs, giving the input vector

$$u_{SG} := \begin{bmatrix} u_t & u_{evc} \end{bmatrix}^T \tag{6.32}$$

To begin the derivation of the SGC control law, the state cost Q is first defined. A simple and logical cost function is

$$Q = \frac{q_w}{2}(W_{cyl} - W_{cyl}^*)^2 \tag{6.33}$$

where $q_w > 0$ is a weighting factor and W_{cyl}^* is the reference flow rate. W_{cyl}^* is derived by first executing the p_{im} reference derivation explained in Sec. 4.2.2, and then transforming the p_{im} reference to a W_{cyl} reference using Eq. 6.28. Note here that no penalty for the distance of EVC timing from its set point, $\theta_{evc} - \theta_{evc}^*$, is incorporated in the cost function, although it was explained that it is desirable to have the EVC timing reach its set point as quickly as possible. The reason is that in Eq. (6.23), u_d for the EVC input is simply θ_{evc}^*, so that with the cost in Eq. (6.33), the controller inherently commands $u_{evc} = \theta_{evc}^*$ when W_{cyl} is perfectly tracked and no EVC adjustment is

necessary to aid in the tracking. If desired, a term for $q_{evc}/2(\theta_{evc}-\theta^*_{evc})^2$ for faster EVC convergence can easily be added to the cost function and carried through the following derivation.

Inserting the state cost defined in Eq. (6.33) into the full SGC cost function in Eq. (6.27) gives

$$J = \frac{q_w}{2}(W_{cyl}-W^*_{cyl})^2 + q_w(W_{cyl}-W^*_{cyl})\dot{W}_{cyl}T_s + \frac{u^2_{t,p}T_s}{\pi_t} + \frac{u^2_{evc,p}T_s}{\pi_{evc}} \tag{6.34}$$

where the look-ahead time interval has been set equal to the sample time T_s, which is the most natural time step to consider for a digital implementation. The input weights π_t and π_{evc} have also been defined, and subscript p on a control input denotes that it constitutes the feedback portion of the full input defined in Eq. (6.23). Substituting for $\dot{W}_{cyl}$ from Eq. (6.29) gives

$$\begin{aligned} J = {} & \frac{q_w}{2}(W_{cyl}-W^*_{cyl})^2 + q_w(W_{cyl}-W^*_{cyl})T_s\times \\ & \left[(\alpha_{1,e}p_{im}+\alpha_{0,e})\dot{\theta}_{evc} + \alpha_1 k_{im}\left(A_{eff}(\theta_t)\frac{p_b}{\sqrt{RT_b}}\phi\left(\frac{p_{im}}{p_b}\right) - W_{cyl}\right)\right] + \frac{u^2_{t,p}T_s}{2\pi_t} + \frac{u^2_{evc,p}T_s}{2\pi_{evc}} \end{aligned} \tag{6.35}$$

where the throttle flow rate W_t has been substituted for using the orifice equation (2.5) to expose the dependence on the throttle angle. Inspection of this equation shows that the throttle and EVC inputs u_t and u_{evc} do not appear explicitly in terms related to the state error cost, because of the actuator dynamics between θ_t and u_t and also θ_{evc} and u_{evc}. The only place that u_t and u_{evc} appear are in the input weighting terms $\frac{u^2_{t,p}T_s}{\pi_t}$ and $\frac{u^2_{evc,p}T_s}{\pi_{evc}}$, for which minimization of J with respect to $u_{t,p}$ and $u_{evc,p}$ simply gives $u_{t,p} = u_{evc,p} \equiv 0$, which is not correct. The actuator dynamics of the throttle and EVC timing must be dealt with in order to obtain a valid Speed-Gradient control law.

One simple option is to ignore the actuator dynamics, and simply set $\theta_t \approx u_t$ and $\theta_{evc} \approx u_{evc}$. Due to the faster actuator dynamics of the throttle than the cam phaser, this method was found in simulation to give functional throttle control. However, results were overall mediocre results because the throttle's actuator dynamics are still significant on the time scale of the severe intake air transient that occurs over the first 1-2 cycles of the SI phase. The controller had to be tuned very aggressively to compensate for the actuator dynamics, which tended to lead to oscillatory responses. The EVC actuator dynamics could not be ignored due to their much slower nature. For this case, another option was pursued where $\dot{\theta}_{evc}$ was defined as a virtual control input in Eq. (6.35) and backstepping was applied to derive the u_{evc} command [68]. Due to a high computational complexity in deriving a traditional backstepping control law, backstepping through dynamic surface control (DSC) [69] was applied. The DSC method proved to be of little help in that it could not achieve convergence of the between the virtual SGC command and the actual $\dot{\theta}_{evc}$ value quickly enough, due to limitations on DSC lowpass filter time constants imposed by the sampling rate. Controller performance thus suffered during the first few critical cycles of the SI phase of the transition where intake manifold pressure is very high, even when DSC gains were tuned very high and caused great

noise amplification. Similar limitations were found when attempting to apply DSC backstepping for the throttle, taking θ_t as a virtual control input. Thus, both methods of ignoring actuator dynamics and DSC backstepping significantly weakened controller performance.

To circumvent the deleterious effects of actuator dynamics on the SGC performance, the state cost is slightly modified in order to force the u_t input to explicitly appear in the cost function. This is done by forming the state cost with respect to a one-step ahead prediction of W_{cyl},

$$Q(t) = \frac{q_w}{2}(W_{cyl}(t+T_s) - W^*_{cyl}(t))^2 \tag{6.36}$$

where it has been assumed that the cylinder flow rate reference remains constant across the look-ahead interval. This is a reasonable assumption given the slow rate of change of the W_{cyl} reference, however if greater fidelity is desired, W^*_{cyl} can be substituted in terms of the reference $NMEP$ and λ and the system state from the derivation in Sec. 4.2.2 and included in the following derivation, at the cost of increased complexity. Note that from this point forward time dependencies will be explicitly stated in all equations as they become important to consider given the differences in time indices introduced by the one-step ahead W_{cyl} dependence. Expanding $W_{cyl}(t+T_s)$ in Eq. (6.36) with a forward Euler approximation yields

$$\begin{aligned} Q(t) = \frac{q_w}{2}\Bigg(W_{cyl}(t) + T_s\Big[&(\alpha_{1,e}(t)p_{im}(t) + \alpha_{0,e}(t))\dot{\theta}_{evc}(t) \\ &+\alpha_1(t)k_{im}\left(A_{eff}(\theta_t(t))\frac{p_b}{\sqrt{RT_b}}\phi\left(\frac{p_{im}(t)}{p_b}\right) - W_{cyl}(t)\right)\Big] - W^*_{cyl}(t)\Bigg)^2 \end{aligned} \tag{6.37}$$

where the pre-throttle pressure and temperature and intake manifold temperature (through k_{im}) have been assumed to be slowly varying and so are not given a time index. Now stepping the state cost ahead in time following the SGC approach in (6.24), the expression (6.37) becomes

$$\begin{aligned} Q(t+T_s) = \frac{q_w}{2}\Bigg(W_{cyl}(t+T_s) + T_s\Big[&(\alpha_{1,e}(t+T_s)p_{im}(t+T_s) + \alpha_{0,e}(t+T_s))\dot{\theta}_{evc}(t+T_s) \\ &+\alpha_1(t+T_s)k_{im}\left(A_{eff}(\theta_t(t+T_s))\frac{p_b}{\sqrt{RT_b}}\phi\left(\frac{p_{im}(t+T_s)}{p_b}\right) - W_{cyl}(t+T_s)\right)\Big] - W^*_{cyl}(t)\Bigg)^2 \end{aligned} \tag{6.38}$$

This rather complicated expression can be simplified multiple ways, though to bring out direct dependencies on u_t and u_{evc}, the discrete approximation of the second order actuator dynamics for the throttle and EVC timing given in Eq. (4.1) is applied, so that the substitutions

$$\theta_t(t+T_s) = b_{1t}u_t(t) - (a_{1t}\theta_t(t) + a_{0t}\theta_t(t-T_s)) \tag{6.39}$$

$$\theta_{evc}(t+T_s) = b_{1v}u_{evc}(t) - (a_{1v}\theta_{evc}(t) + a_{0v}\theta_{evc}(t-T_s)) \tag{6.40}$$

can be made, where the a and b coefficients are based on the identified damping ratio and natural frequency of the throttle and valve timing dynamics. Noting that

$$\alpha_1(t+T_s) = a_{w1}\theta_{evc}(t+T_s)^2 + a_{w2}\theta_{evc}(t+T_s) + a_{w3} \tag{6.41}$$

$$\alpha_{1,e}(t+T_s) = 2a_{w1}\theta_{evc}(t+T_s) + a_{w2} \tag{6.42}$$

$$\alpha_{0,e}(t+T_s) = 2a_{w4}\theta_{evc}(t+T_s) + a_{w5} \tag{6.43}$$

in Eq. (6.38), it can be seen that through these terms and the $\theta_t(t+T_s)$ dependence of A_{eff}, the inputs $u_t(t)$ and $u_{evc}(t)$ appear in Eq. (6.38) when the approximations (6.39), (6.40) are substituted for $\theta_t(t+T_s)$ and $\theta_{evc}(t+T_s)$. The term in Eq. (6.38) where difficulty arises in making the approximations (6.39), (6.40) is the $\dot{\theta}_{evc}(t+T_s)$ term, which when expanded introduces a dependence on $u_{evc}(t+T_s)$ which is acausal. For this reason, $\dot{\theta}_{evc}(t+T_s)$ is approximated equal to its current value $\dot{\theta}_{evc}(t)$, which is reasonable given the significant actuator dynamics of the cam phaser and the short sampling period $T_s = 10$ msec. One further simplification is made to expand $p_{im}(t+T_s)$ using a forward Euler approximation, so that the expression for $Q(t+T_s)$ takes the form

$$\begin{aligned} Q(t+T_s) = \frac{q_w}{2}\Big(W_{cyl}(t+T_s) + T_s\big[(\alpha_{1,e}(t+T_s)(p_{im}(t) + T_s k_{im}(W_t(t) - W_{cyl}(t))) \\ +\alpha_{0,e}(t+T_s))\dot{\theta}_{evc}(t) + \alpha_1(t+T_s)k_{im}\times \\ \left(A_{eff}(\theta_t(t+T_s))\frac{p_b}{\sqrt{RT_b}}\phi\left(\frac{(p_{im}(t) + T_s k_{im}(W_t(t) - W_{cyl}(t)))}{p_b}\right) - W_{cyl}(t+T_s)\right)\Big] - W^*_{cyl}(t)\Big)^2 \end{aligned} \tag{6.44}$$

Note that though technically $p_{im}(t)$ is considered to be a function of $W_{cyl}(t)$ in the transformed coordinates x_{SG}, it is left in the $Q(t+T_s)$ expression since it is easy to evaluate using the current intake manifold pressure measurement. Also note that $W_{cyl}(t+T_s)$ terms are not expanded to keep the equation more compact. Adding in the control effort weight as per Eq. (6.24) gives the final SGC cost function

$$\begin{aligned} J = \frac{q_w}{2}\Big(W_{cyl}(t+T_s) + T_s\big[(\alpha_{1,e}(t+T_s)(p_{im}(t) + T_s k_{im}(W_t(t) - W_{cyl}(t))) \\ +\alpha_{0,e}(t+T_s))\dot{\theta}_{evc}(t) + \alpha_1(t+T_s)k_{im}\times \\ \left(A_{eff}(\theta_t(t+T_s))\frac{p_b}{\sqrt{RT_b}}\phi\left(\frac{(p_{im}(t) + T_s k_{im}(W_t(t) - W_{cyl}(t)))}{p_b}\right) - W_{cyl}(t+T_s)\right)\Big] - W^*_{cyl}(t)\Big)^2 \\ + \frac{u_{t,p}^2 T_s}{2\pi_t} + \frac{u_{evc,p}^2 T_s}{2\pi_{evc}} \end{aligned} \tag{6.45}$$

The multivariable minimization of the cost function J in Eq. (6.53) with respect to $u_{t,p}$ and $u_{evc,p}$ poses a very difficult problem, as multiple $(u_{t,p}, u_{evc,p})$ minimizer candidates may exist,

and finding the roots of the system Jacobian requires the numerical solution of a system of equations which is computationally demanding. To reduce complexity and facilitate real-time implementation, an approximation is made which reduces the minimization of J to two single variable optimization problems, which are much more tractable. The approximation is based on the observation that the only cross-coupling between from u_t and u_{evc} in Eq. (6.53) comes through the term $\alpha_1(t+T_s)k_{im}A_{eff}(\theta_t(t+T_s))$, where $\alpha_1(t+T_s)$ contains a dependence on u_{evc} when Eq. (6.40) is applied, and $A_{eff}(\theta_t(t+T_s))$ contains a dependence on u_t when Eq. (6.39) is applied. Thus, if $\theta_t(t+T_s)$ is set $\approx \theta_t(t)$, Eq. (6.53) can be minimized solely with respect to u_{evc}, independently of u_t. The optimization is thus carried out in two stages, with the first stage setting $\theta_t(t+T_s) \approx \theta_t(t)$ in Eq. (6.53) and minimizing J with respect to $u_{evc,p}$, and then inserting that command back into Eq. (6.53) without the $\theta_t(t+T_s) \approx \theta_t(t)$ approximation and minimizing J with respect to $u_{t,p}$. This method neglects the cross coupling from u_t to u_{evc} in the first stage of the optimization, and thus loses some of the benefit of the centralized MIMO SGC approach. However, the performance of the resulting controller is still adequate as will be seen in the experimental results of Sec. 6.4.

Before proceeding to derive the minimizing control inputs, it is first necessary to examine the conditions for optimality for the cost function J. To ease the derivation of minimizing inputs, it is preferable if J can be shown to have a convex dependence on both u_t and u_{evc} so that the minimizers can be found by simple partial differentiation. To discuss the convexity of J, it is helpful to view J according to the original definition from Eq. (6.24), which for the chosen state cost yields

$$J = q_w(W_{cyl}((t+T_s)+T_s) - W^*_{cyl}(t))^2 + \frac{u^2_{t,p}T_s}{2\pi_t} + \frac{u^2_{evc,p}T_s}{2\pi_{evc}} \tag{6.46}$$

where the simplification of the control cost from Eq. (6.26) has been applied. The control weighting terms $\frac{u^2_{t,p}T_s}{\pi_t}$, $\frac{u^2_{evc,p}T_s}{\pi_{evc}}$ are obviously convex in ut,p and $u_{evc,p}$ due to the quadratic dependence, which means that if the term $(W_{cyl}((t+T_s)+T_s) - W^*_{cyl}(t))^2$ can be shown to be convex in ut,p and $u_{evc,p}$, then J is also convex by the property that a sum of two convex functions is itself convex. Examination of the dependency of $(W_{cyl}((t+T_s)+T_s) - W^*_{cyl}(t))^2$ on the throttle and EVC timing is thus in order. It is first noted both u_t and u_{evc} affect this quantity only through W_{cyl} and not W^*_{cyl}, so that the dependence reduces to the same as that of W_{cyl} on throttle and EVC timing, which is then shifted and squared. The general profile of W_{cyl} versus the u_t and u_{evc} actuators is exemplified in Fig. 6.8, along with the resulting profile of the $(W_{cyl} - W^*_{cyl})^2$ term which comes from shifting the W_{cyl} versus u_t and u_{evc} profiles by a constant W^*_{cyl} and then squaring them. For the throttle input, the dependence of W_{cyl} is monotonic, with higher throttle giving greater flow in all cases, so that the profile of $(W_{cyl} - W^*_{cyl})^2$ versus u_t maintains convexity. For the EVC input, however, the dependence of W_{cyl} has an inflection point near TDC, where the air flow falls off moving both more advanced which increases trapped residual and also more retarded which increases rebreathed residual. This results in a non-convex profile of $(W_{cyl} - W^*_{cyl})^2$ versus u_{evc} which can have two

minima, one with EVC before TDC and one with EVC after TDC. To cope with this problem, the search for the minimizing u_{evc} command is restricted to fall into the bTDC minimum by disallowing u_{evc} solutions which are significantly after TDC. The bTDC minimum is the most physically logical choice because when entering the SI mode in the HCCI-SI transition, the EVC timing will be advanced significantly before TDC, so so very large control signals would be necessary to overcome the cam phase actuator dynamics and quickly reach the aTDC minimum. With this convention, the $(W_{cyl} - W^*_{cyl})^2$ dependence on u_{evc} has only a single minimizer and can be approximated as convex, so that both the u_t and u_{evc} minimizations can be carried out by partial differentiation of the cost function J.

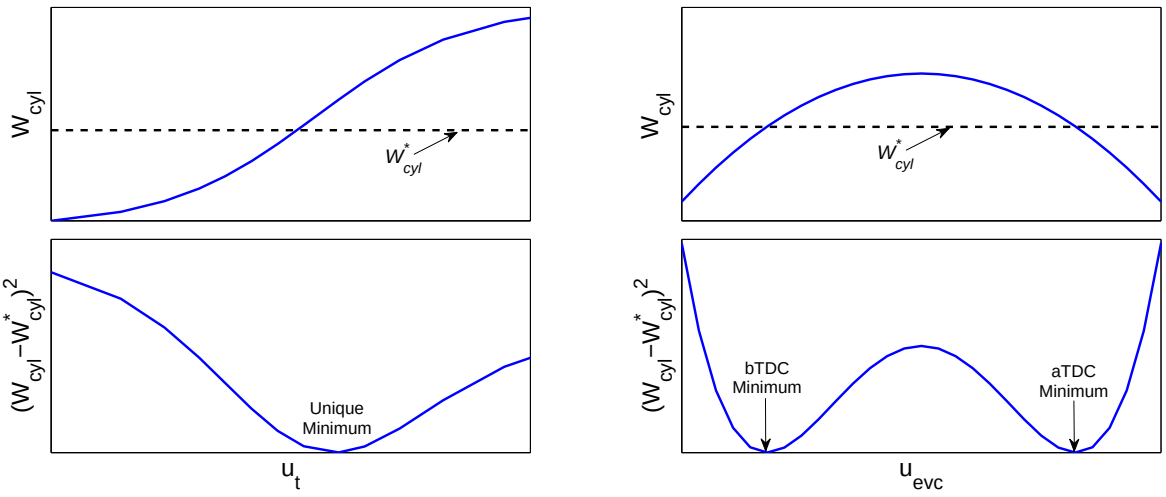

Figure 6.8: Illustrative profiles of cylinder flow rate and the cylinder flow rate state cost term versus throttle (left) and EVC (right) inputs for inspection of minimization conditions.

The first stage of the two-step optimization is the minimization of the cost in Eq. (6.53) with respect to $u_{evc,p}$ with $\theta_t(t+T_s) \approx \theta_t(t)$, which is done by partial differentiation with repsect to $u_{evc,p}$. The differentiation is simplied by differentiating the state cost term with respect to $\theta_{evc}(t+T_s)$, since with the discrete actuator dynamics approximation (6.40), the only place where u_{evc} terms arise are in $\theta_{evc}(t+T_s)$. The chain rule can then be applied to obtain the partial derivative with respect to $u_{evc,p}$,

$$\frac{\partial Q(t+T_s)}{\partial u_{evc,p}} = \frac{\partial Q(t+T_s)}{\partial \theta_{evc}(t+T_s)} \frac{\theta_{evc}(t+T_s)}{\partial u_{evc}(t)} \frac{\partial u_{evc}(t)}{\partial u_{evc,p}(t)} = \frac{\partial Q(t+T_s)}{\partial \theta_{evc}(t+T_s)} (b_{1v})(1) \tag{6.47}$$

where the relations (6.40) and (6.23) have been used. Applying partial differentation,

$$\begin{aligned}\frac{\partial J}{\partial u_{evc,p}} = q_w \big(W_{cyl}(t+T_s) + T_s \big[(\alpha_{1,e}(t+T_s)(p_{im}(t) + T_s k_{im}(W_t(t) - W_{cyl}(t))) \\ +\alpha_{0,e}(t+T_s))\dot{\theta}_{evc}(t) + \alpha_1(t+T_s)k_{im}\times \\ \left(A_{eff}(\theta_t(t))\frac{p_b}{\sqrt{RT_b}}\phi\left(\frac{(p_{im}(t) + T_s k_{im}(W_t(t) - W_{cyl}(t)))}{p_b}\right) - W_{cyl}(t+T_s)\right)\Big] - W^*_{cyl}(t)\Big)\times \\ T_s\left[\left(\frac{\partial}{\partial\theta_{evc}(t+T_s)}(\alpha_{1,e}(t+T_s))(p_{im}(t) + T_s k_{im}(W_t(t) - W_{cyl}(t)))\right.\right. \\ \left. + \frac{\partial}{\partial\theta_{evc}}(\alpha_{0,e}(t+T_s))\right)\dot{\theta}_{evc}(t) + \frac{\partial}{\partial\theta_{evc}}(\alpha_1(t+T_s))k_{im}\times \\ \left.\left(A_{eff}(\theta_t(t))\frac{p_b}{\sqrt{RT_b}}\phi\left(\frac{(p_{im}(t) + T_s k_{im}(W_t(t) - W_{cyl}(t)))}{p_b}\right)\right)\right](b_{1v}) + \frac{u_{evc,p}T_s}{\pi_{evc}} \end{aligned} \quad (6.48)$$

where all terms without $\theta_{evc}(t+T_s)$ dependencies in the state cost term have been dropped and the chain rule has been applied. Evaluating the terms with $\theta_{evc}(t+T_s)$ derivatives,

$$\frac{\partial}{\partial\theta_{evc}(t+T_s)}(\alpha_{1,e}(t+T_s)) = 2a_{w1} \quad (6.49)$$

$$\frac{\partial}{\partial\theta_{evc}(t+T_s)}(\alpha_{0,e}(t+T_s)) = 2a_{w4} \quad (6.50)$$

$$\frac{\partial}{\partial\theta_{evc}(t+T_s)}(\alpha_1(t+T_s)) = 2a_{w1}\theta_{evc}(t+T_s) + a_{w2} \quad (6.51)$$

The final expresion for $\frac{\partial J}{\partial u_{evc,p}}$ is obtained by substituting these expressions into Eq. (6.48) and then replacing $\theta_{evc}(t+T_s)$ with $b_{1v}u_{evc}(t) - (a_{1v}\theta_{evc}(t) + a_{0v}\theta_{evc}(t-T_s))$ everywhere it appears. Note that within this expression the term $u_{evc}(t)$ must be substituted with $u_{evc,d} + u_{evc,p}$ as per Eq. (6.23). The forward Euler expansion

$$W_{cyl}(t+T_s) = W_{cyl}(t) + T_s\left[(\alpha_{1,e}(t)p_{im}(t) + \alpha_{0,e}(t))\dot{\theta}_{evc}(t) + k_{im}(W_t(t) - W_{cyl}(t))\right] \quad (6.52)$$

must also be applied. The resulting equation after these substitutions is large and so is left out for brevity. This equation contains a strongly nonlinear dependence on $u_{evc,p}$ and so its root cannot be found analytically. In implementation, the expression for $\frac{\partial J}{\partial u_{evc,p}}$ is formed using the measured quantities as necessary and numerically solved using a Newton-Raphson routine. Experiments show that the routine tends to converge in 2-3 iterations, though can take 5-6 iterations at the start of the SI phase of the transition when the guess of the $u_{evc,p}$ solution is first initialized. On control actions thereafter, the guess of the $u_{evc,p}$ solution is initialized at the solution from the previous control action.

When the minimizing $u_{evc,p}$ value is found, the second step of the optimization commences by taking the partial derivative of the cost function in Eq. (6.53) with respect to u_t. Because the only place where u_t appears in the state cost is in the $A_{eff}(\theta_t(t+T_s)$ term, the resulting expression is simpler than that for the u_{evc} command, taking the form

$$\begin{aligned}\frac{\partial J}{\partial u_{t,p}} = q_w \left(W_{cyl}(t+T_s) + T_s \left[(\alpha_{1,e}(t+T_s)(p_{im}(t) + T_s k_{im}(W_t(t) - W_{cyl}(t))) \right.\right. \\ \left. +\alpha_{0,e}(t+T_s))\dot{\theta}_{evc}(t) + \alpha_1(t+T_s)k_{im}\times \right. \\ \left(A_{eff}(\theta_t(t+T_s))\frac{p_b}{\sqrt{RT_b}}\phi\left(\frac{(p_{im}(t) + T_s k_{im}(W_t(t) - W_{cyl}(t)))}{p_b}\right) - W_{cyl}(t+T_s)\right)\Big] - W^*_{cyl}(t)\Big) \times \\ T_s\left[\alpha_1(t+T_s)k_{im}\frac{\partial A_{eff}(\theta_t(t+T_s))}{\partial \theta_t(t+T_s)}\frac{\partial \theta_t(t+T_s)}{\partial u_t}\frac{p_b}{\sqrt{RT_b}}\phi\left(\frac{(p_{im}(t) + T_s k_{im}(W_t(t) - W_{cyl}(t)))}{p_b}\right)\right] \\ + \frac{u_{t,p}T_s}{\pi_t} \quad (6.53)\end{aligned}$$

where $\frac{\partial \theta_t(t+T_s)}{\partial u_t} = b1t$ from Eq. (6.39) and $\frac{\partial A_{eff}(\theta_t(t+T_s))}{\partial \theta_t(t+T_s)}$ is straightforward to evaluate with the throttle effective area profile. Similar to the case for the u_{evc} command, the final expression is obtained by subtituting $\theta_t(t+T_s)$ with $b_{1t}u_t(t) - (a_{1t}\theta_t(t) + a_{0t}\theta_t(t-T_s))$ everywhere it appears, and also expanding $W_{cyl}(t+T_s)$ using Eq. (6.52). The resulting equation for $\frac{\partial J}{\partial u_{t,p}}$ is again unsolvable with respect to $u_{t,p}$ and so its root is found in the same way using a Newton-Raphson routine.

With the method for generation of the SG feedback control inputs described, the section is ended with some last implementation notes for the controller. Firstly, in addition to the feedback control terms u_p, the steady-state feedforward terms u_d must also be generated as per Eq. (6.23). For the EVC timing, the steady-state EVC timing is simply the nominal SI set point, $u_{evc,d} = \theta^*_{evc}$. For the throttle, an inversion of the engine model must be carried out at steady-state. This inversion first applies the p^*_{im} reference derivation method given in Sec. 4.2.2 to deduce the intake manifold pressure value at the desired SI steady-state p^{ss}_{im} when $NMEP = NMEP^*$ and $\theta_{evc} = \theta^*_{evc}$. The λ value used in the derivation is $\lambda^m = \frac{\lambda^{lo}+\lambda^{hi}}{2}$ given that slightly rich mixtures may be targeted. Using the steady-state p^{ss}_{im} value, the throttle flow rate at steady-state is calculated by setting $\dot{p}_{im} = 0$ in the intake manifold pressure state equation, giving

$$W^{ss}_t = W^{ss}_{cyl} = \alpha_1(\theta^*_{evc})p^{ss}_{im} + \alpha_0(\theta^*_{evc}) \quad (6.54)$$

The throttle orifice equation can then be inverted for the effective area to obtain the W^{ss}_t,

$$A_{eff}(\theta^{ss}_t) = \frac{\sqrt{RT_b}W^{ss}_t}{p_b\phi\left(\frac{p^{ss}_{im}}{p_b}\right)} \quad (6.55)$$

after which point the throttle effective area can be inverted to give the steady-state throttle value.

On another note pertaining to controller tuning, it was found that performance could be improved by using a switching controller tuning between the early stage of the SI phase of the HCCI-SI transition where intake manifold pressure is far above the reference, and the remainder of the SI phase after the intake manifold pressure is much closer to the reference. The method employed involved scaling up the throttle input weight π_t during the first 2-3 cycles of the SI phase of the transition, in order to give a more aggressive throttle response and achieve faster intake manifold pressure reduction. After the first 2-3 cycles, π_t was returned to its nominally tuned value, in order avoid potential noise amplication and oscillations induced by the scaled up value. To implement this strategy, two new calibration parameters were defined; $k_{t,sg}$, a scaling factor on the nominal π_t value, and $N_{kt,sg}$, the number of control actions after the SI phase begins where the scaling factor is applied.

6.3.3 Combustion Control

The overall architecture of the combustion control is:

- m_f is calculated to give $NMEP = NMEP^*$ assuming $\theta_{50} = \theta^*_{50,S}$ while maintaining $\lambda \in [\lambda^{lo}, \lambda^{hi}]$ through a nonlinear model inversion. If the required m_f value for torque tracking violates the AFR constraints, m_f is chosen on the boundary of the AFR constraints.
- θ_{sp} is calculated to give $\theta_{50} = \theta^*_{50}$ through a nonlinear model inversion.
- The reference θ^*_{50} is derived from a nonlinear inversion of the torque model with respect to θ_{50} as necessary to match the reference torque through use of non-optimal combustion phasing when the fuel quantity must be higher than is preferable to maintain a stoichiometric AFR

The basic functionality of the combustion controller for the SI phase of the HCCI-SI direction is the same as the SI-HCCI direction; both the fuel and spark control inputs are determined through relative degree 0 nonlinear model inverse calculations, with the fuel attempting to track torque while keeping λ within its tolerable bounds, and the spark tracking combustion phasing. These methods are covered in Sec. 4.2.3 are so are not reviewed here. The different aspect from the SI-HCCI direction is that, instead of the spark's θ_{50} reference being fixed at $\theta^*_{50,S}$, it is adjusted dynamically as necessary to prevent torque excursions. As explained in the strategy in Sec. 6.1.2, due to the problem of intake air storage when switching form HCCI-SI, more fuel must be injected during the SI phase of the transition than the appropriate amount to match the reference torque at MBT combustion phasing to maintain a stoichiometric AFR. The combustion phasing must thus take non-optimal values in order to prevent an upwards torque spike. The dynamic calculation of θ^τ_{50} is the means by which this non-optimal combustion phasing is achieved. Note the calculation of θ^τ_{50} is only carried out when it is found that the fuel quantity to match the torque at MBT phasing m^τ_f results in an AFR λ^τ that would force the mixture to be leaned above the upper bound λ^{max}; otherwise, the θ_{50} reference is set at MBT timing.

The method for deriving θ_{50}^{τ} comes from an inversion of the SI combustion model with respect to θ_{50} using the measured valve timings and air path conditions under the constraints $NMEP = NMEP^*$, $\lambda = \lambda^{max}$. The set point for AFR is chosen at λ_{max} because it is the highest allowable AFR and so allows the minimum possible fuel quantity for a given air charge prediction. Observing the model's dependence of gross cycle work W_{cig} on θ_{50} in Eq. (2.59), it can be seen that the effect of θ_{50} on W_{cig} enters through the volume at combustion V_{cmb} which is a function of θ_{50} through Eqs. (2.43) and (2.44). Unfortunately, because Eq. (2.43) is not invertible, the model inversion from torque to θ_{50} cannot be carried out analytically. In this dissertation, the inversion is carried out with a simple numerical routine which steps the guess of the θ_{50} solution away from θ_{50}^{MBT} until the model's $NMEP$ prediction reduces below $NMEP^*$, at which point the θ_{50} solution is linearly interpolated backwards until the predicted $NMEP$ is within some tolerance of $NMEP^*$. Such an approach is chosen over standard Newton-Raphson iteration because of the two θ_{50} roots which always exist to give $NMEP = NMEP^*$, where one solution is at late combustion phasing and one is at early combustion phasing. The numerical routine described above can be set to move the θ_{50} solution in only one direction, ensuring convergence to the desired root. Note that while the numerical inversion from torque to θ_{50} is not exceedingly computationally demanding, a more computationally efficienct way to find the solution may be to determine the required V_{cmb} to match $NMEP = NMEP^*$ from Eq. (2.59), then use a look-up table of cylinder volume versus crank angle to determine the necessary crank angle to give the required V_{cmb}.

One last item involved with the θ_{50}^{τ} derivation concerns the direction in which θ_{50} is phased away from MBT. In general, it is favorable to reduce the torque with advancing θ_{50} when possible, as combustion stability is much greater in the advancing direction than in the retarding direction. However, if the θ_{50} has to advance too far to give $NMEP = NMEP^*$, unacceptably high knocking can occur, in which case the only option is to retard the combustion phasing to reduce the torque. The decision on whether θ_{50}^{τ} is advanced or retarded from MBT is made based on how large of a fuel quantity must be injected to maintain a stoichiometric AFR, as higher fuel quantities will require great perturbation from MBT timing to maintain the torque and will also lead to increased knocking in general. The degree of fuel increase is gauged by the ratio of the fuel quantity necessary to maintain a stoichiometric AFR m_f^{λ} to the baseline fuel quantity necessary to match the torque at MBT phasing m_f^{τ}. If the ratio of m_f^{λ} to m_f^{τ} is greater than some threshold factor k_f, then the θ_{50}^{τ} inversion carries out by retarding θ_{50} from MBT to avoid knock. Otherwise, θ_{50} is advanced from MBT. A uniform θ_{50}^{τ} direction (strictly advance or strictly retard) can easily be enforced by setting k_f to 0 or ∞. The option is also provided to impose an upper bound θ_{50}^{max} on how late θ_{50}^{τ} can be retarded, beyond which point misfires become highly likely. Assuming that θ_{50}^{τ} will be retarded for high fuel quantity discrepancies, the θ_{50}^{max} bound essentially places a limitation on how much the torque can be reduced using spark timing adjustment.

6.3.4 Controller Tuning Variables

The calibration variables for the final constituent of the SI/HCCI control methodology, the SI phase of the HCCI-SI transition, are collected as for the other control components to summarize calibration requirements. The λ bounds $\lambda^{lo}/\lambda^{hi}$ are listed again as they will most likely be tuned to lower values than their counterparts for the SI-HCCI direction, $\lambda^{rich}/\lambda^{lean}$, to maintain a slightly rich mixture. As before, only a small number of intuitive calibration parameters are present, and the set point θ^*_{evc} can be assumed to be taken from the baseline SI calibration which reduces the calibration parameters by one.

Type	Symbol	Description
Gains	q_w	SGC W_{cyl} state weight
	$\pi_t,\ \pi_e$	SGC throttle and EVC input weights
	$k_{t,sg}$	Scaling factor on π_t for initial portion of SI phase
Set Points	k_f	Torque to AFR fuel ratio threshold for combustion phasing control directionality
	θ_{50}^{max}	Maximum allowable θ_{50} retard to compensate for torque disturbances
	$N_{kt,sg}$	Number of control actions after SI phase commences over which $k_{t,sg}$ is applied
	$\lambda^{lo}/\lambda^{hi}$	Minimum/maximum λ bounds
	θ^*_{evc}	θ_{evc} set point for nominal SI operation

Table 6.4: Tuning variables of SI phase controller.

6.4 Experimental Results

As was done for the SI-HCCI direction, the combined HCCI-SI transition control architecture is tested in experiment on the second instance of the prototype SI/HCCI engine using an ETAS ES910 rapid prototyping module. The model-based calculations of the HCCI-SI are carried out using the reparameterized model for this replica engine which is discussed in Appendix A. The fuel used in the experiments is the same 93 AKI, 10% ethanol pump gas used for the SI-HCCI transition experiments, whose properties are listed in Table 4.4. The two of the four cylinders which were observed to have unreasonable torque and AFR responses in the SI-HCCI direction continue to display anomalous responses for the HCCI-SI experiments, and so are omitted in the following experimental results.

Initial attempts to complete the HCCI-SI mode transition with the presented control architecture and model of Appendix A gave poor results in the SI phase of the transition, with large torque decreases at the start of the SI phase caused by partial burns and misfires as the combustion

controller attempted to compensate for the increased fuel quantity by retarding the spark timing. It is postulated that this inadequate combustion phasing control response was due to the initial conditions of the SI phase of the transition (high intake pressure, high fuel quantity, early EVC timing, late spark timing) being significantly outside the range of the SI model parameterization in Appendix A. This is because the data used to parameterize the SI combustion model was more tailored to the conditions of the SI-HCCI direction, where the intake pressure was kept closer to nominal low load SI levels and the spark did not have to be retarded as much. To cope with the shortcomings of the SI combustion model, the adaptation routine described in Sec. 5.1.2 was executed in consecutive HCCI-SI transition trials at on operating point to condition the SI combustion model parameters on transient data from the conditions in HCCI-SI transition which were outside the baseline parameterization. The HCCI combustion model was not adapted due to use of the spark advance in the HCCI phase of the transition, which is an effect not considered in the HCCI model. After several adaptive trials, the controller performance improved significantly, though it is expected that explicit consideration of conditions pertinent for the HCCI-SI direction in the SI model parameterization and potential modification of the SI model's regression functions could yield even better results. In all of the following experimental results, the SI model parameters are fixed at their values from the end of the adaptive HCCI-SI transition trials, since the results with initial the parameter values prior to adaptation were considered failures.

The first experimental HCCI-SI mode transition is carried out at the same mid-load HCCI condition of 2.4 bar NMEP at 2000 RPM as in Sec. 4.4. Similar to the SI-HCCI direction, the presented cylinders are the first two in the firing order to enter SI during the HCCI-SI transition, which serves as a limiting case because it gives the intake manifold pressure the least time to be reduced after switching out of HCCI. The first and second cylinders to enter HCCI are referred to as cylinder $H1$ and cylinder $H2$, respectively, as in Sec. 4.4. The parallel cycle indexing convention to that of the SI-HCCI direction is used where the first SI cycle is labeled as *SI 0*, as introduced in Sec. 4.1.2. Continuous air path valve and output responses are interpolated to be plotted versus cycle along with the discrete combustion input/output responses. In the response plots, the cylinder flow rate reference of the HCCI and SI air path controllers in Secs. 6.2.2 and 6.3.2 is transformed to an intake manifold pressure reference so that the air path tracking can be viewed in terms of intake manifold pressure, which is more intuitive and clearly shows the differences between the HCCI and SI phases. Also, the commanded EVC timing specified by the controller is shown because it is dynamically adjusted in the air path control design of Sec. 6.3.2, however the IVO reference is left out because it is governed by simple step commands. Note that a small error in the IVO timing response is apparent where θ_{ivo} is stepped only part way to θ^*_{ivo} in the HCCI phase of the transition, and the remainder of the way after the SI phase begins. This error however is not a concern due to the minute effect of θ_{ivo} over the distance between the end of the HCCI phase and the final θ^*_{ivo} value in the SI phase.

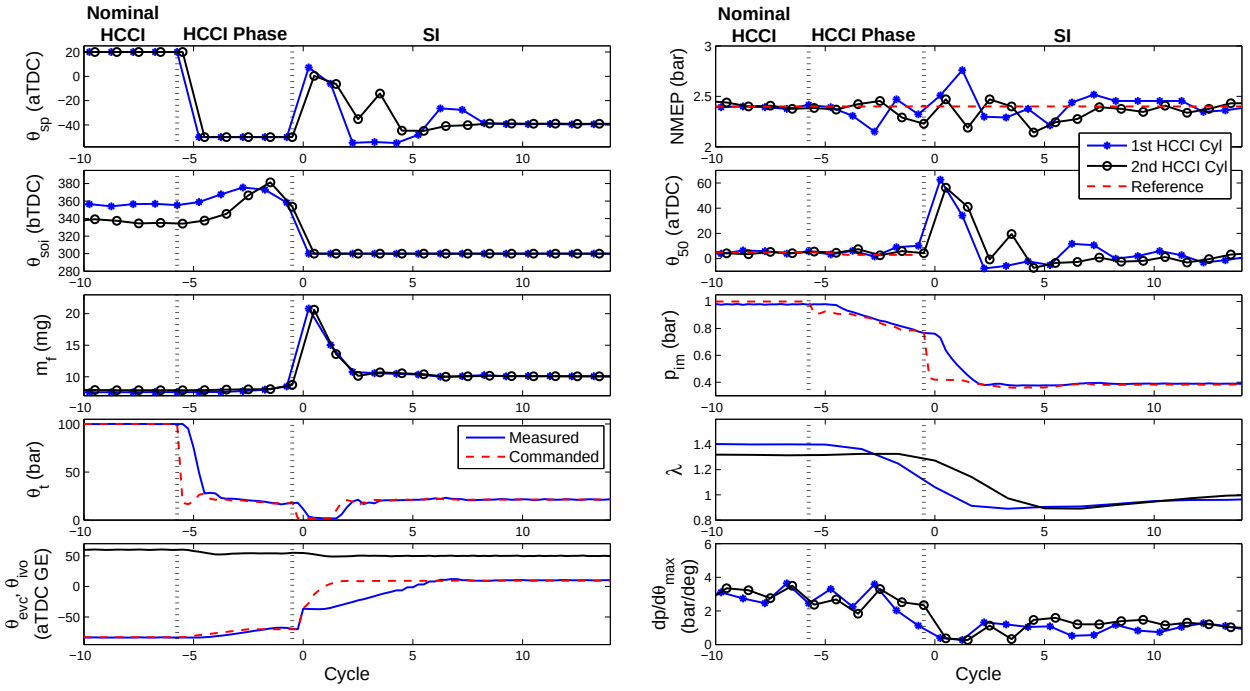

Figure 6.9: Controlled HCCI-SI transition at mid load SI condition at 2000 RPM. Inputs shown in left column and outputs shown in right column. The first and second cylinders to enter HCCI are referred to as $H1$ and $H2$, respectively.

The input (left) and output (right) responses for the mid-load HCCI-SI transition are plotted in Fig. 6.9. At the start of the HCCI phase of the transition, the first major change that is apparent is the jump of θ_{sp} from its nominal aTDC HCCI set point to its transition set point θ_{sp}^{adv} which is significantly bTDC. This spark advance follows from the strategy in Sec. 6.1.2 in an attempt to aid in combustion stabilization as the HCCI combustion is throttled. The other major change is that the LQR throttle controller commands significant throttle closure in order to place the throttle in the $\approx 30\%$ range where it has authority on the intake flow, at first overshooting the remainder of the response to more quickly move from the 100% open position. While the air path becomes more throttled, the EVC timing is ramped from its nominal HCCI set point to the set point for the cam switch θ_{evc}^{swch} following the logic explained in Sec. 6.2.2. As the EVC timing retards to θ_{evc}^{swch}, the intake manifold pressure reference decreases, which arises from the air path control structure of maintaining a constant $\lambda = \lambda^*$. This is because the retarding EVC reduces trapped residual mass and lets more air into the cylinders, so that to maintain a constant AFR the intake manifold pressure has to be reduced, given that the fuel quantity does not vary much as can be seen. The p_{im} measurement displays good tracking of the time varying reference, indicating that the throttle controller keeps the cylinder flow rate close to the necessary value to achieve

$\lambda = \lambda^*$ throughout the HCCI phase of the transition. Because λ^* is less than the nominal HCCI λ value, the λ measurements start to reduce during the HCCI phase of the transition, exhibiting a delayed and gradual response due to transport delays and significant sensor dynamics. A similar effect to that seen in the SI-HCCI transition of longer delay time in the response of the cylinder $H2$ λ measurement as compared to that of cylinder $H1$ is again observed, which corroborates that the discrepancy is due to differences in sensor placement and/or dynamics. Throughout the retard of EVC and reduction of intake manifold pressure, the injection timing actuator tends to advance, which is due both to the advance $\theta^E_{50,H}$ reference as well as the model predictions of later combusiton phasing induced by lower in-cylinder pressure and the AFR being reduced. It can be seen that the θ_{50} response remains close to its reference throughout the HCCI phase except for a small perturbation later on cycle *HCCI -1*, which suggests adequate combustion phasing control performance. The $NMEP$ experiences a modest dip for cylinder $H1$ at one cycle during the HCCI phase, but overall the disturbances to the $NMEP$ are minor throughout the HCCI phase of the transition.

When the HCCI-SI switch point is reached, the throttle is commanded closed (with a 2% saturation margin for safety) slightly prior to the switch of the exhaust cam to high lift. When the exhaust cam is switched, the EVC timing instantaneously shifts later by the offset between the high and low lift cam (see Fig. 2.2) and the SI phase of the transition commences. During the initial SI cycles where p_{im} is high, the SG air path control keeps the throttle at its lower saturation limit, which is the optimal control action to reduce the intake pressure. Nevertheless, the intake pressure still takes roughly two cycles to reach its reference. As p_{im} approaches the reference value, the SG control appropriately opens the throttle to give a soft landing of p_{im} on the reference with minimal overshoot, giving the ideal dynamic characteristics of fast response with minimal overshoot. The SG control also commands earlier EVC timings at the initiation of the SI phase of the transition, which are gradually retarded to the nominal SI set point θ^*_{evc} as the intake pressure reduces closer to its reference. When passed through the cam phaser actuator dynamics, this input trajectory results in an EVC profile which stays early for the first 1-2 cycles of the SI phase to help restrict air flow while intake manifold pumps down, and then quickly retards to its nominal reference once the intake pressure reaches reasonable values. The SG control thus balances the objectives of air flow regulation and fast EVC movement to θ^*_{evc} well.

During the period of high intake pressure over the first ≈ 2 SI cycles, the fuel mass must be greatly increased in order to prevent lean AFRs. As can be seen in the λ responses, the controller appears to perform well in this regard, with the AFR measurements becoming slightly rich shortly after entering SI. This suggests that the combustion is rich immediately upon entering SI mode, which is necessary to bring the λ measurements down below 1 considering the transport delay and sensor dynamics. The problem with the high fuel quantity arises in the torque regulation, where the spark timing must become very retarded in order to reduce the torque to the vicinity of the reference.

In these late phasing regimes, the torque output and combustion phasing can have strong stochastic variability, so even if the controller chooses the perfect θ_{sp} to give$NMEP = NMEP$ in an average sense, significant torque disturbances can result simply due to chance. The late combustion phasing portion of the mode transition is contained to the first two SI cycles, after which the intake manifold pressure sufficiently reduces to allow the spark timing to affect torque through advancing θ_{50} instead retarding for the most part, based on the k_f value of 1.1. Fluctuations in the torque response from this point forward are due mainly to nominal model error as opposed to stochastic cyclic variability.

While the HCCI-SI transition controller performs most tasks set out in the HCCI-SI strategy and control design fairly well, the main shortcoming is in the effect of cyclic variability at late combustion phasing on the torque response during the first few cycles of the SI phase. Because such late combustion phasings can result in high cyclic variability which affects the torque in a random manner, the torque tracking performance of the controller may vary significantly from one run to the next. To illustrate this point, Fig. 6.10 plots a second HCCI-SI transition experimental trial at the same operating condition as in Fig. 6.9, with no controller parameters changed. Note that in this figure and all following, the θ_{ivo} response is omitted to show more detail on the θ_{evc} response, as θ_{evc} is much more critical. Comparison of the two figures shows that though most characteristics of the controller response remain generally the same, the torque deviation for both cylinders $H1$ and $H2$ is significantly greater during the first two late-phased SI cycles. Specifically, the upwards excursion of torque for cylinder $H1$ now lasts for two cycles, and cylinder $H2$ experiences a noticeable torque drop on cycle *SI 0* whereas in Fig. 6.9 it was close to the reference. Overall, the peak excursions in $NMEP$ are roughly 17% for both cylinders $H1$ and $H2$, which may be acceptable for drivability for a short time in transient. Torque tracking performance on the initial late phased SI cycles may also be improved by including data from such conditions in the model parameterization and potentially modifying the model's regression functions, whereas here the model parameters were simply subjected to transient HCCI-SI transition data for several consecutive trials. It may also be possible to heurstically compensate for the torque excursions based in which HCCI is being exited, e.g. bias the controller torwards upwards torque excursions when the driver is exiting the HCCI region in the upper load direction. That being said, it is also possible that torque excursions can be larger than those observed here due to the inherent randomness of cyclic variability, which underscores the main drawback of the cam switching HCCI-SI control architecture given the inherent physical limitations of the valve train hardware.

To corroborate the ability of the controller to handle differing conditions with minimal tuning, a HCCI-SI transition is carried out at a different operating condition than in Figs. 6.9 and 6.10 near the high load HCCI limit. This does not give as extensive validation as for the SI-HCCI direction of the transition, where three different load conditions and a 500 RPM speed range were considered, which is due mainly to experimental time constraints. However, as will be seen, few controller tuning variables had to be changed between the mid load and higher load condition, which illustrates

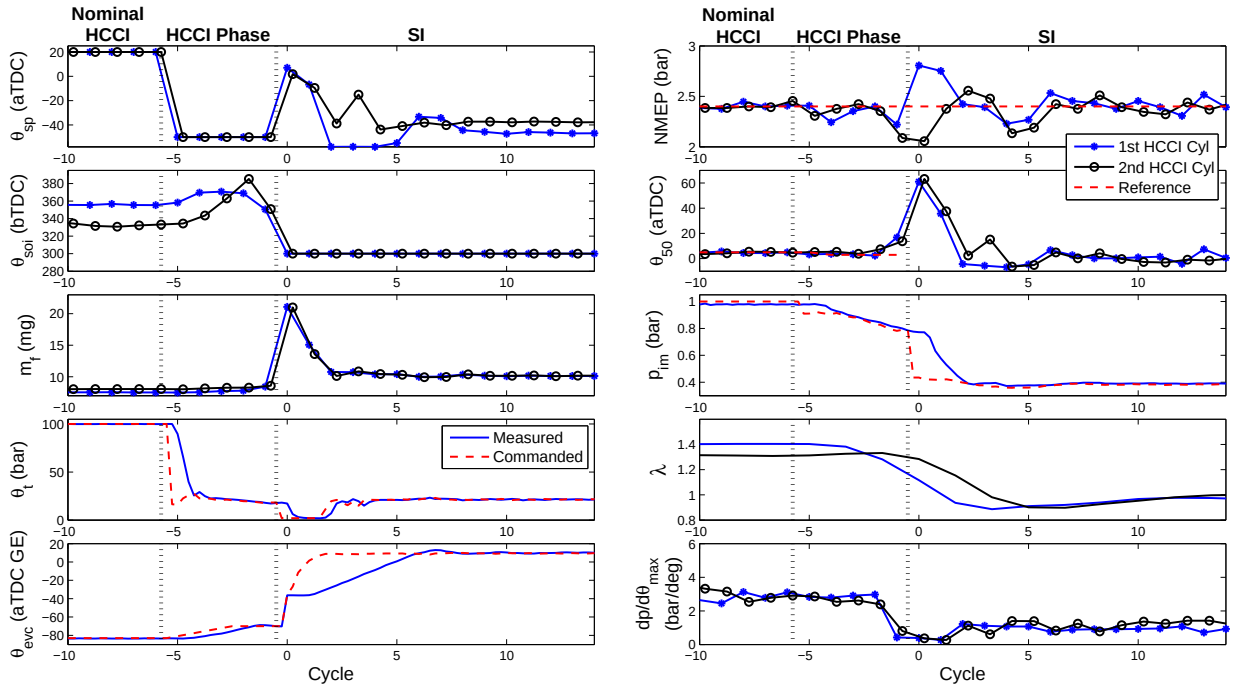

Figure 6.10: Second controlled HCCI-SI transition at mid load condition HCCI at 2000 RPM. Inputs shown in left column and outputs shown in right column. The first and second cylinders to enter SI are referred to as $H1$ and $H2$, respectively.

the controller's generality in at least a minor sense. As was experienced in the SI-HCCI direction, cylinder $H2$ elicited runaway knocking and unreasonable torque and AFR responses at the high load condition, and so had to be operated with a reduced fuel quantity relative to cylinder $H1$. For this reason, its response is omitted in the following results.

The results of the higher load HCCI-SI transition experiment are presented in Fig. 6.11, following the same format as in Figs. 6.9, 6.10. Observing the left column of the figure shows the the inputs follow mainly the same general trends as in the mid-load condition, with the only trajectory standing out as significantly different being the SOI timing. Whereas the controller significantly advanced θ_{soi} during the HCCI phase of the transition at the mid load condition, in Fig. 6.11 the θ_{soi} timing is mildly advanced over most of the HCCI phase, and is placed significantly later on the final HCCI cycle. Despite that θ_{soi} does not advance much, the θ_{50} becomes significantly earlier on cycles *HCCI -3* and *HCCI -2*, resulting in a drop in torque and increased pressure rise rates at one point. The underlying reason for this behavior may be in the advance of the spark timing in the HCCI phase, which has a greater effect at this higher load condition due to increased fuel quantity and lower residual dilution (later θ_{evc}). Since the effect of spark timing is not considered in the HCCI combustion model, the controller does not predict the corresponding advance in combustion phasing,

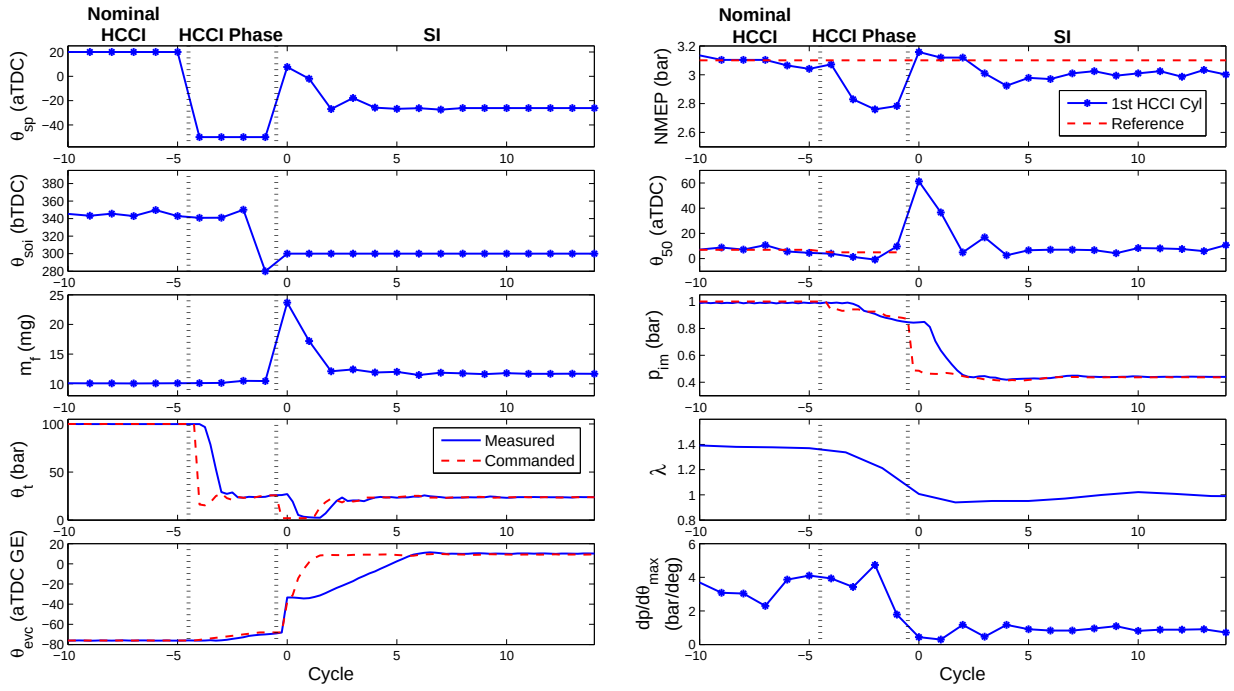

Figure 6.11: Controlled HCCI-SI transition at high load HCCI condition at 2000 RPM. Inputs shown in left column and outputs shown in right column.

and allows the θ_{50} to become early. A simple retuning of the spark advance set point θ_{sp}^{adv} to be more retarded may help alleviate this problem. A more sophisticated method may be to include a θ_{sp} term in the K_{th} adaptation basis function Eq. (5.22) and adapt the HCCI combustion model in the HCCI direction of the HCCI-SI transition. The magnitude of the torque decrease caused by the early combustion in the HCCI phase is $\approx 10\%$, which is not unacceptably high but lasts for a three cycle period and so may present a noticeable disturbance to drivability, so that retuning of the controller to mitigate this drop is warranted.

The most notable difference in the output responses between the high and mid load condition concerns the torque in the SI phase, which in the high load case has very minimal disturbance from the reference during the initial two SI cycles where fuel quantity is high and combustion phasing is retarded. After the initial transient, the NMEP settles slightly below its SI reference, with a $\approx 3\%$ offset that is within a reasonable tolerance for nominal model error. The cause of the more favorable torque response during the initial late phased SI cycles may be that at this higher load condition, the combustion need not be retarded as far to maintain the torque reference for a given fuel quantity as in lower load conditions. The combustion can thus be kept in a more stable regime, reducing effects of cyclic variability and stochastic disturbances to the torque. The higher load experimental result thus suggests that higher load conditions are favorable to mitigating the main drawback of

the cam switching HCCI-SI mode transition strategy associated with late combustion phasing and high cyclic variability on the first few SI cycles where intake pressure and fuel quantity are high.

6.4.1 Calibration Effort

As was done for the SI-HCCI direction of the mode transition, all tuning variable values for the presented HCCI-SI transition experimental results are listed in Table 6.4.1 to convey the effort involved with controller calibration. The presentation of the tuning variable values is structured similarly to the SI-HCCI transition, separating those variables which varied by operating condition from those that did not, and also separating the variable which is necessary for the baseline engine calibration. Table 6.4.1 shows that there are a total of 17 tuning variables for the HCCI-SI controller, where the variable which is specified by the baseline calibration has been omitted. Of these 17 variables, 2 are trivially easy to tune, as the SI AFR bounds $\lambda^{lo}/\lambda^{hi}$ must always be chosen to keep the mixture slightly rich. Moreover, only 4 of the 17 tuning variables are adjusted with operating condition, where θ_{evc}^{swch} and π_t are the more important of these, though λ^{min} and θ_{50}^{max} retained a moderate impact on operating condition-dependent performance. The calibration of the HCCI-SI controller across operating conditions thus involves tuning of two major and two moderate variables, and so is slightly more complex than for the SI-HCCI direction where only 1 major had to be tuned by operating condition with 3 minor variables.

Variable	Mid Load	High Load	Dependence
$\frac{q_W}{r_t}$	500	...	Constant w/ Operating Condition
$\theta_{sp}^{adv}(aTDC)$	-50	...	
N_{ramp}^{evc} (cycles)	3	...	
N_{pre}^{CT} (time steps)	2	...	
$\theta_{50,H}^{E}(aTDC)$	$\theta_{50,H}^{*}-3$	...	
λ^{*}	1.15	...	
q_w	10^8	...	
π_e	0.1	...	
$k_{t,sg}$	3	...	
k_f	1.1	...	
$N_{kt,sg}$ (time steps)	10	...	
$\lambda^{lo}/\lambda^{hi}$	0.93/0.97	...	
θ_{evc}^{swch} (aTDC GE)	-70	-68	Vary w/ Operating Condition
λ^{min}	1.1	1.15	
π_t	0.15	0.12	
$\theta_{50}^{max}(aTDC)$	60	65	
θ_{evc}^{*} (aTDC GE)	9	...	Baseline Cal.

Table 6.5: Tuning variable values for HCCI-SI transition controller.

As discussed in Sec. 4.4.1, an approximate quantitative comparison between the calibration complexity of the proposed model-based feedback control method and a generalized open-loop sequence-based HCCI-SI mode transition method can be made starting from the most extreme case where all inputs of all cycles in the HCCI-SI transition are considered calibration variables. Assuming a duration of the HCCI phase of the transition at the experimental average of 4 cycles, and a 5 cycle transient period after switching to SI, an open-loop method which treats all control actions as calibration variables has 5 inputs $\times$ 4 cycles = 20 calibration variables in the HCCI phase and 4 inputs $\times$ 5 cycles = 20 calibration variables in SI phase, for a total of 40 calibration variables. As was explained in Sec. 4.4.1, simplifications to the approach of treating all control actions as calibration variables are likely to be made in order to reduce the calibration complexity. For the HCCI-SI transition, an examples of such a simplification may be to impose a constant fuel quantity in the HCCI phase, which reduces the fuel trajectory from 4 to 1 calibration variables and the total number of variables to 37. Another simplification may be to specifying simple set points for the valve timings as opposed to full trajectories, which can reduce the number of HCCI calibration variables by 6 and SI calibration variables by 4, dropping the number of variables down to 27. Further simplification may also be possible by specifying the shape of the actuator profiles (e.g. ramp) as opposed to cycle by cycle tuning of trajectories, however it was noted from some simple open-loop mode transition data in Sec. 4.4.1 that sophisticated actuator profiles may be required to yield sufficient performance. Finally, it should again be stated that, as in the SI-HCCI direction, the proposed model-based control scheme handled operating condition changes with the adjustment of only a few calibration variables, whereas for an open-loop method, most or all of the calibration variables must be adjusted between operating conditions.

While the discussion and key points in the comparison of the calibration effort of the proposed model-based feedback control scheme to that of open-loop scheduling based methods parallels the SI-HCCI direction, there is a separate and important point to be made about the HCCI-SI direction. This point is that, due to the severe air path transient in the HCCI-SI direction, the actuator profiles can become very complex. Throttling down the HCCI combustion, coordination of the throttle and EVC timing in the SI mode, choosing the correct fuel quantity and spark timing for proper AFR and torque control on the first few high air flow SI cycles; all these things can be very difficult to deduce through trial and error, and also have a large impact on engine performance throughout the mode transition. It thus seems even more likely that a high degree of sophistication with a large number of calibration variables would result in open-loop scheduling based approaches in the HCCI-SI direction than the SI-HCCI counterpart, making the calibration burden of the model-based feedback control scheme appear even lighter in comparison. Simplifications to the strict sense open-loop scheduling scenario where all control actions for all inputs are treated as calibration variables may also be more difficult to make. Note though that this hypothesis is drawn from experimental observations of the dissertation, and cannot be definitively confirmed without

the availability of an optimized open-loop HCCI-SI mode transition control architecture.

6.4.2 The SI/HCCI Transition Control Architecture as a Full HCCI Controller

The focus of the control development in this dissertation has been on the transient phases during mode transitions between SI and HCCI. The control of the HCCI mode in nominal operation between mode transitions has not been mentioned, and has been the subject of many previous studies, e.g. [8, 52, 57]. While possible to switch between the proposed mode transition control architecture and a different design for the nominal HCCI control, a simpler solution would be to use the mode transition controller directly in HCCI. The proposed HCCI combustion control architecture may also offer some advantages over others in literature, in that it is nonlinear in its model-based calculations, giving better model accuracy across the range of parameterized conditions as compared to linearized approaches, and also makes use of IMC feedback and adaptive parameter tuning to compensate for model error. To test the prospect of using the proposed mode transition control architecture to handle both mode transitions and transients within nominal HCCI mode, a full SI-HCCI-SI scenario is considered wherein the engine starts in SI mode, then enters HCCI and undergoes load steps across the HCCI load range, and finally switches back to SI mode. No tuning variables of the controller are adjusted from their values which were tuned strictly based on mode transition control.

The results of the scenario are presented in Fig. 6.12, with the inputs shown in the left column and the outputs shown in the right column. Note that cylinder $H2$ has been omitted from the figure because it contains high load operation which cylinder $H2$ exhibits anomalous responses and cannot be run at the same fueling as cylinder $H1$. Also note that the convention of using *HCCI 0* to define the first HCCI cycle in an SI-HCCI transition and vice versa for an HCCI-SI transition has been abandoned in this plot, because of the presence of both SI-HCCI and HCCI-SI mode transitions. As can be seen, when starting in SI and switching to HCCI, there is a minor torque disturbance related to the switch, but kept within a small margin. The controller then controls the fuel quantity and injection timing to track load steps down to the low load HCCI limit and up to the high load HCCI limit. During the load steps, the controller quickly brings the $NMEP$ close to its reference, though there is a more gradual tail to the response to achieve zero-offset tracking as the IMC gradually drives the error to zero. Adjustment of the fuel quantity IMC filter constant may help shorten the length of this tail. While tracking the load, the controller simultaneously tracks θ_{50} to its load-dependent reference, without any large excursions and maintaining acceptable pressure rise rates. At the end of the scenario, the controller switches back to SI at the same load condition at which it switched into HCCI. The torque sees a similar upwards excursion of $\approx 18\%$ to that observed in Figs. 6.9 and 6.10 for one cycle, giving a larger torque disturbance than in the SI-HCCI direction but which still may be acceptable for drivability for a short time. The downwards excursion of the

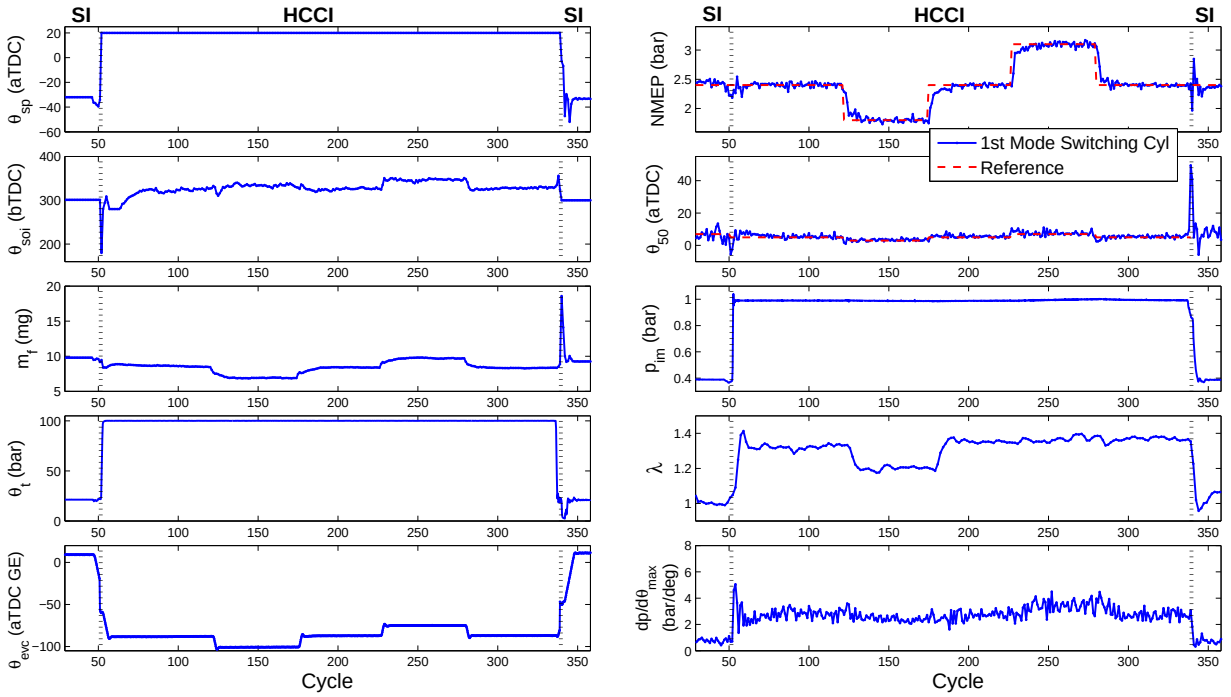

Figure 6.12: Full SI-HCCI-SI experimental scenario using proposed SI/HCCI control architecture to control mode transitions as well as nominal HCCI operation. Inputs shown in left column and outputs shown in right column.

torque on the final HCCI cycle before switching to SI is the result of an implementation issue, where spark advance was not used in the HCCI phase of the HCCI-SI transition, and so gave reduced combustion stability and a torque drop on the final HCCI cycle. While the controller's torque tracking within the HCCI mode may deserve some fine tuning to alleviate the gradual tail in the response, the scenario in Fig. 6.12 suggests that the proposed SI/HCCI mode transition controller can at least reasonably be employed as a full HCCI mode controller to handle both transitions into and out of HCCI as well as transients within HCCI.

Chapter 7
Conclusions and Future Work

7.1 Research Summary and Conclusions

An inherent obstacle to attaining the fuel economy benefits of HCCI combustions is that its range of feasible operation is limited to a low to mid speed and load region of the full regime of conventional gasoline engines. Transitions between SI and HCCI combustion modes must thus be carried out during online operation if HCCI is to be achieved, which poses a difficult control problem because of the differences in operating variables between the two modes. Most SI/HCCI mode transition studies in the literature employ the method of experimental calibration of control input trajectories to carry out mode transitions, which are scheduled in look-up tables versus operating condition and applied in open-loop. The calibration complexity involved with determining full actuator trajectories may be large compared to that involved with tuning a closed-loop controller. The reason is that the closed-loop controller itself generates the input trajectories based on engine measurements and model-based predictions while requiring only gains and set points to be tuned. Moreover, the use of online feedback allows for handling of disturbances and operating condition changes on a case-by-case basis that is reactive to real-time engine feedback. Some studies have pursued the use of model-based feedback control in SI-HCCI mode transitions [30, 39–41]. However, these studies are limited in their scope in that they only apply feedback control to a subset of the SI-HCCI control problem, and take all other aspects of the control problem to be solved with open-loop input sequence calibration. Furthermore, these studies address only the SI-HCCI direction of the mode transition, and are based on high-level strategies which either employ a cam phasing type approach [39–41] or require the use of a fully flexible valve system [30]. These strategies differ from many previous experimental studies [23–28] which use cam switching type approaches and lower cost two-stage cam hardware.

This dissertation pursued the development of a modeling and model-based control methodology for SI/HCCI mode transitions which generalizes to multiple operating conditions through tuning of only controller set points and gains, and incorporates feedback to compensate for errors and disturbances which can arise in online operation. The methodology targets practical two-stage cam SI/HCCI engine configurations that employ a type of mode transition strategy referred to as cam

switching, which to this point has only been investigated in purely open-loop studies. The modeling component of the dissertation was concerned with capturing a wide range of steady-state conditions pertinent for SI/HCCI mode transitions as well as transient SI-HCCI mode transition data with low-order mean value models. The controls component of the dissertation first examined high-level actuator strategies to carry out SI/HCCI transitions, and then developed a control architecture that executed the SI/HCCI mode transition strategy using model-based calculations in conjunction with online measurements.

7.1.1 Control-Oriented Modeling

During SI/HCCI mode transitions, the combustion must pass through conditions which are not experienced in typical SI or HCCI operation. For reliable prediction accuracy during SI/HCCI mode transitions, models must be developed which can adequately reproduce data in these conditions while maintaining a simple structure suitable for control design. It was found that by modifying and adding new features to previous Otto cycle-based control-oriented SI and HCCI models [46, 52], a wide range of steady-state actuator sweep data encompassing conditions passed through in SI/HCCI mode transitions could be captured. The range of conditions in the SI mode included early EVC timings, wide spark timing variation, and lean operation, while in the HCCI mode a wide range of air-fuel ratios and EVC timings as well as throttled operation were included. The most significant new model features were in the HCCI combustion model, and included a new Arrhenius threshold correlation and refromulated cylinder breathing model. The Arrhenius threshold correlation was intended to capture competing effects of recompression chemical reactions on ignition timing based on the observations in [55]. The reformulated cylinder breathing model was able to fit steady-state data better than the models in [56, 57] while extrapolating more reasonably to SI-HCCI transition conditions than the model of [52].

In addition to capturing a range of conditions pertinent for SI/HCCI transitions, the model's transient prediction accuracy during SI-HCCI mode transition is important as well. Despite that the model was shown to fit a large range of steady-state conditions, it exhibited large prediction errors which were much higher than the maximum steady-state error when tested against transient SI-HCCI mode transition data. A simplified GT-Power simulation suggested that the source of the error was in the model's prediction of the in-cylinder temperature on the first HCCI cycle where the conditions are far outside any which can be reached in nominal HCCI operation. A simple empirical correction factor for the model's residual gas temperature calculation on the first HCCI cycle of the transition was introduced, after which the model was able to reproduce SI-HCCI transition data in a variety of operating conditions. The modeling methodology thus maintains a low-order nature suitable for controls purposes by correcting for the extreme conditions on the first HCCI cycle, and letting the nominal model predict the remainder of the cycles where its accuracy

is sufficient. An adaptation routine was also proposed which allowed the residual temperature correction parameter to be updated in online operation, in order to use transient SI-HCCI data to improve the model predictions on the first HCCI cycle where they are very important. The adptation routine was shown in simulation examples to correct for model errors and reliably improve the model prediciton accuracy in the presence of stochastic variations and model perturbations.

A summary of conclusions for the control-oriented modeling work is:

- An atypical SI and HCCI combustion range with conditions relevant for SI/HCCI mode transitions was captured with low-order cycle to cycle models by introducing extensive modifications into previously presented control-oriented SI and HCCI models [46, 52].
- Transient data in SI-HCCI mode transitions could be reproduced with reasonable accuracy by the low-order cycle to cycle SI and HCCI models when the HCCI model was augmented with a transient residual gas temperature parameter, which accounts for the conditions on the first HCCI cycle in SI-HCCI transitions being far outside the range of feasible steady-state HCCI data.
- The SI-HCCI transient residual gas temperature was used as an adaptive tuning factor to allow online feedback to be used to improve model predictions on the first HCCI cycle during SI-HCCI transitions, where a model-based feedback controller must rely completely on the model predictions.

7.1.2 Control Development

SI-HCCI Mode Transition Control

Based on the developed and validated model, a control architecture for the SI-HCCI direction of the mode transition was established. The control architecture is built on a cam switching type strategy wherein the mode is abruptly changed by switching the exhaust cam from a high lift to a low lift profile. Several important features of the cam switching strategy were examined experimentally, including methods to increase the intake manifold pressure prior to switching to HCCI, and the choice of high lift versus low lift intake cam operation in SI mode. It was found that advancing the EVC timing before TDC to increase trapped residual was significantly more effective at increasing the intake manifold pressure at constant load than direct opening of the throttle. The effect of the EVC timing itself on the first few HCCI cycles was found to be more critical than increasing the intake pressure, however. Somewhat counter-intuitively, it was found that for a significant range of intake valve timings, the low lift and high lift intake cams produced similar intake manifold pressure, with the low lift cam actually giving slightly lower intake pressure in most cases. The decision was made to operate the SI combustion with the low lift intake cam prior to switching to HCCI mainly for convenience of calibration and set point phasing.

Once the high-level SI-HCCI mode transition strategy was finalized based on the examined

considerations, a model-based feedback control architecture which implements this strategy while tracking important performance outputs throughout the transition was developed. The combustion control component of the architecture is based on relative degree 0 nonlinear model inverse calculations, which are advantageous because they do not require inversion of dynamics and inherently generalize across operating conditions due to their nonlinear nature. The air path control component uses a simple classical linear feedback controller to track a reference intake manifold pressure using the intake throttle in the SI phase of the transition, which was sufficient due to the mild nature of the air path transient in the SI phase. The valve timings are commanded through open-loop set point based control and are treated as measured disturbances. This is done as a simple way to hasten the movement of the EVC timing to appropriate set points throughout the mode transition, as the EVC timing is the dominant factor determining which combustion mode is in operation and it is desirable to carry out the mode transition as quickly as possible.

The SI-HCCI transition control architecture was experimentally implemented on an prototype engine and exercised to carry out mode transitions at three operating points spanning the HCCI load range at 2000 RPM. These transitions appeared mostly successful, with peak torque deviations ranging from 0.17 bar NMEP (6%) in the highest load case to 0.35 bar (19%) in the lowest load case. Note though that peak torque deviation is not a fully descriptive measure of drivability in that the peak torque deviation tends to occur briefly for one or two cycles, which may have a reduced effect considering the low pass filtering characteristic of the driveline. The larger torque deviation in the lowest load case arises firstly from the lower load making torque disturbances larger on a percentage basis, and also due to higher modeling error in that condition. The controller also maintained acceptable peak pressure rise rates throughout the transition, respecting the preferred steady-state limit of 6 bar/deg except for one cycle in the highest load case, which is tolerable for a short time in transient. Over the three tested operating conditions, the SI-HCCI mode transition controller required only one major calibration variable and three minor calibrations variables to be adjusted by operating condition. Considering that control approaches in the literature would require calibrating entire input trajectories for multiple actuators at each of these conditions, the results suggest that the proposed SI-HCCI control method attains a notable improvement in controller generality and calibration simplicity.

A summary of conclusions for the SI-HCCI mode transition control work is:

- In the cam switching mode transition strategy, advancing the EVC timing before TDC while in SI mode can greatly help increase intake manifold pressure before switching to HCCI, but the strongest effect on the first HCCI cycle is the EVC timing itself and not the intake pressure.
- Switching between low lift and high lift intake cam profiles made had little impact on the cylinder breathing for a large range of intake valve timings, and so the choice of intake cam profile had little effect on the SI-HCCI transition.
- A model-based feedback SI-HCCI transition controller was developed which showed the ability

generalize to multiple operating conditions across the HCCI load range in SI-HCCI mode transition experiments while requiring only one major and three minor tuning variables to be adjusted between operating points. Peak torque deviations in the SI-HCCI experiments were kept to 0.17, 0.18, and 0.35 bar NMEP (6%, 8%, and 19%) for the high, mid, and low load operating points considered, and the preferred steady-state peak pressure rise rate threshold of 6 bar/deg was respected in almost all cases except for a minor 1-2 cycle excursion in the highest load case.

Online Parameter Adaptation

Given that the SI/HCCI control architecture relies heavily on model-based calculations for fast cancellation of disturbances during the extreme transients and short time intervals of mode transitions, the accuracy of the controller's model has a large effect on the controller performance. While the SI and HCCI combustion models were developed specifically to fit a wide range of data pertinent to SI/HCCI mode transitions, model error may increase if the model is extrapolated outside its parameterized range and the engine wears over time. Moreover, the model parameterization is assumed to be carried out on one cylinder of a single engine unit, so that cylinder to cylinder and unit to unit variation is not considered. To cope with these issues and improve robustness to modeling error, a parameter adaptation routine for the model's torque and combustion phasing calculations was created which is tailored for online operation. The adaptation routine also incorporates the HCCI model's residual gas correction factor adaptation on the first HCCI cycle. The controller thus uses feedback not only for direct output error compensation, but for continual improvement of the model-based predictions as well.

The parameter adaptation method was tested in experimental SI-HCCI mode transitions in a perturbed scenario where a different fuel batch was used, which tended to increase engine knocking. Though the baseline SI-HCCI controller performance suffered, it was observed that consecutive adaptations at one operating condition could restore the controller performance to levels better than even prior to disturbance induced by the different fuel. A drawback of such successive adaptations at a single condition was discovered in simulation, however, where it was found that the parameter estimates of the adaptive update could become unstable after a large number of adaptive iterations. The problem was traced to an issue known as estimator wind-up, wherein the measurement information becomes repetitive and the recursive least squares parameter update becomes unstable. The simulation results suggest that the experimental successive adaptive trials were unaffected by this problem due to an insufficiently high number adaptive iterations, so the experimental results are not obscured. However, to confidently prevent any such instability from occuring in practice, a modified recursive least squares algorithm using a technique known as directional forgetting [64] was employed, which was shown in simulation to alleviate the problem of estimator wind-up.

When tested in other operating conditions, the post-adaptation SI-HCCI transition controller again gave predominantly positive results relative to the baseline case, even when the adaptation was conditioned on data from only a single operating condition. Included in these varying operating conditions was the original low load condition which had a peak torque deviation of 19% in the baseline case, which was much improved after adaptation with a peak torque deviation of 10% and tighter regulation to the reference torque overall. The range of conditions also included engine speed perturbations in a 500 RPM window around the nominal parameterized speed of 2000 RPM. Both the baseline and post-adaptation controllers were able to tolerate the speed perturbation without any speed dependent model parameterization, though again the post-adaptation controller faired better.

A summary of conclusions for the online parameter adaptation work is:

- An adaptation scheme for the SI and HCCI combustion model parameters which also incorporates the adaptive HCCI residual gas temperature parameter was developed in order to allow online feedback to be used to improve model predictions and enhance controller performance.
- The parameter adaptation was found to yield notable performance improvements when applied in successive SI-HCCI transition experiments at a single operating condition, in a perturbed scenario where a different fuel batch was used which tended to increase engine knocking.
- The performance improvements attained by the parameter adaptation in successive SI-HCCI transition experiments with a perturbed fuel batch suggest that the adaptive method can compensate for disturbances caused by variations in fuel properties experienced in online operation to at least a partial extent.
- Simulations suggested that carrying out a high number of repeated adaptive SI-HCCI mode transition trials at a single operating condition could lead to instability of the parameter estimates due to a phenomenon known as estimator wind-up. The number of adaptive iterations in the successive adaption experiments was not high enough for such problems to arise, however for reliability of the controller a modified recursive least squares update law was employed which was validated in simulation to prevent estimator wind-up.
- Testing the post-adaptation SI-HCCI transition controller at differing operating conditions showed that the parameter adaptation also had overwhelmingly positive effects on controller performance at these differing operating conditions, even when the parameters were adapted in successive SI-HCCI trials only at one operating condition. The range of conditions tested spanned the HCCI load range at 2000 RPM and a 500 RPM speed range about 2000 RPM.

HCCI-SI Mode Transition Control

The last problem addressed in the dissertation was that of the HCCI-SI direction of the mode transition. The treatment of this direction was not as extensive as for its SI-HCCI counterpart, mainly due to time constraints. However, the results corroborate that the proposed control method performs at least reasonably, and handles operating condition changes with significantly less calibration

complexity than open-loop scheduling-based approaches in the literature.

The main difficulty experienced with the HCCI-SI direction from a high-level point of view concerned the problem of intake manifold air storage with the cam switching type strategy. The problem arises due to build up of air mass in the intake manifold during unthrottled HCCI operation, which takes a finite time to discharge after switching back to SI operation. During this time, the intake pressure and air flow are much higher than desired for stoichiometric SI operation. Effort was made to throttle down the HCCI combustion prior to entry to SI, but experimental sweeps show that the HCCI combustion cannot be throttled down to near-SI levels without inducing excessive combustion instability. The high air charge is a serious problem for SI operation which is typically not allowed to run lean for emissions reasons. Avoiding lean SI operation after switching back from HCCI is especially critical because the catalyst may become saturated with oxygen during lean HCCI operation, and lose the ability to convert NOx. Despite this fact, all experimental studies in the literature employ the policy of operating lean when switching to SI from HCCI. This dissertation departs from the practice of these previous studies and instead targets slightly rich mixtures in the SI phase of the HCCI-SI transition to reduce NOx generation and help deplete the catalyst oxygen storage, which poses a more challenging control problem.

Because the largest high-level concern of the HCCI-SI mode transition strategy relates to the intake air charge, the focus of the control development was on the air path component. The combustion control is kept predominantly the same as for the SI-HCCI direction, with one added feature to allow the spark timing to be used as a secondary control input for the torque. The main feature of the air path control in the HCCI phase of the transition consists of a LQR throttle controller which attempts to maintain the cylinder air charge at an approprite level to give a reasonable AFR as the HCCI combustion is throttled down. The EVC timing is commanded through an open-loop ramp to an appropriate switch point into SI mode and treated as a measured disturbance to the throttle controller. The air path control in the SI phase of the transition takes a two-input nonlinear control structure which coordinates the throttle and EVC actuators to help cope with undesirably high intake pressure initial condition as best as possible. The employed design methodology is referred to as Speed-Gradient Control, and is formulated in an optimal control framework giving intuitive tuning through cost function weights. The standard Speed-Gradient formulation experiences problems when applied directly to the throttle and EVC air path control problem due to actuator dynamics. To circumvent these problems, the Speed-Gradient cost function is slightly reformulated and the new governing optimization equations are derived.

When implemented in experiment, the HCCI-SI controller attained good air path control responses in both the HCCI and SI phases, and acceptable combustion control in the HCCI phase. The problem with the controller response arises in the first few cycles of the SI phase, where the intake pressure and so fuel quantity are very high, necessitating a large degree of spark retard to prevent an upwards excursion in torque. At these late spark timings, cyclic variability is high, which

makes the torque response more susceptible to stochastic disturbances, which can cause changes in the torque tracking performance from one trial to the next. The examined experimental trials maintain a peak torque deviation within roughly 18%, which may be acceptable for a short 1-2 cycle period in transient, and so the results are encouraging. However, it remains uncertain if the employed cam switching strategy can attain sufficient torque tracking performance over many trials at differing operating conditions. What could be established though is that the problem of high fuel quantity and very late spark timing seems to be less troublesome at high load conditions, based on an experimental HCCI-SI transition at a higher load operating point. The reason for this observation is hypothesized to be that at higher loads, the spark need not retard as far to match the torque for a given fuel quantity, so the combustion does not enter as high of a cyclic variability region. At the baseline and higher load operating conditions at which HCCI-SI transition experiments were conducted, only four calibration variables had to be adjusted by operating condition. While these adjustments are slightly more complicated to make than for calibration of the SI-HCCI transition controller, the results still suggest that the proposed HCCI-SI control method gives noteworthy advantages for generality and calibration simplicity as compared to open-loop sequence calibration approaches.

It was finally demonstrated that, with the combined SI-HCCI and HCCI-SI control architecture, the proposed control methodology could act as a complete HCCI mode controller, handling both transitions to and from HCCI as well as torque and combustion phasing tracking within nominal HCCI operation. Using the SI/HCCI transition controller to also handle nominal HCCI operation simplifies the multi-mode combustion control structure in that no additional controller for the HCCI mode must be developed and calibrated. The controller's tracking of HCCI load steps exhibited one unfavorable feature pertaining to a protracted tail in the response when converging to zero-offset reference tracking. However, the controller traversed the majority of the load steps in a short period of time, and also was not at all adjusted from its tuning for the SI/HCCI mode transitions. Further fine tuning of the controller in nominal HCCI operation may give favorable results for improving the shape of the controller's load step tracking response.

A summary of conclusions for the HCCI-SI mode transition control work is:

- Throttling down the HCCI combustion mode was observed to induce combustion instability, which prevented the intake manifold pressure from being reduced down to appropriate levels prior to entering SI in HCCI-SI transitions.
- The high intake manifold pressure when entering SI during an HCCI-SI transition leads to major conflicts between torque and emissions performance objectives, which in previous work have been neglected by addressing only the torque objective.
- A model-based feedback HCCI-SI transition controller was developed which attempts to meet both torque and emissions control objectives simultaneously. The controller was validated in experimental HCCI-SI transitions at two operating points, where only two major and two

moderate calibration parameters were adjusted between the operating points. The torque tracking performance of the controller could not match that of the SI-HCCI direction, with peak torque deviations of 0.34 and 0.4 bar NMEP (10% and 18%) for a 1-3 cycle period in the high and mid load cases considered. However, this performance is encouraging given the difficulty of simultaneously meeting torque and emissions objectives in HCCI-SI transitions.

- The repeatibility of the torque tracking performance of the HCCI-SI transition controller was found to be weaker than for the SI-HCCI counterpart, due to the SI mode needing to enter regions of very late combustion phasing where cyclic variability is high in HCCI-SI transitions in order to simultaneously address torque and emissions performance objectives.
- When the SI-HCCI and HCCI-SI controller designs are combined, the resulting control architecture was demonstrated to be capable of acting as a full HCCI enabling controller, handling both transitions into and out of HCCI, and torque and combustion phasing tracking within the HCCI mode itself.

7.2 Future Work

The most pressing topic for future work pertains to further development for the HCCI-SI direction of the mode transition, which did not receive as much attention as the opposite direction due to time constraints. Firstly, inclusion of conditions passed through in the problematic initial SI cycles with high intake pressure and fuel quantity, late spark timing, and early EVC timing, into the model parameterization may improve the controller performance, as these conditions were left out of the SI model parameterization in this dissertation. Exploring the transient validation of the combined SI/HCCI model in HCCI-SI transitions is a pertinent topic following this reparameterization. In addition to changes to the control software, further optimization of the engine hardware dealing with the two-stage cam mechanism may also improve performance in HCCI-SI transitions. The goal would be to reduce the offset between the high and low lift exhaust cams, so that the EVC timing is earlier upon switching to SI which aids in obstructing air flow and reduces the required fuel quantity necessary to maintain a stoichiometric AFR. This may also be beneficial for the SI-HCCI direction of the mode transition, in that a smaller shift of the EVC timing would result in a later low lift EVC timing when switching to HCCI, which can retard combustion phasing and reduce pressure rise rates. Modification of the intake cam offset to be larger may also give benefits in this regard, because if the intake cam is switched to high lift upon entering HCCI and the IVO timing shifts drastically earlier due to a large cam offset, it may cause a large quantity of exhaust gas to be pushed into the intake manifold, which can further obstruct the air flow.

One topic that can be further explored relating to the parameter adaptation method of Chapter 5 is to implement the directional forgetting recursive least squares algorithm, and carry out a larger number of successive adaptive SI-HCCI transition trials to examine the parameter convergence properties. As earlier stated, too few adaptive iterations were carried out in successive SI-HCCI transition experiments to expect parameter convergence. Carrying out a higher number of adaptive

iterations can investigate experimentally if the parameter estimates do indeed converge when the directional forgetting recursive least squares algorithm is used.

Another avenue for extension of the work in this dissertation is extrapolation of the control methodology to encompass cam phasing type SI/HCCI mode transition strategies and the SACI combustion mode. The control architecture appears suitable for these purposes, given that the combustion control structure can instantaneously compensate for disturbances to the combustion, and the Speed-Gradient method used in HCCI-SI air path control gave good coordination of the throttle and EVC timing which is essential for cam phasing type transitions and SACI air path control. The main challenges to extension of the controller architecture to cam phasing mode transitions and SACI would be in developing a practically implementable control-oriented model which fits the full range of combustion modes with sufficient accuracy for use in model-based control, and dealing with the control allocation problem of using both the spark and injection timing actuators simultaneously while in the SACI mode.

A last detail which was not addressed in this dissertation is the parameterization of the models over the speed space of the HCCI regime. Future work can focus on taking a larger model parameterization dataset over several engine speeds, and potentially making modifications to the combustion model correlations to capture speed variation. It was shown that the SI-HCCI transition controller proposed in the dissertation performed adequately over a 500 RPM speed range without any speed-dependent parameterization, so it appears hopeful that any speed dependent parameterization introduced into the model need only be very basic to attain controller functionality over the full HCCI speed range.

Appendices

Appendix A

Model Reparameterization for Replica Experimental Engine

As stated in their respective Sections, the transient SI/HCCI transition experimental results in Secs. 3.3, 4.4, 5.2, 6.4 were generated with a replica of the experimental engine which was originally used to parameterize the baseline model in Ch. 2. The geometry of the replica engine is the same as that of the original (see Table 2.1), except that the replica has a slightly lower geometric compression ratio of 11.45:1. Before proceeding with SI/HCCI mode transition experiments on the replica engine, the SI and HCCI combustion models were reparameterized to steady-state sweep data from this engine to eliminate any potential obscurity caused by differing model prediction accuracy between the two units. This Appendix gives the details of the reparameterization results and modifications which were made the baseline SI and HCCI combustion models of Secs. 2.3 and 2.4 in the reparameterization.

A.1 SI Combustion Model Reparameterization

Sec. 4.1.3 explained that the mode transition strategy employs the tactic of operating the SI combustion mode with a low lift intake profile during the transition. As a consequence, it is assumed that the SI combustion mode operates exclusively with a low lift intake cam, and so the SI model is parameterized to steady-state data which has the low lift intake cam in place at all times. This changes several of the regression forms, in that dependencies on the intake cam phasing are eliminated as the intake valve timing was observed to have minimal effect on cylinder breathing and combustion with the low lift cam in place over a large range of intake valve timings. Additionally, the parameterization data includes lean mixtures to account for the final cycle of the SI-HCCI transition where the mixture may be leaned following the strategy in Sec. 4.1.3.

The first regression that changes is the cylinder flow rate, where the dependence on θ_{ivo} is

eliminated from the expression of (2.36),

$$W_{cyl} = \alpha_1(\theta_{evc})p_{im} + \alpha_0(\theta_{evc}) \tag{A.1}$$

$$\alpha_i = a_{i1}\theta_{evc}^2 + a_{i2}\theta_{evc} + a_{i3} \tag{A.2}$$

The θ_{ivo} dependence is also eliminated from the residual gas fraction regression

$$x_r = a_1\theta_{evc}^2 + a_2\theta_{evc} + a_3 p_{im} + a_4 m_f^0 + a_5\theta_{sp}^0 + a_6 \tag{A.3}$$

Lastly, the θ_{50} regression is modified to contain a term for the dilution in the cylinder given the lean points in the parameterization data, and has its θ_{ivo} dependence eliminated as well

$$\theta_{50} = a_1\theta_{sp}^2 + a_2\theta_{sp} + a_3 m_f + a_4\theta_{evc}^2 + a_5\theta_{evc} + a_6\lambda'^2 + a_7\lambda' + a_8 \tag{A.4}$$

where $\lambda' = 1/\phi'$ characterizes the total dilution in the cylinder,

$$\lambda' = \frac{m_a + m_r}{AFR_s m_f} \tag{A.5}$$

The remainder of the SI model equations are unchanged from Sec. 2.3.2

The grid of inputs and modeled versus measured outputs in the actuator sweep reparameterization data for the SI combustion model is shown in Fig. A.1. In this dataset, the throttle position θ_t is plotted as opposed to θ_{ivo} , again because the θ_{ivo} timing was found to have little effect and so was held constant. The throttle and fuel were also varied independently at times to change the AFR, which can be seen through the varying λ values in the bottom subplot. Inspection of the modeled versus measured outputs shows that again the SI combustion model attains good fitting accuracy.

A.2 HCCI Combustion Model Reparameterization

Effort is made in the HCCI reparameterization to modify the breathing model for a more physics-based estimate of the residual temperature T_r based on polytropic recompression processes, instead of the original regression Eq. 2.80,

$$T_{ivo} = T_{rc}\left(\frac{V_{evc}}{V_{ivo}}\right)^{n_r - 1} \tag{A.6}$$

$$p_{ivo} = \frac{m_r R T_{ivo}}{V_{ivo}} \tag{A.7}$$

$$T_r = (a_1 T_{ivo} + a_2)\left(\frac{p_{im}}{p_{ivo}}\right)^{1-\frac{1}{n_r}} \tag{A.8}$$

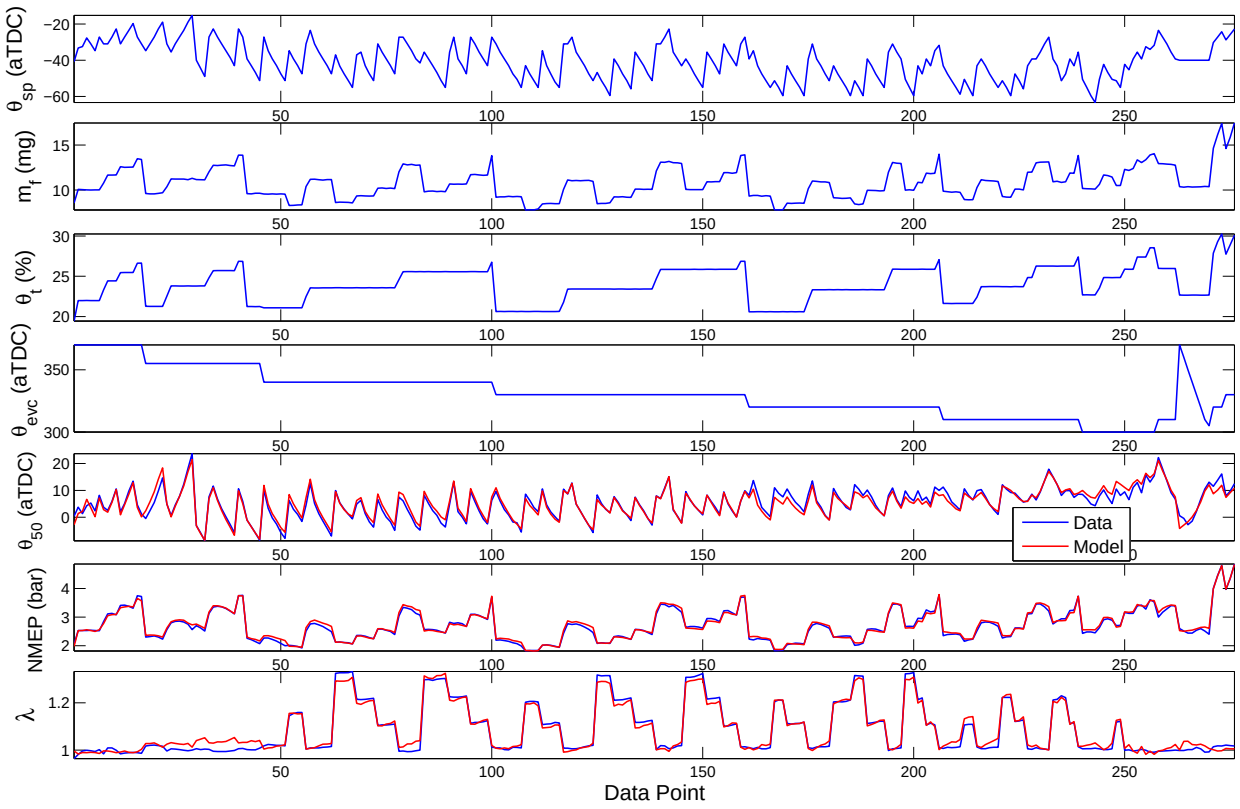

Figure A.1: Input grid and modeled vs. measured outputs for steady-state SI model reparameterization data to replica experimental engine. The λ output is shown as opposed to mass of air to convey the AFR changes that were made in the sweep data.

where the recompression polytropic exponent n_r is fixed at 1.34. The linear scaling on T_{ivo} in Eq. (A.8) was necessary to attain an adequate fit of trapped air mass data. One other modification is made regarding the dependency of the Arrhenius threshold K_{th} on the recompression temperature, where one parameter is eliminated from the original expression (2.88). This was found to still produce an adequate fit of combustion phasing data while reducing the size of the fit:

$$K_{th}(\theta_{soi}, \lambda_r, T_{rc}) = (a_{12}\lambda_r^2 + a_{11}\lambda_r + a_{10})\theta_{soi} + a_{02}\lambda_r^2 + a_{01}\lambda_r + a_{00} + a_T T_{rc} \tag{A.9}$$

The dataset used to parameterize the HCCI combustion model to the replica engine is similar in nature to the original original grid of actuator sweeps in Sec. 2.4.2, though is more condensed due to experimental time constraints. The reparameterization data and fitting resultsl are shown Fig. A.1. As can be seen, the fitting accuracy of the model remains good for the replica engine dataset.

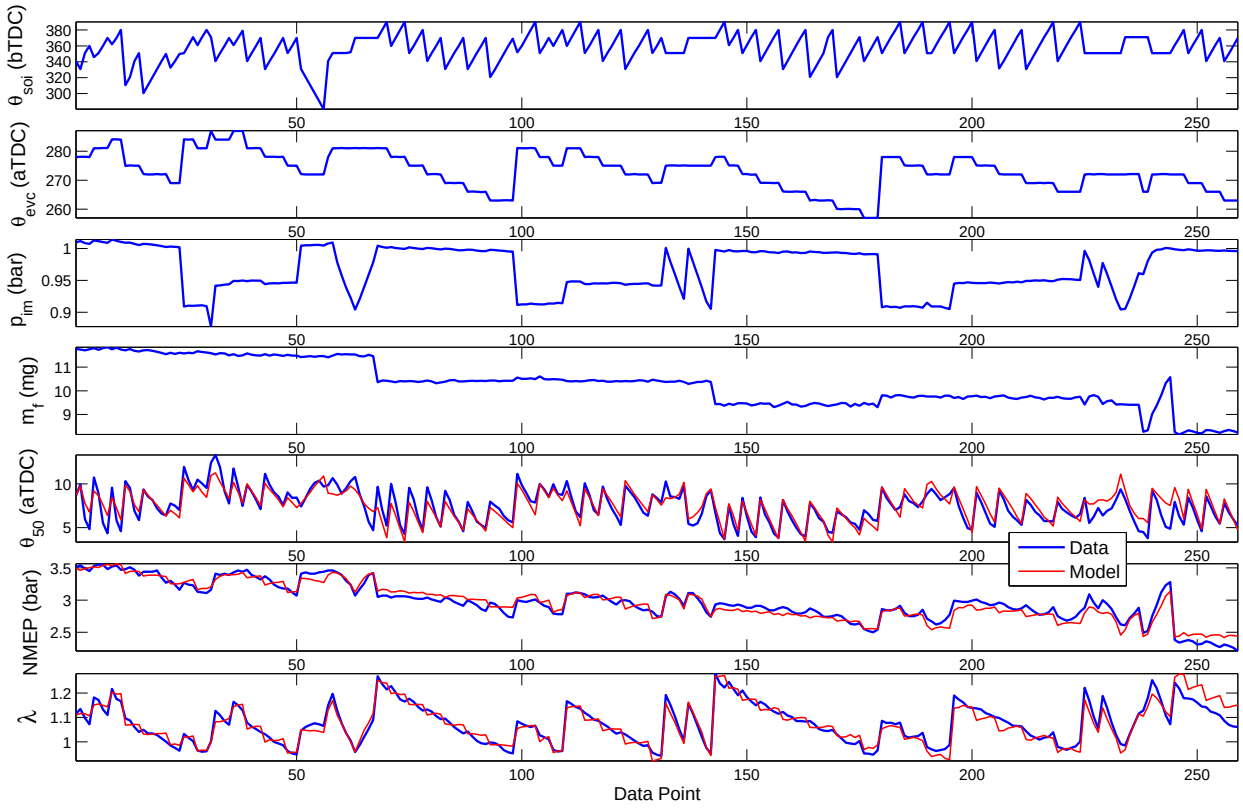

Figure A.2: Input grid and modeled vs. measured outputs for steady-state HCCI model reparameterization data to replica experimental engine.

Appendix B

HCCI Combustion Model Parameterization Routine

As stated in Sec. 2.1, the HCCI model is parameterized in an iterative routine to account for compounding of modeling error through cycle to cycle couplings. The parameterization algorithm also includes the option for simulation of the model with transient mode switch data in the iterative loop, so that the coefficients that describe the dependency of the transient k_r parameter on operating condition as in Eq. (3.6) can be automatically tuned to match transient data. To depict the routine graphically, define parameter vectors a_r to contain the parameters for residual mass m_r (Eq. (2.69)), a_T to contain the parameters for the EVC temperature T_{evc} (Eq. (2.72)), a_m to contain the parameters for inducted air mass m_a^{in} (Eqs. (2.79), (2.80)) as well as the RCHR μ parameter (Eq. (2.74)), a_{50} to contain the parameters for combustion phasing (Eqs. (2.87), (2.88)), and a_τ to contain the parameters for torque (Eq. (2.93)) as well as the polytropic compression and expansion exponents. Alternatively for the reparameterization to the replica experimental engine in Appendix A, a_m contains parameters in Eqs. (2.79), (A.8), and a_50 contains the parameters in Eqs. (2.87), (A.9). Note that θ_{50} is linked to θ_{soc} through the linear function (2.91) whose coefficients are held fixed in the iteration. Also note that the polytropic compression exponent n_c in Eq. (2.89) is held fixed at 1.32 to avoid excessive cross-coupling between the torque and combustion phasing regressions. Additionally, the matrix Ψ^T is defined to contain N_{run} columns of time histories from SI-HCCI mode transition transient data which are N_{cyc} rows in duration. For the SI-HCCI mode transition dataset used to parameterize k_r according to Eq. (3.6), $N_{run} = 9$ and $N_{cyc} = 3$.

A flow chart of the regression routine is shown in Fig. B.1, where n is the iteration index. The routine is initialized with estimates of the model states and individually parameterized regression coefficients from post-processed steady-state data. From here, the routine steps through the model's regressions, fitting each one individually and using the fitted quantities in subsequent regressions to include the effect of compounding modeling error. The regression for the IVC pressure p_{ivc} in Eqn. (2.78) is held fixed in the algorithm because p_{ivc} is regressed solely as a function of the input p_{im} and so compounding error is not an issue. Note that after the T_{evc} and m_a regressions, intermediate variables such as the IVC temperature T_{ivc} which are not directly regressed are calculated as necessary to generate the full set of regressors for the next regression step. When the θ_{50} regression

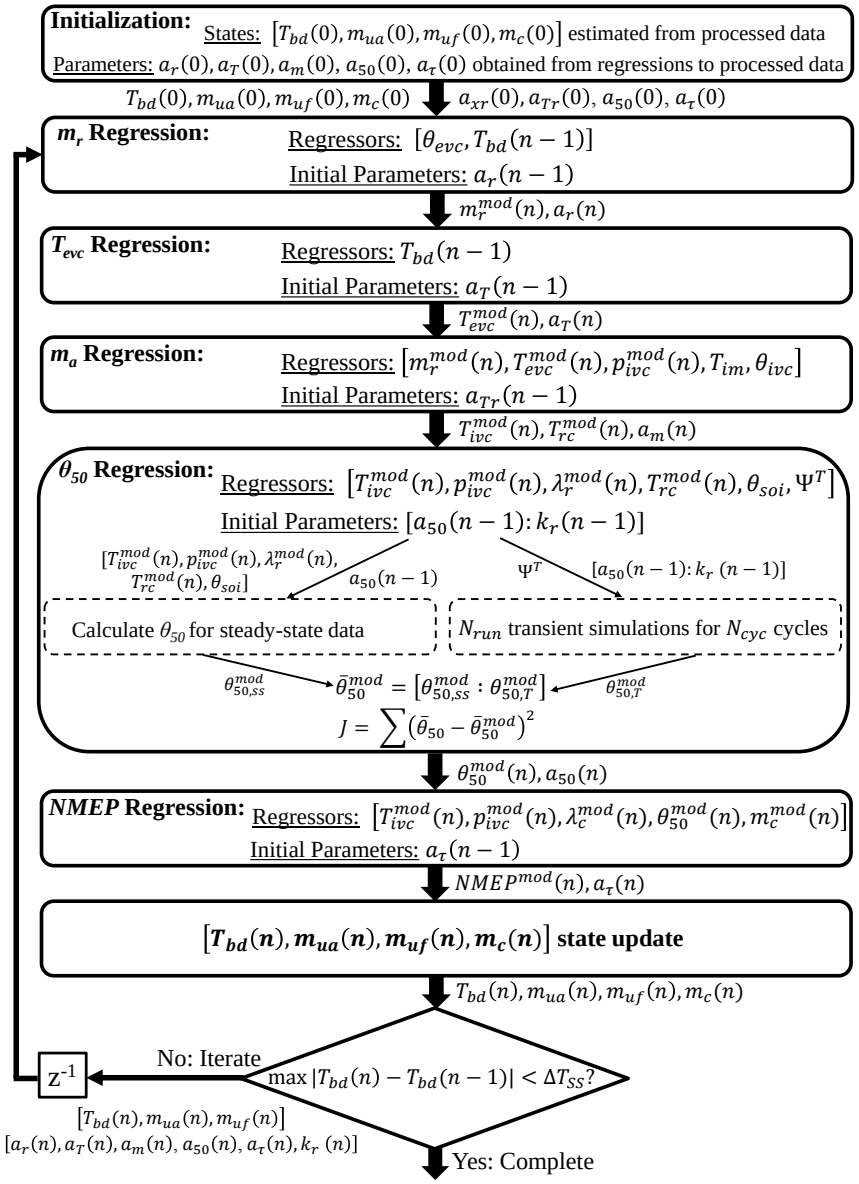

Figure B.1: Flow chart depicting iterative regression method for both steady-state and transient k_r model parameters.

is reached, the a_{50} coefficients are used to calculate the θ_{50} for steady-state data $\theta_{50,ss}^{mod}$, and then concatenated with the k_r parameter to carry out N_{run} transient simulations of SI-HCCI mode transitions to produce $\theta_{50,T}^{mod}$. The $\theta_{50,ss}^{mod}$ and $\theta_{50,T}^{mod}$ vectors are then concatenated into a single vector whose squared error is used to form the cost function for the regression.

At the completion of an iteration, the model states are updated using the calculated variables from the current iteration, and a convergence check is performed on the states. The convergence check adopted here was that the maximum change in the blowdown temperature state from the

previous iteration across all steady-state points was less than some threshold ΔT_{ss}, chosen to be 1 K. If the convergence check is not met, the states from the current iterate are recycled to the beginning of the model calculations, and the next iteration proceeds using the optimized values from the previous iteration as initial parameter guesses.

Appendix C

Estimation of SI/HCCI Mode Transition Fuel Economy Penalty

It was observed in [63] that, because stays in the HCCI mode are often times short during an average drive cycle, the duration of the transition between SI and HCCI to realize can be comparable to the time in HCCI itself. It thus becomes logical to consider how the mode transitions affect the fuel economy obtained by multi-mode SI/HCCI combustion, and how long the mode transitions take on average. To contribute to the database of information on this topic, this Appendix lists figures for fuel economy and duration deduced from the experimental SI/HCCI mode transitions in this dissertation.

In general, when transitioning between SI and HCCI, conditions will have to be passed through which are less fuel efficient than optimized operation in either one of the two modes. To gauge the effect of the mode transitions on fuel economy, the fuel penalty FP is calculated for multiple mode transition trials using the relation

$$FP(\%) := \frac{m_f/NMEP}{m_f^{SS}/NMEP^{SS}} \tag{C.1}$$

where m_f and $NMEP$ are taken for a given cycle during a mode transition, and m_f^{SS} and $NMEP^{SS}$ are calculated from a steady-state average of 10 cycles. Rather than specifying the fuel penalty for each cycle during all of the considered mode transitions, average fuel penalties are calculated over a given phase of a transition, e.g. average fuel penalty during the SI phase of the SI-HCCI transition, and are denoted by $\bar{FP}$. However, some specific cycles which are consistently noticed to have a large effect on fuel economy are given separate attention, e.g. the first SI cycle in an HCCI-SI transition, so that their more extreme values do obscure the average value throughout the transient. Because transient effects of the mode transition on fuel economy tend to decay after 5-6 cycles after switching to a destination mode, all average fuel penalties in destination modes are listed for up to 6 cycles after entering the destination mode.

The fuel penalty and duration information for the SI-HCCI direction of the mode transition is listed in Table C.1. Note in this table that cycle *HCCI 0* is given separate attention due to its typically larger fuel penalty, caused by advanced combustion phasing. It can be seen in the

table that higher load operating conditions tend to have a shorter duration for the SI phase of the transition, which is primarily due to the EVC timing set point for switching to HCCI being later at higher loads. The cam phaser thus need not advance θ_{evc} as far, whose actuator dynamics are the main source of delay in transitioning from SI to HCCI. Note that the statistics in Table C.1 are derived from the post-adaptation mode transitions in Chapter 5, which is taken as indicative of the controller performance when the controller model better predicts the engine data.

Operating Load	Avg. SI Duration (cycles)	$\bar{FP}^{SI}$ (%/cycle)	FP^{HCCI0} (%) (%)	$\bar{FP}^{HCCI1-5}$ (%/cycle)
1.8 bar NMEP	7	1.06	1.12	1.06
2.4 bar NMEP	5	1.07	1.15	1.01
3.2 bar NMEP	4	1.01	1.15	1.02
Average	5.333	1.046	1.140	1.030

Table C.1: Summary estimates for SI-HCCI transition duration and fuel economy penalty. All data are taken at 2000 RPM.

Table C.2 lists the fuel penalty and duration information for the HCCI-SI direction of the mode transition. In this table, the first two SI cycles of the transition *SI 0,1* are given separate attention, as the fuel penalty on these cycles tends to be very high due to the problem of intake manifold air storage discussed in Sec. 6.1.2. Note however that the fuel penalty calculation does not distinguish between the effects of thermodynamic and combustion efficiency on the fuel economy. Recall that the SI mode is run slightly rich when first switching to SI from HCCI, in order to help deplete the catalyst oxygen storage. Also, the typically very late spark timings on cycles *SI 0,1* may leave much of the fuel incompletely oxidized, which can also go onto help deplete the catalyst oxygen storage. Thus, a significant part of the fuel penalty on cycles *SI 0,1* may actually be due to de-oxygenation of the catalyst, and so is not truly a penalty because this would have to be done anyway when nominal SI operation is reached.

Operating Load	Avg. HCCI Duration (cycles)	$\bar{FP}^{HCCI}$ (%/cycle)	FP^{SI0-1} (%/cycle)	$\bar{FP}^{SI2-5}$ (%/cycle)
2.4 bar NMEP	4	1.08	1.69	1.07
3.2 bar NMEP	4	1.11	1.67	1.03
Average	4	1.095	1.680	1.050

Table C.2: Summary estimates for HCCI-SI transition duration and fuel economy penalty. All data are taken at 2000 RPM.

Appendix D

Modified Recursive Least Squares Parameter Update Law to Avoid Estimator Wind-Up

In Sec. 5.2.1, it was observed that after a large number of adaptive iterations, the model-inverse based SI-HCCI combustion control structure with adaptive model parameters could exhibit diverging parameter estimates, which could result in outrageous controller performance. The source of this phenomenon was traced to an issue known as estimator wind-up, wherein the controller tracks the reference very well so that little new information is obtained in successive observations, which can be shown to cause the standard recursive least squares algorithm with exponential forgetting to become unstable. The are several methods to deal with this problem, the simplest one being to conditionally prevent the recursive least squares algorithm from updating under certain criteria which gauge the information in the measurements. For the implementation in this dissertation, a method known as directional forgetting is used, which has the advantage that it automatically rules out redundant information through its mathematical formulation, without having to tune any threshold-based criteria. The applied directional forgetting algorithm can be found in [64], though several variants of the algorithm exist.

To demonstrate the efficacy of the directional forgetting recursive least squares algorithm, the SI-HCCI transition simulation stability study of Sec. 5.2.1 is repeated using the directional forgetting algorithm without changing any other simulation parameters. Example trajectories of the parameter estimates in succesive SI-HCCI mode transition iterations are plotted in Fig. D.1, in the same style as for Fig. 5.5 for comparison. As can be seen, the parameter estimates remain flat as the number of adaptive iterations increases, and no explosion of the parameter values occurs as was observed with the baseline recursive least squares algorithm. Also plotted are the condition numbers of the P matrix in successive adaptations in Fig. D.2, where it can be seen that the update law remains much more well conditioned than in the baseline case. Note that condition numbers for the combustion phasing correlations P matrix does not settle to a constant, however its number itself is very small and so should not be a concern. Also, the condition number of the P matrix for the k_r adaptation is still fairly high compared to the other correlations, but this is hard to avoid for the k_r correlation due to the much larger size of one parameter than the other. Finally, the input and output trajectories at the same iteration instances as for the baseline recursive least

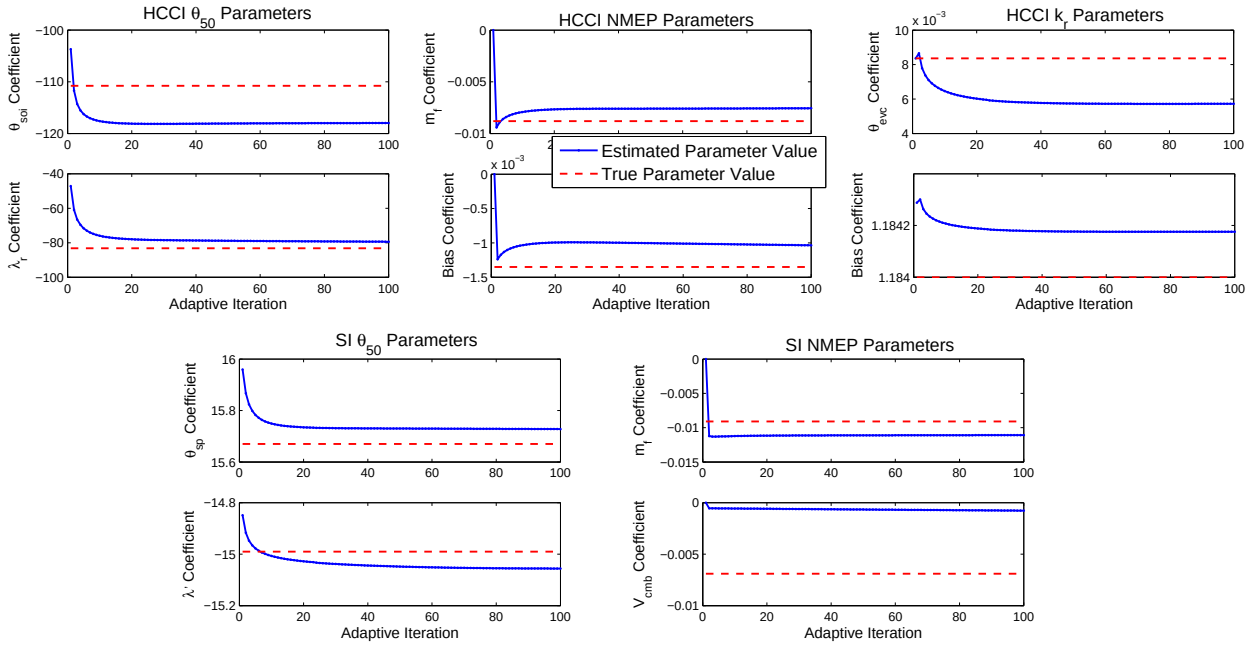

Figure D.1: Parameter trajectories for each adaptive model correlation in simulation of successive closed-loop SI-HCCI adaptive trials for the modified recurisve least squares algorithm with directional forgetting. Forgetting factor kept at value of 0.94 from successive adaptation experiments.

squares update in Fig. 5.6 are plotted in Fig. D.3. As can be seen, on the 82nd adaptive iteration where the baseline controller exhibited a very poor performance, the modified control scheme with the directional forgetting update law retains the same strong performance as in the 15th adaptive iteration, since very little new information is obtained between the 15th and 82nd iteration.

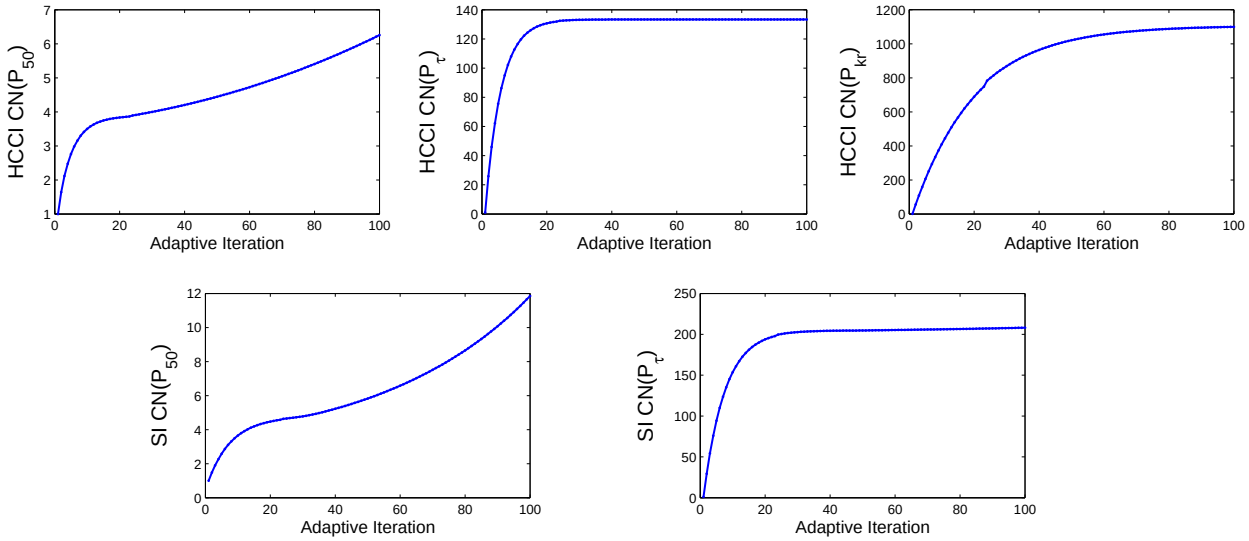

Figure D.2: P matrix condition number of directional forgetting recursive least squares algorithm in simulation of successive closed-loop SI-HCCI adaptive trials. Forgetting factor kept at value of 0.94 from successive adaptation experiments.

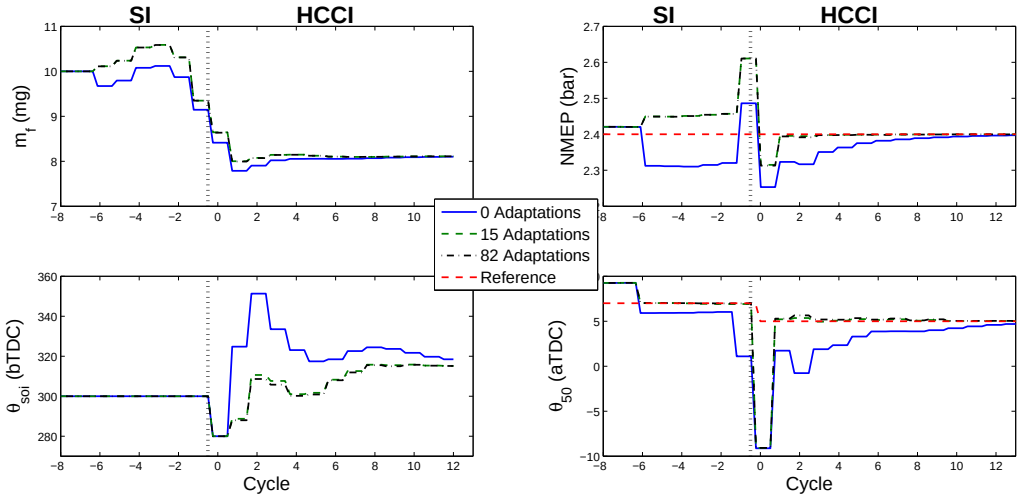

Figure D.3: Input (left) and output (right) simulation responses at severeal instances throughout successive closed-loop SI-HCCI adaptive trials with directional forgetting recursive least squares algorithm. Forgetting factor kept at value of 0.94 from successive adaptation experiments.

Bibliography

[1] G. A. Lavoie, E. Ortiz-Soto, A. Babajimopoulos, J. B. Martz, and D. N. Assanis. Thermodynamic sweet spot for high-efficiency, dilute, boosted gasoline engines. *Int. J. Engine Res*, 0(0):1–19, 2012.

[2] Advanced combustion engine R and D: Goals, strategies, and top accomplishments. Technical report, US Department of Energy, 2012.

[3] A. Cairns and H. Blaxill. The effects of combined internal and external exhaust gas recirculation on gasoline controlled auto-ignition. *SAE Technical Paper 2005-01-0133*.

[4] J. Farrell, J. Stevens, and W. Weissman. Second law analysis of high efficiency low emission gasoline engine concepts. *SAE Technical Paper*, 2006-01-0491.

[5] S. Onishi, S. Hong Jo, K. Shoda, P. Do Jo, and S. Kato. Active thermo atmospheric combustion (atac) - a new combustion process for internal combustion engines. *SAE Technical Paper*, 790501, 1979.

[6] F. Zhao, T. Asmus, D. Assanis, J. Dec, J. Eng, and P. Najt. *Homogeneous Charge Compression Ignition (HCCI) Engines: Key Research and Development Issues*. SAE International, 2003.

[7] H. Sherazi and Y. Li. Homogeneous charge compression ignition engine: A technical review. IEEE Conference on Automation and Computing, 2010.

[8] G. Shaver, J. Gerdes, and M. Roelle. Physics-based modeling and control of residual-affected HCCI engines. *J. Dyn. Sys., Meas., Control*, 131(2), 2009.

[9] S. Jade, E. Hellström, A. Stefanopoulou, and L. Jiang. On the influence of composition on the thermally-dominant recompression HCCI combustion dynamics. ASME Dynamic Systems and Control Conference, 2011.

[10] N. Ravi, H. Liao, A. Jungkunz, and J. Gerdes. Modeling and control of exhaust recompression HCCI using split injection. IEEE American Control Conference, 2010.

[11] P. Caton, A. Simon, J. Gerdes, and C. Edwards. Residual-effected homogeneous charge compression ignition at low compression ratio using exhaust reinduction. *Int. J. Engine Res.*, 4(3):163–177, 2003.

[12] C. Chiang and A. Stefanopoulou. Control of thermal ignition in gasoline engines. IEEE American Control Conference, 2005.

[13] G. Haraldsson, P. Tunestal, B. Johansson, and J. Hyvonen. HCCI closed-loop combustion control using fast thermal management. *SAE Technical Paper*, 2004-01-0943.

[14] Y. Wang, S. Makkapati, M. Jankovic, M. Zubeck, and D. Lee. Control-oriented model and dynamometer testing for a single-cylinder, heated air HCCI engine. *SAE Technical Paper*, 2009-01-1129.

[15] G. Haraldsson, P. Tunestal, and B. Johansson. HCCI combustion phasing in a multi-cylinder engine using variable compression ratio. *SAE Technical Paper*, 2002-01-2858.

[16] L. Manofsky, J. Vavra, D. Assanis, and A. Babajimopoulos. Bridging the gap between HCCI and SI : Spark- assisted compression ignition. *SAE Technical Paper*, 2011-01-1179.

[17] G. Lavoie, J. Martz, M. Wooldridge, and D Assanis. A multi-mode combustion diagram for spark assisted compression ignition. *Combustion and Flame*, 157(6):1106–1110, 2010.

[18] T. Itoh, A. Iiyama, S. Muranaka, and Y. Takagi. Combustion characteristics of a direct-injection stratified charge SI engine. *JSAE Review*, 19, 1998.

[19] E. Hellström, A. Stefanopoulou, J. Vavra, A. Babajimopoulos, D. Assanis, L. Jiang, and H. Yilmaz. Understanding the dynamic evolution of cyclic variability at the operating limits of HCCI engines with negative valve overlap. *SAE Int. J. Engines*, 5(3):995–1008, 2012.

[20] L. Koopmans, H. Ström, S. Lundgren, O. Backlund, and I. Denbratt. Demonstrating a SI-HCCI-SI mode change on a Volvo 5-cylinder electronic valve control engine. *SAE Technical Paper 2003-01-0753*.

[21] H. Santoso, J. Matthews, and W. Cheng. Managing SI/HCCI dual-mode engine operation. *SAE Technical Paper 2005-01-0162*.

[22] Y. Zhang, H. Xie, N. Zhou, T. Chen, and H. Zhao. Study of SI-HCCI-SI transition on a port fuel injection engine equipped with 4VVAS. *SAE Technical Paper*, 2007-01-0199.

[23] N. Milovanovic, D. Blundell, S. Gedge, and J. Turner. SI-HCCI-SI mode transition at different engine operating conditions. *SAE Technical Paper 2005-01-0156*.

[24] G. Tian, Z. Wang, Q. Ge, J. Wang, and S. Shuai. Control of a spark ignition homogeneous charge compression ignition mode transition on a gasoline direct injection engine. *Proceedings of the Institution of Mechanical Engineers, Part D: Journal of Automobile Engineering*, 221(867), 2007.

[25] A Cairns and H. Blaxill. The effects of two-stage cam profile switching and external EGR on SI-CAI combustion transitions. *SAE Technical Paper 2007-01-0187*.

[26] N. Kalian, H. Zhao, and J. Qiao. Investigation of transition between spark ignition and controlled auto-ignition combustion in a v6 direct-injection engine with cam profile switching. *Proc. of the Institution of Mech. Engineers, Part D: J. Automobile Engineering*, 222:1911–1926, 2008.

[27] H. Wu, N. Collings, S. Regitz, J. Etheridge, and M. Kraft. Experimental investigation of a control method for SI-HCCI-SI transition in a multi-cylinder gasoline engine. *SAE Technical Paper 2010-01-1245*.

[28] T. Nier, A. Kulzer, and R. Karrelmeyer. Analysis of the combustion mode switch between SI and gasoline HCCI. *SAE Technical Paper 2012-01-1105*.

[29] H. Kakuya, S. Yamaoka, K. Kumano, and S. Sato. Investigation of a SI-HCCI combustion switching control method in a multi-cylinder gasoline engine. *SAE Technical Paper 2008-01-0792*.

[30] A. Widd, R. Johansson, P. Borgqvist, P. Tunestål, and B. Johansson. Investigating mode switch from SI to HCCI using early intake valve closing and negative valve overlap. *SAE Technical Paper 2011-01-1775*.

[31] T. Matsuda, H. Wada, T. Kono, T. Nakamura, and T. Urushihara. A study of a gasoline-fueled HCCI engine mode changes from SI combustion to HCCI combustion. *SAE Technical Paper 2008-01-0050*.

[32] J. Etheridge, S. Mosbach, M. Kraft, H. Wu, and N. Collings. A detailed chemistry simulation of the SI-HCCI transition. *SAE Technical Paper*, 2010-01-0574.

[33] T. Kuboyama, Y. Moriyoshi, K. Hatamura, T. Yamada, J. Takanashi, and Y. Urata. A study of control strategy for combution mode switching between HCCI and SI with the blowdown supercharging system. *SAE Technical Paper*, 2012-01-1122.

[34] M. Roelle, G. Shaver, and J. Gerdes. Tackling the transition: A multi-mode combustion model of SI and HCCI for mode transition control. ASME International Mechanical Engineering Congress and Exposition, 2004.

[35] G. Shaver, M. Roelle, and J. Gerdes. Modeling cycle-to-cycle dynamics and mode transition in HCCI engines with variable valve actuation. *Control Engineering Practice*, 14:213–222, 2006.

[36] J. Ghojel. Review of the development and applications of the wiebe function: a tribute to the contribution of ivan wiebe to engine research. *Int. J. Engine Res.*, 11(297), 2010.

[37] X. Yang, G. Zhu, and Z. Sun. A control oriented SI and HCCI hybrid combustion model for internal combustion engines. ASME DSCC, 2010.

[38] X. Yang and G. Zhu. A two-zone control oriented SI-HCCI hybrid combustion model for the HIL engine simulation. IEEE American Control Conference, 2011.

[39] X. Yang and G. Zhu. SI and HCCI combustion mode transition control of an HCCI capable SI engine. *IEEE Trans. Control Sys. Tech.*, 2012.

[40] S. Zhang and G. Zhu. Model-based mode transition control between SI and HCCI combustion. ASME Dynamic Systems and Control Conference, 2014.

[41] N. Ravi, M. Jagsch, J. Oudart, N. Chaturvedi, D. Cook, and A. Kojic. Closed-loop control of SI-HCCI mode switch using fuel injection timing. ASME Dynamic Systems and Control Conference, 2013.

[42] P. Gorzelic, P.Shingne, J. Martz, A. Stefanopouou, J. Sterniak, and L. Jiang. A Low-Order Adaptive Engine Model for SI-HCCI Mode Transition Control Applications with Cam Switching Strategies. *Int. J. Eng. Research*, 2015, Accepted.

[43] D. Lee, L. Jiang, H. Yilmaz, and A.G. Stefanopoulou. Air charge control for turbocharged spark ignition engines with internal exhaust gas recirculation. IEEE American Control Conference, 2010.

[44] L. Eriksson. Modeling and control of turbocharged SI and DI engines. *Oil & Gas Science and Technology-Rev. IFP*, 62(4), 2007.

[45] A. Karnik, J. Buckland, and J. Freundenberg. Electronic throttle and wastegate control for turbocharged gasoline engines. IEEE American Control Conference, 2005.

[46] L. Jiang, A. Stefanopoulou, J. Vanier, and H. Yilmaz. Parameterization and simulation for a turbocharged spark ignition direct injection engine with variable valve timing. *SAE Technical Paper*, 2009-01-0680.

[47] J. Jensen, A. Kristensen, S. Sorenson, N. Houbak, and E. Hendricks. Mean value modeling of a small turbocharged diesel engine. *SAE Technical Paper*, 910070.

[48] P. Moraal and I. Kolmanovsky. Turbocharger modeling for automotive control applications. *SAE Technical Paper*, 1999-01-0908.

[49] L. Eriksson and I. Andersson. An analytic model for cylinder pressure in a four stroke SI engine. *SAE Technical Paper*, 2002-01-0371.

[50] M. Jankovic and S. Magner. Variable cam timing: consequences to automotive engine control design. IFAC Triennial World Conference, 2002.

[51] L. Eriksson. Mean value models for exhaust system temperatures. *SAE Technical Paper*, 2002-01-0374.

[52] S. Jade, E. Hellström, J. Larimore, A. Stefanopoulou, and L. Jiang. Reference governor for load control in a multi-cylinder recompression HCCI engine. *submitted to IEEE Transactions on Control Systems Technology.*

[53] E. Hellström and A. Stefanopoulou. Modeling cyclic dispersion in autoignition combustion. IEEE Conference on Decision and Control, 2011.

[54] C. Marriott and R. Reitz. Experimental investigation of direct injection-gasoline for premixed compression ignited combustion phasing control. *SAE Technical Paper*, 2002-01-0418.

[55] H. H. Song and C. F. Edwards. Understanding chemical effects in low-load-limit extension of homogeneous charge compression ignition engines via recompression reaction. *Int. J. Engine Research*, 10:231–250, 2009.

[56] C. Mayhew, K. Knierim, N. Chaturvedi, S. Park, J. Ahmed, and A.Kojic. Reduced-order modeling for studying and controlling misfire in four-stroke hcci engines. IEEE Conference on Decision and Control, 2009.

[57] N. Ravi, M. Roelle, H. Liao, A. Jungkunz, C. Chang, S. Park, and J. Gerdes. Model-based control of HCCI engines using exhaust recompression. *IEEE Trans. Control Sys. Tech.*, 18(6):1289–1302, 2010.

[58] G. Shaver, J. Gerdes, M. Roelle, P. Caton, and C. Edwards. Dynamic modeling of residual-affected homogeneous charge compression ignition engines with variable valve actuation. *J. Dyn. Sys. Meas. Control*, 127(3):374–81, 2005.

[59] D. Rausen, A. Stefanopoulou, J. Kang, J. Eng, and T. Kuo. A mean value model for control of homogeneous charge compression ignition (HCCI) engines. *J. Dyn. Syst. Meas. Control*, 127(3):355–362, 2005.

[60] N. Ravi, H.-H. Liao, A. Jungkunz, C.-F. Chang, H. Song, and J. Gerdes. Modeling and control of an exhaust recompression HCCI engine using split injection. *J. Dyn. Syst. Meas. Control*, 134:231–250, 2012.

[61] H. Yun, O. Guralp, R. Grover, and P. Najt. The effect of temperature and oxygen concentration on auto-ignition at low-load operating conditions in a gasoline homogeneous charge compression ignition engine. *Int. J. Engine Research*, 14(5):512–524, 2013.

[62] X. He, M. Donovan, B. Zigler, T. Palmer, S. Walton, M. Woolridge, and A. Atreya. An experimental and modeling study of iso-octane ignition delay times under homogeneous charge compression ignition conditions. *Combustion and Flame*, 142:266–275, 2005.

[63] S. Nüesch, A. Stefanopoulou, L. Jiang, and J. Sterniak. Fuel Economy of a Multimode Combustion Engine With Three-Way Catalytic Converter. *ASME J. Dyn. Systems, Measurement, and Control*, 137, 2015.

[64] K. Astrom and B. Wittenmark. *Adaptive Control*. Addison-Wesley, 1995.

[65] P. Gorzelic and A. Stefanopoulou. Model-based Feedback Control for Cam Switching SI-HCCI Mode Transitions without Open-Loop Sequence Scheduling Part 1: Baseline Control Architecture and Experimental Validation. *IEEE Trans. Control Sys. Tech.*, 2015, Submitted.

[66] D. Schwarzmann. *Nonlinear Internal Model Control with Automotive Applications*. PhD thesis, Ruhr-Universität Bochum, 2007.

[67] P. Gorzelic and A. Stefanopoulou. Model-based Feedback Control for Cam Switching SI-HCCI Mode Transitions without Open-Loop Sequence Scheduling Part 2: Online Parameter Adaptation. *IEEE Trans. Control Sys. Tech.*, 2015, Submitted.

[68] I. Kolmanovsky and D. Yanakiev. Speed Gradient Control of Nonlinear Systems and its Applications to Automotive Engine Control. *Japanese Journal of Automatic Control*, 47(3):160–168, 2008.

[69] D. Swaroop, J. Gerdes, P. Yin, and J. Hedrick. Dynamic Surface Control of Nonlinear Systems. IEEE American Control Conferencel, 1997.